

---

This item was submitted to [Loughborough's Research Repository](#) by the author.  
Items in Figshare are protected by copyright, with all rights reserved, unless otherwise indicated.

## Modelling CPV

PLEASE CITE THE PUBLISHED VERSION

PUBLISHER

© Ian Richard Cole

PUBLISHER STATEMENT

This work is made available according to the conditions of the Creative Commons Attribution-NonCommercial-NoDerivatives 4.0 International (CC BY-NC-ND 4.0) licence. Full details of this licence are available at:  
<https://creativecommons.org/licenses/by-nc-nd/4.0/>

LICENCE

CC BY-NC-ND 4.0

REPOSITORY RECORD

Cole, Ian R.. 2019. "Modelling CPV". figshare. <https://hdl.handle.net/2134/18050>.

# Modelling CPV

---

*by Ian Richard Cole*

## **DOCTORAL THESIS**

Submitted in partial fulfilment of the requirements for the reward of

**Doctor of Philosophy of Loughborough University**

January 2015

Copyright © 2015

by Ian Richard Cole

# Abstract

A methodology for the simulation of CPV systems is presented in four distinct sections: input, optics, uncertainty and electrical output.

In the input section, existing methods of describing the solar irradiation that is incident at the primary optical element of a CPV system are discussed, the inadequacies of the existing methods are explored and conditions of validity for their use drawn. An improved and spectrally extended model for a variable, spatially resolved solar image is arrived at. The model is used to analyse losses at the primary concentration device stage under varying solar profiles and air masses. A contextual analysis of an example Seattle based CPV system operating with constant solar tracking errors of 0.3-0.4° show a corresponding loss in isolation available to the optical system of 5-20%, respectively.

In the optics section, an optical ray trace model is developed specifically for this work. The optical ray trace model is capable of the spectrally resolved ray tracing of all insolation input models discussed above. Plano-convex and Fresnel lenses are designed, investigated and compared using each of the insolation models described in the input section. Common CPV component material samples for the plano-convex and Fresnel lenses are analysed for their spectrally resolved optical properties. The computational expense of high resolution spatial and spectral modelling is addressed by means of a spectrally weighted banding method. The optical properties parameter spectral weighting method can be applied to any arbitrary spectral band. The bands used herein correspond to the active ranges of a typical triple-junction solar cell. Each band shows a different spectral dependency. Banded beam irradiation proportions are shown to change by as much as 10% in absolute terms within the air mass range of 1 to 3. Significant variations in spectrally banded illumination profiles are found with the extended light source insolation model. These banded variations are mostly unaccounted for with the use of approximated insolation models, further compounding the argument for extended light source Sun models in CPV system simulations.

In the uncertainty section, the limitations of the manufacturing process are explored. Manufacturing tolerance errors from manufacturer datasheets are presented. These production uncertainties are used in the design of an erroneous plano-convex lens which is then analysed with the optical modelled presented in the optics section and compared to the ideal design specification. A 15% variation in maximum intensity value is found alongside a linear shift in the focal crossover point of approximately 0.2mm, although the optical efficiency of the lens remains the same. Framing manufacture errors are

investigated for a square Fresnel lens system resulting in a linear shift of the focal centre of approximately 0.85mm. A process for the calculation of wind loading force on a CPV array is also presented. The process uses real 2 second resolution wind data and highlights the chaotic nature of loading force. A maximum force of 1.4kN was found on an example day for a 3m by 3m by 0.1m cuboid (i.e. CPV array); corresponding to a wind speed of approximately 13m/s, which is well within the typical operating range of a CPV tracking system.

In the electrical output section, a spatially resolved solar cell model is identified and used for the investigation of solar cell performance under the inhomogeneous cell illumination profiles produced in the uncertainty section. Significant differences in the maximum power point of the cell IVs are found for the ideal and erroneous system illumination profiles. Approximately, a 15% variation is found in the plano-convex lens example, with a relative difference of 4% attributable to illumination profile distortion, and a 6% variation in the module framing component example. These results further highlight the need for the consideration of production uncertainties in CPV system simulation.

# Acknowledgements

I would like to thank my supervisor, Ralph Gottschalg, for his support, advice and patience throughout the course of this PhD. Ralph's honesty is refreshing among the complexities of academia.

I would also like to thank Tom Betts for his time and support throughout. Tom is someone of real integrity and his commitment to his principles is heart-warming.

All at CREST, past and present, deserve thanks for their part in making it such a pleasant environment in which to work. I've heard of many places where PhD research is a lonely undertaking and I am thankful that this was not the case for me.

The list of deserved thanks is numerous, though the reasons for them are simple. To this end, I would mostly like to express my wonder and joy at all acts of love and kindness. For without these not only would I not have succeeded in this but we would not be here.

Finally, I express my thanks to you, the reader. For without you this is pointless. May you find something here.



# Table of Contents

<b>1. Introduction</b>	<b>12</b>
1.1. Overview	12
1.2. Classification of CPV Systems	13
1.3. Subsystem Specification	14
1.3.1. Input Power Source	15
1.3.2. Optical Systems	15
1.3.3. Behavioural Uncertainties	16
1.3.4. Power Conversion System	16
<b>2. Input</b>	<b>17</b>
<b>2.1. Introduction</b>	<b>17</b>
2.1.1. Standardised Solar Flux	17
2.1.1.1. Incident Power	18
2.1.1.2. Spectrum	21
2.1.2. Synopsis	27
<b>2.2. Approximated Solar Distribution Models</b>	<b>28</b>
2.2.1. The Point Source Sun	29
2.2.1.1. Analysis	29
2.2.1.2. Conditions of Validity	32
2.2.2. The Pillbox Distribution	33
2.2.2.1. Analysis	33
2.2.2.2. Conditions of Validity	37
<b>2.3. The Sun as a Variable Extended Light Source</b>	<b>38</b>
2.3.1. Circumsolar Ratio (CSR) Modelling	39
2.3.1.1. CSR Definition & Visualisation	41
2.3.1.2. CSR Variation and Frequency	44
2.3.2. The Buie et al Model	46
2.3.2.1. Analysis	46
Extended Light Source Sunshapes	47
Volumetric Analysis	50
Model Output Analysis	52
2.3.3. Model Improvement	53
2.3.3.1. Overview	53

2.3.3.2. Test Case	56
2.3.4. Model Extension	58
<b>2.4. Results</b>	<b>60</b>
2.4.1. Conditions of Validity	60
2.4.2. Solar Profiles	61
2.4.2.1. 2D Solar Profiles	61
2.4.2.2. 3D Solar Profiles	62
2.4.3. Contextual Analysis	66
2.4.3.1. Ideal Solar Tracking	66
2.4.3.2. Non-ideal Solar Tracking	68
2.4.3.3. Annual Energy Harvests – Example Case	70
<b>2.5. Conclusions</b>	<b>72</b>
<b>3. Optics</b>	<b>74</b>
<b>3.1. Introduction</b>	<b>74</b>
3.1.1. Geometric Optics	75
3.1.1.1. Law of Reflection	75
3.1.1.2. Law of Refraction	76
3.1.2. Concentration	78
3.1.2.1. Maximal Concentration	78
3.1.2.2. Geometric Concentration	80
3.1.2.3. Optical Concentration	80
3.1.2.4. Examples of Concentrators	80
2D – Parabolic Trough	80
3D – Paraboloidal Dish	83
3.1.2.5. System Classification	84
3.1.3. Synopsis	85
<b>3.2. Material Properties</b>	<b>86</b>
3.2.1. Absorption Coefficient	86
3.2.1.1. Overview	86
3.2.1.2. Absorption Coefficient Data	87
Low Iron Soda-lime Glass	87
PMMA	89
3.2.2. Refractive Index	91
3.2.2.1. Overview	91
3.2.2.2. Refractive Index Data	92
Low Iron Soda-lime Glass	92

PMMA	94
3.2.3. Anti-reflection Coatings (ARCs)	96
3.2.3.1. Overview	96
Index Matching ARCs	98
Interference ARCs	99
Textured ARCs	99
3.2.3.2. Example	99
3.2.4. CPV Material Properties Overview	100
<b>3.3. The Plano-convex Lens</b>	<b>101</b>
3.3.1. Description	101
3.3.1.1. Parametric Description	101
3.3.1.2. Volume	102
3.3.2. Use in CPV	103
3.3.3. Focal Point Calculation	103
3.3.3.1. Lensmaker's Equation	104
3.3.3.2. Edge Ray Case Analysis	105
Convex Surface Primary	106
Planar Surface Primary	107
3.3.3.3. Focal Point Calculation Summary	108
Convex Surface Primary	108
Planar Surface Primary	109
<b>3.4. The Fresnel Lens</b>	<b>110</b>
3.4.1. Description	111
3.4.1.1. Parametric Description	111
3.4.1.2. Volume	112
3.4.2. Use in CPV	113
3.4.3. Focal Length Calculation	114
3.4.3.1. Focal Point Calculation Summary	114
Convex Surface Primary	114
Planar Surface Primary	115
<b>3.5. Modelling</b>	<b>116</b>
3.5.1. Reference Frame	116
3.5.2. Lens Front Mesh Generation	118
3.5.2.1. The Ideal Lens	118
The Ideal Plano-convex Lens Front Mesh	119
The Ideal Fresnel Lens Front Mesh	120
3.5.2.2. The General Lens	123

The General Plano-convex Lens Front	126
The General Fresnel Lens Front	126
3.5.3. Ray Trace Traversal	127
3.5.3.1. Input Rays	127
Primary Trace Phase	128
3.5.3.2. Plano-convex Lens Ray Tracing	128
Spherical Shell Rays	130
Planar Lens Back Rays	131
3.5.3.3. Fresnel Lens Ray Tracing	132
Spherical Shell Rays	134
Planar Lens Back Rays	136
Cylindrical Wall Rays	137
3.5.3.4. Ray Directional Changes – A Note on Optimisation	140
<b>3.6. Results</b>	<b>141</b>
3.6.1. Lens Volumes	141
3.6.2. Banded Irradiation Variations	142
3.6.3. 2D Modelling Illumination Profiles	145
3.6.3.1. Point Source Sun Traces	145
Plano-convex Lens	145
3 Facet Fresnel Lenses	147
20 Facet Fresnel Lens	148
3.6.3.2. Pillbox Source Sun Traces	150
Plano-Convex Lens	150
3 Facet Fresnel Lens	151
20 Facet Fresnel Lens	152
3.6.3.3. Extended Light Source Sun Traces	154
Plano-Convex Lens	154
3 Facet Fresnel Lens	155
20 Facet Fresnel Lens	157
3.6.4. 3D Modelling Illumination Profiles	159
<b>3.7. Conclusions</b>	<b>161</b>
<b>4. Uncertainty</b>	<b>163</b>
<b>4.1. Introduction</b>	<b>163</b>
4.1.1. Production Uncertainties	164
4.1.1.1. Lenses	165
Parameter Variation	165

Deformation	167
4.1.1.2. System Frames	167
The Array Frame	167
The Module Frame	171
4.1.2. Operational Uncertainties	172
4.1.2.1. Sun Tracking	173
Closed-loop Tracking Systems	173
Open-loop Solar Tracking Systems	175
Solar Tracking Accuracies	175
4.1.2.2. System Effects	176
Maximum Power Point Tracking	176
Cell & Module Interconnection Structures	177
DC to AC Conversion	178
4.1.3. Synopsis	178
<b>4.2. Lens Parameter Variation Effects</b>	<b>178</b>
4.2.1. Material Boundary Interface	179
4.2.2. 2D Lens Investigations	180
<b>4.3. Framing Variation Effects</b>	<b>186</b>
4.3.1. Example Frame Design	186
4.3.2. Optical Misalignment	189
<b>4.4. Sun Tracking – Wind Loading</b>	<b>194</b>
<b>4.5. Conclusions</b>	<b>199</b>
<b>5. Electrical Output</b>	<b>200</b>
<b>5.1. Introduction</b>	<b>200</b>
5.1.1. Solar Cells	201
5.1.1.1. Single-junction Solar Cells	202
Design Considerations	202
Operational Overview	204
5.1.1.2. Multi-junction Solar Cells	206
5.1.2. Synopsis	208
<b>5.2. Solar Cell Modelling</b>	<b>208</b>
5.2.1. 1D Solar Cell Modelling	208
5.2.1.1. One Diode Model	209
5.2.1.2. Two Diode Model	211
5.2.2. Spatially Resolved Device Modelling	212

<b>5.3. Illumination – Electrical Modelling</b>	<b>214</b>
5.3.1. PVONA Cell Design & Parameter Definition	214
5.3.2. Plano-convex Lens – Lens Manufacturing Uncertainty	215
5.3.2.1. Profile 1	215
5.3.2.2. Profile 2	217
5.3.2.3. IV Curve Comparison	218
5.3.3. Square Fresnel Lens – Module Framing Uncertainty	219
5.3.3.1. Profile 1	219
5.3.3.2. Profile 2	221
5.3.3.3. IV Curve Comparison	222
<b>5.4. Conclusions</b>	<b>223</b>
<b>6. Conclusions</b>	<b>224</b>
<b>6.1. Thesis Conclusions</b>	<b>224</b>
6.1.1. Input Modelling	224
6.1.2. Optical Modelling	224
6.1.3. Uncertainty Modelling	225
6.1.4. Electrical Modelling	226
<b>6.2. Recommendations for Future Work</b>	<b>226</b>
6.2.1. Input Modelling	226
6.2.2. Optical Modelling	227
6.2.3. Uncertainty Modelling	227
6.2.4. Electrical Modelling	228
<b>7. References</b>	<b>229</b>
<b>8. List of Publications</b>	<b>237</b>
<b>9. Appendix</b>	<b>238</b>
<b>9.1. Lens Volume Derivations</b>	<b>238</b>
9.1.1. The Plano Convex Lens	238
9.1.2. The Fresnel Lens	240
<b>9.2. Rotation Matrix Derivation</b>	<b>243</b>
9.2.1. Background	243
9.2.2. Reference Frame	243
9.2.3. Rotations about Conventional Axes	244
9.2.3.1. Derivation of 2D Rotation Matrix	244

9.2.3.2. 3D Rotation Matrices about Conventional Axes	246
Rotation about the x-axis	247
Rotation about the y-axis	247
Rotation about the z-axis	247
9.2.4. Rotations about Arbitrary Axes	247
9.2.4.1. Rotate to the x-z plane	248
9.2.4.2. Rotate to the z-axis	250
9.2.4.3. Rotate About the z-axis	252
9.2.4.4. Reverse Rotate from z-axis	252
9.2.4.5. Reverse Rotate from x-z plane	254
9.2.4.6. Rotation About an Arbitrary Axis	256
9.2.5. Reference Calculations	257
9.2.5.1. To the z-axis	257
9.2.5.2. To the z-axis and about	258
9.2.5.3. To the z-axis, about & to x-z plane projection	259
9.2.5.4. To the z-axis, about & back to original axis	259

# 1. Introduction

## 1.1. Overview

Concentrator photovoltaics (CPV) is a solar energy conversion technology that utilises optical concentration systems to achieve high efficiency conversion of sunlight to electrical power. These concentration systems increase the effective insolation intensity at the PV device and hence reduce the amount of active PV material required to generate a given power intensity. This proves an economically effective strategy as the expense of high efficiency PV devices, such as multi-junction solar cells (MJSCs), can be offset by relatively inexpensive optical components.

For the most part, optical systems are used in CPV to compound the economic argument for the terrestrial application of MJSCs. The most efficient solar cells in production today are known as multi-junction (MJ) cells. The current<sup>1</sup> efficiency record for these cells is 44.7%[1].

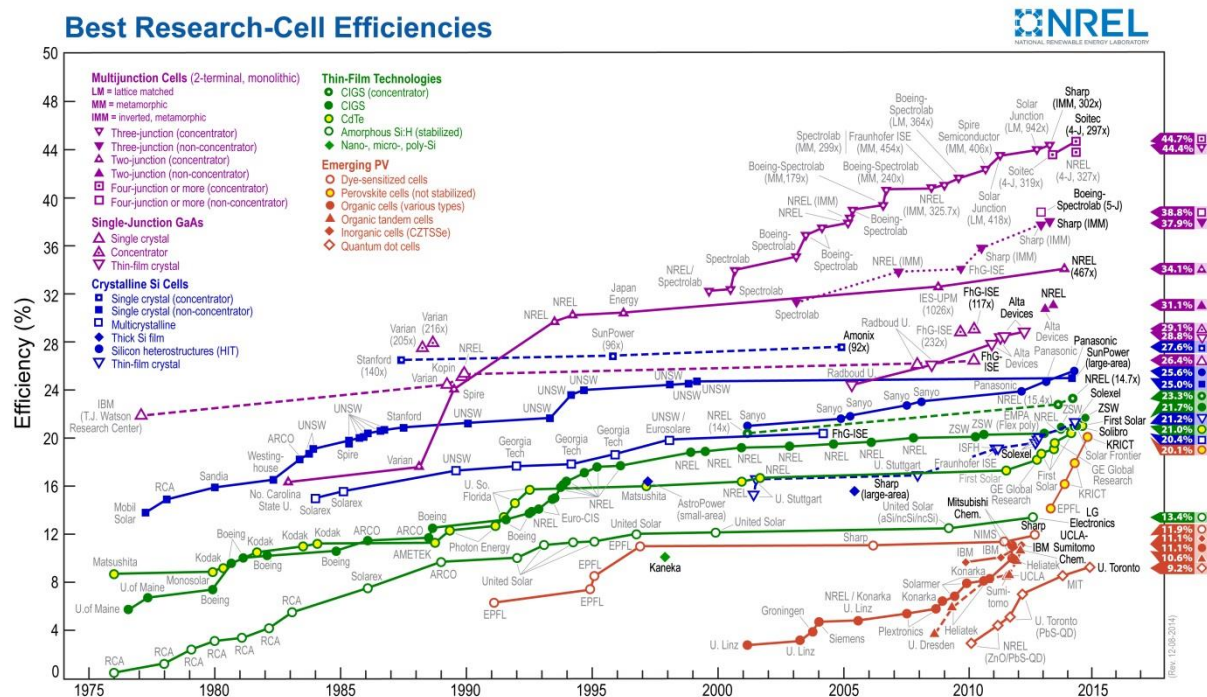


FIGURE 1.1: NREL BEST RESEARCH-CELL CONVERSION EFFICIENCIES (JANUARY 2015)

As can be seen from Figure 1.1, MJSCs (top right) are currently around twice as efficient as their crystalline silicon counterpart. These multi-junction solar cells are commonplace in space applications where the ratio of concern is output power per unit mass. However, terrestrial applications are typically concerned with output power per unit currency and the relatively complicated manufacturing

<sup>1</sup> Date of publication: January 2015

process of multi-junction cells cannot compete economically with other cell technologies for direct use.

The first CPV System was developed in 1976 by Sandia National Laboratories, USA. A 1kW peak power array was built to help understand and overcome the problems associated with CPV technology. Much was learnt from this project and accordingly CPV development was expedited[2].

Since its inception, CPV technology has been a promising player in the quest for cheap photovoltaic electricity. Although the current CPV market share is small (<1% of the PV market[3]) the technology still holds much promise as a viable, efficient and renewable terrestrial energy generation technology in regions of high direct normal irradiance (DNI)[4-8]. The market share is expected to increase towards the 1% figure by 2017, due mainly to developments in the USA Sunbelt region, although there are few companies now dealing in large scale CPV. This development opportunity is an exciting prospect for CPV technologists, particularly with respect to energy yield prediction and performance analysis. To fully realise this potential will require accurate modelling tools as any uncertainty in the modelling will result in increased financial risk (and thus higher financing costs).

## 1.2. Classification of CPV Systems

Modern CPV systems generally fall under one of four categories:

TABLE 1.1: CONCENTRATOR SYSTEM CLASSIFICATION AND EXAMPLES

	Reflective	Refractive
2D (Linear Focus)	Parabolic Trough	Cylindrical Lens
3D (Point Focus)	Paraboloidal Dish	Fresnel Primary

Table 1.1 gives a general classification of CPV systems differentiated by dimensional requirements and primary concentration mechanism. However, this is by no means an exhaustive list. There are many mechanisms for concentration and thus much experimentation in its exploitation. For example, there exist luminescent and radiative concentration mechanisms though these are rarely applied to the field of CPV. It is not uncommon for both reflective and refractive mechanisms to be used in a given concentration system although the design specification of these systems is typically determined by the primary concentration mechanism, hence the classifications of Table 1.1 are mostly suitable. For reference, more exhaustive overviews can be found in[9, 10] where further differentiations are drawn, such as: imaging and non-imaging systems.

Typically, reflective concentration systems utilise inexpensive, highly reflective materials to focus the incident sunlight. Example materials are polished aluminium, silvered glass and coated plastics with broadband reflection coefficients of around 85, 90 and 95%, respectively. Refractive systems, on the other hand, utilise inexpensive, lightweight, refractive materials with high transmission coefficients to focus the incident sunlight. Common materials include polymethyl methacrylate (PMMA) and silicone on glass (SOG) with broadband optical transmission coefficients of around 85 and 95%, respectively.

This thesis is concerned primarily with 3D point focus refractive systems employing the Fresnel lens as a primary concentration device. These are currently the most prolific CPV systems in deployment and typically operate under the highest solar concentrations. As such, they are referred to as high concentration photovoltaic (HCPV) systems.

### 1.3. Subsystem Specification

In the following section, the technological basis of the CPV system is discussed, the subsystems identified and the thesis structure outlined.

CPV systems are among the most complex PV power generation systems on the market. This is due to the increased number of system components. For example, a typical CPV System comprises tracking mechanisms that hold arrays of solar modules and orient them normal to the Sun. CPV solar modules comprise receivers that retain optical concentration devices that cast solar rays onto a solar cell. This interdependent subsystem structure means that the process of holistic system modelling is a non-trivial problem.

The logical flow of the interdependencies of CPV system components allows for a simple segregation of subsystems, as presented schematically in Figure 1.2.

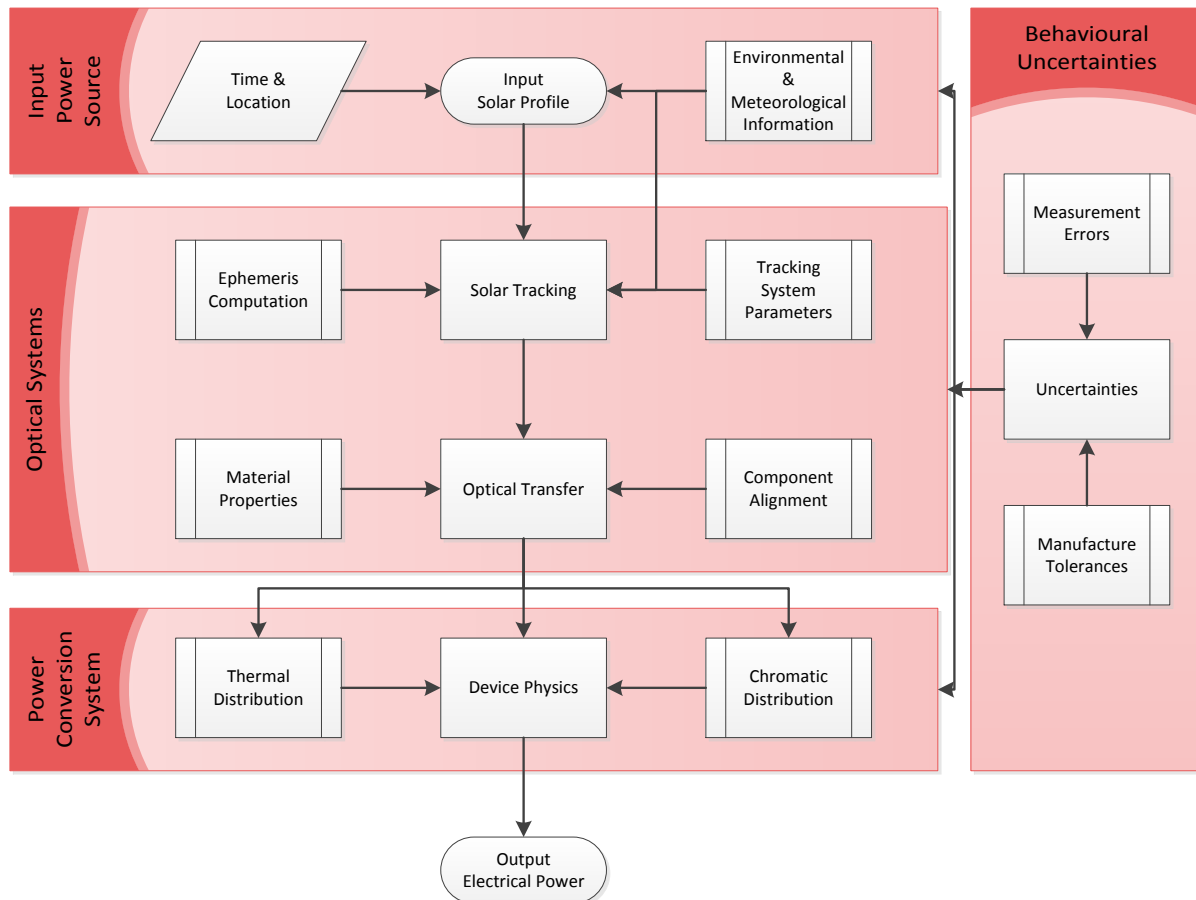


FIGURE 1.2: CPV SYSTEM &amp; SUBSYSTEMS FLOWCHART

Each of the CPV subsystems, presented in Figure 1.2, present their own technological challenges. Likewise, the simulation of each subsystem presents its own logistical challenge. This thesis is structured such that each subsystem is considered individually. A brief overview of these subsystems follows.

### 1.3.1. Input Power Source

By definition, the input power source to any solar energy conversion system is the Sun. Chapter 2, 'Input', introduces solar models of various complexities and compares and contrasts these models in the context of CPV. Problems with the use of overly assumptive solar models in CPV system simulations are identified and an updated input solar resource model, offering more insight into variations in the distribution of solar irradiation in the context of CPV, is presented.

### 1.3.2. Optical Systems

Both active (solar tracking) and passive (component alignment) optical systems are dealt with in chapter 3, 'Optics'. Insolation transfer through the concentration system is here discussed. Key optical material parameters; such as absorption coefficient and refractive index; are here addressed in the

CPV context. Particular attention is paid to spectral variation and resolution in CPV system simulation. Appropriate methods for the consideration of spectrally dependent phenomena at low resolutions; and the inclusion of optical misalignment and component placement errors are presented. Various example lenses are analysed and their behaviours discussed.

### 1.3.3. Behavioural Uncertainties

Chapter 4, ‘Uncertainty’, deals with uncertainties in the production and operation of CPV systems and discusses the effects of these uncertainties on system performance. In particular: lens production error, aluminium extrusion error, frame bending, and tracking error are discussed. Resultant variations in the illumination profile at the solar cell are analysed.

### 1.3.4. Power Conversion System

The focus of chapter 5, ‘Electrical Output’, is to provide an overview of PV device physics simulations and discuss the effects of the results of subsystem uncertainties on the output power of the CPV system.

# 2. Input

*the Solar Resource*

## 2.1. Introduction

The output of any conversion system is a function of input. In the context of photovoltaics the input of concern is sunlight and the output electrical power:

$$P = f(\varphi)$$

EQUATION 2.1

*Where P is electrical power and φ solar flux*

The very nature of this direct relationship highlights the importance of realistic source description on solar energy conversion system performance predictions.

Today, the Sun is described as a near spherical plasmonic mass with a radius of greater than 695,000km and a surface temperature of approximately 5,800K about which the Earth orbits on an elliptical path at over 100,000km/h. Day and night come about from the Earth's rotation and declination. Storms and meteorological phenomena from atmospheric disturbances often attributed to variations in pressure.

This chapter serves as an investigation into the description of terrestrially received solar flux and offers model comparisons and improvements in the context of high concentration photovoltaic systems.

### 2.1.1. Standardised Solar Flux

*'In space no one can hear you scream...'<sup>2</sup>*

...but at least it's constantly predictably sunny. Outside of the Earth's chaotic atmosphere, the flux density of solar irradiation at 1 astronomical unit from the Sun varies approximately between 1.361 and 1.362kW/m<sup>2</sup> measured at solar minimum and maximum, respectively[11]. This near constant measure of distributed solar power is termed the solar constant. Due to the elliptical orbit of the Earth about the Sun, there is approximately a 7% variation in the solar irradiation as measured just outside the Earth's atmosphere throughout the year from aphelion to perihelion of 1.321 to 1.412 kW/m<sup>2</sup>, respectively.

---

<sup>2</sup> A quote from the 1979 film 'Alien'

In photovoltaic science the standard description of terrestrially received solar flux is an astronomical angular coordinate pair defining the relative solar position and an associated spectrally resolved power intensity in  $\text{W/m}^2/\text{nm}$ . Prediction of the relative location of the Sun is achievable to a high degree of accuracy by a variety of methods[12-19] and the angular coordinate pair for a given latitude, longitude and time is determined with very little uncertainty. Contrastingly, the weather is considered a chaotic system. The prediction of time-specific flux intensity is therefore too complicated for our current scientific models and prediction uncertainty increases greatly with time until the moment prediction and temporal resolution. There is, however, relatively little variation in net annual insolation and long-term predictive models are built on statistical interpretations of historical datasets[20, 21]. It is also possible to define predictive models assuming a given (often clear-sky) weather condition. The intensity generated by these models is then altered afterwards using a weather dependent variable. In the standard models this is done through the use of a clearness index that takes a value between zero and one and acts as a multiplication factor of the insolation predicted under clear-sky conditions. A review of many of the standard models as well as a further proposition is given by[22].

Some exceptions exist to the rule of chaos in the weather. Some terrestrial locations have very specific seasons during which the weather can be predicted with very little uncertainty. An example of such a predictable weather system is Almeria<sup>3</sup> in southern Spain where clouds typically appear in the sky for less than one week in the year only. On the other hand, the UK is subject to a particularly chaotic weather system, so much so that in 2009 the UK Met Office withdrew its seasonal forecasting service. The extreme difficulty of UK weather prediction arises from a number of factors, including the combined influences of weather systems from one of the Earth's largest oceans and one of the Earth's largest land masses that sit either side of the UK.

For brevity, solar flux intensity is often given integrated over the solar spectrum as an incident power value in  $\text{W/m}^2$ .

#### 2.1.1.1. Incident Power

At the Earth's surface solar flux density varies greatly. The most basic descriptions of solar flux are found in the qualitative conversational form in which descriptors such as 'sunny', 'clear', 'cloudy' and 'gloomy' are used to characterise the intensity of penetrative sunlight. The quantitative scientific equivalent of this simplistic description is found in the form of power per unit area at the Earth's surface and is normally given in units of  $\text{W/m}^2$ . At noon on a clear summer's day in the UK, one would

---

<sup>3</sup> Almeria's sunny climate is the major driving force behind it being Europe's fruit growing capital. It's also where John Lennon wrote Strawberry Fields Forever

expect to receive around 1000 watts of solar power per horizontal square metre. This is around 75% of the solar constant. Figure 2.1 shows the typical frequency distribution of hourly averaged global horizontal solar flux values for a typical year in Birmingham, UK. A total of 4538 hours are used here as the other 4122 hours were averaged as zero.

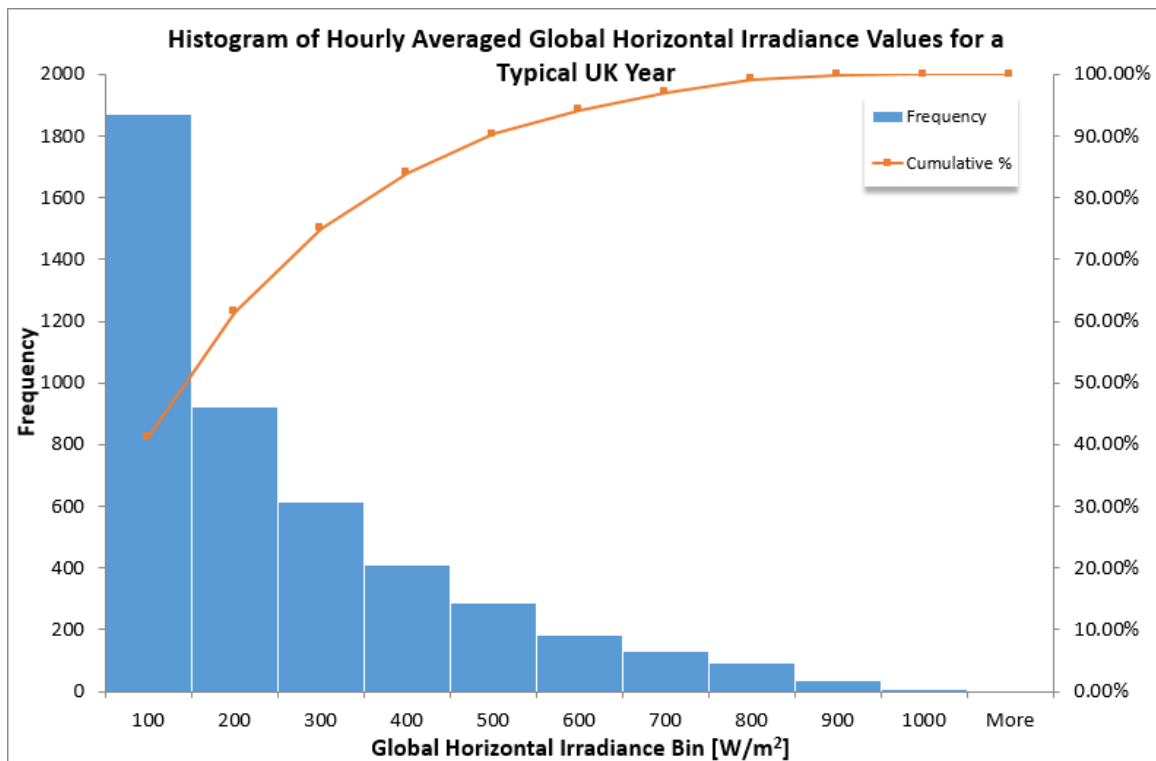


FIGURE 2.1: HISTOGRAM OF HOURLY AVERAGED GLOBAL HORIZONTAL SOLAR IRRADIANCE VALUES FOR BIRMINGHAM, UK

The low insolation values and high cloud levels associated with Birmingham, UK, ensure it is not an appropriate location for the application of CPV systems . For contrast, the frequency distribution for a more suitable location, The Gambia, is shown in Figure 2.2. Again, a total of 4538 hours are used here as the other 4122 hours were averaged as zero.

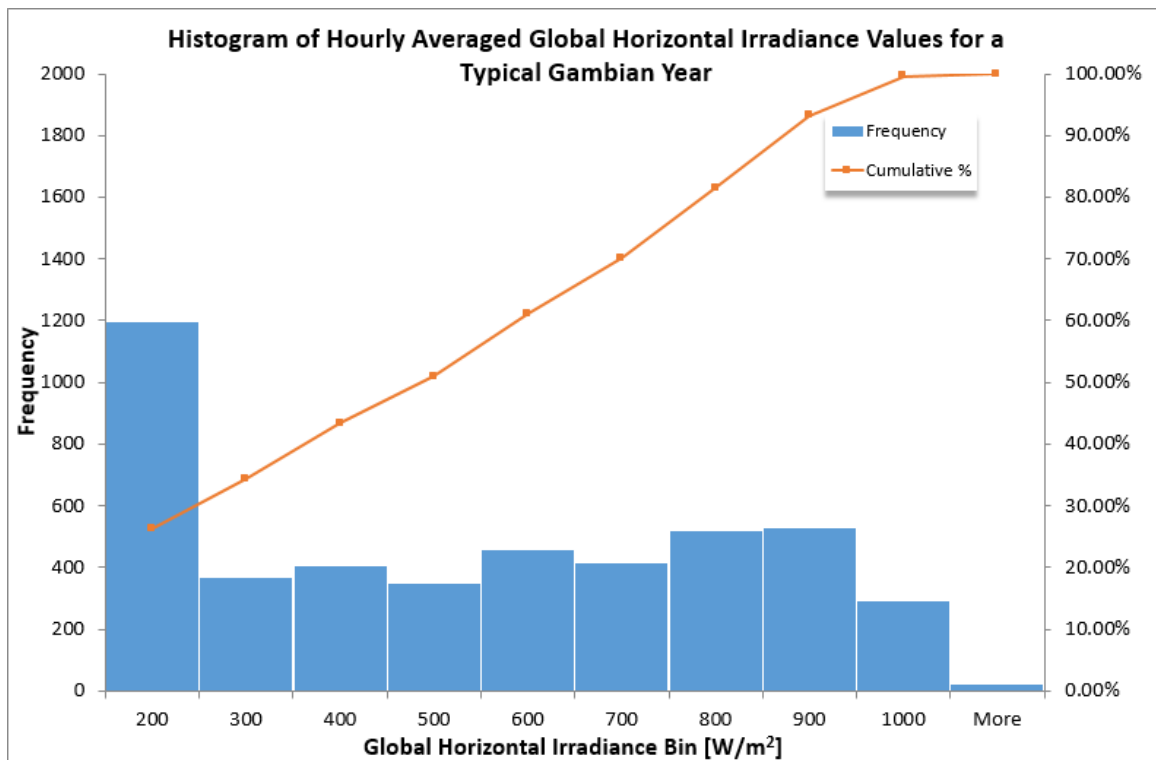


FIGURE 2.2: HISTOGRAM OF HOURLY AVERAGED GLOBAL HORIZONTAL SOLAR IRRADIANCE VALUES FOR DAKAR, SENEGAL

A significant difference is found between the two distributions. Birmingham, UK, has an average hourly insolation value of  $104\text{W/m}^2$  and Dakar, Senegal, an average of  $245\text{W/m}^2$ . The global meteorological database, Meteonorm[20] was used to generate the above data. The use of data for Dakar, Senegal, to represent the Gambian solar climate is indicative of the low spatial resolution of available meteorological data in much of Africa. Regardless, this comparison confirms the intuitive notion that terrestrial insolation patterns are very much localised.

A somewhat more informative description of insolation is arrived at by subdividing solar flux into 3 categories: beam, diffuse and albedo. Beam radiation comes directly from the Sun and is incident within some paraxial limit; diffuse radiation is scattered throughout the sky and mostly appears blue due to Rayleigh scattering; and albedo radiation is that radiation reflected from Earth-bound entities.

A very general indication of relative proportions is that at midday with a clear sky, solar irradiance composed of about 85% beam, 13% diffuse and 2% albedo radiation would be considered normal. In reality the composition changes dramatically with variables such as: cloud cover, air mass, atmospheric particulates, visible horizon outline and surrounding materials.

Many of the models referred to above include such differentiation. A variety of models exist to subdivide global irradiation[23, 24]. A notable difference between global irradiance division models is found in their consideration of diffuse irradiation, namely isotropic or anisotropic sky models. This is essentially a very basic form of spatial distribution consideration. Spatially distributed irradiation

profiles are necessary for the effective implementation of HCPV performance simulations and are discussed in detail in 2.3, ‘The Sun as a Variable Extended Light Source’.

### 2.1.1.2. Spectrum

Further detail is added to the solar flux description by means of spectral resolution. In this description, the incident solar energy is split into electro-magnetic frequency bands and the power residing in each band is presented. It is in this form that one finds the standard reference solar spectrum, AM1.5G where ‘G’ denotes ‘global’[25].

The extra-terrestrial spectrum, with which the solar constant is associated, has a static wavelength distribution near that of black body radiation at the surface temperature of the Sun, around 5800K. Black body radiation is calculated from Planck’s law[26].

$$B_\lambda(T) = \frac{2hc^2}{\lambda^5 \left( e^{\frac{hc}{\lambda k_B T}} - 1 \right)}$$

EQUATION 2.2

Where  $B_\lambda$  is the black body radiation at wavelength  $\lambda$  for temperature  $T$ ,  $h$  Planck’s constant,  $c$  the speed of light in a vacuum and  $k_B$  Boltzmann’s constant

Measured extra-terrestrial solar spectra, or top of the atmosphere spectra, often denoted as  $F_0(\lambda)$ , show some disagreement in certain wavelength bands. The maximal difference of 3 – 5% is found in the 445 – 510nm (blue) range. This difference is believed to be due to instrument calibration issues and a standardisation procedure has been developed to correct for these inconsistencies[27]. Thuiller et al’s measurement[28] is used in Figure 2.3.

Measurement of the extra-terrestrial spectra and comparison with prediction was another evidential confirmation for quantum theory, from which Planck’s law is derived. Classical theory proves an inadequate tool in this prediction. The Rayleigh-Jeans law makes the following prediction[29].

$$B_\lambda(T) = \frac{2ck_B T}{\lambda^4}$$

EQUATION 2.3

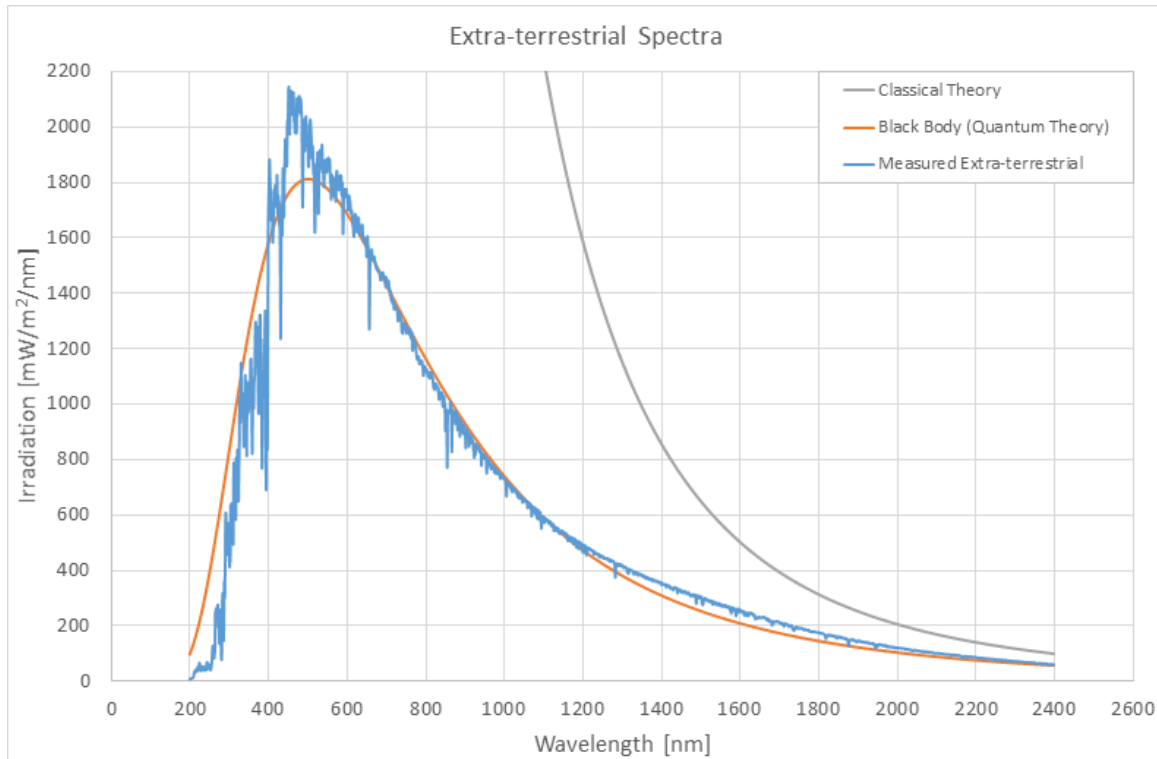


FIGURE 2.3: COMPARISON OF MEASURED EXTRA-TERRESTRIAL SOLAR SPECTRUM AND A BLACK BODY SPECTRUM AT THE SUN'S SURFACE TEMPERATURE

Figure 2.3 shows the measured extra-terrestrial spectrum and the calculated black body spectrum generated by a body in thermal equilibrium at a temperature of 5778K subtending a solid angle of  $6.87 \times 10^{-5}$  steradians calculated, from Equation 2.2. For interest the classical prediction, from Equation 2.3, is also shown.

The extra-terrestrial spectrum is a well-defined, standardised spectrum with little variation. Contrastingly, the terrestrially received spectrum varies greatly due to attenuation by the Earth's atmosphere. The prefix AM denotes air mass. AM is a measure of the amount of the Earth's atmosphere incident insolation traverses before reaching the surface. If one defines the relative location of the Sun as an angle,  $\theta$ , deviant from the normal to the Earth's surface, the AM is then approximated as:

$$AM \approx \frac{1}{\cos \theta}$$

EQUATION 2.4

*Where AM is air mass and  $\theta$  the solar angle deviation from the surface normal*

This approximation overlooks the curvature of the Earth. More accurate models exist for calculating effective air mass[30-33] but that is beyond the scope of this work and the above will suffice for the purpose of illustration.

Both the IEC6904-3 and ASTM G173 standards dictate the use of the AM1.5 spectrum in the standard test procedure used in obtaining a nameplate efficiency value for a flat plate solar module. From Equation 2.4 this corresponds to an angular abnormality in solar incidence, or solar zenith angle of approximately 48°. The atmospheric attenuation with AM1.5 results in an incident power of approximately 970W/m<sup>2</sup> it is the accepted convention to normalise this spectrum so that the total incident power becomes 1000W/m<sup>2</sup>. There are few standard models today considered acceptable for the adequate description of spectrally resolved solar energy[34, 35]. The AM1.5 spectrum generated by the SMARTS model[25, 36] is commonplace.

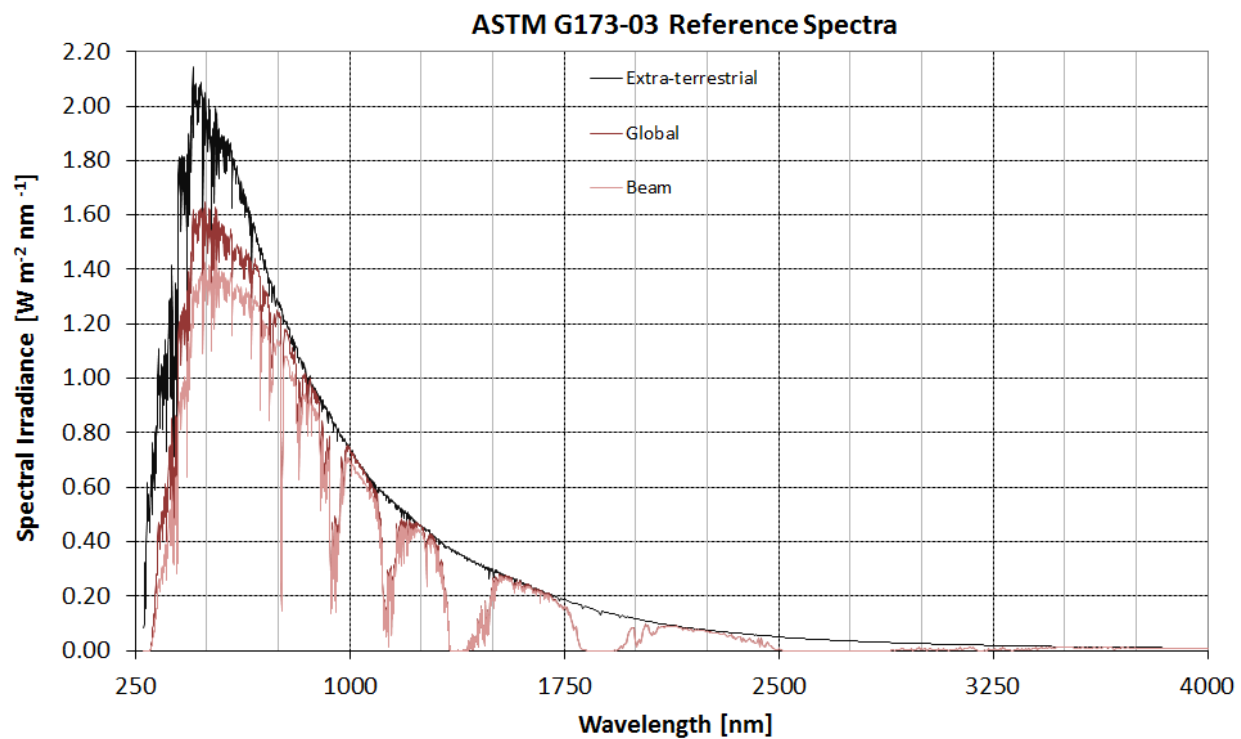


FIGURE 2.4: AM1.5 SOLAR SPECTRUM AS GENERATED BY SMARTS

Figure 2.4 shows the ASTM G173-03 standard reference spectra as generated by SMARTS. These are available freely online at[37]. The spectra are generated in spectral bands from 280 to 4000nm. The extra-terrestrial spectrum is given at one astronomical unit (au) from the Sun (the average Earth-Sun distance); the global tilt is given as that collected by a surface normal to the Sun (37° in this case) and is inclusive of diffuse and albedo components; and the beam spectrum is given as that radiation collected from the sky patch within a 2.5° radial half angle from the solar centre by a surface normal to the Sun. Although these spectra are used to characterise solar technologies and provide nameplate efficiencies, alone they are insufficient for system performance predictions as the intensity and spectral changes throughout the day are significant. Example hourly variations in solar spectrum are given in Figure 2.5.

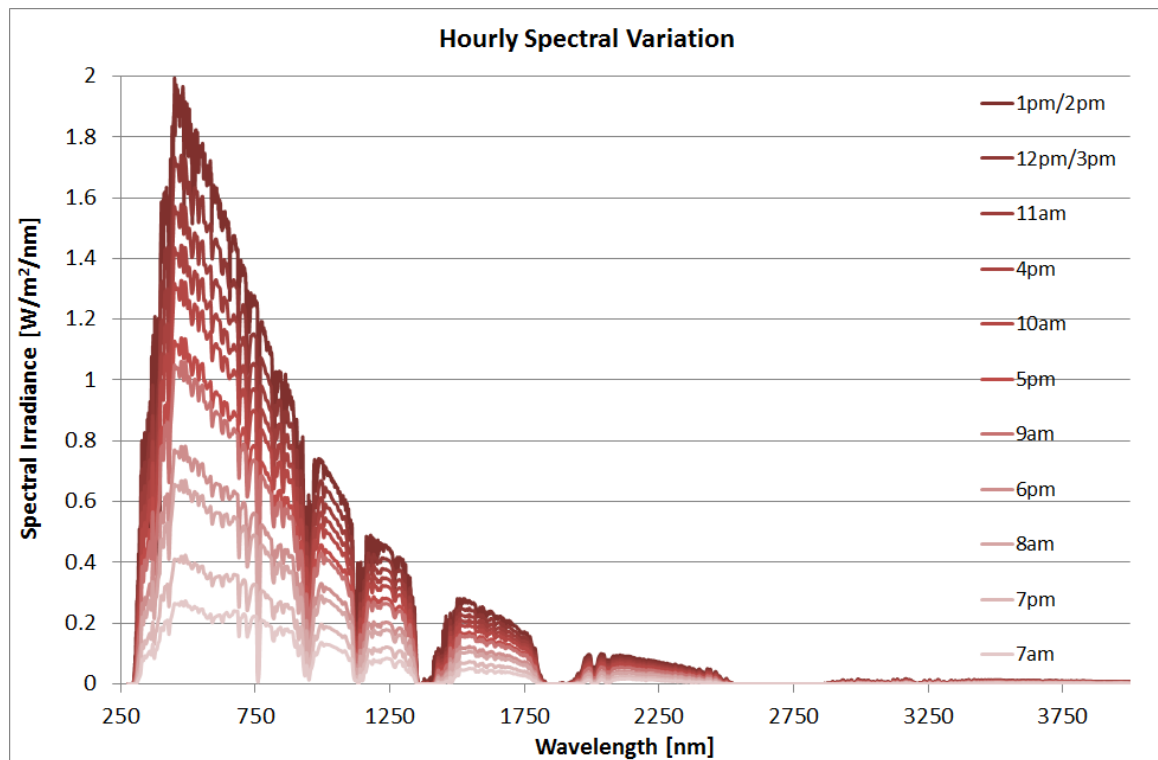


FIGURE 2.5: HOURLY VARIATIONS IN GLOBAL HORIZONTAL SOLAR SPECTRUM FOR THE SUMMER SOLSTICE IN ALMERIA

Figure 2.5 shows the hourly variations of solar spectrum as received from the whole sky by a flat horizontal surface on 21<sup>st</sup> June for Almeria, Spain, under clear sky conditions. The corresponding air masses for above the spectra as calculated from Equation 2.4 are given alongside net incident power summations in Table 2.1.

TABLE 2.1: CORRESPONDING AIR MASS AND INCIDENT POWER (GLOBAL HORIZONTAL) FOR TIME OF DAY ON 21<sup>ST</sup> JUNE IN ALMERIA, SPAIN

Time of Day	Air Mass	Incident Power [W/m <sup>2</sup> ]
7am	5	165
8am	2.5	393
9am	1.7	618
10am	1.4	771
11am	1.2	916
12pm	1.1	1009
1pm	1	1119

<b>2pm</b>	1	1119
<b>3pm</b>	1.1	1009
<b>4pm</b>	1.3	838
<b>5pm</b>	1.6	662
<b>6pm</b>	2.2	457
<b>7pm</b>	3.6	251

Standard flat-plate PV modules use the AM1.5 global spectrum for characterisation and the determination of nameplate efficiency values. The calculation of actual in-field performance is a wide topic with much academic research in the field[38-41] and the development of commercially available off-the-shelf software[42]. CPV module ratings use AM1.5 the direct spectrum. This standard is disputed by some as it ensures that all CPV modules have an inherent performance overestimation by comparison but the choice of the direct spectrum as the referencing standard for CPV is a result of the restriction on input radiation due to optical system design and the requirement of biaxial solar tracking. A triple junction cell active band specific analysis of direct spectrum variation with air mass is given in Table 2.2.

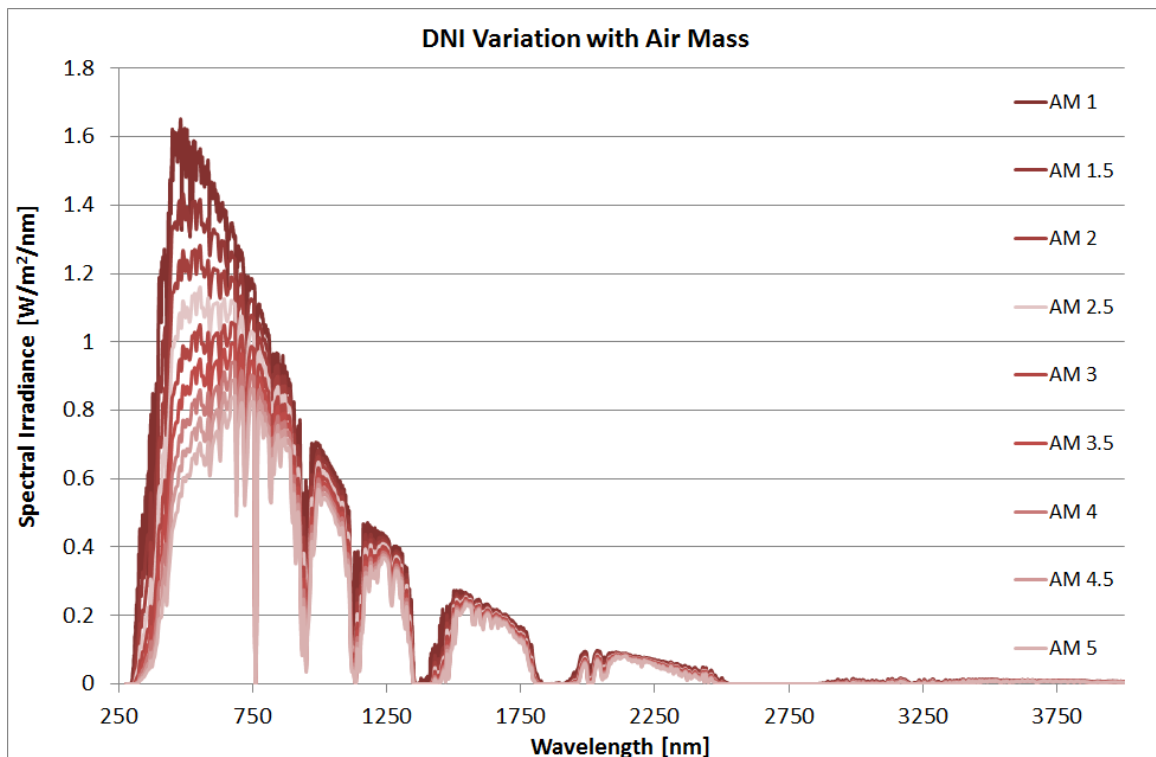


FIGURE 2.6: VARIATIONS IN DIRECT SPECTRUM WITH AIR MASS

Due to the spectral sensitivity of multi-junction cells, variations in air mass can prove detrimental to system performance. A typical germanium substrate triple junction cell operates with series connected semi-conductor band gaps of 1.86, 1.4 and 0.65eV[43]; corresponding to spectral responses in the wavelength bands 280-667, 667-886, and 886-1908nm; respectively. A variety of triple junction solar cell designs exist that utilise band gaps of around these energies. For generality, the wavelength ranges of 280-680, 680-880 and 880-1880nm are used for apportioned investigations herein. Table 2.2 gives an indication of the potential mismatch problems presented by variations in the band-biased attenuation of incident spectra. The absolute irradiation values are not a good indicator of mismatch as the junction absorptions vary, however, significant variations are found in normalised power. This is a better indicator of mismatch problems.

TABLE 2.2: POWER AVAILABLE IN SPECTRAL BANDS FOR VARIOUS INCIDENT DIRECT NORMAL SPECTRA

Air Mass	Power in Spectral Band [W/m <sup>2</sup> ]			Net Power [W/m <sup>2</sup> ]
	Absolute / Normalised			
	280-680nm	680-880nm	880-1880nm	
1	444 / 1	209 / 0.47	350 / 0.79	1004

<b>1.5</b>	387 / 1	197 / 0.51	327 / 0.84	911
<b>2</b>	340 / 1	188 / 0.55	312 / 0.92	840
<b>2.5</b>	300 / 1	178 / 0.59	293 / 0.98	770
<b>3</b>	269 / 1	169 / 0.63	282 / 1.05	720
<b>3.5</b>	236 / 1	160 / 0.69	269 / 1.14	665
<b>4</b>	210 / 1	152 / 0.72	257 / 1.22	619
<b>4.5</b>	188 / 1	145 / 0.77	247 / 1.32	579
<b>5</b>	168 / 1	138 / 0.82	211 / 1.26	516

The consideration of spectrally resolved solar irradiance as detailed above is useful for a great deal of applications in solar energy, especially flat-plate photovoltaics. Performance predictions of many varieties of solar cell technologies are calculated using the irradiance descriptions discussed. Atmospheric science understands well the effects of atmospheric changes on spectral composition and there exist many well established measurement campaigns and models that aid the understanding of these effects of solar cell behaviour.

This thesis, however, concerns HCPV. Not only are spectral variations more impactive in this technology due to the spectral sensitivity of multi-junction solar cells, but the coarse spatial separation of beam, diffuse and albedo irradiation is entirely insufficient in this context. The use of sub degree input aperture optical systems, being in the range of the approximately  $0.266^\circ$  angular subtense of the Sun, demand high resolution spatially resolved descriptions of the solar resource and spectral variations within this range should also be accounted for given that spectrally dependent phenomena may well be amplified by optical systems due to chromatic aberration.

### 2.1.2. Synopsis

As witnessed by a static terrestrial observer, the Sun is a bright, hazy circular patch of sky that moves through the visible celestial hemisphere with variations in intensity and colour that are most noticeable at dawn, midday and dusk. This Sun can be modelled with varying degrees of realism by assertions of approximation. Two extremely common solar source descriptions are the point source and pillbox Sun approximations[44-46]. Less common are extended light source descriptions[47, 48].

The extent to which modelling CPV with these input source descriptions affects the output is not well understood.

This chapter is concerned with the consideration of the Sun, as viewed from the surface of the Earth, as a spatially and spectrally resolved dynamic light source. Existing standard models are investigated and improved upon and comparisons are drawn.

## 2.2. Approximated Solar Distribution Models

The concept of direct normal irradiance is somewhat of a misnomer. A more befitting descriptor would be direct paraxial irradiance as only an infinitesimally small portion of that radiation directly from the Sun is truly normal, the rest is near normal or paraxial. In fact, that radiation from the Sun can be considered paraxial due to the small angular subtense of the solar disk. The ‘beam’ irradiation as measured by most meteorological systems, however, is that irradiation that radiation emanating from within 5° of the solar centre and the assumption that all this irradiation can be considered paraxial is ill-founded.

The standard method of locating the Sun is by a single astronomical coordinate pair. Underlying this method is the assumption that the Sun occupies an infinitesimally small portion of sky. This assumption is suitable in the application of modelling flat plate PV systems. However, the small entry aperture optical concentration systems used in HCPV require a more accurate model that better represents the physical properties of beam irradiation.

The zero subtended Sun in flat plate PV modelling is a reasonable approximation given that the acceptance angle of such systems is so large, having a near 90° half angle. The validity of the zero subtended Sun approximation can be investigated simply by assessing the ratio of the subtended areas. If this ratio is near zero, the approximation is effectively validated. The Sun actually subtends a half angle of 0.266°. The ratio of the two-dimensional areas subtended by the solid angles is found as the ratio of the squares of their sines:

$$\frac{\sin^2(0.266)}{\sin^2(90)} = 2 \times 10^{-5}$$

Approximating this as zero does not cause problems in flat plate PV modelling. However, in HCPV sub degree aperture angles are commonplace. For optical system with a 0.5° half angle input aperture the ratio of subtended solid angles is found as:

$$\frac{\sin^2(0.266)}{\sin^2(0.5)} = 0.283$$

Which means that 28.3% of the field of view of an HCPV optical system may be taken up by the solar disk. Approximating this as zero creates a troublesome source of error in CPV modelling.

This ratio of subtended angles is a useful metric in the validation of source description methods. To elaborate:

$$R_S = \frac{\sin^2 \theta_{Sun}}{\sin^2 \theta_{Lens}}$$

EQUATION 2.5

Where  $R_S$  is the ratio of subtended angles,  $\theta_{Sun}$  the radial half angle of the Sun and  $\theta_{Lens}$  the half angle entry aperture of the primary concentration lens

In the following section, two common approximations to the distribution of solar beam irradiation are analysed, namely the point source Sun and the pillbox distribution.

### 2.2.1. The Point Source Sun

#### 2.2.1.1. Analysis

CPV system performance models are commonly based on the assumption of a point source Sun. By considering the Sun as a point source, all solar power is assumed to radiate from one infinitesimally small point in sky:

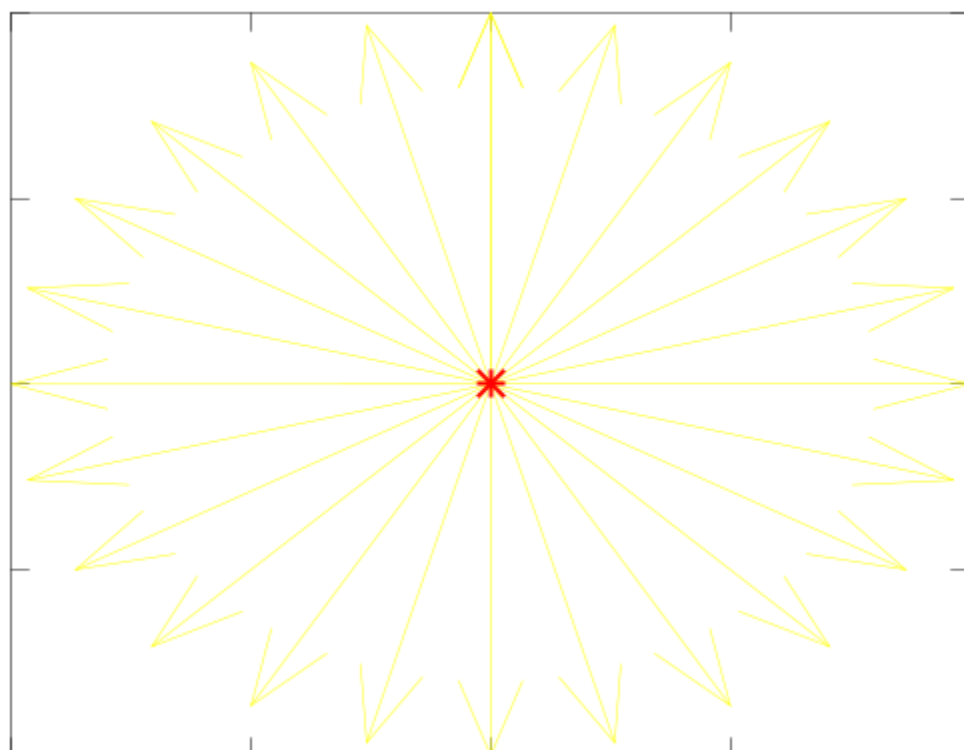


FIGURE 2.7: POINT SOLAR SOURCE SCHEMATIC

The average Earth-Sun distance, known as an astronomical unit (au), is approximately 150 Tm. Thus the apparent angular deviation of the point source Sun across an optical system of 1m is found as:

$$\sin^{-1} \frac{1}{150 \times 10^9} = 1 \times 10^{-13}$$

Thus, inherent in the point source Sun approximation is the assumption that all radiation from the Sun is received as a near perfect beam. This approximation is acceptable for many forms of research. Its validity for CPV simulations is investigated here.

Given that position of the Sun is known as an astronomical coordinate pair relative to the orientation of a defined optical system, rays can be generated from the point source and traced through the optical system onto a specified receiver plane. Hence an illumination pattern at the receiver can be determined. Rays can be defined to represent different spectral bands and some analysis of aberration performed.

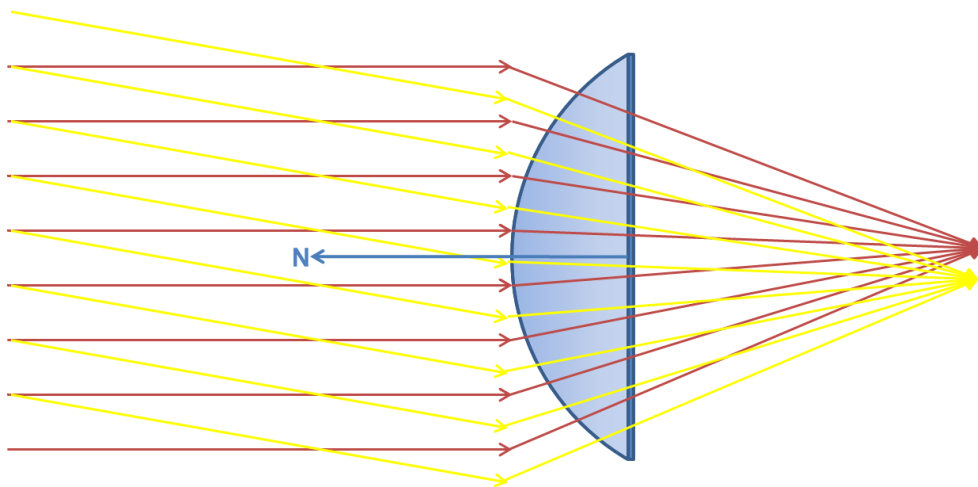


FIGURE 2.8: POINT SOURCE RAY TRACE SCHEMATIC WITH NORMAL (RED) AND ABNORMAL (YELLOW) SOLAR TRACKING

Figure 2.8 is a schematic representation of ray tracing the point source Sun through an optical system. The vector,  $\mathbf{N}$ , is the lens orientation vector (the tangent normal from the pinnacle point on the convex surface). Two scenarios are shown: normally and abnormally incident light in red and yellow, respectively. All light rays from the point source are considered parallel prior to interaction with the optical system.

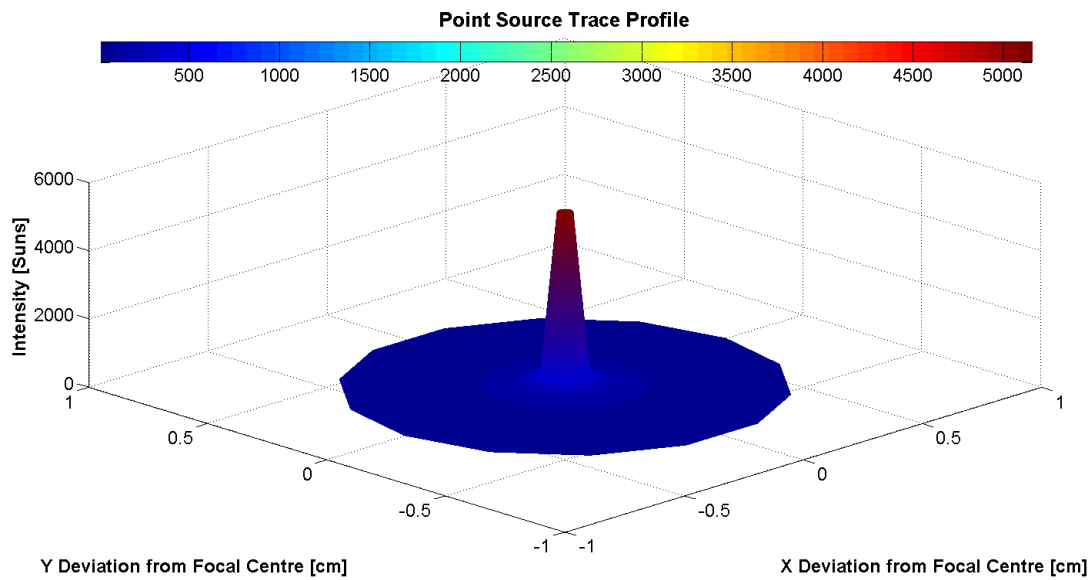


FIGURE 2.9: RECEIVER PLANE ILLUMINATION PROFILE EXAMPLE FOR A POINT SOURCE SOLAR DISTRIBUTION

Figure 2.9 is an example illumination profile as generated by ray tracing a normally incident point source Sun through a plano-convex lens. The lens had a front radius of 10cm and an angular restriction on the spherical section of  $\frac{\pi c}{6}$ . The receiver surface is placed approximately at the focal length of the lens. The refractive index was set to 1.49 and the absorption coefficient to  $0.05\text{cm}^{-1}$ . An intensity of one Sun is defined here as  $1000\text{W/m}^2$ .

The principle problem with this method is highlighted when considering the insolation available to the optical system as function of tracking error (solar abnormality). In this analysis large overestimations of incident power contained within the illumination profile are found with solar tracking errors near to the value of the primary lens entry aperture angle and invalid net power zeros are returned with tracking errors greater than the lens aperture. In fact, considering tracking error vs potential optical system irradiation harvest, the solar flux available to the optical system is bi-regional about the primary lens entry aperture angle for the point source estimation:

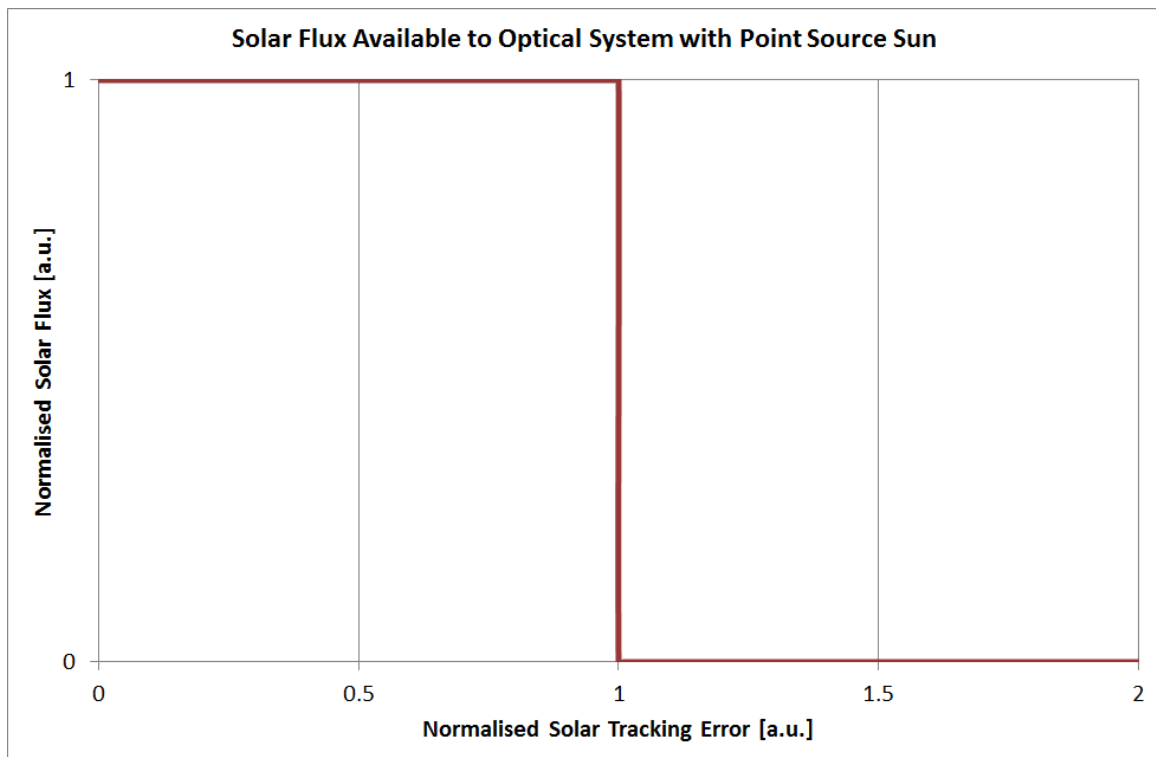


FIGURE 2.10: SOLAR FLUX AVAILABLE TO AN OPTICAL SYSTEM WITH A POINT SOURCE SUN

In Figure 2.10 the solar flux is normalised to the power incident on the primary concentration surface and the tracking error is normalised to the half-angle input aperture of the optical system. Technically, the flux = zero line would extend from a normalised tracking error of 1 to  $\frac{2\pi}{\theta_{Lens}} - 1$  at which point the flux = one line would extend to a normalised tracking error of  $\frac{2\pi}{\theta_{Lens}}$  before the pattern repeated, as it is periodic with period  $\frac{2\pi}{\theta_{Lens}}$ . Fortunately though, such wild tracking errors are not physically meaningful and the above figure simply offers a visualisation of the phenomenon.

This analysis is only representative of that solar flux available to the optical system at its surface in relation to its aperture. The actual collected solar flux is, of course, a function of its optical efficiency which is itself dependent on the solar tracking error. For example, the optical efficiency of the system used to generate Figure 2.9 as described above, is 38.3%. The input power at the lens front was 31.4W and the collected power at the receiver plane 12.0W.

#### 2.2.1.2. Conditions of Validity

This method may be considered valid if, and only if, the Sun is near normal to the optical system and the atmospheric conditions are such that nearly all solar beam irradiation is contained close to the solar centre. 'Close', however, is a relative term. For large angle entry aperture lenses, the radial angular extent of the solar disk can be considered close to the solar centre, i.e. the ratio of subtended angles,  $R_S$ , can be approximated as zero (see Equation 2.5).

One could impose the mathematical condition that, for low resolution simulations, the point source approximation is valid if:

$$\Delta T \ll \theta_{Lens}$$

EQUATION 2.6

and

$$\theta_{Sun} \ll \theta_{Lens}$$

$$\therefore R_S \approx 0$$

EQUATION 2.7

Where  $\Delta T$  is the solar tracking error,  $\theta_{Lens}$  the lens entry aperture half angle and  $\theta_{Sun}$  the radial angular extent of the central solar disk ( $\sim 0.266^\circ$ )

There are proposed as well as existing CPV systems for which these conditions are satisfied. However, in HCPV system design the compromise between system size, component cost and weight reduction results in the use of small entry aperture lenses, often in the sub-degree range. Thus the condition  $\theta_{Sun} \ll L_A$   $\theta_{Sun} \ll L_A$  is not satisfied and the point source approximation is invalid. Furthermore, given the accuracy of today's economically viable tracking systems[49], the condition  $\Delta T \ll L_A$   $\Delta T \ll L_A$  is rarely satisfied for systems with  $L_A < 1^\circ$ .

## 2.2.2. The Pillbox Distribution

### 2.2.2.1. Analysis

Another approximation to incident power distribution is achieved by spatial extension of the point source approximation. The pillbox distribution recognises that the Sun is better described as a solid circular disk, or pillbox:

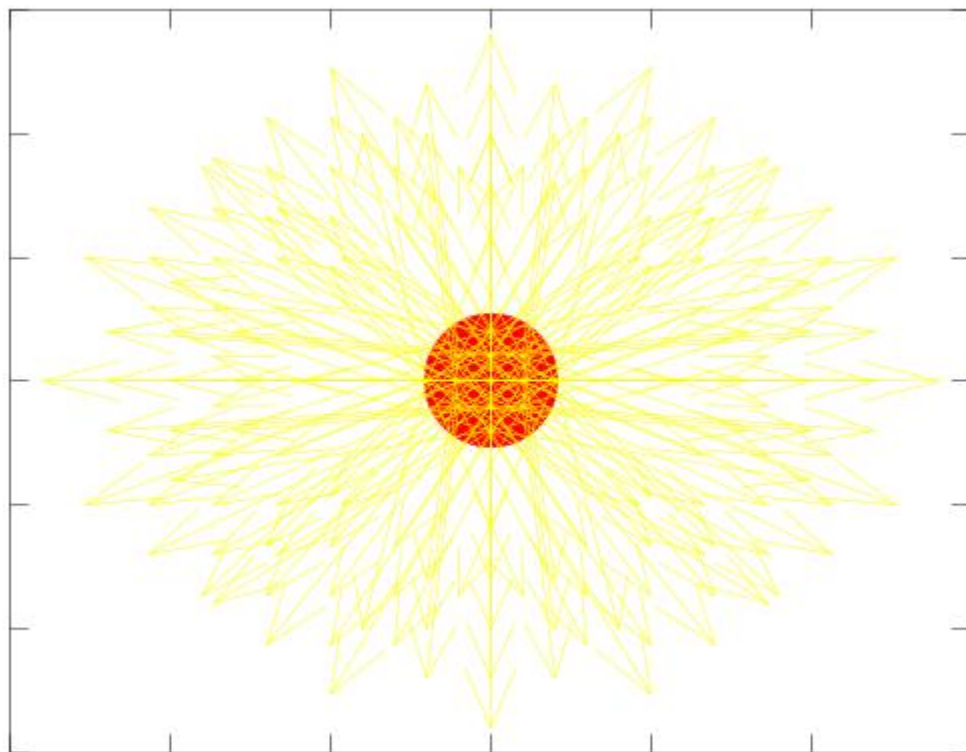


FIGURE 2.11: PILLBOX SOLAR SOURCE SCHEMATIC

The central solar disk is effectively the apparent size of the Sun due to Earth-Sun geometry. The radial half angle subtended by the central solar disk varies over the course of a year between 4.58 and 4.74mrad, the average being 4.65mrad or  $0.266^\circ$ [48, 50, 51]. Static averages at 1 au tend to be used for simulation, hence the pillbox subtends a radial half angle of  $0.266^\circ$ .

The use of the pillbox approximation somewhat mitigates the problems with large overestimations of incident power and invalid net power zeros found with near under and over aperture solar tracking errors in the point source description, respectively. With the pillbox distribution, an angularly resolved set of input rays can be generated and traced through a defined optical system on to a receiver plane. Rays can be defined to represent different spectral bands and a more realistic analysis of aberration performed.

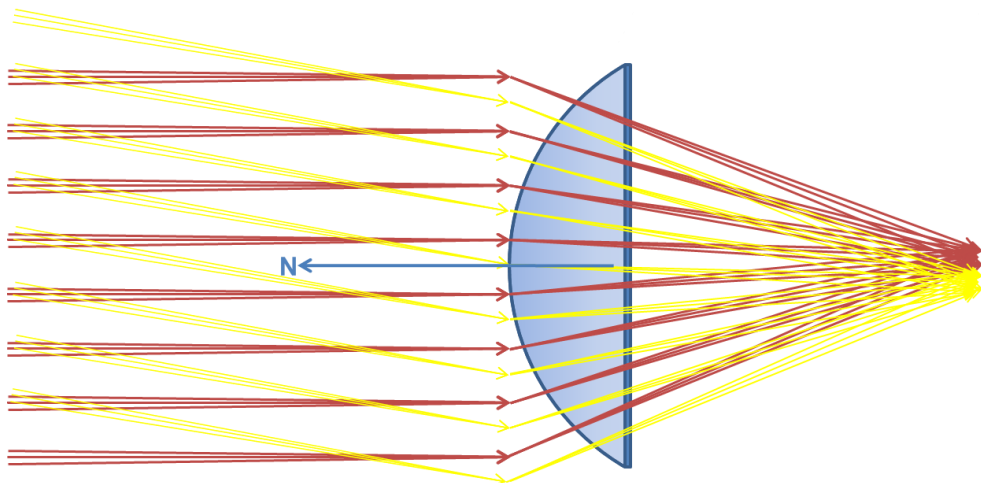


FIGURE 2.12: PILLBOX RAY TRACE SCHEMATIC

Figure 2.12 is a schematic representation of ray tracing the pillbox-distributed Sun through an optical system. The vector,  $\mathbf{N}$ , is the lens orientation vector (the tangent normal from the pinnacle point on the convex surface). Two scenarios are shown: normally and abnormally incident light in red and yellow, respectively. The light rays from the pillbox distribution have some angular deviation, although they are equal in intensity.

The pillbox distribution is a definite improvement on the point source approximation. Problems remain, however, with the unphysical assumption that all the solar beam irradiation is emitted homogeneously over a single solid angle segment of the sky hemisphere. Overestimations of flux available to the optical system are found when system solar tracking error approaches  $\theta_{Lens} - \theta_{Sun}$ . This is due to the inherent assumption that zero solar flux is contained outside the central solar disk, which is unrealistic. The resultant available flux overestimations become more radical when the true solar source has a greater spread of beam irradiation. Typically, the proportion of beam irradiation contained outside of the central solar disk varies between 2 and 30%, in dependence of a variety of atmospheric factors most notably including air mass, particulates, humidity and aerosol optical depth (AOD). This is elaborated in 2.3.3 Model Improvement. The insolation available to the optical system as function of solar abnormality for the pillbox distribution is plotted in Figure 2.13.

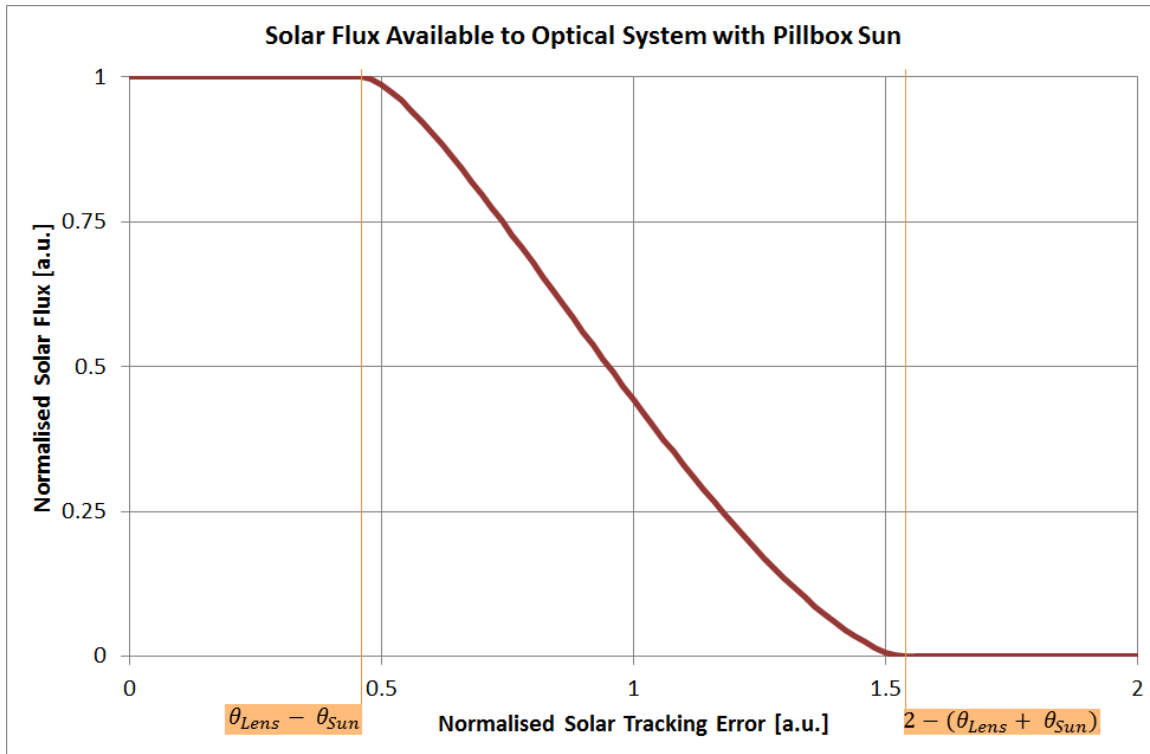


FIGURE 2.13: NORMALISED BEAM IRRADIATION HARVEST VS TRACKING ERROR FOR A 0.5° HALF ANGLE ENTRY APERTURE LENS

Figure 2.13 shows the drop in irradiance available to the optical system with increased solar tracking error for a pillbox-distributed Sun. The solar flux is normalised to the power incident on the primary concentration surface and the tracking error is normalised to the half-angle input aperture of the optical system. The extreme points of the variation at normalised fluxes of 1 and zero are found at normalised solar tracking errors of  $\theta_{Lens} - \theta_{Sun}$  and  $2 - (\theta_{Lens} + \theta_{Sun})$ , respectively. The point of inflection found at the normalised tracking error value of 0.874 is due to the move from divergence to convergence in the geometry of the overlapping circles as the pillbox escapes the lens entry aperture. The turning point varies as a function of input aperture. The system described above has a lens aperture of 0.5°. The actual point varies from near zero to near 1 as input aperture varies from  $\theta_{Sun}$  to 90°. The variation of this turning point is shown in Figure 2.14.

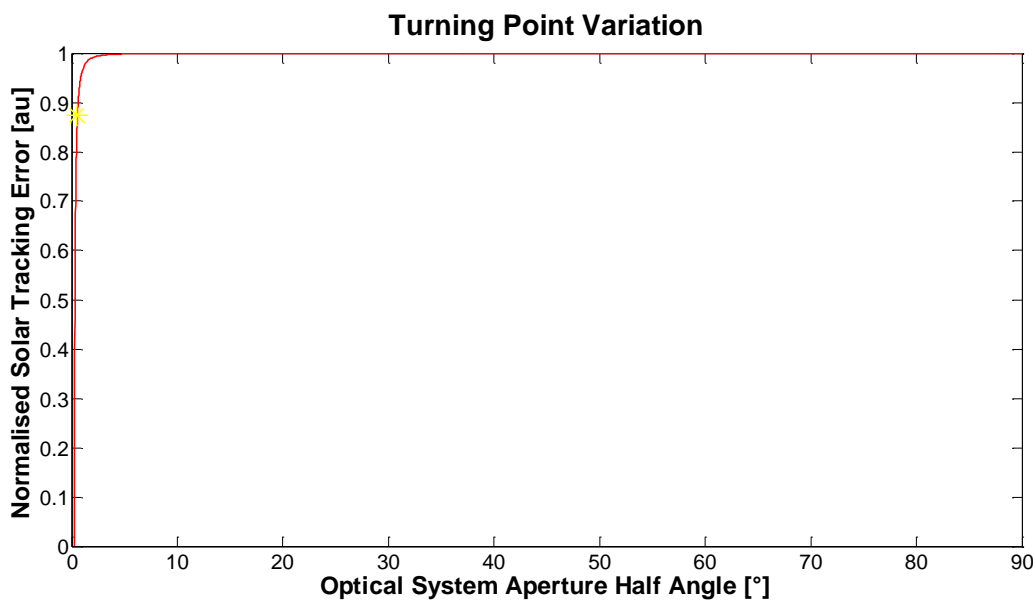


FIGURE 2.14: TURNING POINT VARIATION IN PILLBOX SOURCE AVAILABLE FLUX ANALYSIS

Figure 2.14 shows the variation of the turning point of Figure 2.13, as a function of optical system radial half angle input aperture, the  $0.5^\circ$  aperture system is highlighted for reference. Beyond radial half angle input apertures of  $5^\circ$  the turning point may well be estimated as 1 and the normalised available flux to solar tracking error (Figure 2.13) assumed symmetric about 1, with 1 corresponding to approximately 50% of available flux. For radial half angle input apertures less than  $5^\circ$  more care should be taken when considering available incident flux. The significance of the turning point is that it defines the tracking error value where the irradiation capture moves from overestimation to underestimation or vice versa.

#### 2.2.2.2. Conditions of Validity

The solar image is subject to changes in atmospheric conditions, such as humidity, air mass and composition of atmospheric particulates[52]. Changes in these parameters can change not only the power and spectrum received at the surface of the Earth, but also the scattering of the solar image and thus the distribution of beam irradiance about the solar centre. Therefore, a realistic calculation of spectrally resolved terrestrially received solar flux cannot be obtained with a static model. Both the point source and pillbox approximations constitute static models.

As the proportion of beam irradiation contained within the solar aureole increases, so does the inaccuracy of the pillbox approximation both in terms of power and spectrum associated with the projected illumination profile. As a general rule, spectral composition of irradiance changes more significantly with increased angular spread of the beam irradiation[52]. This is due to the scattering effect and the associated wavelength shift found in the circumsolar region.

One could impose the mathematical condition that, for low resolution simulations, the pillbox approximation is valid if:

$$\int_0^{\theta_{Sun}} \varphi d\theta \gg \int_{\theta_{Sun}}^{\theta_{Aureole}} \varphi d\theta$$

EQUATION 2.8

Where  $\theta_{Sun}$  is the angular extent of the central solar disk ( $\sim 0.266^\circ$ ),  $\theta_{Aureole}$  the angular extent of the solar aureole ( $\sim 2.49^\circ$ ),  $\varphi$  solar flux and  $\theta$  the angular distance from the solar centre

In many terrestrial locations this condition is not often enough met for simulations employing the above method to be considered valid if operating over any real extended time period.

Given that neither of the above approximations to power source descriptions are wholly satisfactory for HCPV simulation purposes, a description of solar flux for input modelling in HCPV simulations that is both spatially and spectrally resolved is now introduced.

## 2.3. The Sun as a Variable Extended Light Source

An Earth-bound entity receives angularly dependent radiation from the sky. The nature of this radiation changes with time, not only in its intensity but also in its spatial and spectral distribution. The relative movement of the Sun through the sky and the temporal and seasonal changes of the apparent colour of light are familiar to most. The idea that the spatial distribution of irradiation within that patch of sky we call the Sun also changes, is familiar to many. The appreciation of the beauty of sunsets, for example, evidences this. However, such variation is not considered in most CPV system simulations. Segmenting and mapping that patch of sky we call the Sun in such a way as to account for this variation is achieved through the use of a spatially and spectrally resolved solar image. This gives an input into CPV simulation that considers the Sun as a variable extended light source. Not only does this allow for CPV simulations to experience sunsets (which is not particularly useful given the low light intensity and solar elevation angle), but it also allows for the consideration of atmospheric effects that alter the distribution of solar flux; seasonal changes of the air-mass; and the resultant changes the illumination profile at the receiver. Ultimately, describing the Sun as a variable extended light source facilitates the investigation of changes in electrical output. The importance of these atmospheric effects have been recognised, for example, in the proposal of solar simulator adaptations for concentrator modules[53].

### 2.3.1. Circumsolar Ratio (CSR) Modelling

It can be derived from the laws of geometric optics that as the required concentration of an angular subtense tends to the maximum, the entry aperture of the concentration system tends toward that of the angular subtense. In order to achieve very high solar concentration ratios, HCPV uses small entry aperture lenses in the sub-degree range. The Sun occupies a significant proportion of this input range (see Equation 2.5). Unphysical approximations to the distribution of solar energy result in compromised system designs and energy ratings. Considering the Sun as a variable extended light source permits a more thorough investigation into system behaviour, mitigating the problems associated with these compromises.

For a given time, solar flux intensity varies with two angles:

$$\varphi_t = f(\alpha, \varepsilon, t)$$

EQUATION 2.9

Where  $\varphi_t$  is solar flux at time  $t$ ,  $\alpha$  azimuth angle and  $\varepsilon$  elevation angle

At a given point in time it is possible to calculate the position of the Sun relative to any terrestrial location. By assuming radial symmetry, the beam portion solar flux can then be reduced to a one dimensional dependency, as a function of angular deviation from the solar centre:

$$\varphi_{t,\theta} = f(\theta)$$

EQUATION 2.10

Where  $\theta$  is angular deviation from the solar centre

The variation of flux intensity with angular deviation from the solar centre has been measured. Throughout the 1970s and 1980s the Lawrence Berkley Laboratory (LBL) of California, U.S., conducted research into the properties of solar profiles. For this research, 11 sites across the United States were chosen, exhibiting different atmospheric characteristics such as altitude, proximity to sources of large particulates and humidity. Over 200,000 solar profiles were collated in the measurement process[54]. The data logged in these experiments is freely available online[55, 56]. More recent measurements were made by Neumann et al who conducted investigations into the frequency and variation of solar profiles at 3 different terrestrial locations, namely Cologne, Almeria and Odeillo[48]. Both groups reported similar findings, namely normalised distributions that were near constant in the solar disk and variably linear beyond. These radial intensity solar distributions are typically referred to as solar profiles. Unfortunately there is not much high resolution solar profile data available, although there now exist established measurements efforts to this end[57, 58].

The current standard model for solar profile descriptions is the circumsolar ratio (CSR) model developed by Buie et al[47]. This model is based on a statistical analysis of the data from the LBL measurement campaign. The model generates a one dimensional intensity distribution describing power as a function of angular deviation from the solar centre for a given CSR.

In analysing the LBL measurement campaign data, Buie et al noted a significant relationship with solar intensity and angular deviation from the solar centre. When graphed in log-log space, a bi-regional distribution is apparent.

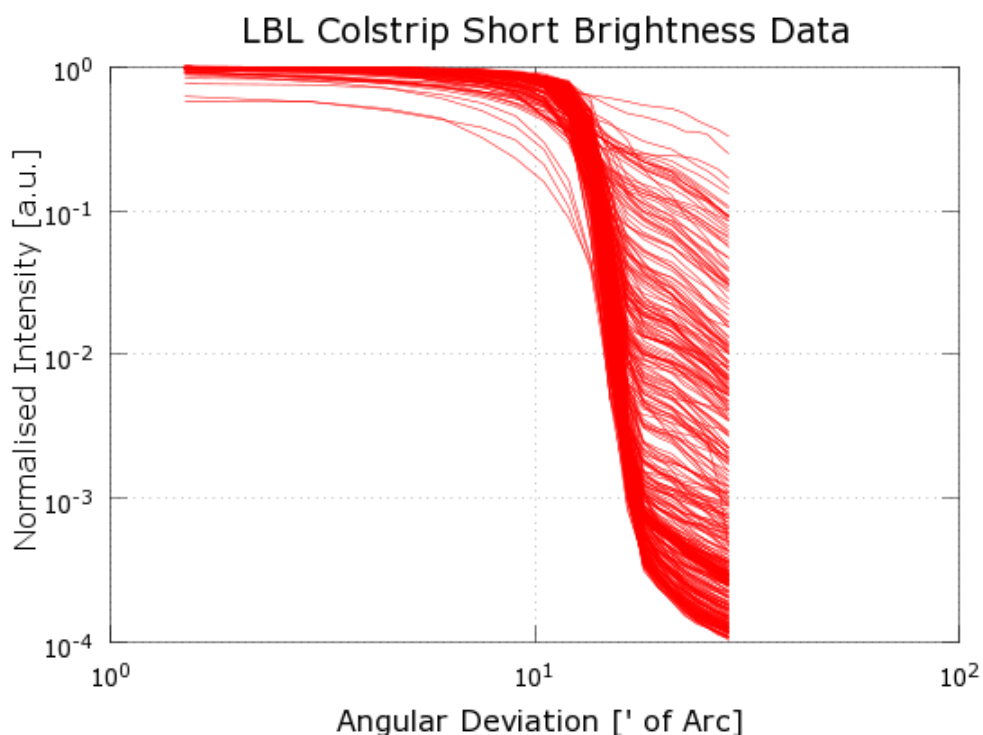


FIGURE 2.15: NORMALISED FLUX INTENSITY VS ANGULAR DEVIATION FROM THE SOLAR CENTRE AS EXTRACTED FROM THE LBL COLSTRIP SHORT DATA SWEEP

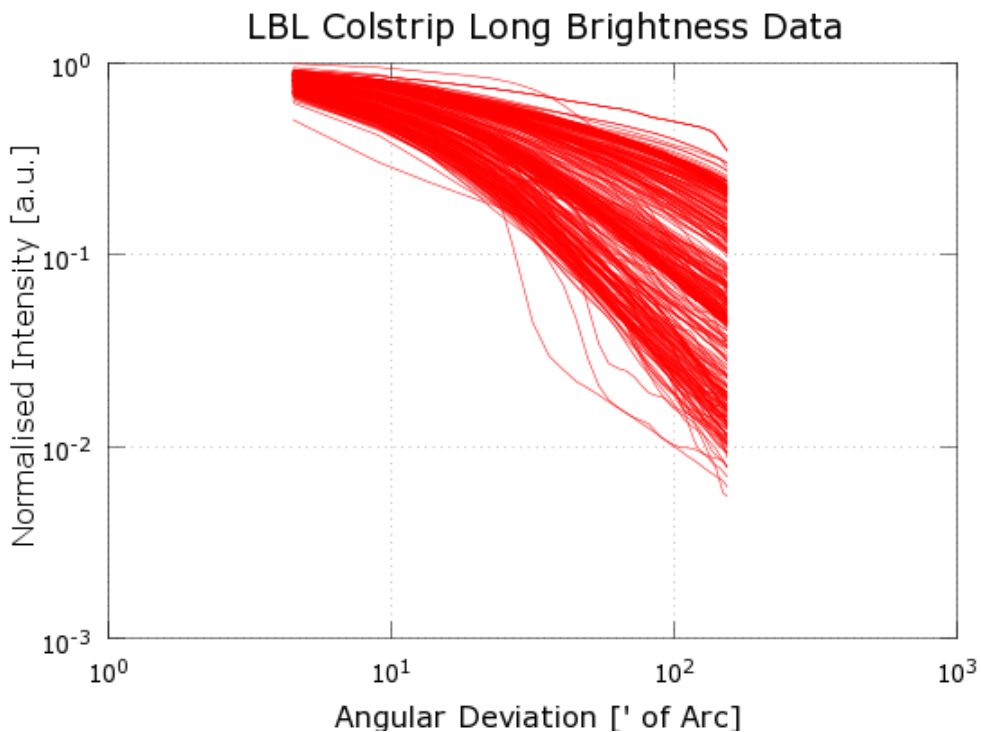


FIGURE 2.16: NORMALISED FLUX INTENSITY VS ANGULAR DEVIATION FROM THE SOLAR CENTRE AS EXTRACTED FROM THE LBL COLSTRIP LONG DATA SWEEP

Figure 2.15 and Figure 2.16 show log-log graphs of normalised flux intensity vs angular deviation from the solar as generated from data from the short and long data sweeps measured at Colstrip, USA in the LBL reduced database. The data here is shown as extracted from the database[56] for a single site with little data filtering, thus some anomalous data is present. The Buie et al analysis takes good advantage of the 29 data flags associated with each measurement in order to filter out erroneous data and, furthermore, includes data from all 11 measurements sites, minimising the possibility of extracting geographically specific phenomena.

There are two distinct, separable regions visible in the solar profile data. The regions are separated not by a unitary value, but by a band. This band is directly related to the Earth-Sun distance variation and is the range of the apparent half angle radius of the Sun, with an average value of 4.65mrad (approximately 16'). The primary region of the graph,  $<4.65\text{mrad}$ , shows little variation. This is approximately a region of constant distribution for all solar profiles and is referred to as the central solar region. The secondary region,  $>4.65\text{mrad}$ , shows a series of lines approximated, in log-log space by straight lines with varying gradients and y-intercepts. This is the circumsolar region.

#### 2.3.1.1. CSR Definition & Visualisation

It is appropriate to introduce a parameter to help describe the construct of varying solar profiles, as illustrated above. Given that each solar profile is split into two regions, one approximately constant

and the other variable, a parameter comparing the areas of these two regions makes for a good single value description of a solar profile. An established parameter relating these two regions is the circumsolar ratio (CSR).

The circumsolar ratio is defined as the ratio of flux contained in the circumsolar region (the solar aureole) to flux contained within the entirety of the solar disc (the central solar disc plus the solar aureole).

$$C = \frac{\varphi_{\text{Circumsolar}}}{\varphi_{\text{Beam}}} = \frac{\int_{\theta_{\text{Sun}}}^{\theta_{\text{Circumsolar}}} \varphi \cdot d\theta}{\int_0^{\theta_{\text{Circumsolar}}} \varphi \cdot d\theta}$$

EQUATION 2.11

Where  $C$  denotes circumsolar ratio,  $\varphi$  solar flux intensity,  $\theta$  angular deviation from the solar centre,  $\theta_{\text{Circumsolar}}$  the angular limit of the circumsolar region and  $\theta_{\text{Sun}}$  the angular limit of the central solar disc

The central solar region is essentially the effective size of the Sun due to Earth-Sun geometry. Measurement of the absolute astronomical unit (au) subtended radial half angle of the solar centre is a non-trivial task. Depending on location of measurement, measurement technique and measurement time; one will find small variations in subtended solar semi-diameter[59].

In modern measurement studies subtended radial solar half angle averages tend to be quoted around  $959''$  or  $4.65\text{mrad}$ [28, 50] which coincides with the average apparent solar semi-diameter used by the Buie et al model.

The apparent solar semi-diameter changes with Sun-Earth distance according to:

$$\delta = \tan^{-1} \left( \frac{d}{2D} \right)$$

EQUATION 2.12

Where  $\delta$  is the apparent solar semi-diameter,  $d$  the diameter of the Sun and  $D$  the Sun-Earth distance

Due to the elliptical orbit of the Earth about the Sun, there is approximately a 3% variation in the apparent solar semi-diameter throughout the year from perihelion to aphelion of  $4.742$  to  $4.584\text{mrad}$ , respectively. These variations should be included in extended light source modelling[48] , namely because the calculated circumsolar ratio changes with defined central solar boundaries.

Beyond the solar disk paraxial refraction and atmospheric scattering contribute to the circumsolar region. The circumsolar region encompasses the solar aureole and extends to the start of the diffuse

radiation region. The exact point at which the solar irradiation can be considered diffuse is arguable and different interpretations exist. The circumsolar region may extend somewhat beyond 43.6mrad but it is this limit that is used in the Buie et al model due to the measurement restrictions on the available data in the Lawrence Berkley Laboratory (LBL) reduced database on which the model is based. Furthermore, due to the exponential fall off of radiation in the circumsolar region with angular deviation from the solar centre, contributions beyond this limit may be considered negligible.

The circumsolar ratio is a parameter that itself describes the proportion of solar beam irradiation

contained in the circumsolar region. A solar profile with a low circumsolar  $C = \frac{\varphi_{\text{aureola}}}{\varphi_{\text{beam}}}$  ratio will have

most of its solar flux contained in the central solar disk, whereas as a high circumsolar  $C = \frac{\varphi_{\text{aureola}}}{\varphi_{\text{beam}}}$  ratio solar profile has a significant proportion of its solar flux contained in the solar aureole and appears flared. Good visual examples of these phenomena are given in Figure 2.17 and Figure 2.18.



FIGURE 2.17: A Low CSR SOLAR PROFILE[60]

Figure 2.17 is a perspective photograph of somebody ‘holding’ a low CSR Sun. Most of the flux in this low CSR example is contained within the central solar disk. Very little solar flare can be seen here.

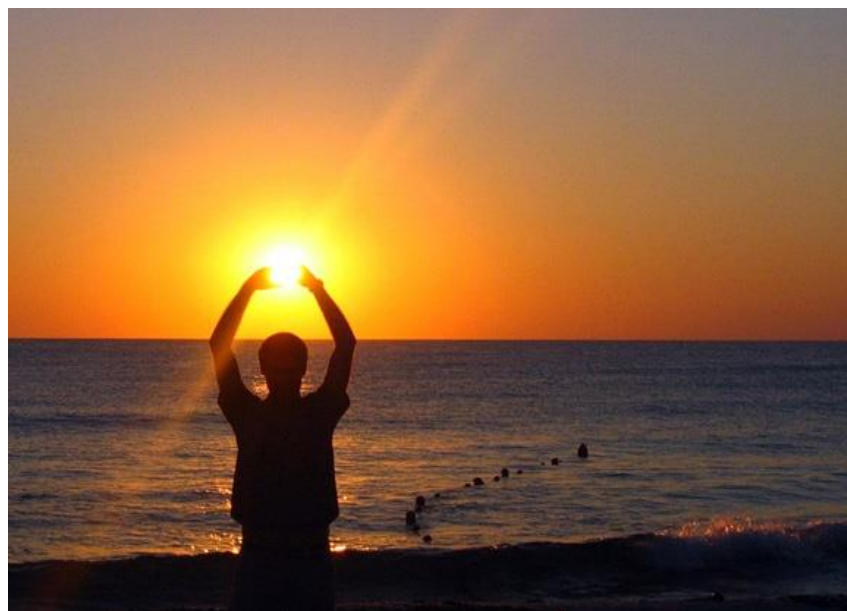


FIGURE 2.18: A HIGH CSR SOLAR PROFILE[61]

Figure 2.18 is a perspective photograph of somebody ‘holding’ a high CSR Sun. Much of the flux in this high CSR example is contained outside the central solar disk. A significant amount of solar flare can be seen here. Further photographic examples as taken at DLR can be found in[57].

### 2.3.1.2. CSR Variation and Frequency

The dependency of CSR on atmospheric variables is not well known, though it is thought that the primary dependencies are: air mass, humidity and aerosol optical depth. The Neumann et al solar profile analysis[48] splits CSRs into 6 banded categories and organises them by discretised DNI bands in steps of  $200\text{W/m}^2$ . Some degree of negative correlation is found. The data is displayed in Figure 2.19.

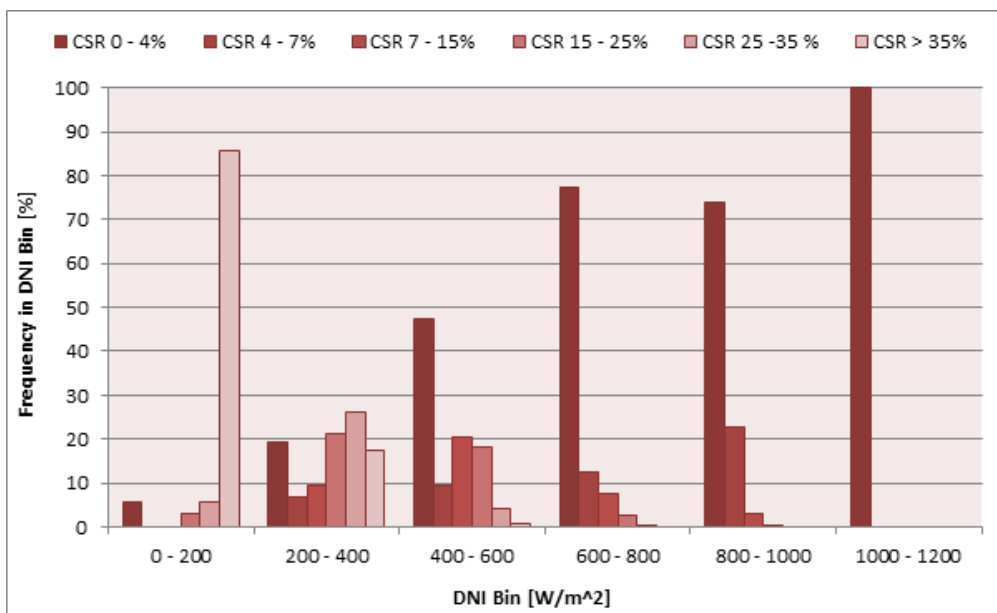


FIGURE 2.19: CSR AND DNI VARIATION AND FREQUENCY RELATIONSHIPS

Figure 2.19 shows the frequency of 6 CSR bands (0 - >35%) within 6 DNI bands (0 – 1200W/m<sup>2</sup>). The low CSRs are shown on the left of each DNI band in dark red and the high CSRs on the right in light red. Some degree of negative correlation can be seen here. The DLR measurement campaign includes data from Cologne, Germany; Odeillo, France; and Almeria, Spain. There is a total of approximately 2300 measurements of which 350 were recorded in Spain, 500 in France, and the rest in Germany. The site-to-site variability was considered as low compared to the variability seen with changing CSR.

This DNI banded CSR variation and frequency analysis is not ideal. The empirical, probabilistic basis of this approach is simplistic and overlooks dependencies on environmental variables that are easily accessible from meteorological datasets. It would be preferable to have more information on CSRs with regard to atmospheric variables such as air mass and humidity. However, Neumann's analysis is one of the first investigations of its kind and such data is an important acquisition for CPV simulations as it at least allows for the algorithmic implementation of CSR variation through probabilistic interpretation.

The application of the above CSR and DNI relationships to hourly insolation data enables the approximation of location-specific CSR variation. For the following analysis, hourly insolation data generated by the popular meteorological database, Meteonorm™[62], was used. This was probabilistically translated to banded CSR according to the distribution of Figure 2.19.

Figure 2.20 provides a comparison of CSR variation and frequency plots for the locations Edinburgh, UK (55° 55', 3° 10') (annual DNI ~ 800kWh) and Almeria, Spain (36° 50', -2° 27') (annual DNI ~ 1900kWh).

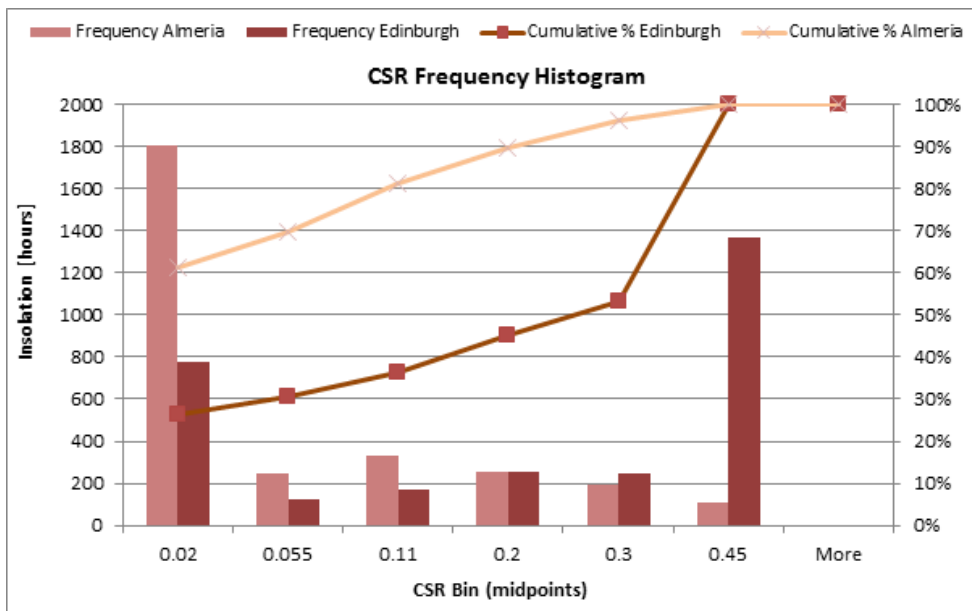


FIGURE 2.20: CSR FREQUENCY HISTOGRAM FOR EDINBURGH, UK; AND ALMERIA, SPAIN

Figure 2.20 shows that Edinburgh, a location typically considered unsuitable for HCPV, has a variation of solar irradiation profiles weighted in the high CSR region, whereas a much more suitable region for HCPV, Almeria, has solar a profile variation weighted in the low CSR region. This analysis uses the probabilistic framework of Figure 2.19 applied to the generated hourly DNI values for each location. It would be most interesting to compare this analysis with measured data but there is currently no such data available.

### 2.3.2. The Buie et al Model

The current standard model for the description of circumsolar irradiation is the CSR model developed by Buie et al. The model generates a one dimensional intensity distribution describing power as a function of angular deviation from the solar centre for a given CSR.

#### 2.3.2.1. Analysis

The CSR ratio is a valid parameter for solar profile definition so long as there is a relationship between solar profile structure and CSR value that is well defined with little variance. Given that the flux distribution in the central solar region is independent of CSR, it is only necessary to consider the relationships in the circumsolar region for validation. It can be seen from Figure 2.15 and Figure 2.16 that, to a reasonable approximation, there is a straight line relationship in log-log space in the circumsolar region for all solar profiles. This is especially the case if one carries out a more stringent data filtering process than is done therein. Buie et al justify the use of a log-log extension of the  $y = mx + c$  relationship by statistical analysis, showing that there exist functions that predict the y-

intercept and gradient of the log-log space lines and fit the measured data with little variance. The following relationships are then established:

$$\varphi(\theta) = \begin{cases} \frac{\cos(0.326\theta)}{\cos(0.308\theta)}, & 0 \leq \theta \leq \theta_{Sun} \\ e^{\kappa\theta^\gamma}, & \theta_{Sun} < \theta \leq 43.6mrads \end{cases}$$

EQUATION 2.13

$$\kappa = 0.9 \ln(13.5 * CSR) CSR^{-0.3}$$

EQUATION 2.14

$$\gamma = 2.2 \ln(0.52 * CSR) CSR^{0.43} - 0.1$$

EQUATION 2.15

Where  $\theta$  is angular deviation in mrads from the solar centre;  $\theta_{Sun}$  is the angular extent of the central solar disk ( $\sim 0.266^\circ$ ); and  $\kappa$  and  $\gamma$  are the y-intercept and gradient of the log space straight line approximation in the circumsolar region, respectively

Assuming rotational symmetry, one can utilise this model to develop an intensity distribution as a function of azimuth and elevation angle coordinate pairs. The resulting extended light source distribution facilitates three-dimensional ray trace simulations and hence offers analytical insights into CPV optical system design.

### Extended Light Source Sunshapes

Equation 2.13, Equation 2.14 and Equation 2.15 have been used here to generate an extended light source solar profile for a characteristic CSR of 0.3. This circumsolar ratio was chosen as it is particularly interesting for CPV – an occurring solar profile that is rarely considered in CPV optical system design. The resultant intensity profile as a function of azimuth and elevation angle as generated by the application of rotational symmetry is shown in Figure 2.21. It should be noted that this profile is not typical but is used here as it offers a visually impactive distinction between the central solar and circumsolar regions.

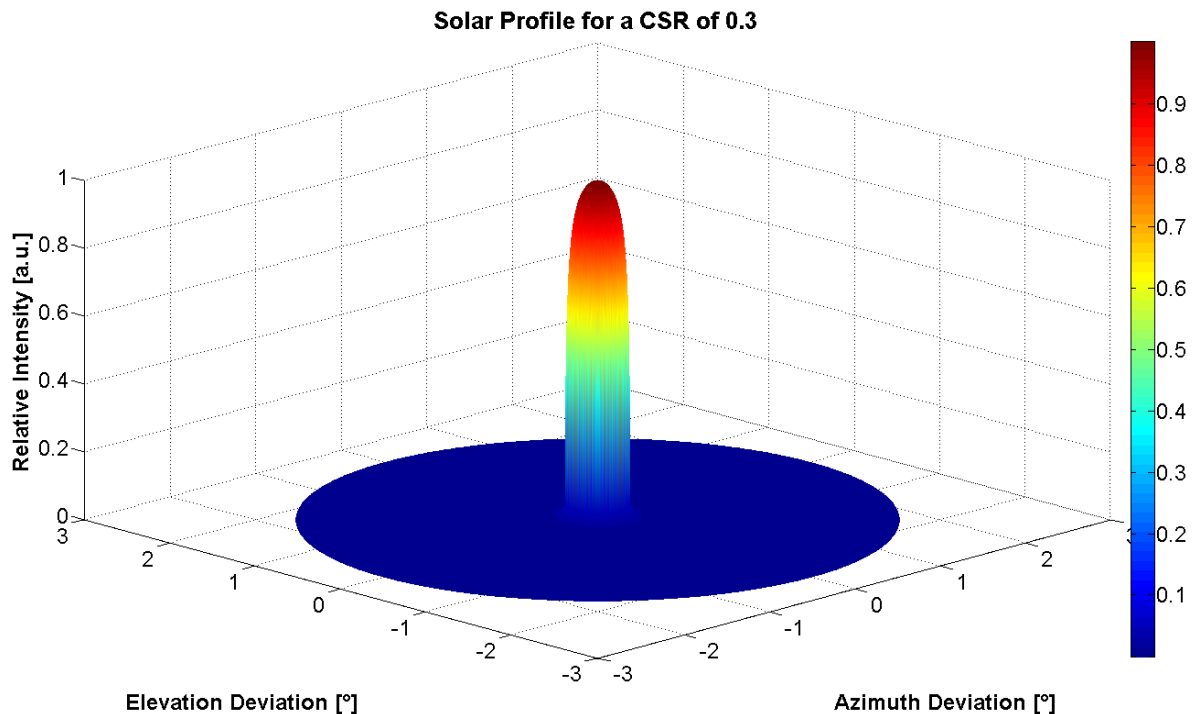


FIGURE 2.21: 3D RELATIVE SOLAR PROFILE FOR AN INPUT CSR OF 0.3

Figure 2.21 shows a surface plot of 1 million random homogeneously distributed mesh points over the full solar profile region as generated by the model. The spatially bi-regional nature of solar irradiation is clearly visible here, namely in the differentiation between central solar and circumsolar regions. A significant drop in radiation intensity can be seen at the transition from the central solar region to the circumsolar region. Though the intensity drop is sharp, the area contribution of the circumsolar region is much larger than that of the central solar region.

It is possible to check this model by means of geometric interpretation. By considering the solid angle within which the model operates as a circular boundary in an x-y plane and the power at a given angular coordinate pair as an associated z value, the net power within a region of space is computed as a volume integral over the correspondingly confined x-y space.

By definition, for the above solar profile (Figure 2.21) the ratio of volume over the circumsolar region, as defined by Equation 2.16, to volume over the central solar region, as defined by Equation 2.17, should be 0.3.

$$D_{Circumsolar} = \sqrt{x^2 + y^2} > 4.65\text{mrad}$$

EQUATION 2.16

$$D_{Central Solar} = \sqrt{x^2 + y^2} \leq 4.65\text{mrad}$$

EQUATION 2.17

However, the actual model output is around 9% lower than this (see Table 2.3). In[60, 61] the model authors note these discrepancies and interpret them as deviations in the model's prediction of the edge of the solar disk. However, it is apparent from Equation 2.13 that the edge of the solar disk is inherently defined by the model as 4.65mrad, which is the average apparent solar semi-diameter. Moreover, the projected deviations in effective solar disk size fall beyond the physical boundaries governed by Equation 2.12. An alternative approach to the model correction is advocated here by means of an input CSR correction. This facilitates output smoothing without the need for unphysical assertions. Empirical correction formulae have been derived though given their complexity a correction table is also provided for reference.

The central solar and circumsolar regions, as defined by Equation 2.13, Equation 2.14 and Equation 2.15, for an input CSR of 0.3 are presented separately in Figure 2.22 and Figure 2.23.

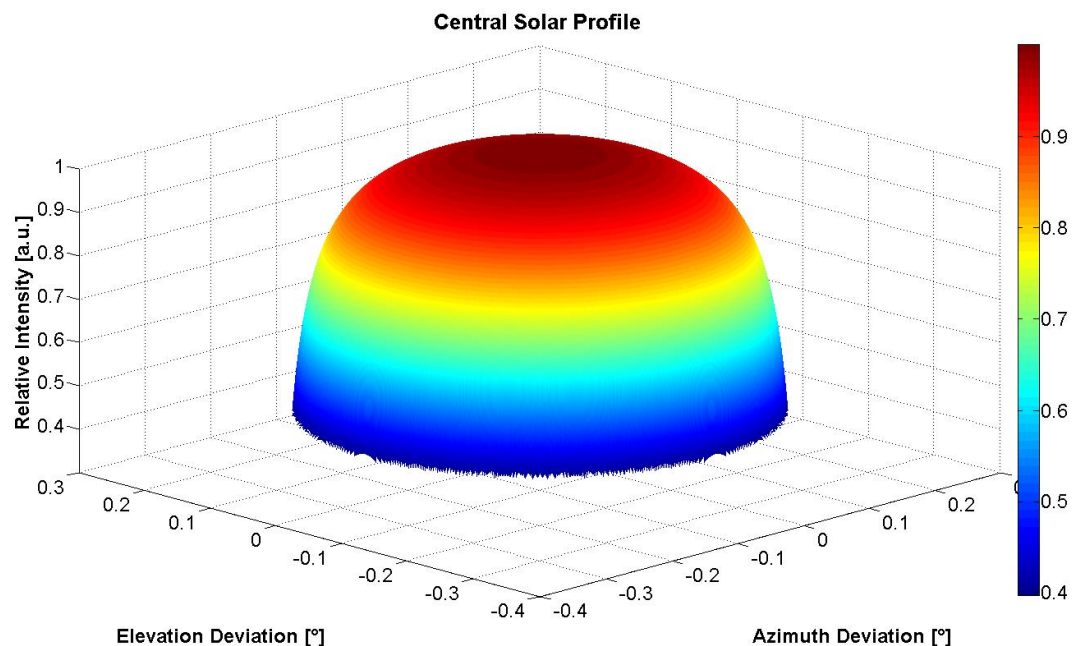


FIGURE 2.22: CENTRAL SOLAR REGION INTENSITY DISTRIBUTION FOR AN INPUT CSR OF 0.3 NORMALISED TO A MAXIMUM SOLAR INTENSITY OF 1

Figure 2.22 shows a surface plot of 1 million random homogeneously distributed mesh points over the central solar region. There is a very slight slope of decreasing intensity in the centre with an increase in intensity drop with angular deviation towards the circumsolar region. The resultant volumetric surface is a thimble-shaped distribution. According to the model, the normalised central solar profile is invariant under changes in CSR.

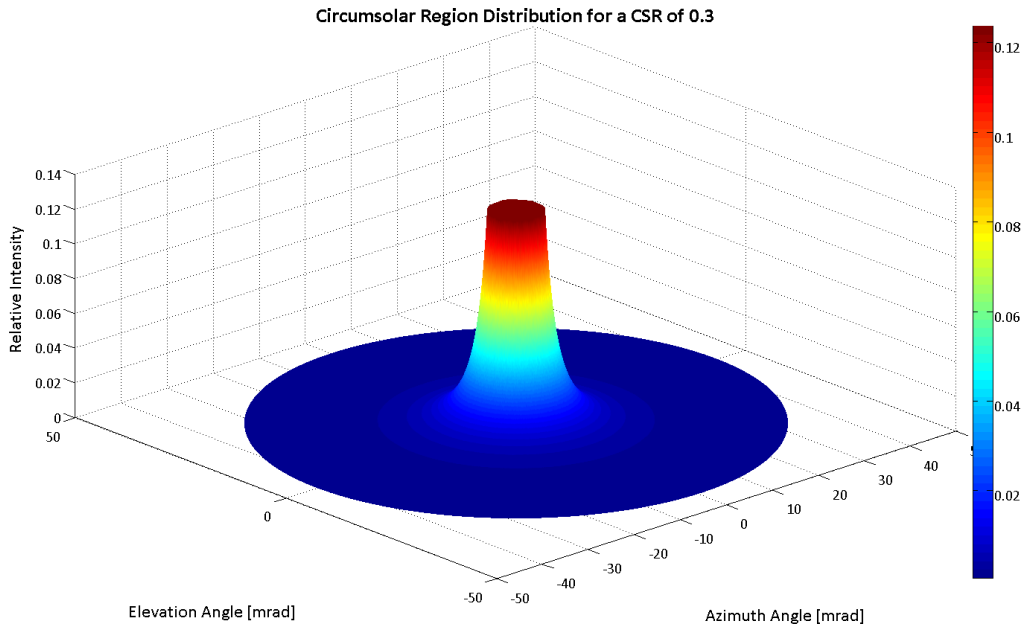


FIGURE 2.23: CIRCUMSOLAR REGION INTENSITY DISTRIBUTION FOR AN INPUT CSR OF 0.3 NORMALISED TO A MAXIMUM SOLAR INTENSITY OF 1

Figure 2.23 shows a surface plot of 1 million random homogeneously distributed mesh points over the circumsolar region. The logarithmic intensity decrease with radial distance is clearly visible. If the intensity were displayed in 2D log space, the enveloped shape would be a trapezium.

By comparing the volumes of each region as generated by the model the output and input CSRs can be compared. Numerical analysis is used here for volume calculation, a potential benefit of this method is that it facilitates the investigation of averaging effects due to angular resolution. The process is outlined in the following section.

### Volumetric Analysis

The region volumes can be calculated as triple integrals according to:

$$V = \iint dA \cdot d\varphi$$

EQUATION 2.18

Where  $A$  is subtended area and  $\varphi$  power

In the following, the volumes are calculated by means of numerical analysis by geometric interpretation.

### *Central Solar Region*

The area contribution for a given annular central solar region,  $i$ , is found as:

$$A_i = \pi(\sin(i\Delta\theta)^2) - \pi(\sin(i\Delta\theta - \Delta\theta)^2)$$

The central angular deviation reference point for the region is found as:

$$\Theta = i\Delta\theta - \frac{\Delta\theta}{2}$$

The volume contribution for the region is then found as:

$$V_i = A_i \frac{\cos(0.326\Theta)}{\cos(0.308\Theta)}$$

The angular step in the numerical analysis is defined by the resolution,  $n$ , as:

$$\Delta\theta = \frac{4.65}{n}$$

The total volume of the central solar region is then:

$$V = \sum_{i=1}^{i=n} V_i = \sum_{i=1}^{i=n} A_i \frac{\cos(0.326\Theta)}{\cos(0.308\Theta)} = \sum_{i=1}^{i=n} \pi(\sin(i\Delta\theta)^2) - \pi(\sin(i\Delta\theta - \Delta\theta)^2) \frac{\cos\left(0.326\left(i\Delta\theta - \frac{\Delta\theta}{2}\right)\right)}{\cos\left(0.308\left(i\Delta\theta - \frac{\Delta\theta}{2}\right)\right)}$$

**EQUATION 2.19**

Where  $n$  is large

### Circumsolar Region

The area contribution for a given annular circumsolar region,  $i$ , is found as:

$$A_i = \pi \sin(4.65 + i\Delta\theta)^2 - \pi \sin(4.65 + i\Delta\theta - \Delta\theta)^2$$

The central angular deviation reference point for the region is found as:

$$\Theta = 4.65 + i\Delta\theta - \frac{\Delta\theta}{2}$$

The volume contribution for the region is then found using Equation 2.13, Equation 2.14 and Equation 2.15 as:

$$V_i = A_i e^{\kappa\Theta^\gamma}$$

Where

$$\kappa = 0.9 \ln(13.5 C) C^{-0.3}$$

$$\gamma = 2.2 \ln(0.52 C) C^{0.43} - 1$$

The angular step in the numerical analysis is defined by the resolution,  $n$ , as:

$$\Delta\theta = \frac{43.6 - 4.65}{n}$$

The total volume of the circumsolar region is then:

$$\begin{aligned}
 V &= \sum_{i=1}^{i=n} V_i = \sum_{i=1}^{i=n} A_i e^{\kappa \theta^y} \\
 &= \sum_{i=1}^{i=n} \pi((\sin(4.65 + i\Delta\theta))^2 - (\sin(4.65 + i\Delta\theta - \Delta\theta))^2) e^{0.9 \ln(13.5C) C^{-0.3}} \left( 4.65 \right. \\
 &\quad \left. + i\Delta\theta - \frac{\Delta\theta}{2} \right)^{2.2 \ln(0.52C) C^{0.43} - 1}
 \end{aligned}$$

EQUATION 2.20

Where  $n$  is large

### Model Output Analysis

The output CSR calculated from the Buie et al model is compared with input CSR in Figure 2.24 and Figure 2.25. The CSR range 0.2-0.4 is highlighted as this range is of particular interest for CPV, representing high but occurring CSR values for which extended light source models are required for realistic system performance predictions.

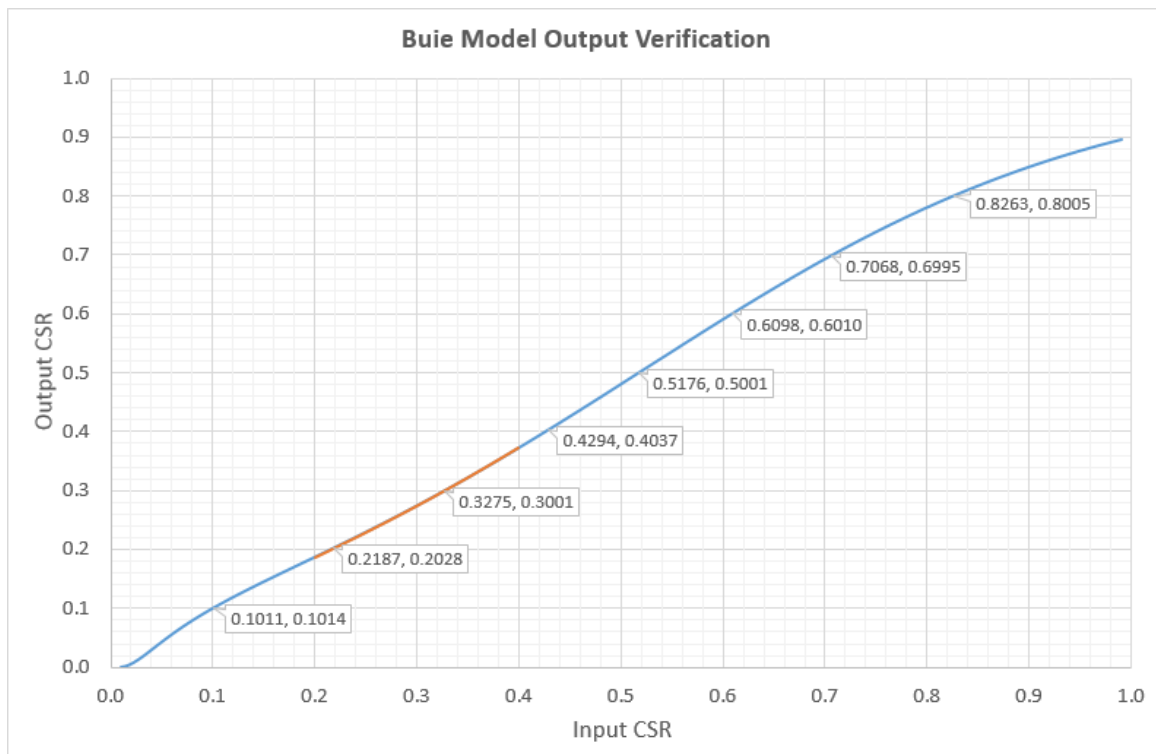


FIGURE 2.24: BUIE MODEL VERIFICATION - INPUT CSR VS OUTPUT CSR

Figure 2.24 directly compares the model input and output CSRs. A straight line graph with a constant gradient of 1 is expected but a different result is obtained.

Other than a slight overestimation around an input CSR of 0.1, the model seems to consistently underestimate the output CSR. For clarification, in Figure 2.25 the output CSR is plotted as a proportion of input CSR.

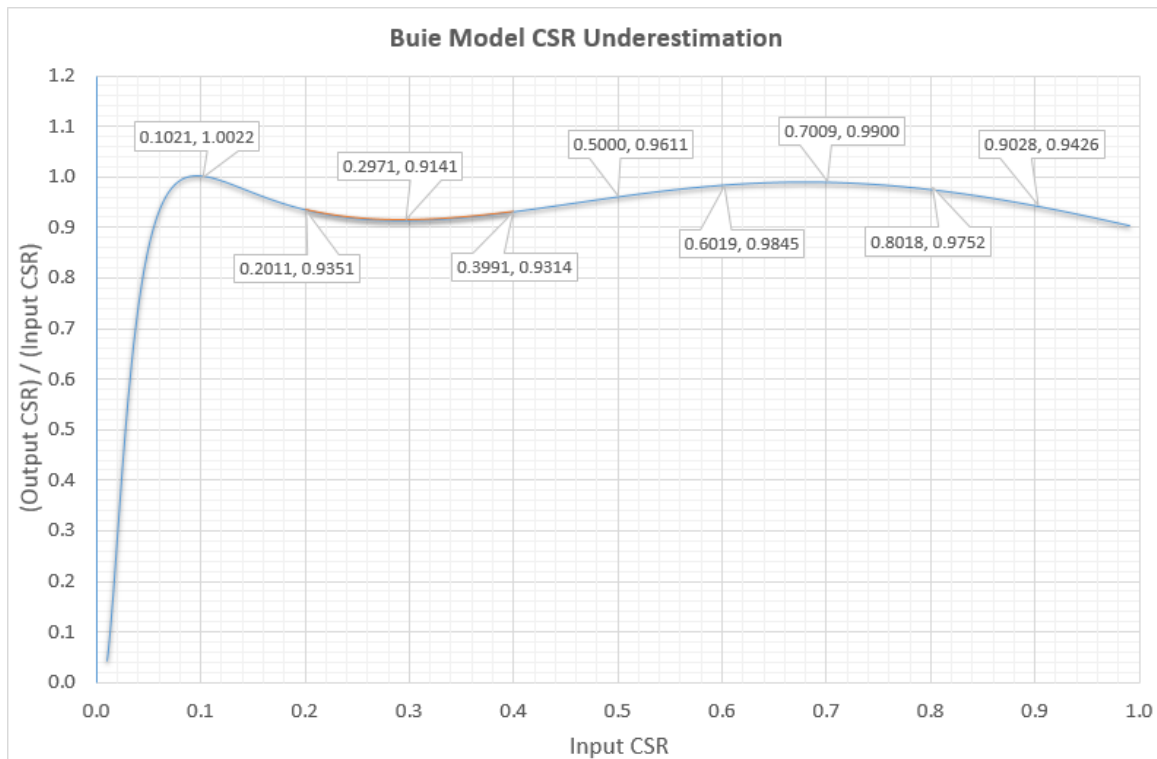


FIGURE 2.25: BUIE MODEL VERIFICATION - OUTPUT CSR AS A PROPORTION OF INPUT CSR

It can be seen from Figure 2.25 that the Buie et al model generally underestimates CSR. In the CSR region of 0.1 to 0.6 the average underestimation is ~5%. Moreover, beyond a CSR of 0.1, the maximal underestimation of ~9% is found in a particular region of interest for CPV system modelling. The maximum underestimation occurs at an input CSR of 0.3 and amounts to almost 10%. Here one would expect 70% of beam irradiation to be central solar and 30% circumsolar, the model returns 73% central solar and 27% circumsolar. Thus direct use of the Buie et al CSR model leads to overestimations of incident irradiation for CRSs above 0.08 and spectral inconsistencies. For an input CSR resolution of 0.01, the mean and standard deviation of the output CSR are 0.937 and 0.107, respectively.

### 2.3.3. Model Improvement

It is possible to calculate a correction, which will then remove this systematic underestimation.

#### 2.3.3.1. Overview

Correction formulae have been calculated by polynomial fitting to adjust to a near 1:1 Input:Output ratio. These are presented as a bisectional analysis:

$$C_I = \begin{cases} 14.66C^6 - 42.315C^5 + 49.513C^4 - 28.761C^3 \\ \quad + 8.0542C^2 + 0.137C + 0.0291 & , \quad 0 < C < 0.096 \\ -915401C^6 + 293962C^5 - 37145C^4 + 2355.9C^3 \\ \quad - 77.581C^2 + 1.981C + 0.0104 & , \quad 0.096 < C < 1 \end{cases}$$

EQUATION 2.21

Where  $C_I$  denotes input CSR and  $C$  desired CSR

Using these polynomials to correct the input CSR in the original model the output/input ratios approach unity, as shown in Figure 2.26.

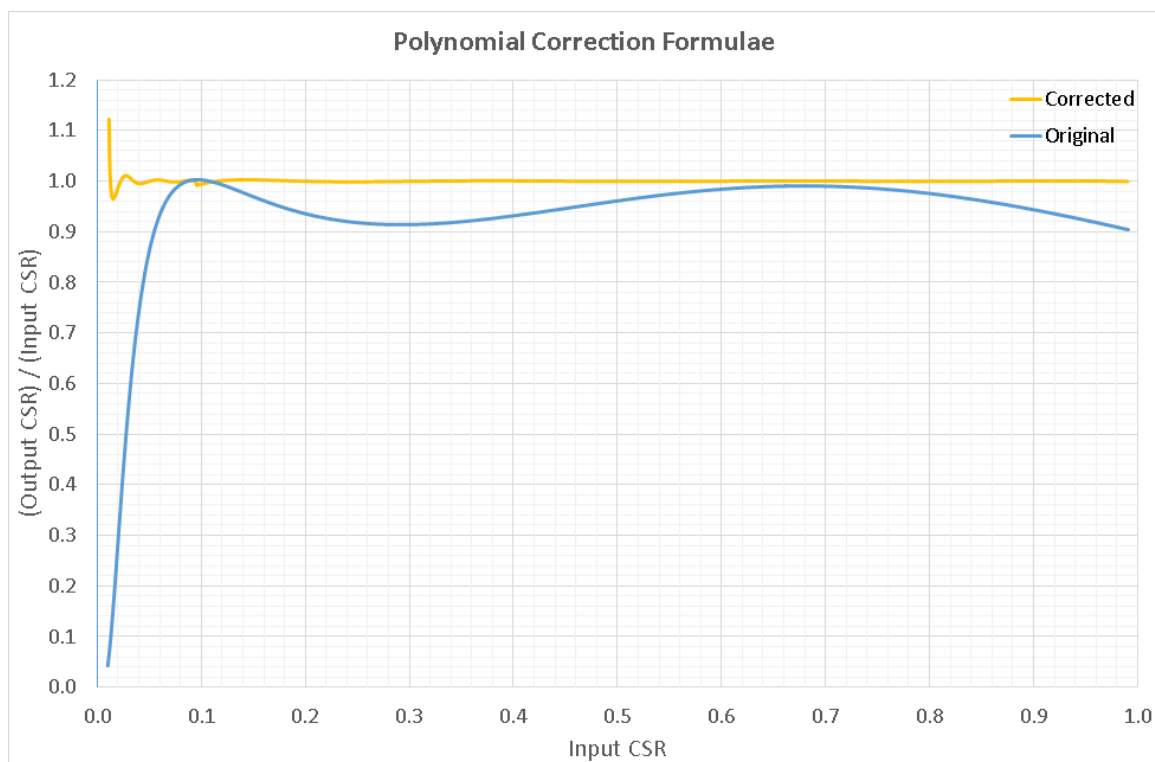


FIGURE 2.26: POLYNOMIAL CORRECTION FORMULAE COMPARISON WITH ORIGINAL BUIE ET AL MODEL INPUT VS OUTPUT

Figure 2.26 shows the model improvement by input CSR correction according to Equation 2.21. For an input CSR resolution of 0.01, the mean and standard deviation of the output CSR are 1.000 and 0.005, respectively. This compares favourably to the previous values of 0.937 and 0.107, the ideal values being 1 and 0. A clear improvement can be seen. The correction formulae can obviously be further improved in the near-zero input CSR region, although the above will be sufficient for the majority of all applications. The near-zero region is less critical as the impact of circumsolar radiation here is relatively insignificant.

As Equation 2.21 is an inelegant formula resulting from a high order polynomial fitting algorithm, the corresponding correction table is presented in Table 2.3.

TABLE 2.3: INPUT PARAMETER CORRECTION TABLE FOR THE BUIE ET AL CSR MODEL

Input CSR	Output CSR	Input CSR	Output CSR	Input CSR	Output CSR	Input CSR	Output CSR
0.0100	0.0004	0.2550	0.2339	0.5000	0.4806	0.7450	0.7346
0.0149	0.0022	0.2599	0.2382	0.5049	0.4860	0.7499	0.7389
0.0198	0.0056	0.2648	0.2425	0.5098	0.4914	0.7548	0.7432
0.0247	0.0104	0.2697	0.2468	0.5147	0.4968	0.7597	0.7474
0.0296	0.0162	0.2746	0.2512	0.5196	0.5022	0.7646	0.7516
0.0345	0.0224	0.2795	0.2556	0.5245	0.5077	0.7695	0.7557
0.0394	0.0289	0.2844	0.2600	0.5294	0.5131	0.7744	0.7598
0.0443	0.0355	0.2893	0.2644	0.5343	0.5185	0.7793	0.7639
0.0492	0.0421	0.2942	0.2689	0.5392	0.5239	0.7842	0.7679
0.0541	0.0485	0.2991	0.2734	0.5441	0.5294	0.7891	0.7718
0.0590	0.0548	0.3040	0.2780	0.5490	0.5348	0.7940	0.7758
0.0639	0.0608	0.3089	0.2825	0.5539	0.5402	0.7989	0.7796
0.0688	0.0667	0.3138	0.2871	0.5588	0.5456	0.8038	0.7835
0.0737	0.0724	0.3187	0.2917	0.5637	0.5510	0.8087	0.7872
0.0786	0.0779	0.3236	0.2964	0.5686	0.5563	0.8136	0.7910
0.0835	0.0833	0.3285	0.3011	0.5735	0.5617	0.8185	0.7947
0.0884	0.0885	0.3334	0.3058	0.5784	0.5671	0.8234	0.7983
0.0933	0.0936	0.3383	0.3105	0.5833	0.5724	0.8283	0.8019
0.0982	0.0985	0.3432	0.3153	0.5882	0.5777	0.8332	0.8054
0.1031	0.1033	0.3481	0.3201	0.5931	0.5831	0.8381	0.8090
0.1080	0.1080	0.3530	0.3249	0.5980	0.5884	0.8430	0.8124
0.1129	0.1126	0.3579	0.3298	0.6029	0.5936	0.8479	0.8158
0.1178	0.1171	0.3628	0.3347	0.6078	0.5989	0.8528	0.8192
0.1227	0.1216	0.3677	0.3396	0.6127	0.6041	0.8577	0.8225
0.1276	0.1260	0.3726	0.3445	0.6176	0.6094	0.8626	0.8258
0.1325	0.1303	0.3775	0.3495	0.6225	0.6146	0.8675	0.8290
0.1374	0.1346	0.3824	0.3545	0.6274	0.6197	0.8724	0.8322
0.1423	0.1388	0.3873	0.3595	0.6323	0.6249	0.8773	0.8353
0.1472	0.1430	0.3922	0.3646	0.6372	0.6300	0.8822	0.8384
0.1521	0.1472	0.3971	0.3696	0.6421	0.6351	0.8871	0.8415
0.1570	0.1513	0.4020	0.3747	0.6470	0.6402	0.8920	0.8445
0.1619	0.1554	0.4069	0.3799	0.6519	0.6452	0.8969	0.8474
0.1668	0.1595	0.4118	0.3850	0.6568	0.6502	0.9018	0.8503

0.1717	0.1636	0.4167	0.3902	0.6617	0.6552	0.9067	0.8532
0.1766	0.1677	0.4216	0.3953	0.6666	0.6602	0.9116	0.8560
0.1815	0.1718	0.4265	0.4006	0.6715	0.6651	0.9165	0.8588
0.1864	0.1758	0.4314	0.4058	0.6764	0.6700	0.9214	0.8616
0.1913	0.1799	0.4363	0.4110	0.6813	0.6748	0.9263	0.8643
0.1962	0.1840	0.4412	0.4163	0.6862	0.6797	0.9312	0.8669
0.2011	0.1881	0.4461	0.4216	0.6911	0.6844	0.9361	0.8695
0.2060	0.1921	0.4510	0.4269	0.6960	0.6892	0.9410	0.8721
0.2109	0.1962	0.4559	0.4322	0.7009	0.6939	0.9459	0.8746
0.2158	0.2004	0.4608	0.4375	0.7058	0.6986	0.9508	0.8771
0.2207	0.2045	0.4657	0.4429	0.7107	0.7032	0.9557	0.8795
0.2256	0.2086	0.4706	0.4482	0.7156	0.7078	0.9606	0.8819
0.2305	0.2128	0.4755	0.4536	0.7205	0.7124	0.9655	0.8843
0.2354	0.2170	0.4804	0.4590	0.7254	0.7169	0.9704	0.8866
0.2403	0.2212	0.4853	0.4643	0.7303	0.7214	0.9753	0.8889
0.2452	0.2254	0.4902	0.4697	0.7352	0.7258	0.9802	0.8912
0.2501	0.2296	0.4951	0.4751	0.7401	0.7302	0.9851	0.8934

### 2.3.3.2. Test Case

The irradiance harvest vs tracking error vs half angle input aperture has been calculated using both the original model and the corrected case. A CSR of 0.3 was chosen for analysis and a corrected input CSR of 0.3274 was derived from the correction table. Figure 2.27 and Figure 2.28 show the overestimation of the standard model in terms of absolute percentage of DNI.

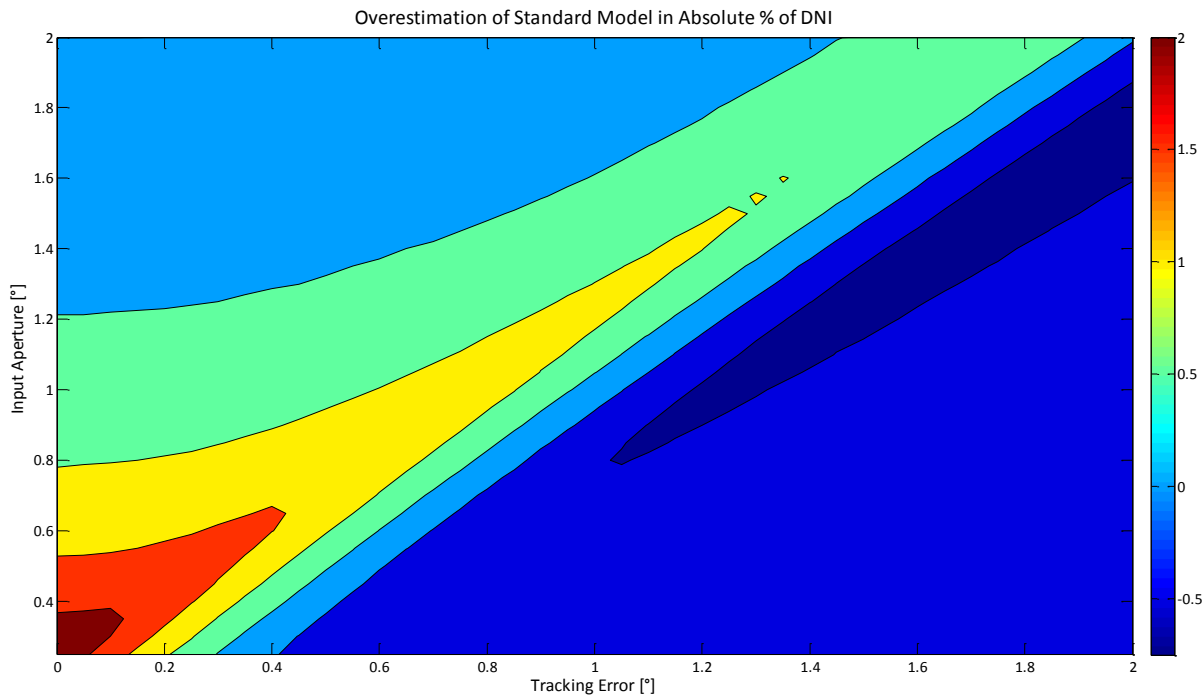


FIGURE 2.27: MODEL IRRADIATION HARVEST OVERESTIMATION FOR AN INPUT CSR OF 0.3 - CONTOUR PLOT

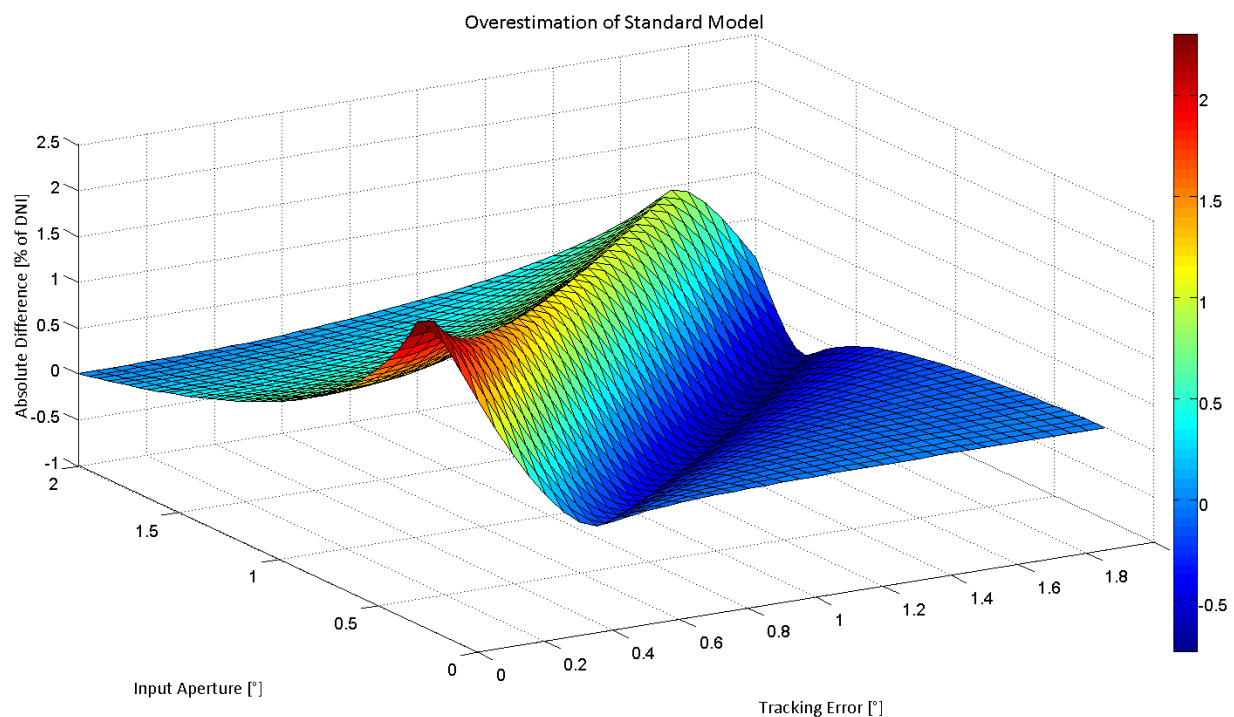


FIGURE 2.28: MODEL IRRADIATION HARVEST OVERESTIMATION FOR AN INPUT CSR OF 0.3 - SURFACE PLOT

Figure 2.27 and Figure 2.28 show regions of both overestimation and underestimation of irradiation collection by the standard model for an input CSR of 0.3, with overestimation dominating. An irradiation harvest overestimation of ~2.3% of absolute DNI is found with an input aperture of 0.25

and ideal solar tracking. For a given input aperture, maximum overestimation is found at approximately  $T = A - \theta_{Sun}$  and maximum underestimation at approximately  $T = A + \theta_{Sun}$ . These threshold values are the same for any distribution with underestimated circumsolar contributions, though the space between varies.

### 2.3.4. Model Extension

The above model describes well the spatial distribution of power within the beam irradiation region – from the solar centre to an angular deviation of  $2.5^\circ$  – for a wide and realistic range of solar profiles according to CSR. It is thus a powerful tool for the investigation of the spherical aberrations of optical systems, both longitudinal and transverse. However, there are still assumptions therein that make the model incomplete and unsuitable for the investigation of chromatic aberrations for high CSR Suns. A model extension is here proposed that enables use of the model for all aberrations, including chromatic aberrations.

The bi-regional nature of beam irradiation is a direct result of the physical phenomena producing the central solar and circumsolar regions, namely the relative location of the Sun and atmospheric lensing, respectively. Given this, it is not surprising that it is not just the power distribution of solar flux that is bi-regional, but the spectral composition of power too. The model extension then is to include the bi-regional distribution of spectrum in the extended light source description of the Sun.

There exists software today capable of generating simulated separate spectral profile data for the central solar and circumsolar beam irradiance[25, 63]. When such information is used in conjunction with the above solar profile model, both the power and spectral distributions can be incorporated in solar beam flux modelling. Generated solar profiles are split here into central solar and circumsolar regions and SMARTS-generated spectra are apportioned according to relative intensity levels. The amalgamation of these two methods results in a solar profile generation model that is a powerful tool for CPV modelling, enabling the investigation of longitudinal, lateral and chromatic aberrations.

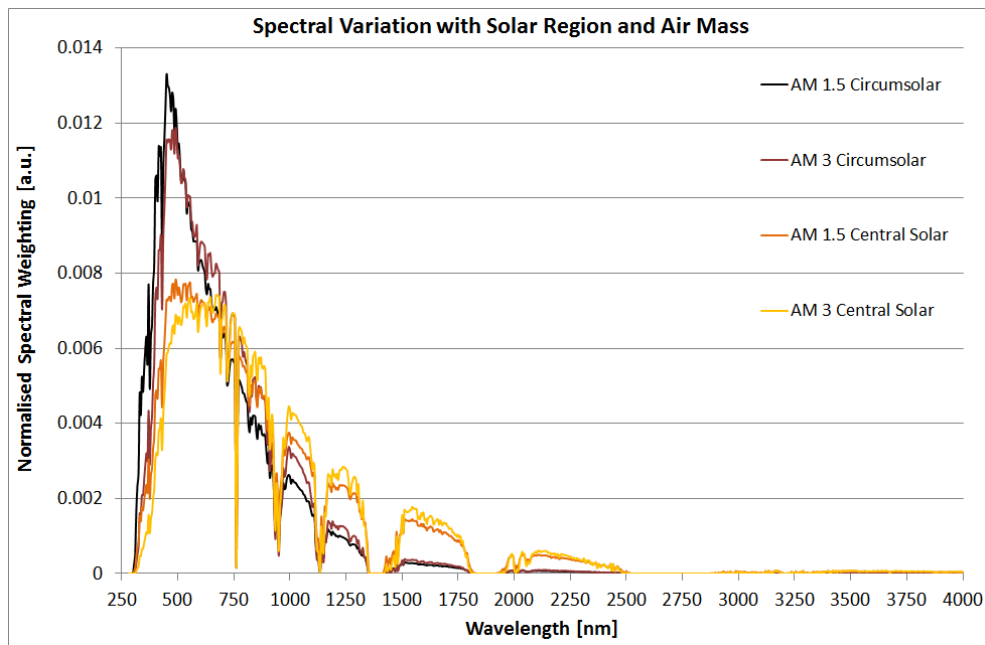


FIGURE 2.29: CENTRAL AND CIRCUMSOLAR SPECTRA FOR AIR MASSES 1.5 &amp; 3

Figure 2.29 shows both the significant difference in the spectra of the central solar and circumsolar regions and the significant variation of both these spectra with air mass. Given that the two regions result from different physical phenomena, their spectral components vary differently with air mass. This difference is shown explicitly in Figure 2.30.

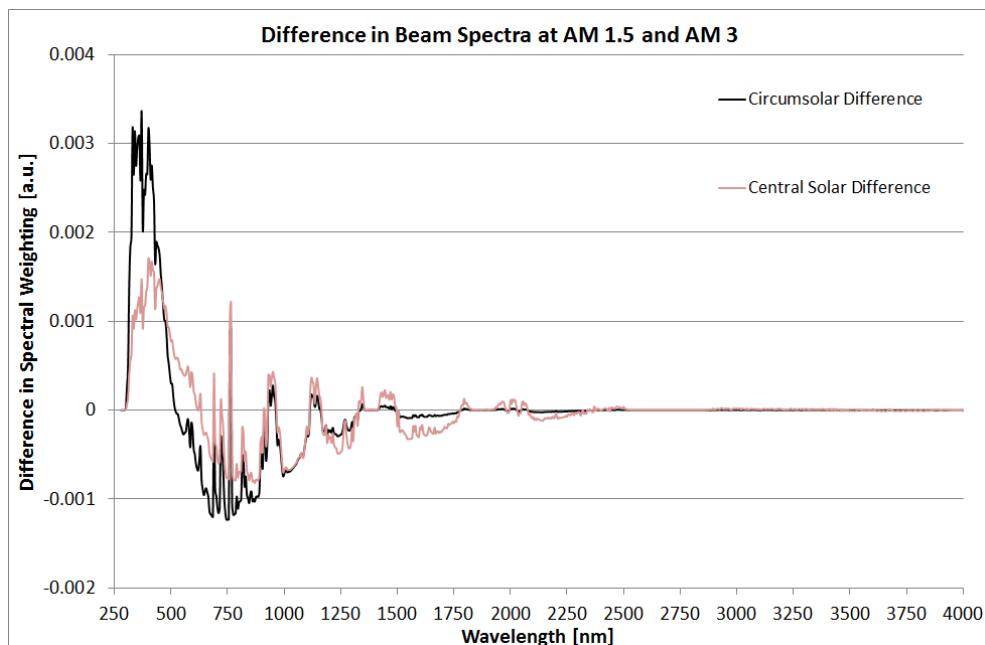


FIGURE 2.30: DIFFERENCE IN SPECTRAL WEIGHTING AT AIR MASS 1.5 &amp; 3 FOR THE CENTRAL SOLAR AND CIRCUMSOLAR BEAM REGIONS

The variation of spectral composition with air mass is apparently simplified when considering the change in average photon energy (APE), as shown in Figure 2.31.

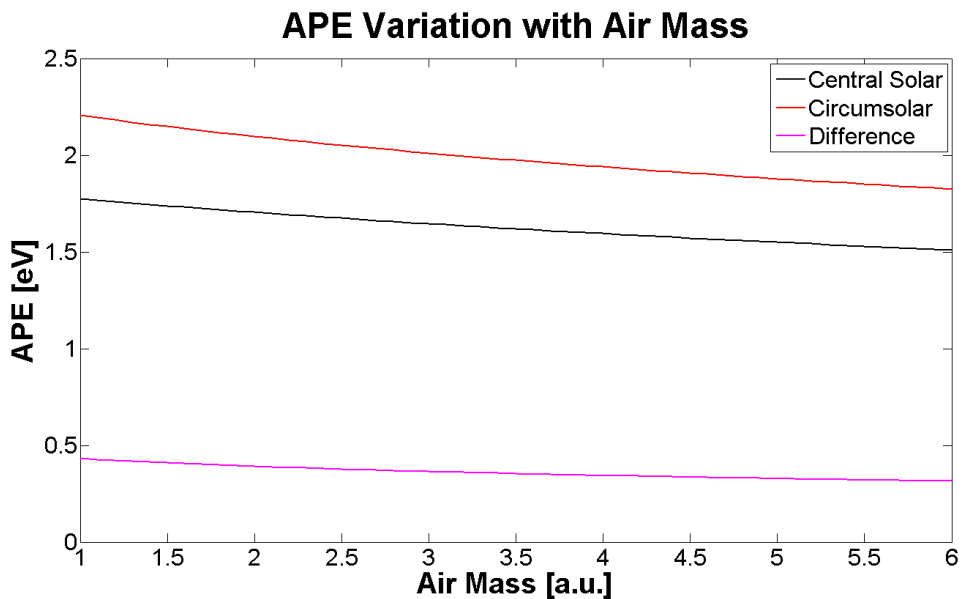


FIGURE 2.31: APE VARIATION WITH AIR MASS IN THE BEAM REGIONS WITHIN THE WAVELENGTH RANGE 280-4000NM

Given the sizeable variation of these spectra with air mass, it is proposed that the CSR model be extended to include air mass as an input.

## 2.4. Results

Existing commonplace solar models have been analysed for validity (2.4.1 Conditions of Validity) and improvements and extensions offered. The improved and extended models as described above have been used to generate solar profiles. Example profiles are presented here both singularly for specific analysis (2.4.2 Solar Profiles) and contextually for the consideration of system level effects (2.4.3 Contextual Analysis).

The data is analysed here in terms of the insolation visible to the primary optical system element, i.e. the Fresnel lens of CPV. Thus any negative performance impacts highlighted herein are only those at the primary optical stage and may well be amplified before arriving at the receiver plane, i.e. the solar cell.

### 2.4.1. Conditions of Validity

For low resolution optical simulations:

The point source Sun approximation is valid if:

$$\Delta T \ll \theta_{Lens}$$

&

$$\theta_{Sun} \ll \theta_{Lens}$$

$$\therefore R_S = \frac{\sin^2 \theta_{Sun}}{\sin^2 \theta_{Lens}} \approx 0$$

The pillbox Sun approximation is valid if:

$$\int_0^{\theta_{Sun}} \varphi d\theta \gg \int_{\theta_{Sun}}^{\theta_{Aureole}} \varphi d\theta$$

$$\therefore C = \frac{\int_{\theta_{Sun}}^{\theta_{Circumsolar}} \varphi d\theta}{\int_0^{\theta_{Circumsolar}} \varphi d\theta} \approx 0$$

Where  $\Delta T$  is the solar tracking error,  $\theta_{Lens}$  the lens entry aperture half angle and  $\theta_{Sun}$  the radial angular extent of the central solar disk ( $\sim 0.266^\circ$ ),  $\theta_{Aureole}$  the angular extent of the solar aureole ( $\sim 2.49^\circ$ ),  $\varphi$  solar flux and  $\theta$  the angular distance from the solar centre

### 2.4.2. Solar Profiles

The extended light source description of solar flux is often given in the form of a 1D distribution as flux intensity vs angular deviation from the solar centre. The profiles presented here are after the application of rotational symmetry both to give a more familiar visual impression of solar intensity and flux distribution and for the later application of restricted view analysis according to optical system entry aperture and solar abnormality.

#### 2.4.2.1. 2D Solar Profiles

2D solar profiles offer insight into the spatial distribution of the beam insolation. These profiles prove useful for the analysis of energy losses at the optical primary concentration stage. Some analysis of spherical aberration by ray tracing can also be performed using 2D solar profiles.

The use of Equation 2.13, Equation 2.14, Equation 2.15 and Equation 2.21 and the application of rotational symmetry results in solar profiles herein termed 2D solar profiles as the solar flux intensity at a given point can be described as a function of 2 variables, such that for a given circumsolar ratio:

$$P = f(\alpha, \varepsilon)$$

EQUATION 2.22

Where  $P$  is power,  $\alpha$  is angular deviation in azimuth and  $\varepsilon$  is angular deviation in elevation

An example 2D solar profile is given in Figure 2.32 and Figure 2.33.

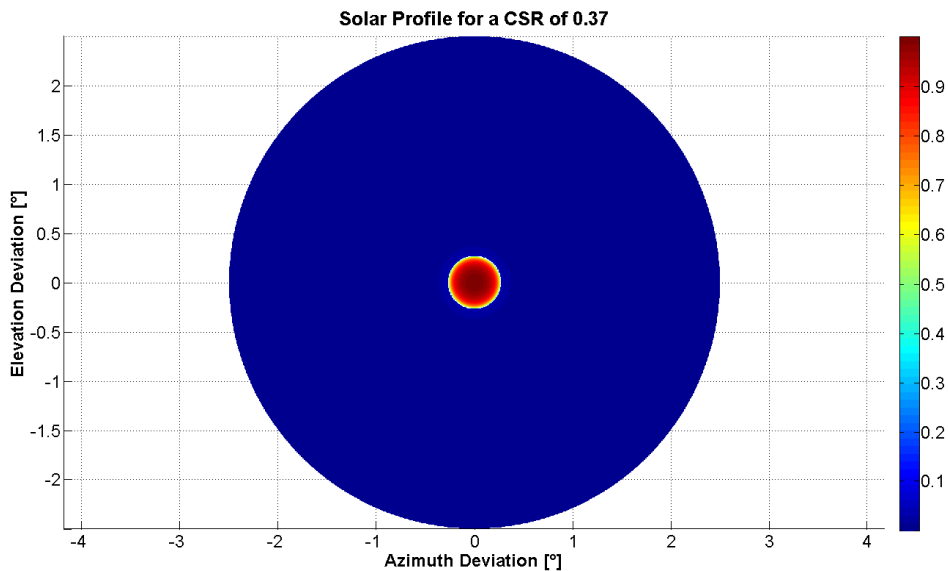


FIGURE 2.32: 2D SOLAR PROFILE FOR A CSR OF 0.37 WITH NORMALISED RELATIVE FLUX INTENSITY – BIRDS EYE VIEW

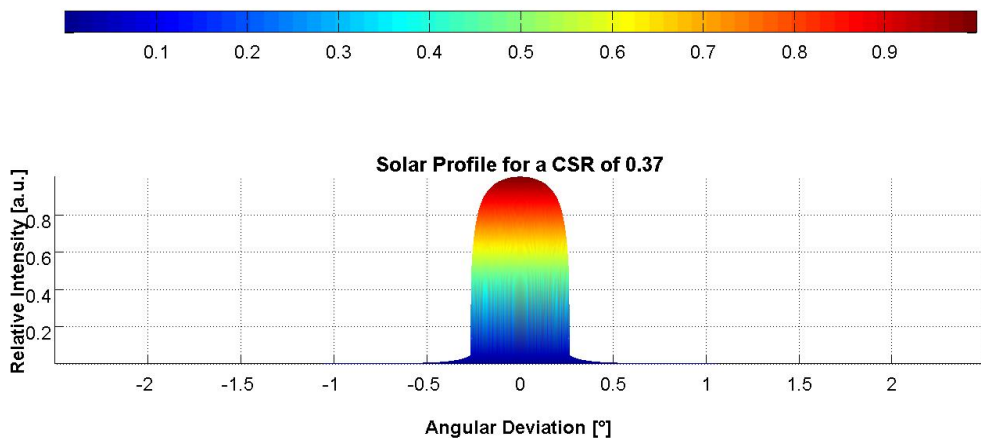


FIGURE 2.33: 2D SOLAR PROFILE FOR A CSR OF 0.37 WITH NORMALISED RELATIVE FLUX INTENSITY – SIDE VIEW

Figure 2.32 and Figure 2.33 show an extended light source 2D solar profile as generated for a CSR of 0.37. The relative flux intensity is displayed in colour, normalised to a maximum intensity of 1. Data of this form can be used as an input source description for a ray tracing simulation in order to investigate the optical illumination pattern formed at the receiver after traversing an optical concentration system.

#### 2.4.2.2. 3D Solar Profiles

3D solar profiles are particularly useful for the investigation of spectrally dependent effects in CPV systems such as mismatches in MJSC junction performance. Chromatic aberration can also be investigated by ray tracing using 3D solar profiles.

The model extension (as described in 2.3.4 Model Extension) is to include the spatial distribution of solar flux spectra, as well as intensity. These solar profiles are herein termed 3D solar profiles as the intensity at a given point can be described as a function of 3 variables, such that for a given circumsolar ratio:

$$P = f(\alpha, \varepsilon, \lambda)$$

EQUATION 2.2.23

Where  $P$  is power,  $\alpha$  is angular deviation in azimuth,  $\varepsilon$  is angular deviation in elevation and  $\lambda$  is wavelength of light

To elaborate effectively on these profiles and their potential application to CPV simulations, the net spectral flux contained in defined spectral bands is here chosen as the medium for their presentation. The spectral bands echo the active ranges of the three junctions in a typical triple junction solar cell for CPV, namely 280-680nm, 680-880nm and 880-1880nm. Furthermore, given, the air mass dependence on the spectral composition of solar flux (see Figure 2.29, Figure 2.30 and Figure 2.31), a specific air mass has to be defined for the presentation of these profiles. As per the standard reference spectrum, AM 1.5 is chosen here. The resultant 3D solar profile is presented as a tri-band analysis in Figure 2.34, Figure 2.35 and Figure 2.36.

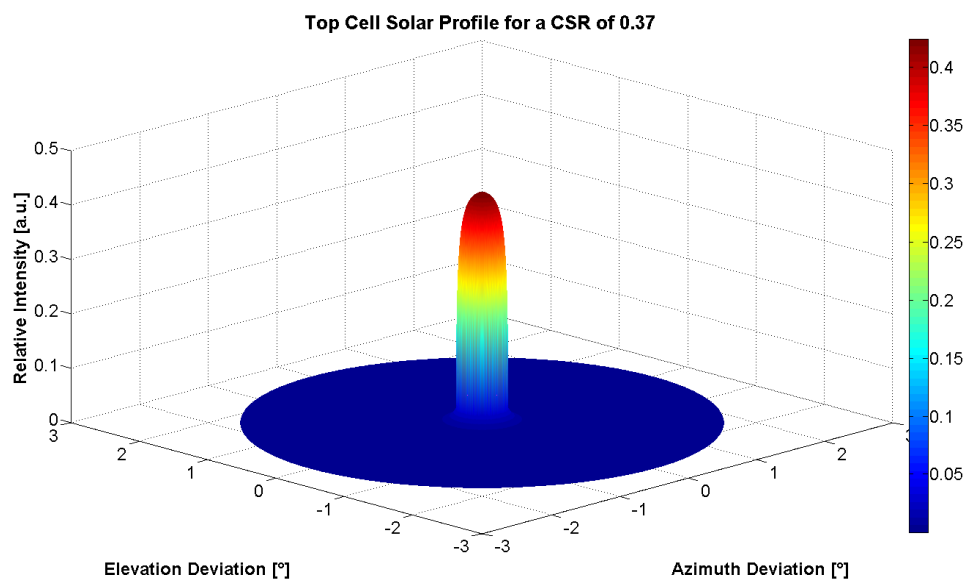


FIGURE 2.34: 3D SOLAR PROFILE PORTION IN THE 280-680nm WAVELENGTH RANGE FOR A CSR OF 0.37

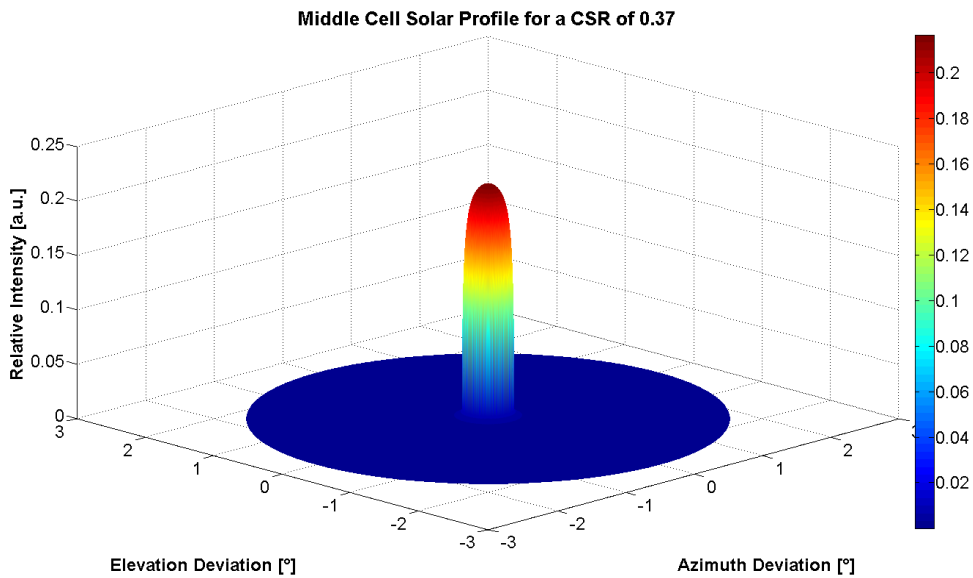


FIGURE 2.35: 3D SOLAR PROFILE PORTION IN THE 680-880nm WAVELENGTH RANGE FOR A CSR OF 0.37

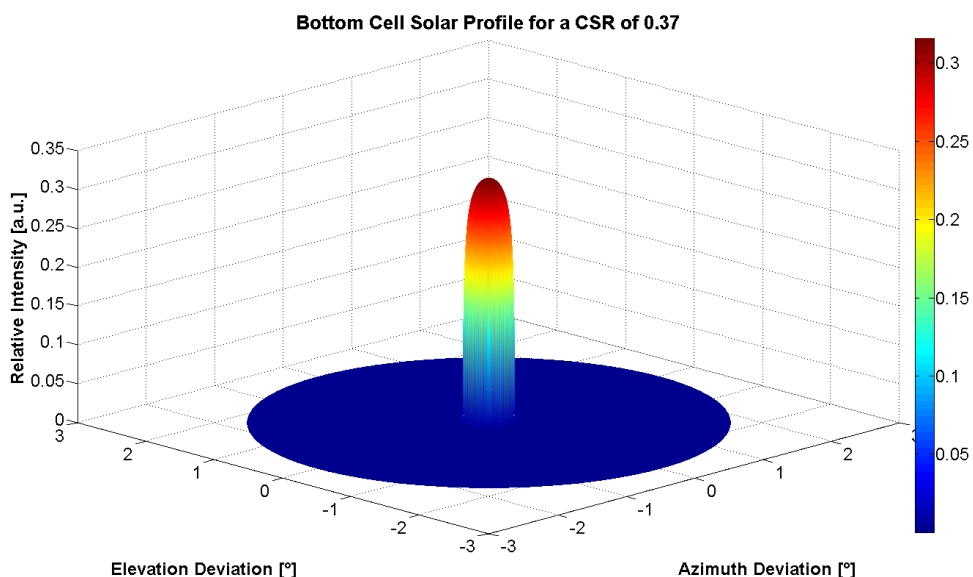


FIGURE 2.36: 3D SOLAR PROFILE PORTION IN THE 880-1880nm WAVELENGTH RANGE FOR A CSR OF 0.37

Figure 2.34, Figure 2.35 and Figure 2.36 show the apportioned contributions of the 3D solar profile for a CSR of 0.37 at air mass 1.5 in the 280-680nm, 680-880nm and 880-1880nm spectral bands, respectively. It can be seen that the relative contribution of the circumsolar region reduces from the top cell to the bottom cell due to the spectral differences of the central and circumsolar regions. The effective CSRs for the top, middle and bottom cell spectral bands are then: 0.47, 0.35 and 0.23, respectively.

This triple band split 3D solar profile is essentially based on a combination of the profile of Figure 2.32 and the AM 1.5 separated beam spectra as presented in Figure 2.37.

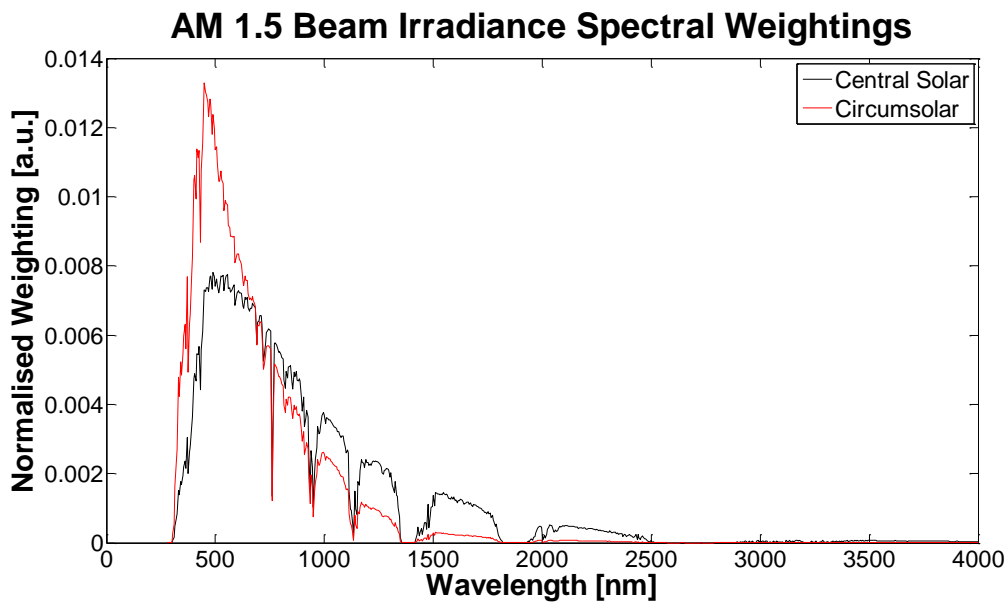


FIGURE 2.37: AM 1.5 SEPARATED BEAM SPECTRAL WEIGHTINGS

A major advantage of the 3D solar profile is the computation of variations in incident beam spectra as made possible by the spatially binomial consideration of the beam spectral distribution. This is a particularly advantageous feature for CPV applications due to the spectral sensitivity of MJ solar cells. The average photon energy (APE) proves a useful metric for the presentation of this spectral variation although it should be noted that the actual spectral composition is more complex than the APE suggests (see 2.3.4 Model Extension). Figure 2.38 shows the variation in APE with air mas and CSR.

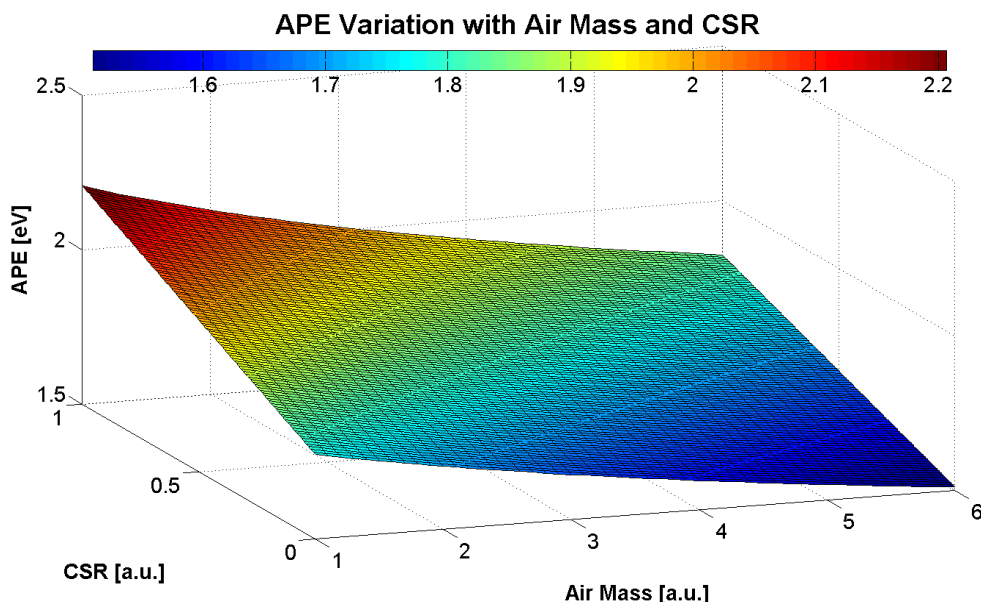


FIGURE 2.38: APE FOR SPECTRA WITH VARYING AIR MASS AND CSR

Figure 2.38 demonstrates the combined effects of a negative APE-AM correlation and a positive APE-CSR correlation. The vast majority of CSR variation is found in the 0.0-0.4 range, a CSR of 1 occurs only at a solar eclipse.

### 2.4.3. Contextual Analysis

The results as presented above may well be considered academic outside the context of real CPV system operation. This section considers the insolation harvest at the primary lens as determined by the lens entry aperture and the incident solar profile. Analyses are presented for cases with and without solar tracking errors.

#### 2.4.3.1. Ideal Solar Tracking

The energy incident on a CPV system is primarily restricted by the system field of view. The system field of view, as determined by the primary lens entry aperture, is defined as that area of sky visible to the primary lens. An area of sky is here termed a ‘sky-patch’. In the case of ideal solar tracking, there is no optical misalignment with the input source and the solar centre coincides with the visible sky-patch centre.

Figure 2.39 shows the sky-patch visible to a  $0.5^\circ$  aperture lens with an incident solar profile CSR of 0.2.

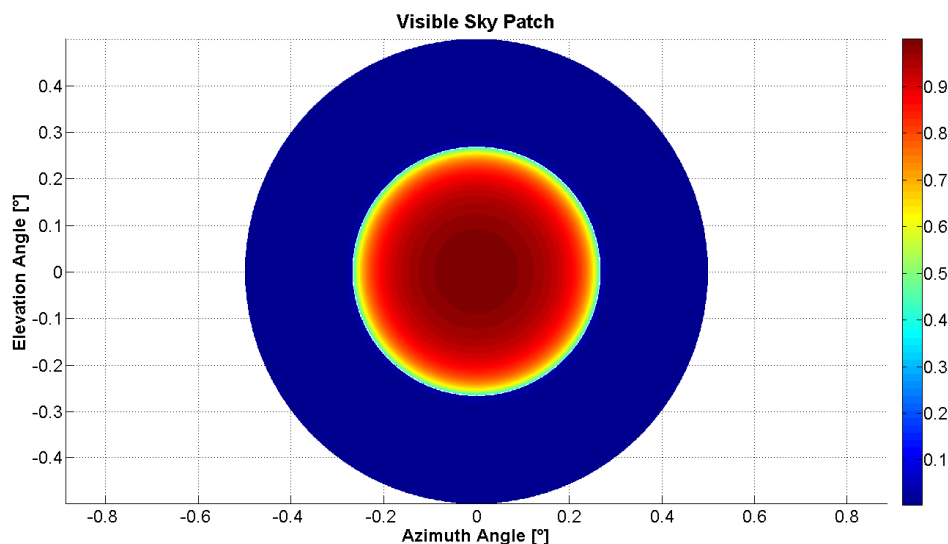


FIGURE 2.39: AN EXAMPLE SKY-PATCH VISIBLE TO A  $0.5^\circ$  APERTURE LENS NORMAL TO THE SUN WITH A CSR OF 0.2

Figure 2.39 shows the spatial intensity distribution of the sky-patch visible to a  $0.5^\circ$  aperture lens normal to the Sun. The net beam spectrum of this sky-patch for an air mass of 1.8 is shown in Figure 2.40.

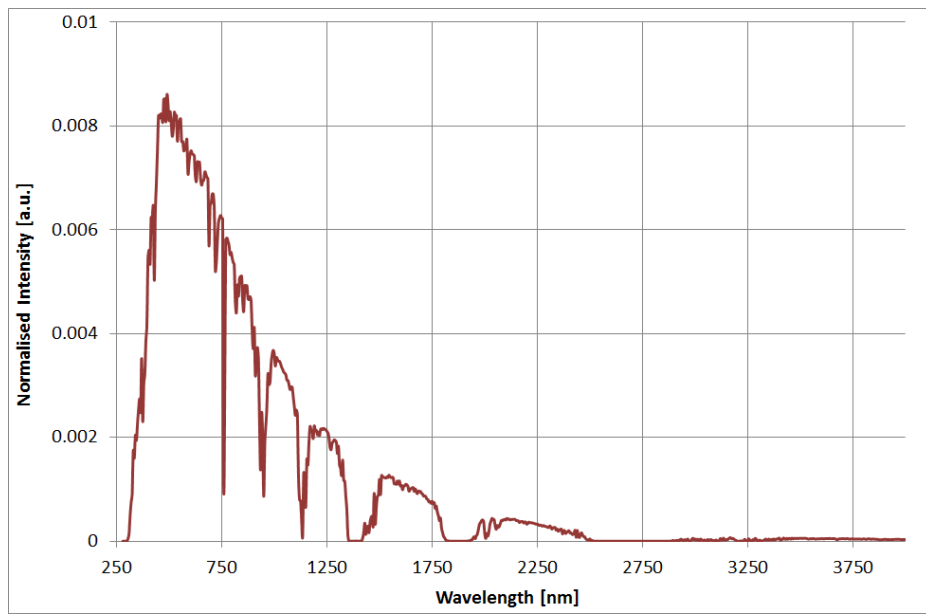


FIGURE 2.40: RELATIVE NET BEAM SPECTRUM VISIBLE TO A  $0.5^\circ$  APERTURE LENS NORMAL TO THE SUN WITH A CSR OF 0.2

Figure 2.40 shows the spectrum contained within the above visible sky-patch (see Figure 2.39). The APE of this spectrum is 1.77eV, which is significantly greater than the APE of the central solar spectrum of 1.72eV. Figure 2.41 gives the APE variation with air mass for the above visible sky-patch and an incident solar profile CSR of 0.2.

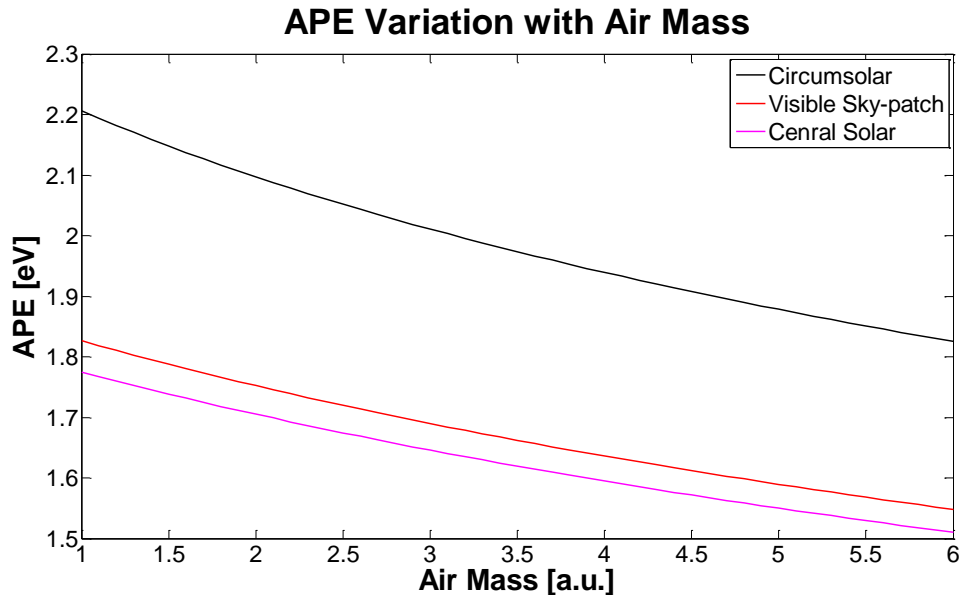


FIGURE 2.41: APE VARIATION WITH AIR MASS FOR A  $0.5^\circ$  APERTURE LENS NORMAL TO THE SUN WITH A CSR OF 0.2

Figure 2.41 shows the net beam spectrum of the above visible sky-patch with air mass alongside the central solar and circumsolar variations.

Given the reduction of the contributory area of the circumsolar region that results from envelopment by the lens aperture, calculation of the net visible sky-patch spectrum in the case of ideal solar tracking

is equivalent to calculation by effective CSR reduction. In the above case the effective CSR is reduced from 0.2 to 0.12. Effective CSR is a useful metric when considering the general composition of spectral irradiation that is active in the optical system. However, ray trace investigations of further optical effects through the concentration system require the use of the actual solar profile (0.2 in this case) as the spatial distribution of irradiation is a necessary consideration in the assessment of chromatic aberration. Moreover, the effects of solar tracking errors make for a more complex calculation of encompassed spectrum as the enveloped region analysis requires a more complex geometrical analysis.

#### 2.4.3.2. Non-ideal Solar Tracking

The non-ideal solar tracking results allow for the specific investigation of irradiation losses due to tracking error for a given system design. The analysis here can be performed for any concentration system given information on the input optical aperture and the incident solar profile (CSR). For temporally resolved data this analysis can be applied at every time step in a given period to analyse energy capture losses.

Normality with the Sun is achieved with a perfect solar tracking system. Though perfect tracking is often simulated in CPV, it is realistically an implausible achievement. One of the major causes of poor system CPV performance is tracking error and the associated distortions in illumination profile. These effects can be investigated with the generation of misaligned solar images.

Figure 2.42 shows the sky-patch visible to a  $0.5^\circ$  aperture lens with an incident solar profile CSR of 0.12 and solar tracking error of  $0.4^\circ$  in the azimuth axis.

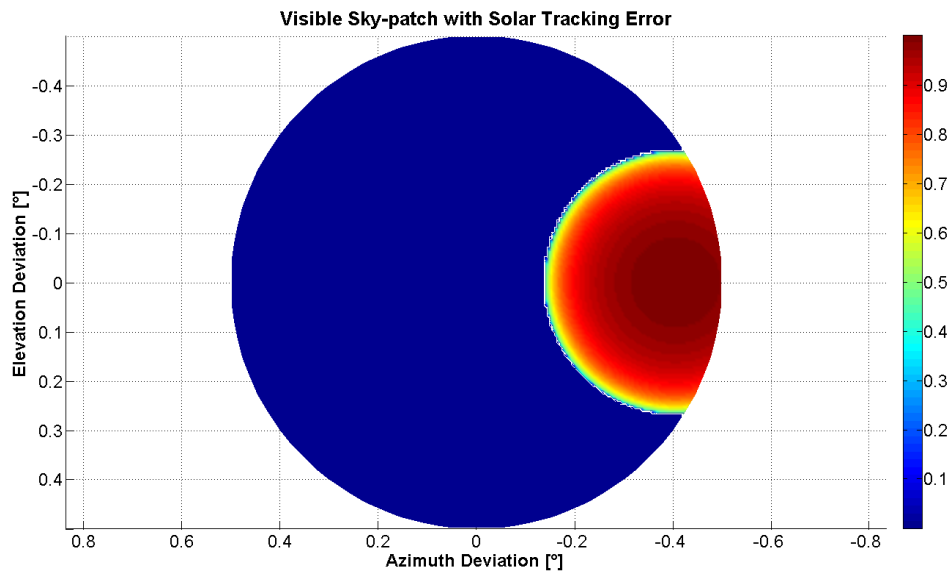


FIGURE 2.42: AN EXAMPLE SKY-PATCH VISIBLE TO A  $0.5^\circ$  APERTURE LENS ABNORMAL TO THE SUN BY  $0.4^\circ$  WITH A CSR OF 0.2

Figure 2.42 shows the spatially distributed intensity profile of the visible sky-patch for a  $0.5^\circ$  aperture lens abnormal to the Sun by  $0.4^\circ$  with a CSR OF 0.2. In this case, the ratio of enveloped circumsolar power to total enveloped power is 0.086. Thus there is a spectral shift with tracking error from 1.77 to 1.75eV. The net weighted net enveloped spectrum for an air mass of 1.8 is given in Figure 2.43, alongside the difference in normalised net spectral contribution between the ideally tracked sky-patch of Figure 2.39 and the above sky-patch.

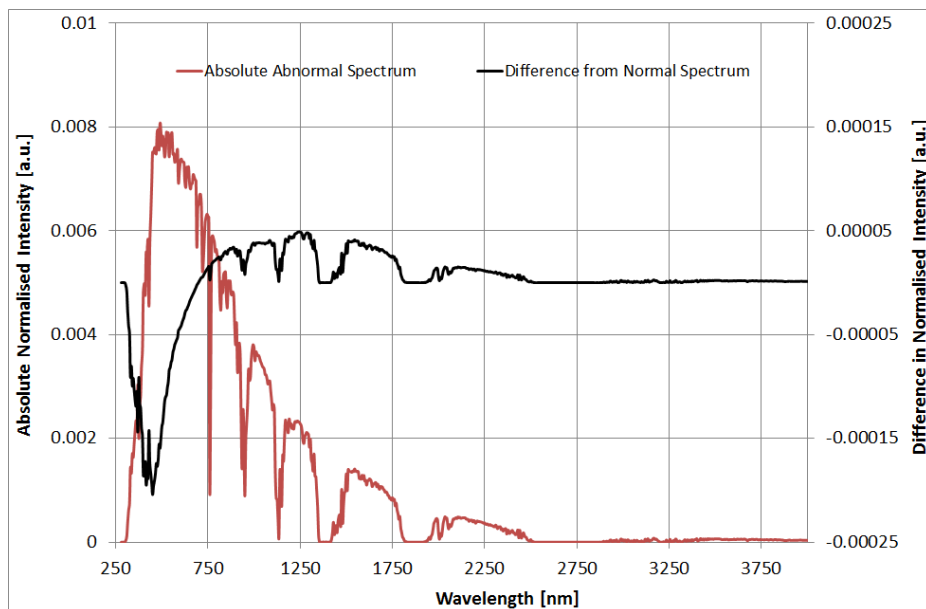


FIGURE 2.43: SPECTRUM VISIBLE TO A  $0.5^\circ$  APERTURE LENS SKY-PATCH ABNORMAL TO THE SUN BY  $0.4^\circ$  AT AM1.8 AND COMPARISON WITH NORMAL SPECTRUM

Figure 2.43 elaborates on the 177 to 1.75 APE shift above by showing the spectral composition of the abnormal sky-patch and highlighting the difference between it and that of the normal sky-patch.

The spectral composition of a visible sky-patch can be computed as a function of 4 parameters, namely: lens entry aperture angle, solar tracking error, air mass and circumsolar ratio. Test cases are used here to demonstrate the effects of variable alteration.

Figure 2.44 shows the variation of insolation power available to above lens for varying tracking error and CSR.

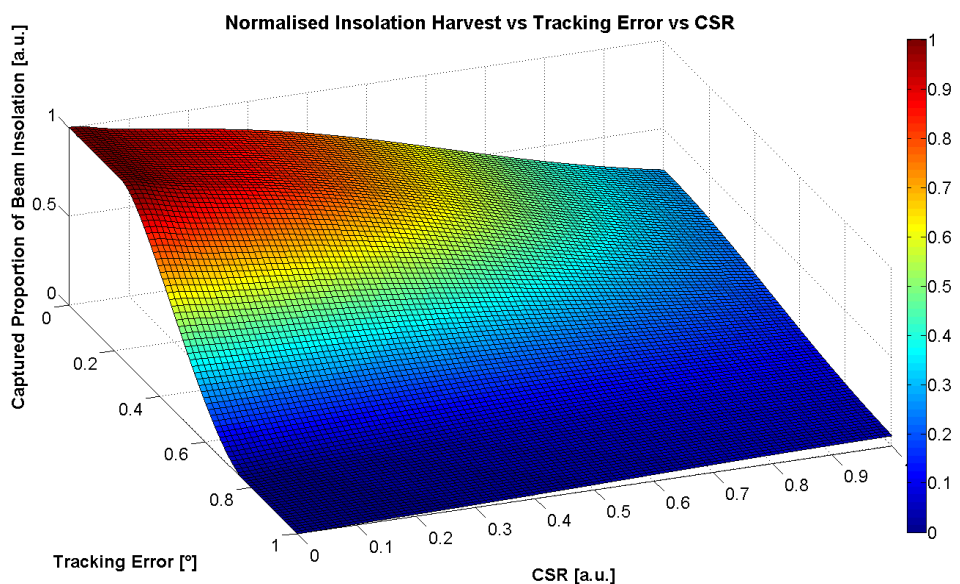


FIGURE 2.44: NORMALISED BEAM INSOLATION AVAILABLE TO A 0.5° APERTURE LENS VS CSR VS TRACKING ERROR FOR AN AIR MASS OF 1.2

Figure 2.44 shows only the variation of total flux intensity with tracking error and CSR for a given lens aperture. Two ridges can be seen in the distribution, one at  $\theta_{Lens} - \theta_{Sun}$  and one at  $\theta_{Lens} + \theta_{Sun}$ . This variation changes with lens aperture, although the general form remains the same. The spectral composition of the intensity within the above information changes with air mass, some insight into the air mass effects can be gathered from Figure 2.38. With a CSR of 0, the distribution is well approximated by use of the pillbox Sun (see Figure 2.13) although discrepancies near  $\theta_{Lens} - \theta_{Sun}$  are notable.

#### 2.4.3.3. Annual Energy Harvests – Example Case

Annual energy harvest predictions are a necessity for system financing, the results of this chapter are here considered in terms of their effects on annual energy harvest. An example case is here used for demonstration purposes, although the method can be applied to any system so long as there is system specification data as well temporally resolved data on the incident irradiation, CSRs and solar tracking errors.

By combining location-specific meteorological data, optical system information and parameter variation investigations such as the above, various system tolerance limits can be defined. This analysis is a useful tool in system design, allowing for the optimisation of the complex symbiotic parametric relationship between environmental phenomena, solar tracker operation errors and optical system component behaviour.

The effect of using extended light source solar profile descriptions on the annual incident energy harvest for Seattle (annual DNI ~ 1100kWh) is shown below. Meteonorm was used to generate a set of hourly insolation averages. Appropriate CSRs for each hourly step were then chosen using the analysis of Neumann et al (see 2.3.1.2 CSR Variation and Frequency). The variation and frequency of CSRs for Seattle is shown in Figure 2.45.

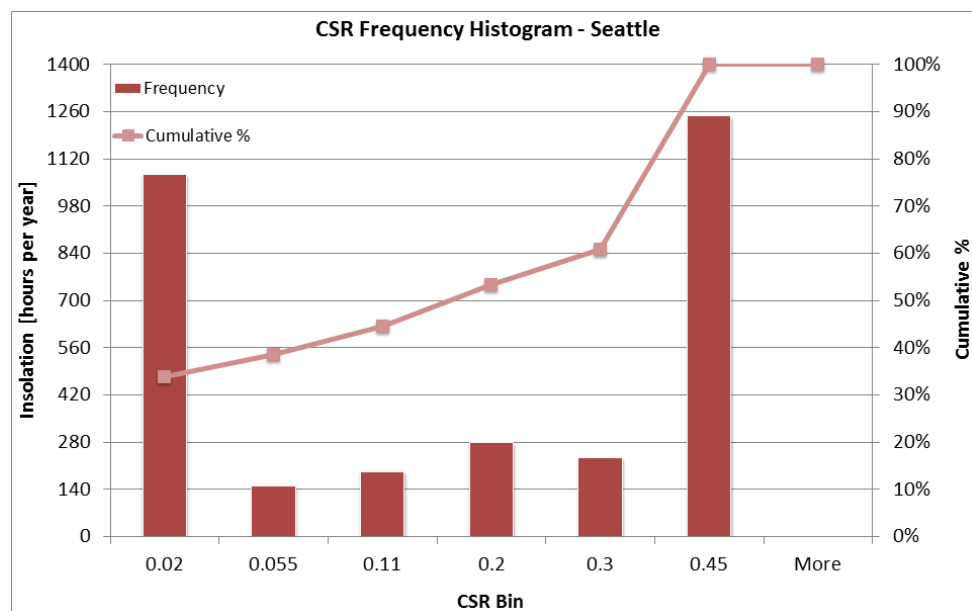


FIGURE 2.45: PROBABILISTICALLY DETERMINED CSR VARIATION AND FREQUENCY FOR SEATTLE, USA

Figure 2.45 shows Seattle as having a CSR variation and frequency with an almost equal weighting of extremely high and low CSRs. Seattle is considered as a comparatively (see Figure 2.20) better location for CPV than Edinburgh but worse than Almeria.

Each hourly data set was used to construct an effective system input image for a given primary lens aperture and 2D solar profile. Three optical system primary lens entry apertures were investigated: 0.5, 0.75 and 1°. 11 constant tracking error scenarios were simulated: (0 to 1 in steps of 0.1). The net incident flux at each time-step was calculated. This was integrated over full simulated year and normalised to a complete beam irradiance collection of 1. The results are presented in Figure 2.46.

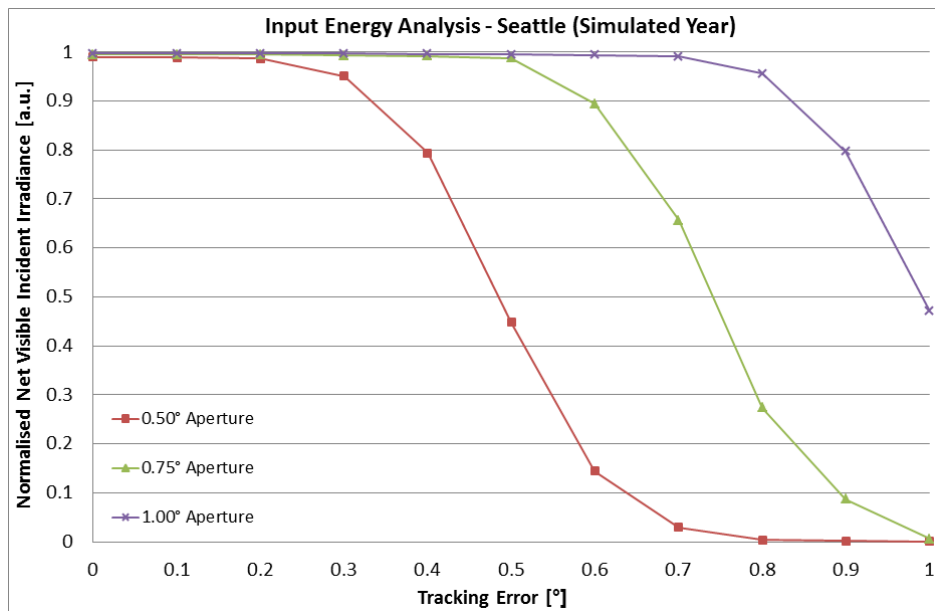


FIGURE 2.46: EFFECT OF TRACKING ERROR AND PRIMARY LENS APERTURE ON ANNUAL VISIBLE INCIDENT BEAM ENERGY HARVEST FOR SEATTLE

Figure 2.46 shows that a  $0.5^\circ$  primary lens aperture CPV system in Seattle operating with a  $0.3^\circ$  tracking error will only have 95% of incident beam irradiation available to the optical system over the year. It is important to note that the numbers presented here represent an initial loss only, effectively the energetic loss at the primary lens. This analysis does not include any further losses due to component misalignment. All losses presented here will be amplified at the receiver. The exact mechanisms of the loss amplification are determined by the specifics of the optical system, these mechanisms are investigated in the following chapter, 3 Optics.

## 2.5. Conclusions

Approximated solar source descriptions in the form of a point source and a pillbox Sun have been investigated and conditions of validity drawn. For most terrestrial locations and CPV system designs, particularly HCPV system designs, these conditions of validity are not often enough met to justify the use of these approximated solar source descriptions in CPV system simulations. To rectify this problem, an empirically derived spatially resolved model of beam irradiation was presented, improved and extended to include spectral variation. The developed model is principally based on the input of a circumsolar ratio (CSR). The input to output response of the model has here been improved from a mean and standard deviation of 0.937 and 0.107 to 1.000 and 0.005. The use of this model is proposed for CPV simulations.

A test case investigation into the combined effects of tracking abnormality and CSRs has been undertaken. Losses in beam irradiation available to example CPV optical concentration systems in Seattle, USA, over a year were simulated. The results demonstrate the significance of the inclusion of

such variables in CPV simulations. Tracking errors ( $0.3 - 0.4^\circ$ ) can result in a 5 – 20% loss of incident energy for a  $0.5^\circ$  aperture system. Such information ought to be a primary consideration in system design and the definition of acceptable tracking tolerance levels, particularly given that these losses are at the primary optical stage and further losses will be introduced by the specific behaviours of the optical system and the solar cell. The results confirm the notion that, for CPV systems with input aperture half angles in the sub degree range, extended light source Sun models are necessary for the accurate prediction of system performance as the use of point source and pillbox Sun models results in overestimations of system performance[64, 65].

Solar tracking errors and dependencies have been investigated using each of the presented Sun models. The differences in the prediction of irradiation collection losses at the primary concentration stage are clear and well defined. The tracking error analysis presented herein can be used to improve production and operational tolerance specifications for HCPV system designs.

Furthermore, the model spectrally differentiates between the central solar and circumsolar regions. Using this, it is shown that the incident spectrum changes significantly as a function of CSR, air mass, lens entry aperture and solar tracking error. The model thus provides a better framework for the optimisation of multi-junction cell structures, especially local and system specific optimisation. Such optimisation procedures can result in system energy production gains at no additional cost.

It has been shown that the inclusion of CSR variation, multidimensional solar profiling and spatially distributed spectra in CPV system performance modelling will improve both the effectiveness of the system designs and the accuracy of system energy ratings energy generation predictions.

In general, this work has added valuable information to the understanding of how input description variation alters the results of CPV system modelling.

# 3. Optics

*from Source to Cell*

## 3.1. Introduction

For many, the first experience of optics is a rather primitive one: fire. Concentration of the Sun's rays by a magnifying glass can provide enough energy to start a fire.



FIGURE 3.1: USING A MAGNIFYING GLASS TO START A FIRE BY FOCUSING THE SUN'S RAYS

This chapter offers optical analyses of CPV system components by means of Geometric Optics. Geometric Optics is an approximation to the behaviour of light which is valid as long as the dimensions associated with the interactive media of concern are much greater than the wavelength of light considered. The condition is illustrated in Figure 3.2, where Geometric Optics is a valid analytical tool given that  $d \gg \lambda$ , where  $\lambda$  is the wavelength of light.

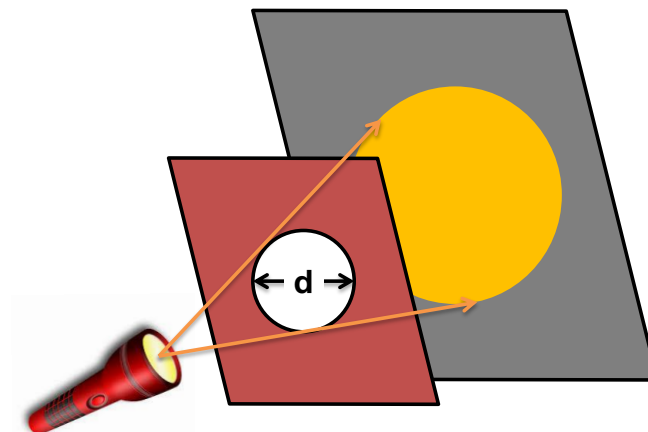


FIGURE 3.2: GEOMETRIC OPTICS WITH MACROSCOPIC MEDIA

### 3.1.1. Geometric Optics

In the approximation of geometric optics, the behaviour of light is governed by the principle of least time, or Fermat's principle. The principle of least time states that the path taken between two points by a ray of light is the path traversed in the least time. It is this theory underlying ray tracing, a method of calculating the paths of light rays through a system of interactive media. Furthermore, the laws of reflection and refraction may be derived from this principle.

#### 3.1.1.1. Law of Reflection

Consider 2 points the same side of a mirror at heights  $y_1$  and  $y_2$ , separated in the dimension parallel to the mirror plane by a distance,  $d$ . Figure 3.3 gives a schematic representation of this.

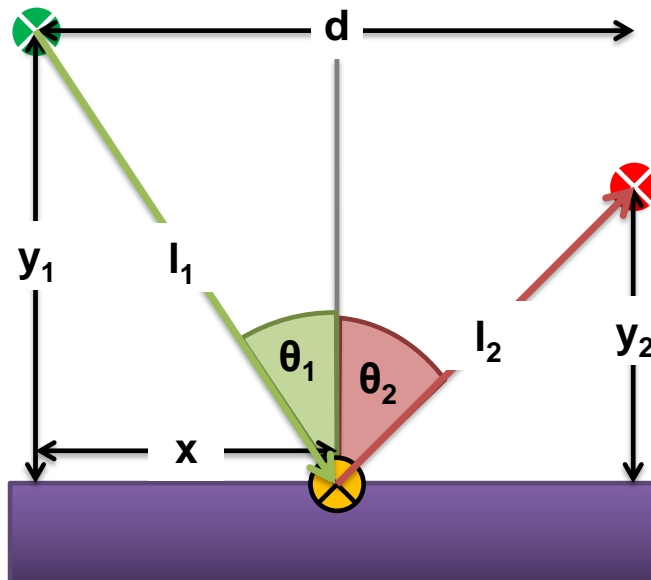


FIGURE 3.3: REFLECTION DERIVATION FROM PRINCIPLE OF LEAST TIME SCHEMATIC

Light travels at a constant speed,  $c$ , thus the time taken,  $t$ , for light to reflect off the mirror and arrive at the end point is given by the sum of the ray distances,  $l_1$  and  $l_2$ .

$$t = \frac{l_1 + l_2}{c} = \frac{\sqrt{y_1^2 + x^2} + \sqrt{y_2^2 + (d-x)^2}}{c}$$

According to the principle of least time, light will travel in such a way that the time taken from start point to end point is minimised. Thus:

$$\frac{d}{dx} \left( \sqrt{y_1^2 + x^2} + \sqrt{y_2^2 + (d-x)^2} \right) \frac{1}{c} = 0$$

$$\frac{x}{\sqrt{y_1^2 + x^2}} - \frac{(d-x)}{\sqrt{y_2^2 + (d-x)^2}} = 0$$

$$\frac{x}{l_1} = \frac{(d-x)}{l_2}$$

$$\sin \theta_1 = \sin \theta_2$$

$$\theta_1 = \theta_2$$

#### EQUATION 3.1: LAW OF REFLECTION

Which is the law of reflection in the common form.

#### 3.1.1.2. Law of Refraction

Consider 2 points in media of different refractive indices,  $n_1$  and  $n_2$  at heights  $y_1$  and  $y_2$  from a horizontal media boundary, separated in the dimension parallel to the boundary by a distance  $d$ .

Figure 3.4 gives a schematic representation of this.

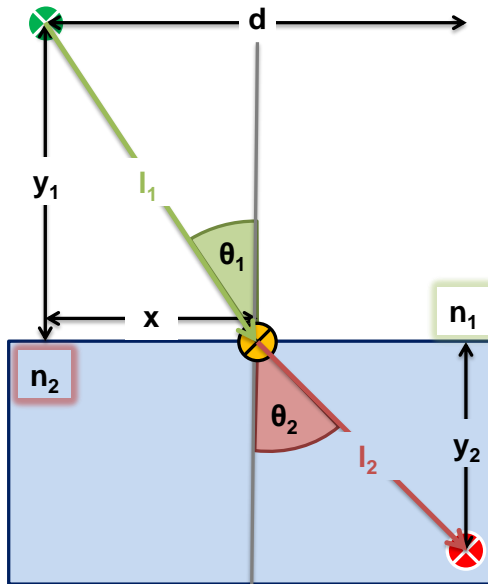


FIGURE 3.4: REFRACTION DERIVATION FROM PRINCIPLE OF LEAST TIME SCHEMATIC

The refractive index is defined as a modifier of the speed of light such that:

$$c_n = \frac{c}{n}$$

Where  $c$  is the speed of light in a vacuum,  $n$  the refractive index and  $c_n$  the speed of light in the medium of refractive index  $n$ .

Thus the time taken,  $t$ , by a ray of light from start point to end point is given by:

$$t = \frac{l_1 n_1 + l_2 n_2}{c} = \frac{n_1 \sqrt{y_1^2 + x^2} + n_2 \sqrt{y_2^2 + (d-x)^2}}{c}$$

According to the principle of least time, light will travel in such a way that the time taken from start point to end point is minimised. Thus:

$$\frac{d}{dx} \left( \frac{n_1 \sqrt{y_1^2 + x^2} + n_2 \sqrt{y_2^2 + (d-x)^2}}{c} \right) = 0$$

$$\frac{n_1 x}{\sqrt{y_1^2 + x^2}} = \frac{n_2 (d-x)}{\sqrt{y_2^2 + (d-x)^2}}$$

$$\frac{n_1 x}{l_1} = \frac{n_2 (d-x)}{l_2}$$

$$n_1 \sin \theta_1 = n_2 \sin \theta_2$$

EQUATION 3.2: LAW OF REFRACTION

Which is the law of refraction in the common form.

### 3.1.2. Concentration

For the most part, optical systems take advantage of the phenomena of refraction and reflection in affecting the directional change of light. Respectively, CPV optical systems mostly comprise lenses and mirrors used to focus the light falling over a given area to a smaller one, a process known as light concentration. The maximal concentration of a given source depends both on the geometry of the concentration system and the angular subtense of the source.

#### 3.1.2.1. Maximal Concentration

The generalised étendue, as explained in detail elsewhere[66-69], is an invariant property of geometrical optical systems that can be used to derive the theoretical upper limits of concentration. Considering a 2-dimensional optical concentration system with an input aperture width,  $2a_i$ , and source angular subtense,  $2\theta_i$ ; a corresponding output aperture width,  $2a_o$ , and output angular subtense,  $2\theta_o$ ; with the optical source in a medium of refractive index  $n_i$  and the optical concentration in a medium of refractive index  $n_o$ ; as depicted in Figure 3.5.

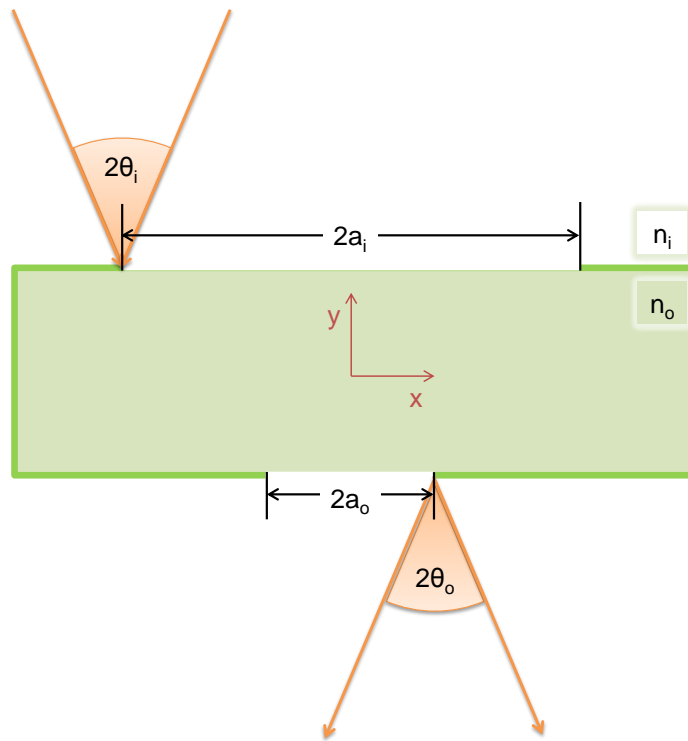


FIGURE 3.5: 2D OPTICAL CONCENTRATION SYSTEM - GENERALISED ÉTENDUE SCHEMATIC

For a given ray origin on the input aperture at a point  $(x, y)$  and directional cosines for infinitesimally small movements within the aperture,  $dx$ , and infinitesimally small directional changes,  $dB$ , the generalised étendue is expressed as:

$$n_i dx_i dB_i = n_o dx_o dB_o$$

Which, integrated over the aperture width and directional cosines becomes:

$$n_i 2a_i 2 \sin \theta_i = n_o 2a_o 2 \sin \theta_o$$

The concentration ratio is then the ratio of input to output aperture according to:

$$X = \frac{a_i}{a_o} = \frac{n_o \sin \theta_o}{n_i \sin \theta_i}$$

The concentration is then at the theoretical maximum when  $\theta_o = \frac{\pi}{2}$ . Thus, for the two dimensional concentration system the theoretical maximum is related to the angular subtense of the source according to:

$$X_{max2D} = \frac{n'}{n \sin \theta}$$

EQUATION 3.3

From symmetry the theoretical maximum for three dimensional concentration systems is then:

$$X_{max3D} = \left( \frac{n'}{n \sin \theta} \right)^2$$

EQUATION 3.4

*Where n is the refractive index at the source, n' the refractive index at the receiver, θ the angle subtended by the source to the receiver and the X the concentration factor*

Due to the elliptical orbit of the Earth about the Sun, there is approximately a 3% variation in the apparent solar semi-diameter throughout the year from perihelion to aphelion of 4.742mrad to 4.584mrad, respectively (see 2.3 The Sun as a Variable Extended Light Source). Thus maximal concentration is found as:

$$211 \leq X_{max2D} \leq 218$$

$$44471 \leq X_{max3D} \leq 47590$$

In standard optical analysis, i.e. paraxial or Gaussian, infinite concentration appears possible. This is, of course, not the case. One of the reasons for the inaccuracy of paraxial optical analysis is that it does not consider aberrations. Aberrations are a form of image distortion due to divergent ray paths. Spherical aberration is the term used to describe lateral and longitudinal aberrations in common lenses (as discussed in 3.3.3.3 Focal Point Calculation Summary), chromatic aberration is that aberration resulting from spectrally dependent phenomena such as refraction and absorption (as discussed in 3.2 Material Properties).

In describing real optical systems there are two key parameters of concentration: geometric concentration and optical concentration.

### 3.1.2.2. Geometric Concentration

The geometric concentration ratio is quite simply the ratio of collector area to receiver area:

$$X_G = \frac{A_C}{A_R}$$

EQUATION 3.5

The geometric concentration ratio is an indicator of the dimensional requirements of a concentration system and the maximal optical concentration. However, this ratio can take any value, including values beyond the theoretical maxima, and thus its use is limited without knowledge of the optical efficiency.

### 3.1.2.3. Optical Concentration

The optical concentration ratio is a more useful measurement. It is defined as the averaged flux over the collector area to the averaged flux over the receiver area:

$$X_O = \frac{\frac{1}{A_C} \int I dA_C}{\frac{1}{A_R} \int I dA_R} = \frac{A_R \int I dA_C}{A_C \int I dA_R}$$

EQUATION 3.6

The optical concentration ratio,  $X_O$ , is related to the geometric concentration,  $X_G$ , by the optical efficiency,  $\eta$ , according to:

$$X_O = \eta X_G$$

EQUATION 3.7

For systems employing perfect solar tracking, the concentration ratios are static and often referred to as a number of Suns, denoted by 'X'.

### 3.1.2.4. Examples of Concentrators

The dimensional geometry of the optical system defines the solar tracking requirements. Single axis tracking – most commonly of elevation angle – is required in 2-dimensional (or linear) concentration systems and biaxial tracking in 3D systems.

#### 2D – Parabolic Trough

2D linear concentrators are dimensional extrusions of 2-dimensional concentration principles, a popular and extensively researched example of which is the parabolic mirror.



FIGURE 3.6: 2D PARABOLIC MIRROR[70]

The parabolic mirror can be derived from the principle of least time. Consider a beam of light rays from infinity such that all rays travel perpendicular to the wave front, as depicted schematically in Figure 3.7.

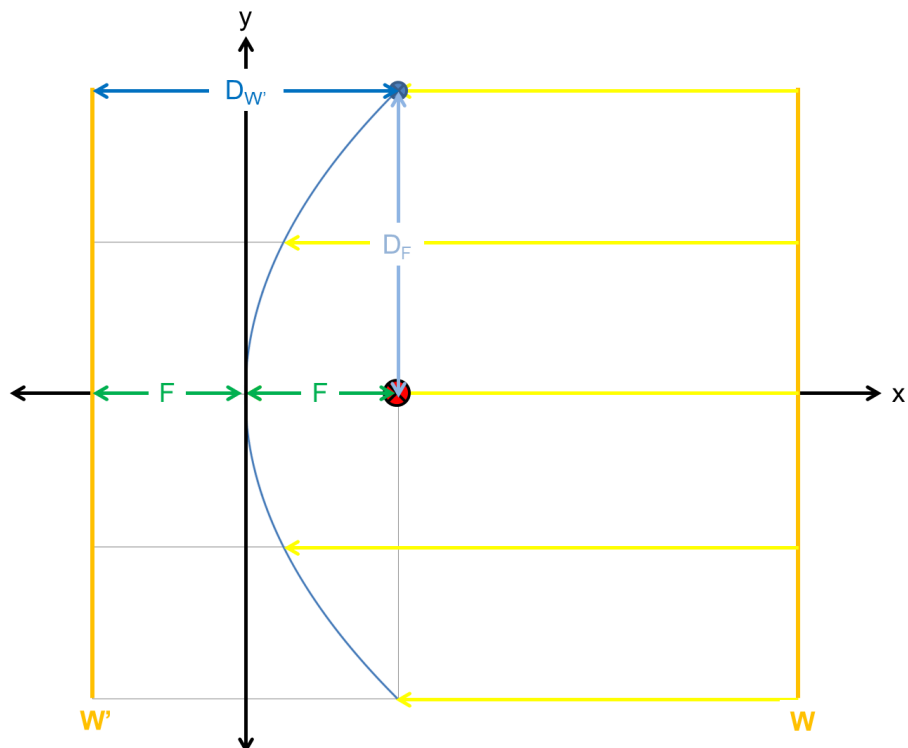


FIGURE 3.7: 2D PARABOLIC MIRROR DERIVATION FROM THE PRINCIPLE OF LEAST TIME

With no mirror, all rays on the wave front,  $W$ , will simultaneously arrive at the projected wave front,  $W'$ . Consider a reference frame such that the vertex of the parabola is at the origin and the focal point a distance  $F$  along the x-axis. The projected wave front,  $W'$ , is shown at  $x = -F$ . From the principle of least time, for all rays to arrive at the focal point, the mirrored surface must be constructed such that at all points the distance to the focal point,  $D_F$ , is equivalent to the distance to the projected wave front,  $D_{W'}$ . Thus it follows from specification that:

$$F + x = \sqrt{(F - x)^2 + y^2}$$

EQUATION 3.8

Which rearranges to the common form:

$$y^2 = 4xf$$

EQUATION 3.9

Parabolic mirrors are often used in solar thermal applications to focus light onto a cylindrical receiver. In practice the maximum geometric concentration ratio for such an application has been calculated as ~70, which is approximately one third of the maximum concentration ratio for 2D concentrators. This reduction from the ideal is due to beam spread errors[71].

The manufacture cost of a parabolic mirror is typically much higher than that of a circular mirror. Given this, circular segments are often used as a cheap approximation to the parabola. For consistency with Figure 3.7, the segment vertex of the circle shall be placed at the origin such that:

$$y^2 = r^2 - (x - r)^2 = 2rx - x^2$$

EQUATION 3.10

Which is a good approximation to Equation 3.9 given that  $r = 2f$  and  $x$  is small. This approximation is demonstrated in Figure 3.8 for a parabolic mirror of focal length 5 and a semi-circular mirror of radius 10.

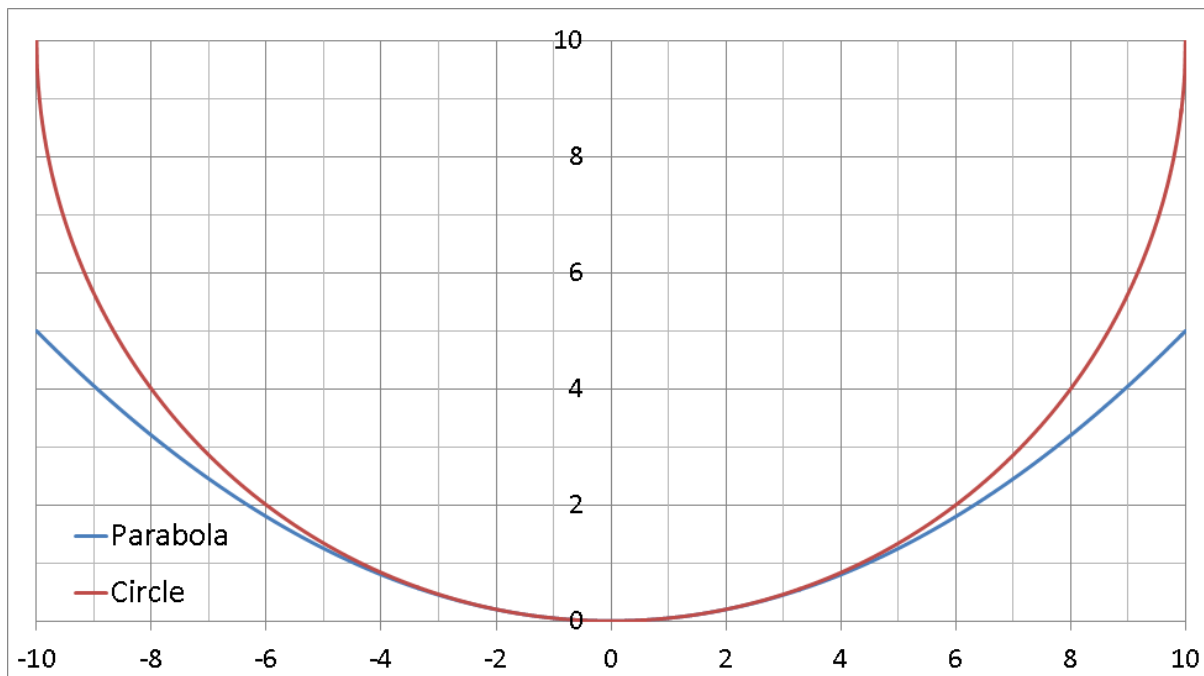


FIGURE 3.8: CIRCLE AND PARABOLA - NEAR VERTEX APPROXIMATION

### 3D – Paraboloidal Dish

3D concentrators are can be derived from dimensional rotations of 2-dimensional concentration principles. The dimensional extension of the parabola is termed the paraboloid.



FIGURE 3.9: CONCENTRATING PARABOLOID - EURODISH[72]

The concentrating paraboloid of CPV is derived as a dimensional rotation of the parabola about the axis of symmetry. In mathematics this is a special case of a paraboloid termed a 'paraboloid of revolution'. A paraboloid is derived from Figure 3.7 by rotation about the x-axis, into the z-axis.

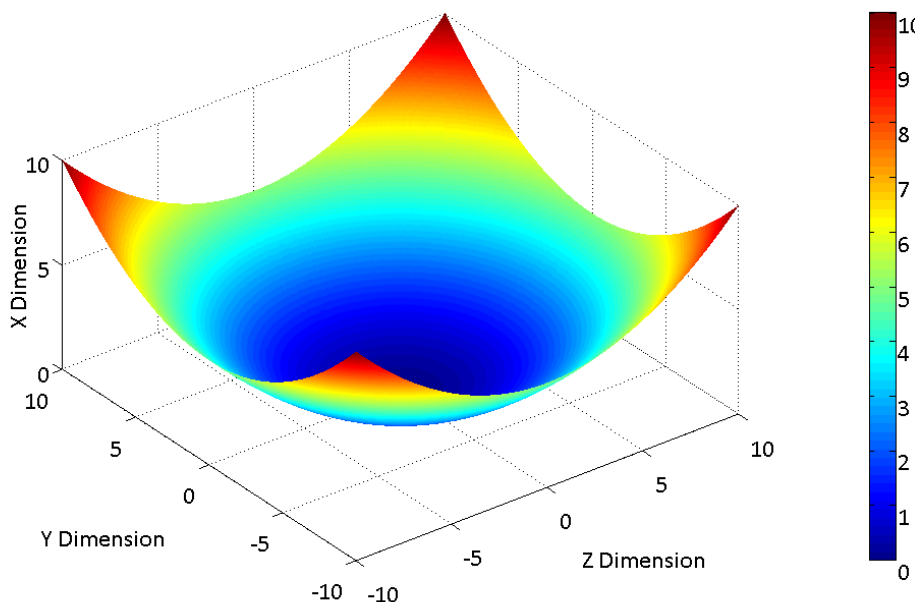


FIGURE 3.10: 3D PARABOLOID WITH FOCAL LENGTH 5

The concentrating paraboloid can be derived as an extension of Equation 3.9 such that:

$$(F + x) = \sqrt{(F - x) + y^2 + z^2}$$

Leading to:

$$y^2 = 4xf - z^2$$

Which rearranges to the common form:

$$x = \frac{y^2}{4f} + \frac{z^2}{4f}$$

EQUATION 3.11

### 3.1.2.5. System Classification

The concentration system examples given above are just 2 of many. General classification of concentrator systems is not a trivial task. This is due in part to the complexity of the technology and in part to its relative infancy. One cannot simply chart the evolution of solar concentration systems and point to a modern standard, there are various technological approaches to concentrated solar power (CSP) and the field still bears witness to experimentation and novel designs. There does, however, seem to be an established general trend that optical systems with reflective primary concentrators are most popular for solar thermal applications whereas optical systems with refractive primary concentrators are most popular for solar photovoltaic applications. Table 3.1 gives a generalised overview of concentrator systems classification according to technological specification.

TABLE 3.1: CSP GENERAL SYSTEM CLASSIFICATION WITH SPECIFIC EXAMPLES

Refractive Primary	Reflective Primary	
Linear Focus (2D)	<b>CPV</b> Asymmetric compound parabolic concentrator trough with dielectric to single junction solar cells	
Point Focus (3D)	<b>HCPV</b> Fresnel lens to multi-junction solar cell with biaxial solar tracking	<b>CST</b> Parabolic trough to cylindrical receiver with solar elevation tracking
	<b>HCST</b> Paraboloidal dish to Sterling engine with biaxial solar tracking	

Table 3.1 gives a generalised overview of CSP technologies according to base technological principles. The acronyms refer to a general category and the text to a specific example. This is by no means an exhaustive or exclusive list, although it covers well most commercially successful technologies. A more exhaustive overview is given in[70].

### 3.1.3. Synopsis

CPV systems exploit the optical phenomena of reflection and refraction in the design of solar focussing systems to cast insolation incident over the primary concentration device onto a small area, high efficiency solar cell. The most common form of analysis for this process is ray tracing, a technique grounded on the principles of geometric optics. In particular, ray tracing of the Fresnel lens is a non-trivial process given the multiplicity of surfaces involved. Often, in existing simulation methods, component placement and orientation errors are ignored or generalised to a one-dimensional analysis.

This chapter is concerned mainly with HCPV systems according to the example provided in Table 3.1 (point focus with a refractive primary concentrator), serving as an investigation of the Fresnel and plano-convex lenses and their behaviour with respect to optical phenomena. A ray trace system is developed to offer further insight into the behaviour of CPV optical systems. Example concentration lenses are designed and their spectrally dependent behaviour investigated for each of the solar source descriptions analysed in the previous chapter (see 2, ‘Input’).

## 3.2. Material Properties

The two principle material properties of concern in optical system design are absorption/transmission and refractive index. Both properties are required for simulating the behaviour of optical systems and assessing potentially indecorous phenomena such as aberrations and image distortion. Both these properties are spectrally dependent phenomena and ideally should be considered as such in optical simulation. However, is not currently computationally practical to perform satisfactorily high spatial resolution ray tracing simulations with high resolution spectral resolutions. It is suggested that a satisfactory number of spectral bands should be used as a spectral resolution and that at minimum this should correspond to the active junctions of the solar cell under investigation. This section presents such information for the main materials of concern in CPV alongside a process for the spectral weighting of averages in these spectral bands.

### 3.2.1. Absorption Coefficient

In the visible spectrum at least, one can relate the opacity/transparency of a material directly to the transmission of light through that material. Transmission and absorption are directly related in that their sum is unity. An important distinction between these values and the absorption coefficient is that, unlike transmission and absorption, the absorption coefficient is not path length dependent.

#### 3.2.1.1. Overview

Material transmissivity is defined as:

$$T = \frac{I}{I_0} = e^{-\alpha l}$$

EQUATION 3.12: BEER-LAMBERT LAW

Where  $T$  denotes transmissivity;  $I$  and  $I_0$  intensity of transmitted and incident light, respectively;  $\alpha$  the absorption coefficient; and  $l$  the material traversal path length

Given its path length dependence, absorption can well be considered a source of image distortion as the path length taken through the material varies for the incident light lens front position and incidence angle. As can be seen from the data below, material absorption coefficients can vary greatly over the solar spectrum with no apparent predictability. As such, nominal values are of little use and rarely found in the literature. Spectrally resolved material absorption coefficients have been measured for a variety of common CPV specific materials for the purpose of this work. The measurements have been recorded at 1nm resolution over the full active range of the solar spectrum for CPV

The transmission/absorption data herein is presented as measured at Loughborough University by spectrophotometry. Reflection losses at the material interface have been accounted for according to the Fresnel equations (Equation 3.13, Equation 3.14 and Equation 3.15).

Absorption coefficients tend not to be given at a nominal value, although the phenomena itself is often ignored in simulation. In this work, the absorption coefficient is given as spectrally weighted averages corresponding to the operational bands of a typical triple-junction solar cell (see Table 3.2), for consistency with the standard approach to the refractive index, the value at 589nm is highlighted for reference.

### 3.2.1.2. Absorption Coefficient Data

Material absorption data is presented for those materials common to CPV optical systems, specifically those relating to primary and secondary optical components.

#### Low Iron Soda-lime Glass

The most common plano-convex lens material for CPV secondary concentration is soda-lime glass. Low iron varieties are preferred in optical applications due to reduced tinting and increased transmission. Figure 3.11 and Figure 3.12 show measured material absorption coefficient alongside AM1.5 DNI spectrally weighted average values for the 280-1880nm spectral range for single and triple band analysis, respectively.

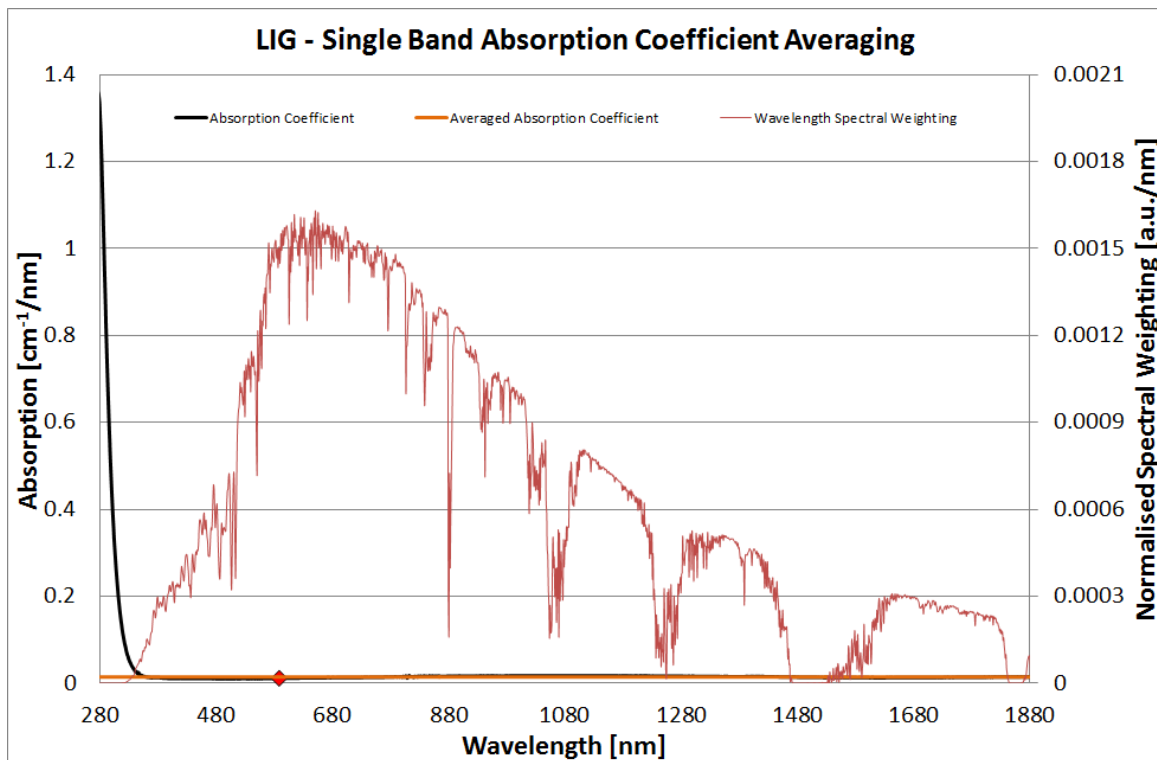


FIGURE 3.11: SINGLE BAND SPECTRALLY WEIGHTED AVERAGE ABSORPTION COEFFICIENT FOR LOW IRON SODA-LIME GLASS WITH THE AM1.5 DIRECT SPECTRUM

Figure 3.11 shows the measured absolute and single band (280-1880nm) spectrally weighted average absorption coefficients of low iron soda-lime glass. The absolute value of the measured absorption coefficient varies between  $1.333\text{ cm}^{-1}$  and  $0.010\text{ cm}^{-1}$ , while the spectrally weighted average is found as  $0.014\text{ cm}^{-1}$ . A nominal value at 589nm of  $0.011\text{ cm}^{-1}$  is highlighted for reference. Triple band weighted averages corresponding to the active regions of a typical triple junction solar cell are given in Figure 3.12.

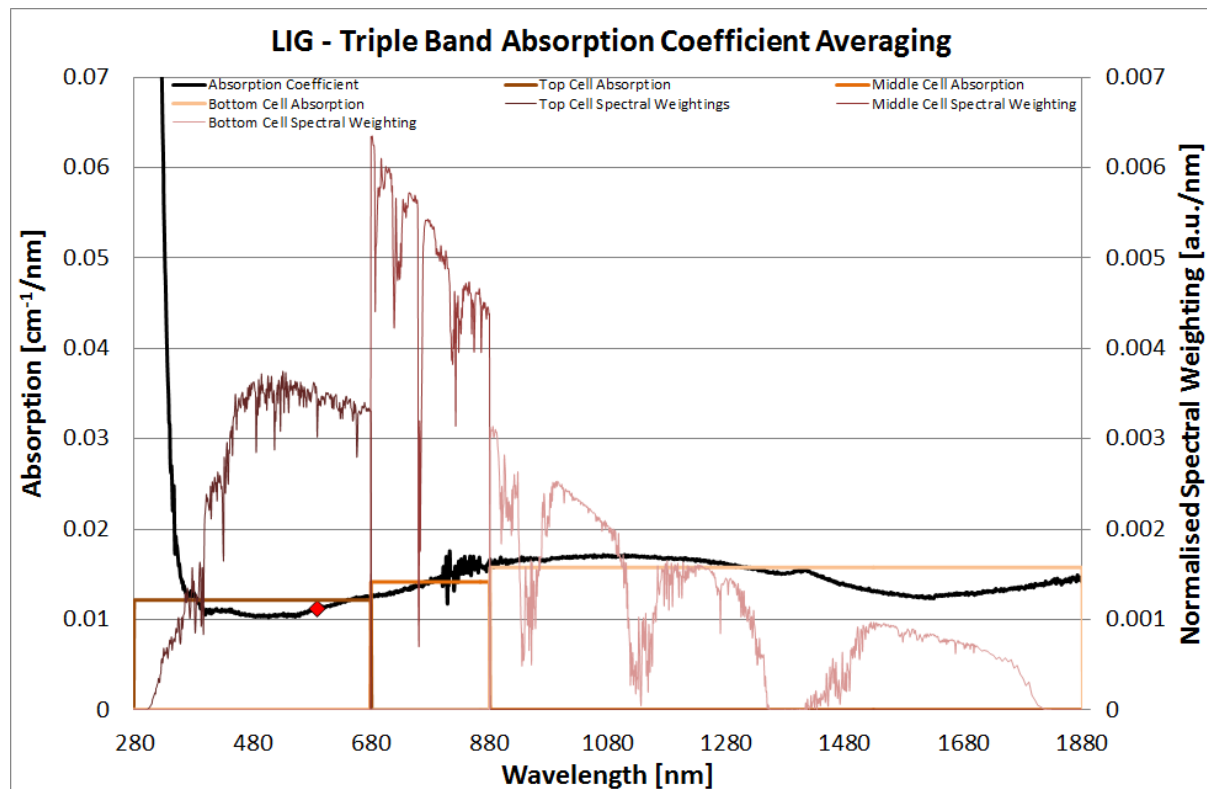


FIGURE 3.12: TRIPLE BAND SPECTRALLY WEIGHTED AVERAGE ABSORPTION COEFFICIENT FOR LOW IRON SODA-LIME GLASS WITH THE AM1.5 DIRECT SPECTRUM

Figure 3.12 shows the measured absolute and triple band (280-680, 680-880 & 880-1880nm) spectrally weighted average absorption coefficients of low iron soda-lime glass. The distortion at around 800nm in the measured absorption curve is due to a changeover of sensors in the spectrophotometer. The absolute value of the measured absorption coefficient varies between  $1.333\text{ cm}^{-1}$  and  $0.010\text{ cm}^{-1}$ , while the spectrally weighted averages are found as  $0.012$ ,  $0.014$ , and  $0.016\text{ cm}^{-1}$ , respectively. A nominal value at 589nm of  $0.011\text{ cm}^{-1}$  is highlighted for reference.

### PMMA

The most common material for Fresnel lens manufacture is poly(methyl) methacrylate (PMMA). PMMA proves a cost effective solution for the manufacture of thin Fresnel lenses for CPV application. Its choice as a material for CPV primary concentration device was driven both by economic incentive and the existing processes of the lens manufacture industry. Figure 3.13 and Figure 3.14 show measured material absorption coefficient alongside AM1.5 DNI spectrally weighted average values for the 280-1880nm spectral range for single and triple band analysis, respectively. As can be seen from Figure 3.13 and Figure 3.14, PMMA is highly absorbent in the UV wavelengths. This has a variety of ramifications for material degradation which are beyond the scope of this work.

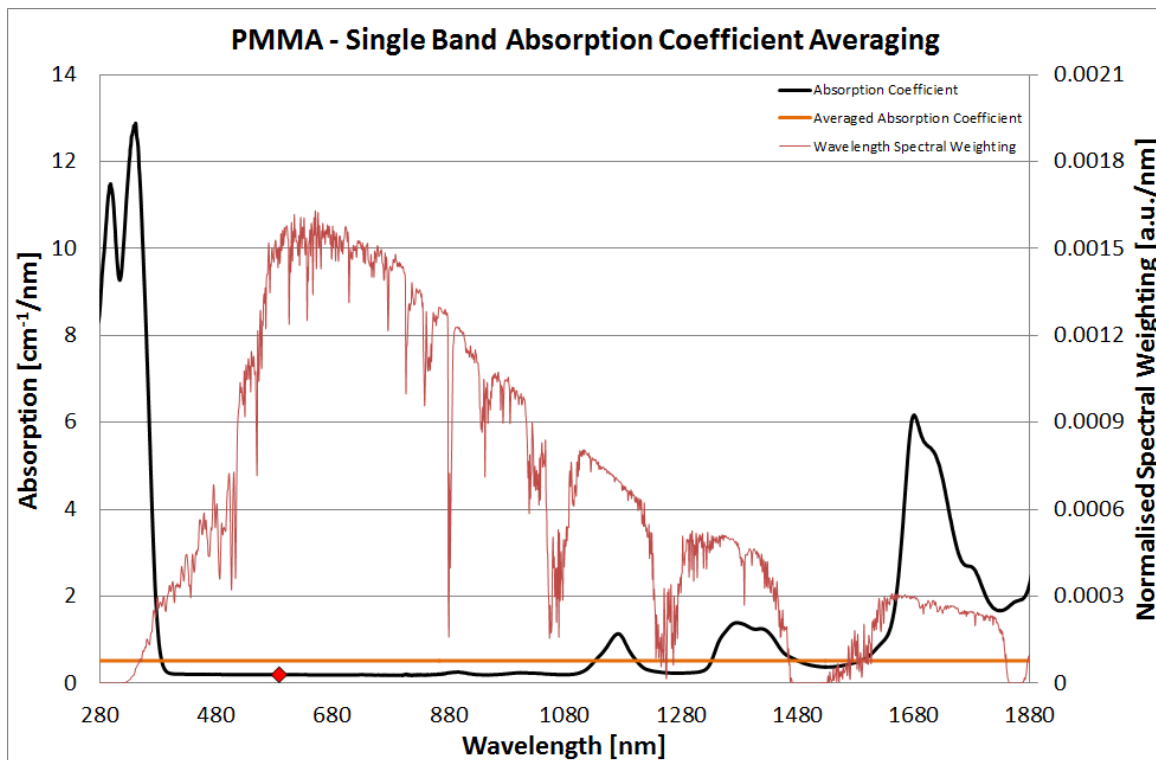


FIGURE 3.13: SINGLE BAND SPECTRALLY WEIGHTED AVERAGE ABSORPTION COEFFICIENT FOR PMMA WITH THE AM1.5 DIRECT SPECTRUM

Figure 3.13 shows the measured absolute and single band (280-1880nm) spectrally weighted absorption coefficients of PMMA. The absolute value of the measured absorption coefficient varies between  $12.880$  and  $0.173\text{cm}^{-1}$ , while the spectrally weighted average is found as  $0.516\text{cm}^{-1}$ . A nominal value at 589nm of  $0.195\text{cm}^{-1}$  is highlighted for reference. Triple band weighted averages corresponding to the active regions of a typical triple junction solar cell are given in Figure 3.14.

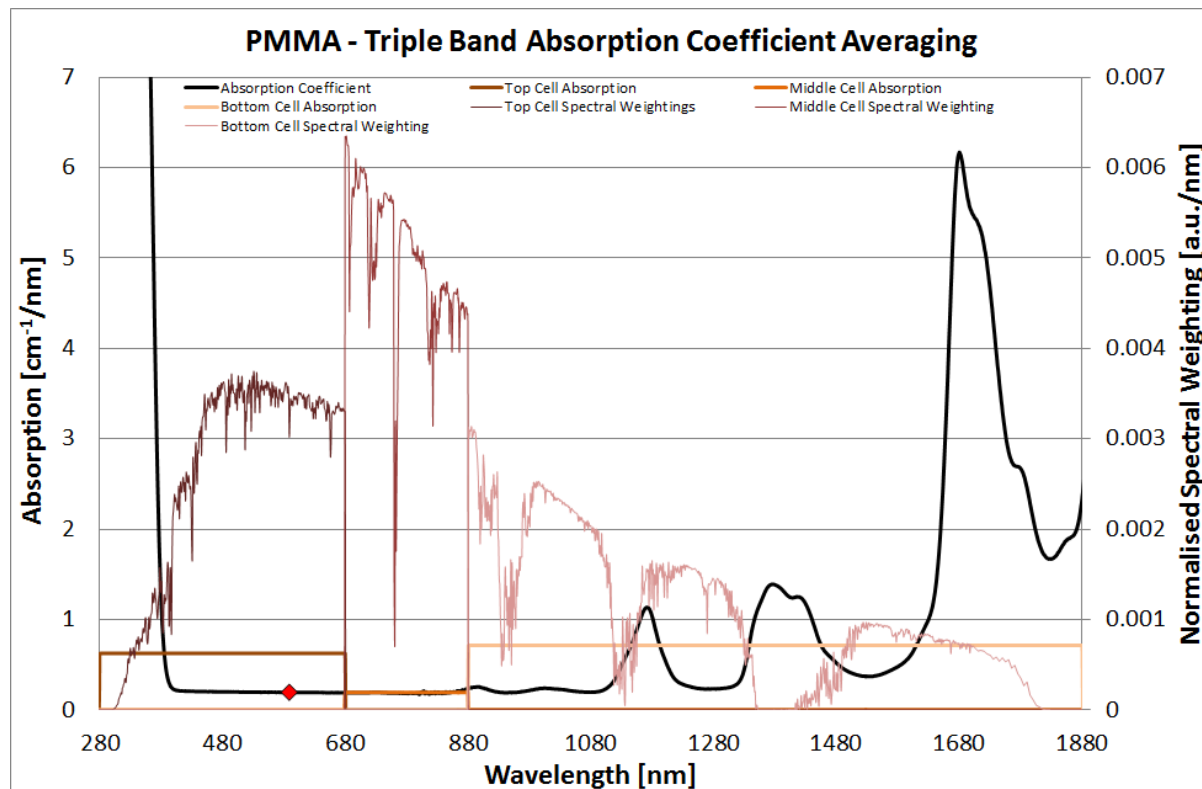


FIGURE 3.14: TRIPLE BAND SPECTRALLY WEIGHTED AVERAGE ABSORPTION COEFFICIENT FOR PMMA WITH THE AM1.5 DIRECT SPECTRUM

Figure 3.14 shows the measured absolute and triple band (280-680, 680-880 & 880-1880nm) spectrally weighted absorption coefficients of PMMA. The absolute value of the measured absorption coefficient varies between  $12.880$  and  $0.173\text{cm}^{-1}$ , while the spectrally weighted averages are found as  $0.624$ ,  $0.192$ , and  $0.714\text{cm}^{-1}$ , respectively. A nominal value at 589nm of  $0.195\text{cm}^{-1}$  is highlighted for reference.

Given that the typical Fresnel lens of CPV is built on a PMMA substrate with a thickness in the order of mm, these absorption coefficients are far from negligible. For example:

$$e^{-0.5*0.1} = 95.1\%$$

### 3.2.2. Refractive Index

The refractive index, as described in detail in 3.1.1.2 Law of Refraction, is a parameter that describes the speed of light in a given material and thus, from the principle of least time, is directly related to the directional change of light through the material.

#### 3.2.2.1. Overview

The refractive index of a given material is often quoted as some nominal value. For example, the refractive index of glass is commonly quoted as 1.49. This is the value of the refractive index at 589nm, which is an emission wavelength of sodium[72]. In reality, refractive index is a spectrally dependant

parameter and should well be considered as such in solar energy simulations as this is the underlying cause of chromatic aberration. Furthermore, the nominal refractive index is not a good indicator for the behaviour of light when spectral weightings are considered.

The refractive index of a material is also directly related to its reflectivity. The relationship is governed by the Fresnel equations:

$$R = \frac{R_s + R_p}{2}$$

EQUATION 3.13

Where  $R$  denotes the reflection coefficient,  $R_s$  the reflectance for light polarised perpendicular to the material interface normal and  $R_p$  the reflectance for light polarised parallel to the material interface normal

$$R_s = \left( \frac{n_1 \cos \theta_i - n_2 \cos \theta_t}{n_1 \cos \theta_i + n_2 \cos \theta_t} \right)^2$$

EQUATION 3.14

$$R_p = \left( \frac{n_1 \cos \theta_t - n_2 \cos \theta_i}{n_1 \cos \theta_t + n_2 \cos \theta_i} \right)^2$$

EQUATION 3.15

Where  $n_1$  denotes the refractive index of the primary material,  $n_2$  the refractive index of the secondary material,  $\theta_i$  the incident angle to the material interface normal and  $\theta_t$  the transmission angle to the material interface normal

The refractive index data presented in this thesis is as measured at Loughborough University by ellipsometry.

### 3.2.2.2. Refractive Index Data

Material refractive index data is presented for those materials common to CPV optical systems, specifically those relating to primary and secondary optical components.

#### Low Iron Soda-lime Glass

The most common plano-convex lens material is soda-lime glass. The nominal refractive index of soda-lime glass varies with material composition between 1.45 and 1.6. Low iron varieties are preferred in optical applications due to the reduced tinting and increased transmission. The refractive indices of the low iron varieties tend to be a little higher than those of the typical commercial glasses. Figure 3.15 and Figure 3.16 show measured material absorption coefficients alongside AM1.5 DNI spectrally

weighted average values for the 280-1880nm spectral range for single and triple band analysis, respectively.

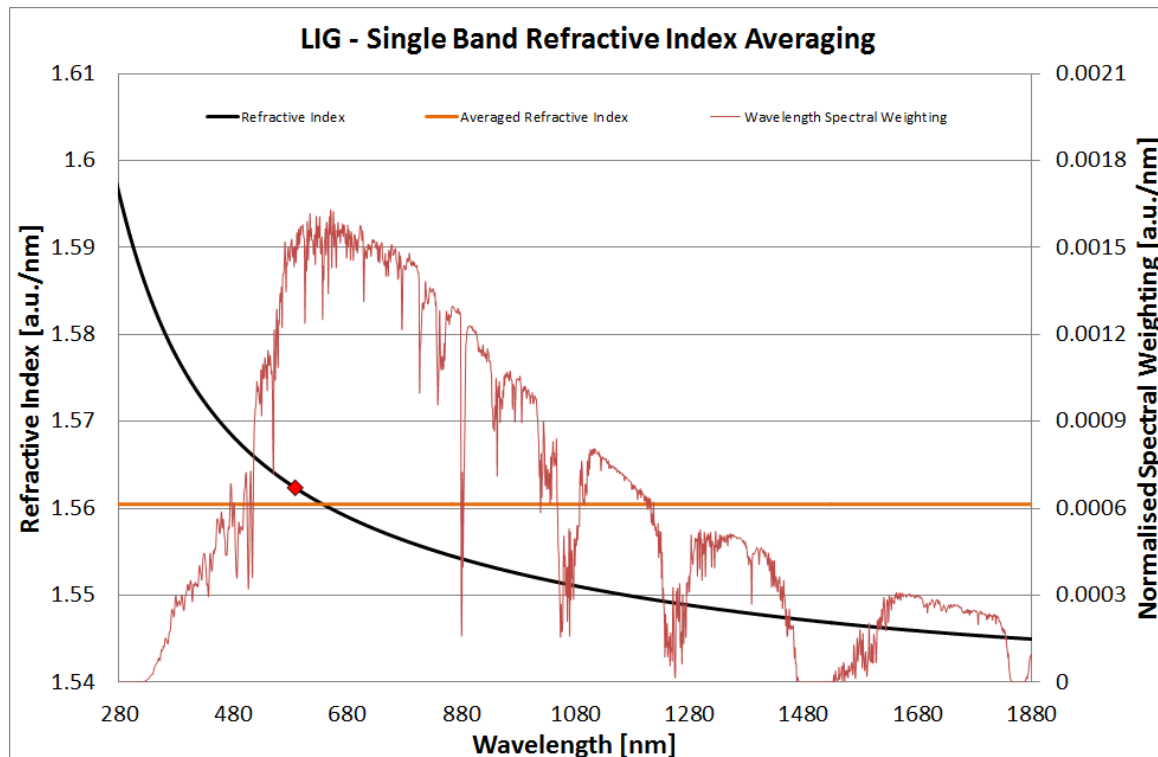


FIGURE 3.15: SINGLE BAND SPECTRALLY WEIGHTED AVERAGE REFRACTIVE INDEX FOR LOW IRON SODA-LIME GLASS WITH THE AM1.5 DIRECT SPECTRUM

Figure 3.15 shows the measured absolute and single band (280-1880nm) spectrally weighted AM1.5 DNI average refractive indices of low iron soda-lime glass. The spectrally weighted average is calculated as 1.560 whereas the nominal refractive index (highlighted) is measured as 1.562. The measured absolute value of refractive index varies from 1.596 to 1.545. Triple band weighted averages corresponding to the active regions of a typical triple junction solar cell are given in Figure 3.16.

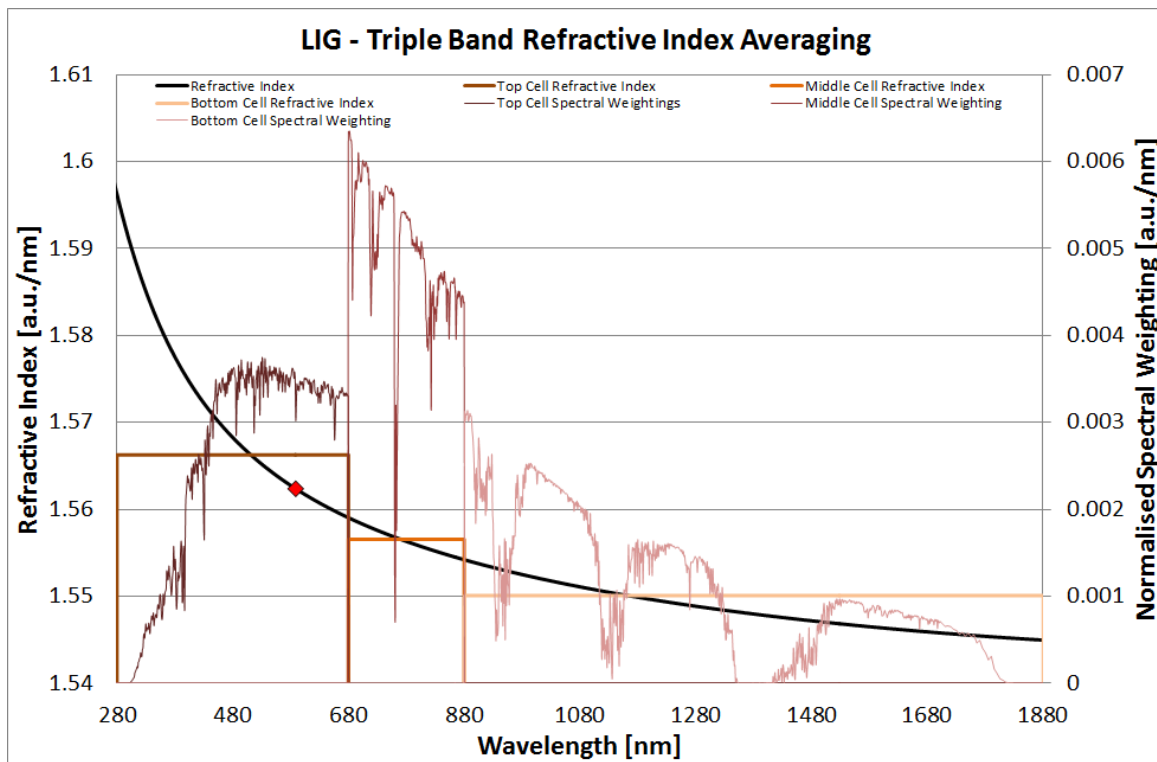


FIGURE 3.16: TRIPLE BAND SPECTRALLY WEIGHTED AVERAGE REFRACTIVE INDEX FOR LOW IRON SODA-LIME GLASS WITH THE AM1.5 DIRECT SPECTRUM

Figure 3.16 shows the measured absolute and triple band (280-680, 680-880, 880-1880nm) spectrally weighted AM1.5 DNI average refractive indices of low iron soda-lime glass. The spectrally weighted averages are calculated as 1.566, 1.557 & 1.550, respectively, whereas the nominal refractive index (highlighted) is measured as 1.562. The absolute value of measured refractive index varies from 1.596 to 1.545.

### PMMA

Figure 3.17 and Figure 3.18 show measured refractive index alongside AM1.5 DNI spectrally weighted average values for the 280-1880nm spectral range for single and triple band analysis, respectively.

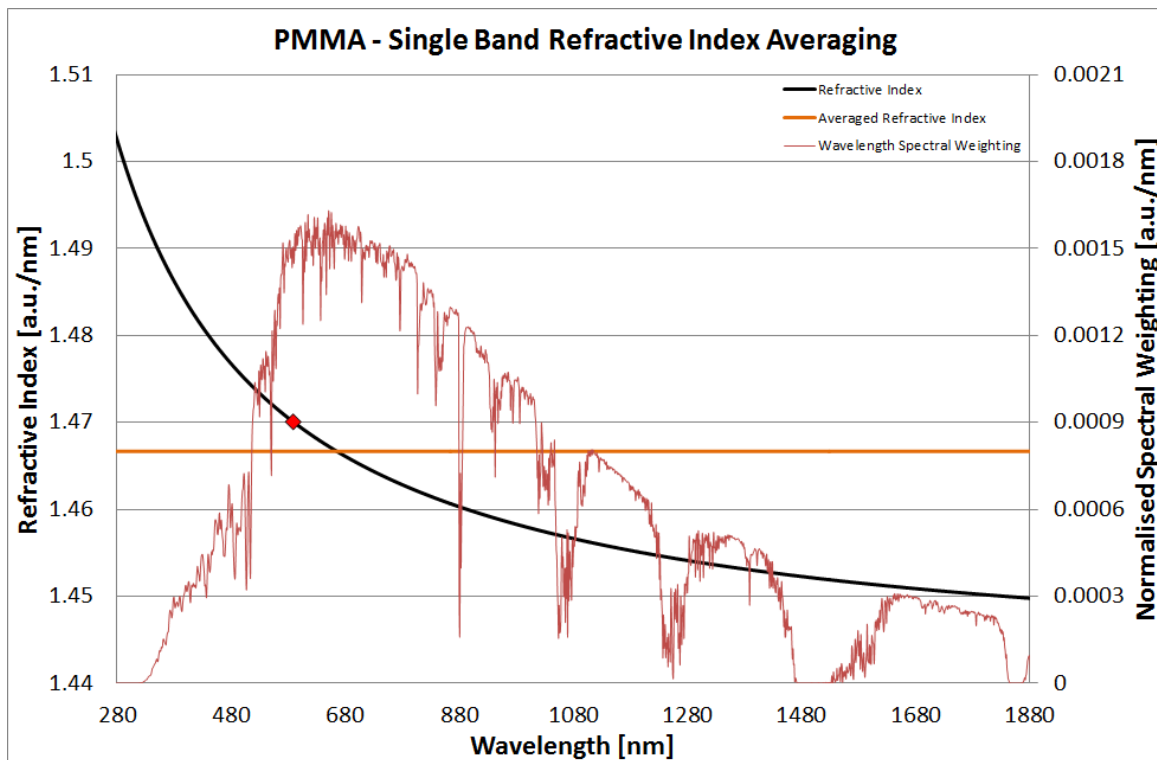


FIGURE 3.17: SINGLE BAND SPECTRALLY WEIGHTED AVERAGE REFRACTIVE INDEX FOR PMMA WITH THE AM1.5 DIRECT SPECTRUM

Figure 3.17 shows the measured absolute and single band (280-1880nm) spectrally weighted refractive indices of PMMA. The spectrally weighted average is calculated as 1.467 whereas the nominal refractive index (highlighted) is measured as 1.470. The absolute value of refractive index varies from 1.503 to 1.450. Triple band weighted averages corresponding to the active regions of a typical triple junction solar cell are given in Figure 3.18.

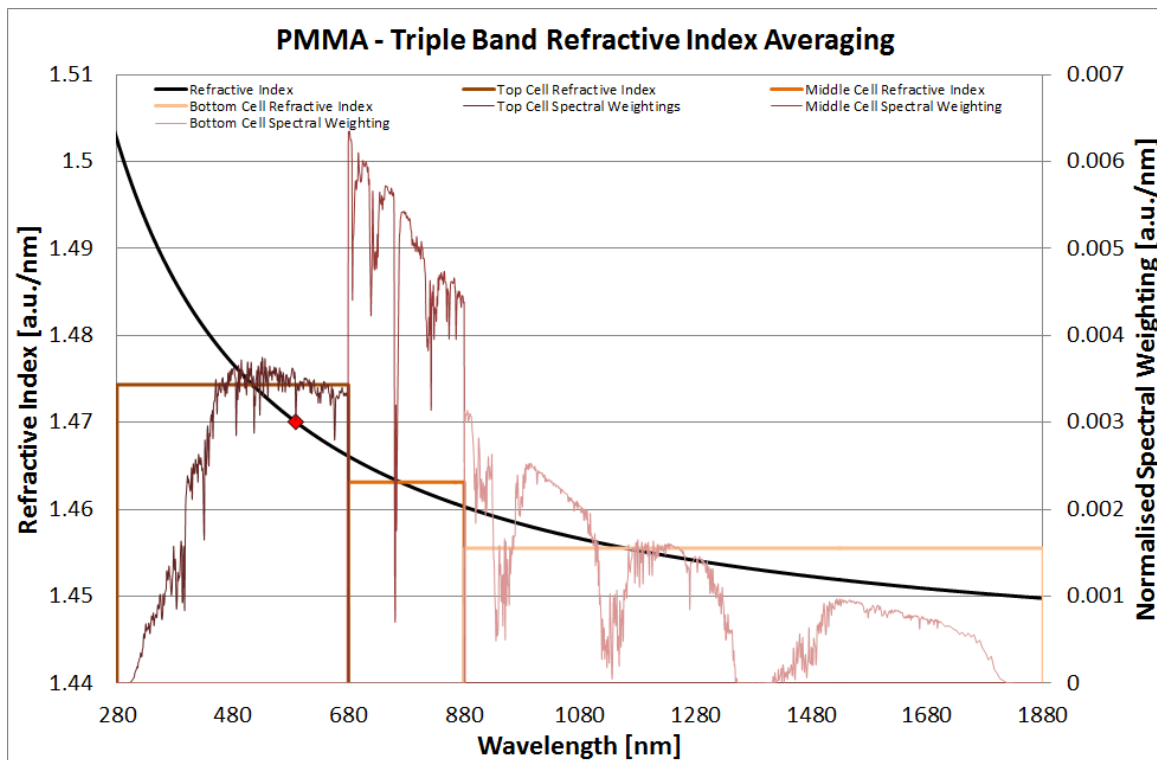


FIGURE 3.18: TRIPLE BAND SPECTRALLY WEIGHTED AVERAGE REFRACTIVE INDEX FOR PMMA WITH THE AM1.5 DIRECT SPECTRUM

Figure 3.18 shows the measured absolute and triple band (280-680, 680-880, 880-1880nm) spectrally weighted AM1.5 DNI average refractive indices of PMMA. The spectrally weighted averages are calculated as 1.474, 1.463 & 1.456, respectively, whereas the nominal refractive index (highlighted) is measured as 1.470. The absolute value of refractive index varies from 1.503 to 1.450.

### 3.2.3. Anti-reflection Coatings (ARCs)

Insolation transmission loss due to surface reflectivity is a known problem for CPV optical components. Energy loss due to PMMA surface reflection at the Fresnel lens has been estimated from the Fresnel equations (Equation 3.13, Equation 3.14 and Equation 3.15) at around 4%, which is similar to the amount of energy lost by reflection at the glass-air interface of flat-plate photovoltaics. Such significant losses are obviously undesirable and are mitigated by the application of thin film coatings designed specifically to reduce reflection at the material interface and increase insolation transfer, these coatings are termed anti-reflection coatings (ARCs).

#### 3.2.3.1. Overview

Figure 3.19 shows the angular dependence of the reflection of light at an air-[n] interface were [n] is a material of refractive index n as plotted on the ‘Refractive Index’ axis. The input angle is here defined as the angular deviation from the surface normal.

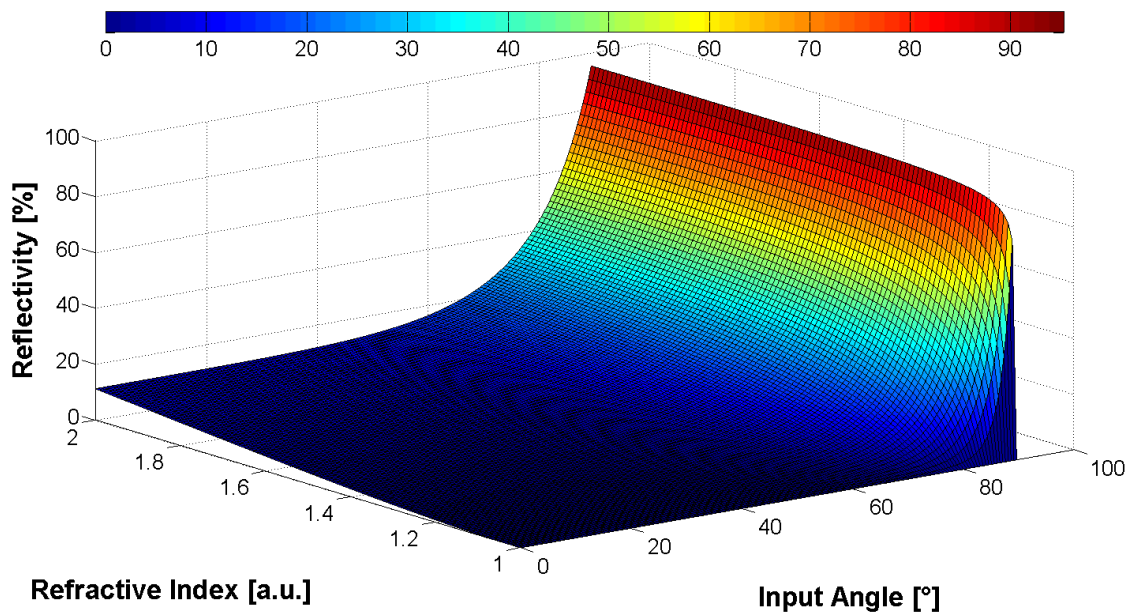


FIGURE 3.19: FRESNEL EQUATION INTERFACE REFLECTIVITY WITH AIR ( $n = 1$ ) VERSUS REFRACTIVE INDEX VERSUS INPUT ANGLE

For reference, the cross section for the nominal air-glass interface ( $n = 1.5$ ) is given in Figure 3.20.

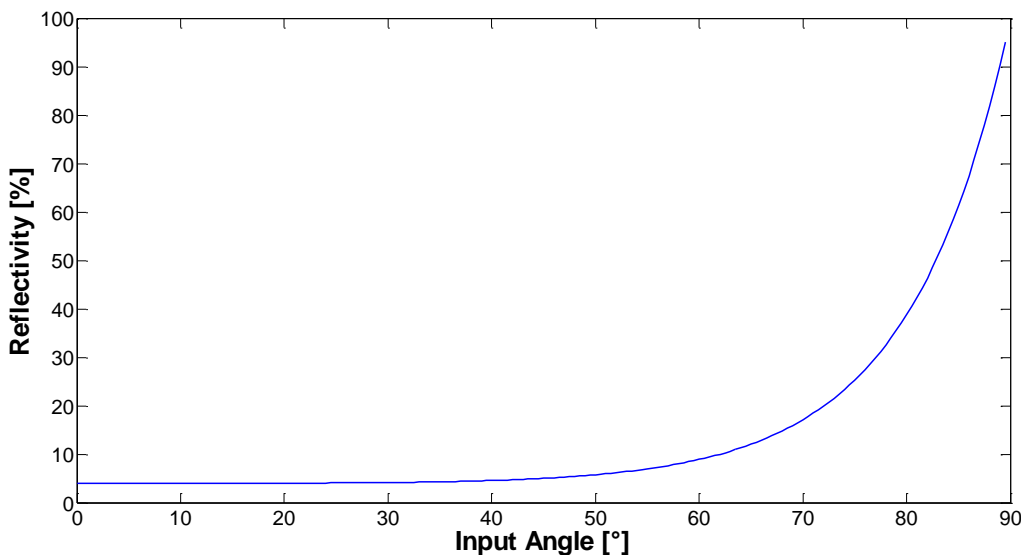


FIGURE 3.20: REFLECTIVITY VERSUS INPUT ANGLE FOR LIGHT AT THE  $n = 1$  TO  $n = 1.5$  MATERIAL INTERFACE

The reflections shown in Figure 3.19 and Figure 3.20 are mitigated by the use of ARCs. ARCs are commonplace in the ophthalmic optics and precision optics industries and are often found on spectacle and camera lenses for glare reduction and image contrast improvement. A variety of anti-reflection methods exist. The field of PV has seen the application of index matching ARCs, single and multilayer interference ARCs, textured layer ARCs and combinations of these[73].

### Index Matching ARCs

Index matching ARCs work by introducing a mediating interface between two materials. It can be seen from Figure 3.19 that there is a positive correlation with reflection and the difference in refractive indices of the boundary materials. The reflection is reduced by the introduction of a thin material layer with a refractive index between that of the two boundary materials. It is derived from the Fresnel equations (Equation 3.13, Equation 3.14, and Equation 3.15) that the optimal refractive index of the mediating interface is determined by the geometric mean of the boundary material refractive indices:

$$n_{ARC} = \sqrt{n_1 n_2}$$

EQUATION 3.16

Referring to the earlier example of glass, the approximated 4% loss due to reflection can be nearly halved to 2.04% by this method. However, in practice it is rarely possible to employ a material of the optimal refractive index as the mediating interface. The refractive index used is governed by material availability and properties such as adhesion, stability and ease of deposition. It is for these reasons that the suboptimal ( $n = 1.38$ ) magnesium fluoride ( $MgF_2$ ) tends to be used as an ARC for the glass-air interface resulting in a reduction of reflection loss to 2.72%. The optimal and commonly used refractive indices for the air-glass interface are highlighted in Figure 3.21, which is a reflection analysis for normally incident light at the nominal refractive index (corresponding to a wavelength of 589nm).

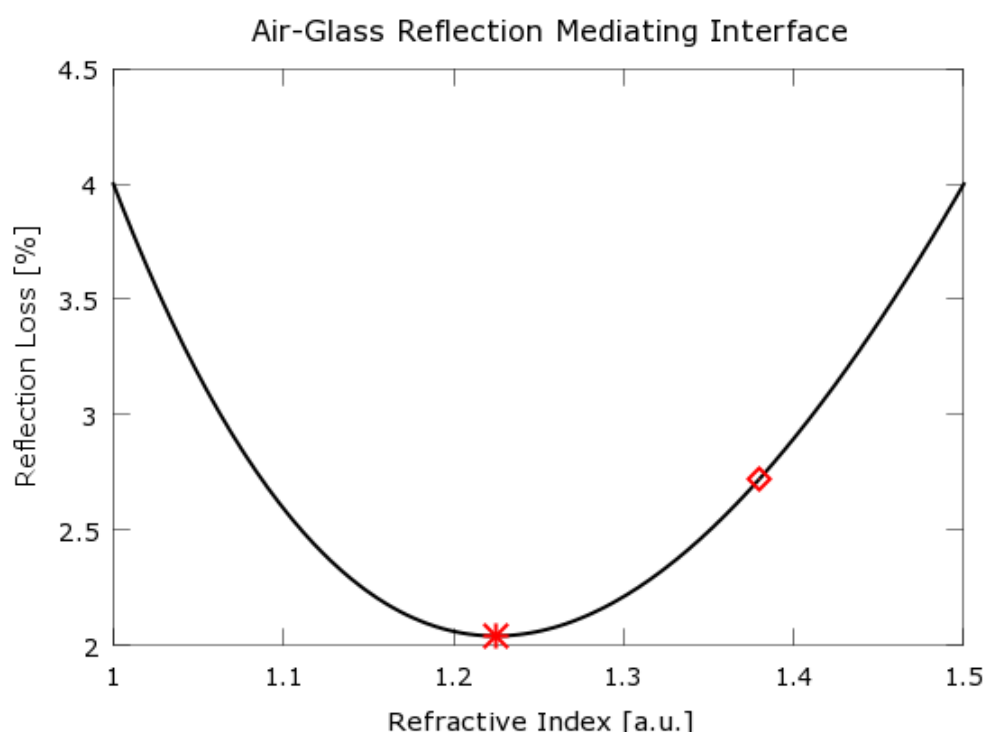


FIGURE 3.21: REFLECTION LOSSES AT THE AIR-GLASS INTERFACE WITH MEDIATING ARCS OF VARYING INTERMEDIATE REFRACTIVE INDICES WITH THE OPTIMAL AND COMMONLY USED ARCS HIGHLIGHTED

### Interference ARCs

Interference ARCs work by the destructive interference of light waves by anti-phase superposition according to wave theory. Single layer interference ARCs are often called ‘quarter wavelength ARCs’ as they are applied with a thickness that is one quarter the wavelength of the light for which they are calibrated. For normally incident light, a secondary reflection interface at this distance from the primary interface produces secondary reflection waves that are out of phase with the primary reflection waves, causing them to cancel by superposition. To optimise the ARC for light at other angles of incidence the thickness is adjusted by cosine correction. These single layer interference ARCs are only effective at narrow frequency bands. Their effectiveness is extended to broadband frequencies by a linear extension of the above theory and the use of multi-layered ARCs (MARCs). MARCs currently tend to be optimised only for the visible spectrum (400-700nm) and as such are rarely found in CPV, although some theoretical solutions have been proposed[74-76]. Practical PV applications have been produced[77].

### Textured ARCs

Textured ARCs worked by the introduction of surface textures that form shapes with dimensions smaller than the wavelength of light considered. The dimensional requirements are related to wavelength and phasing effects. These textured surfaces reduce reflectivity by increasing the number of average reflections required for an input light ray to be directed away from the surface. Textured ARCs can be particularly useful when reducing the multidirectional reflection with an air interface. Theoretically, a gradual reduction of refractive index from that of the base media to that of air ( $n = 1$ ) by MARCs would be a reasonable solution here. In practice though, MARCs of this form are near impossible to achieve. This is in part due to there being no available solid material with a refractive index near to 1. Surface texturing facilitates this effect by a gradual reduction of material from the solid surface, such that the average refractive index is gradually reduced[78, 79].

#### 3.2.3.2. Example

A typical ARC used with low iron soda-lime glass is silicone. The material properties of silicone are shown in Figure 3.22.

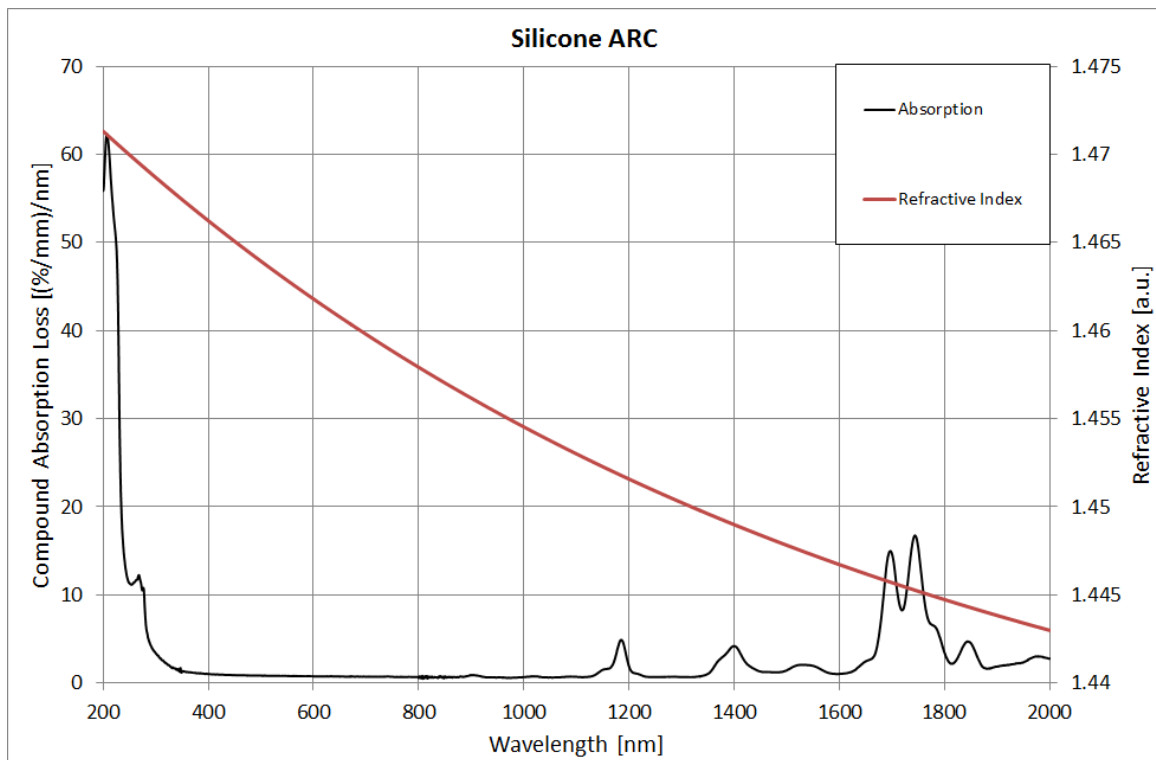


FIGURE 3.22: SPECTRALLY RESOLVED ABSORPTION AND REFRACTIVE INDEX DATA FOR SILICONE - A COMMON ARC FOR LOW IRON SODA-LIME GLASS

In comparison with low iron soda-lime glass, silicone has a lower variation in refractive index and a higher average absorption. To maximise optical transmission only a very fine (typically in the order of nanometres) layer of silicone is used in order to minimise absorption losses and, in the case of interference ARCs, further reduce reflection at a specific wavelength. Such small layers have negligible effects on the directional change of incident light and as such the refractive effects, other than those pertaining to reflective losses, of ARCs are typically ignored in simulation.

For brevity, the detailed analysis as outlined above is not provided here, but the results are given in Table 3.2.

### 3.2.4. CPV Material Properties Overview

For reference, Table 3.2 gives an overview of the CPV material properties presented herein.

TABLE 3.2: CPV MATERIAL PROPERTIES REFERENCE TABLE

Reference Point	Low Iron Soda-lime Glass		PMMA		Silicone ARC	
	Absorption Coefficient	Refractive Index	Absorption Coefficient	Refractive Index	Absorption Coefficient	Refractive Index

---

<b>Nominal (589nm)</b>	0.011	1.562	0.195	1.470	0.028	1.462
<b>Whole Cell Averaged</b>	0.014	1.560	0.516	1.467	0.026	1.459
<b>Top Cell Averaged</b>	0.012	1.566	0.624	1.474	0.038	1.463
<b>Middle Cell Averaged</b>	0.014	1.557	0.192	1.463	0.020	1.458
<b>Bottom Cell Averaged</b>	0.0156	1.550	0.714	1.456	0.011	1.452

---

### 3.3. The Plano-convex Lens

The plano-convex lens is arguably the archetypal lens, it has one flat, planar side and one convex side from a spherical section.

#### 3.3.1. Description

##### 3.3.1.1. Parametric Description

The geometry of the plano-convex lens allows for a 3 parameter description, as shown in Figure 3.23.

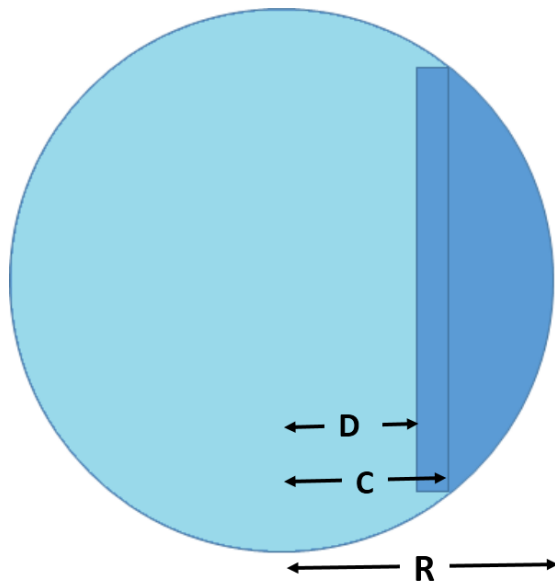


FIGURE 3.23: PLANO-CONVEX LENS THREE PARAMETER DESCRIPTION SCHEMATIC

The three parameters;  $D$ ,  $C$  and  $R$ ; correspond to depth, extent of curvature and spherical shell radius, respectively. For description of a plano-convex lens within a three-dimensional reference frame see 3.5 Modelling.

Another usual parameter of reference is the lens front radius,  $r$ , which is hence calculated as:

$$r = \sqrt{R^2 - C^2}$$

EQUATION 3.17

### 3.3.1.2. Volume

The volume of a plano-convex lens is found as the volume of the spherical section plus the volume of the cylindrical substrate. The cylindrical substrate has the volume:

$$(C - D)\pi r^2$$

EQUATION 3.18

The spherical section volume is found by integration according to:

$$V = 4 \int_C^R \int_0^{\sqrt{R^2 - z^2}} \int_0^{\sqrt{R^2 - y^2 - z^2}} 1 dx dy dz = \frac{2}{3}\pi R^3 - \pi R^2 C + \frac{\pi}{3} C^3$$

EQUATION 3.19

For the derivation of this please see section 9.1.1, 'The Plano Convex Lens'.

### 3.3.2. Use in CPV

The plano-convex lens is often used as a secondary concentration mechanism in CPV. The general purpose of a secondary concentration device is to increase the solar tracking error tolerance of the optical system. The imaging focal point of the Fresnel lens shifts, predominantly laterally, with solar abnormality. Secondary concentration mechanisms help mitigate the performance loss associated with tracking error by somewhat correcting for the lateral focus shift. The use of the plano-convex lens as a secondary concentration device has associated disadvantages such as: increased material cost, decreased optical transmission for small tracking errors and reduced passive cell cooling by convection. The secondary concentration principle is depicted in Figure 3.24.

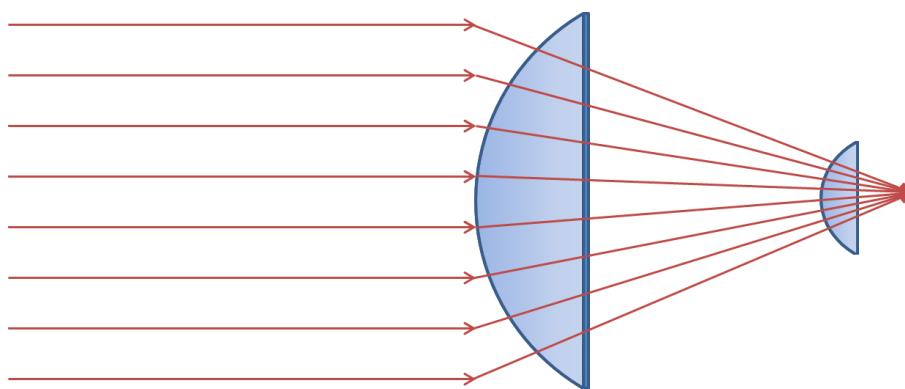


FIGURE 3.24: SECONDARY OPTICS FOR FRESNEL CONCENTRATION SYSTEMS

### 3.3.3. Focal Point Calculation

There are two methods commonly used to calculate the focal point of a given lens, namely the lensmaker's equation and the edge ray case analysis. In CPV, lens design is often based on a desired concentration ratio and some restriction on module size. This section serves to highlight the differences between methods of calculation and lens orientation on the derived focal length of the lens.

To illustrate this process a lens design with a geometric concentration ratio of 100x is here considered. For convenience a lens of front radius 10cm focussing to a 1cm radius image is considered. We shall calculate the receiver placement depth for a lens subtending a radial half angle of  $\frac{\pi c}{6}$  to the origin of spherical symmetry. This specification is shown schematically in Figure 3.25.

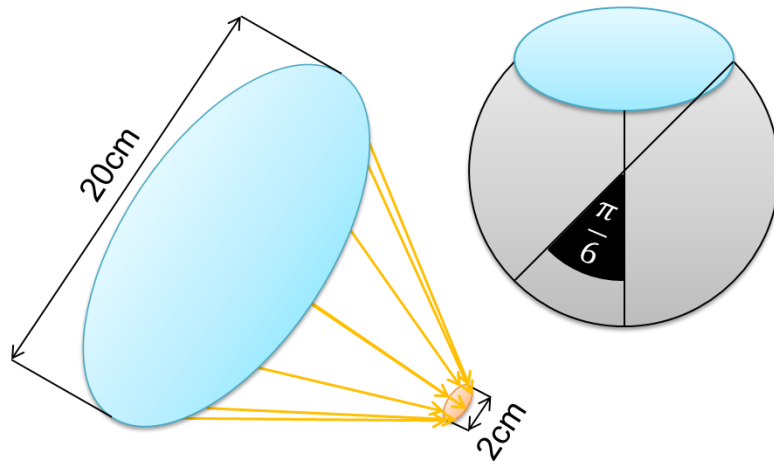


FIGURE 3.25: EXAMPLE SYSTEM SPECIFICATION SCHEMATIC

The lens back cylinder is considered as a solid of negligible volume. The three parameter description for this lens is:

$$\begin{pmatrix} R \\ C \\ D \end{pmatrix} = \begin{pmatrix} \frac{10}{\sin \frac{\pi}{6}} \\ \frac{10}{\tan \frac{\pi}{6}} \\ C \end{pmatrix} = \begin{pmatrix} 20 \\ 17.3205 \\ 17.3205 \end{pmatrix}$$

This lens is displayed in Figure 3.26.

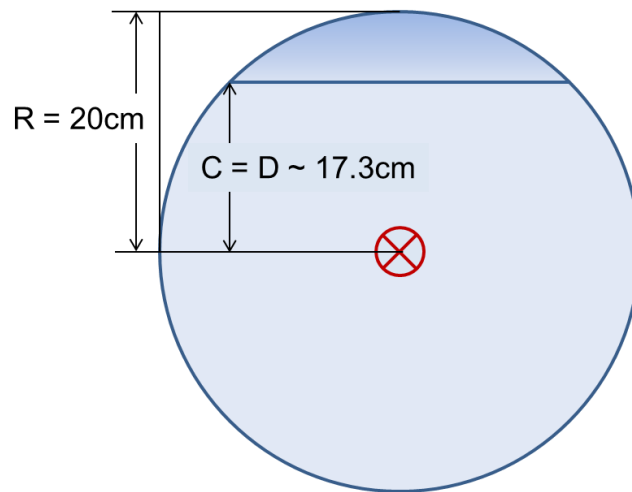


FIGURE 3.26: INVESTIGATIVE PLANO-CONVEX LENS DIMENSIONS

### 3.3.3.1. Lensmaker's Equation

The lensmaker's equation gives an approximation of the focal length of the biconvex lens in a medium with a refractive index of 1, such as air:

$$\frac{1}{F} = (n - 1) \left[ \frac{1}{R_1} - \frac{1}{R_2} + \frac{(n - 1)d}{nR_1R_2} \right]$$

EQUATION 3.20: THE LENSMAKER'S EQUATION

Where  $F$  denotes focal length,  $n$  refractive index,  $R_1$  the radius of curvature of the first surface,  $R_2$  the radius of curvature of the second surface and  $d$  the distance along the central axis between the two surface vertices

For the plano-convex lens the second surface is planar and the corresponding spherical radius,  $R_2$ , tends to infinity, thus the focal length is found as:

$$F = \frac{R_1}{(n - 1)}$$

EQUATION 3.21

The nominal refractive index of soda-lime-silica glass is 1.46. Thus, for a plano-convex lens constructed of conventional glass, the focal length is found as around  $1.79R_1$ .

For the aforementioned investigative lens design the focal point is hence found as:

$$F = \frac{20}{(1.49 - 1)} = 40.8163$$

### 3.3.3.2. Edge Ray Case Analysis

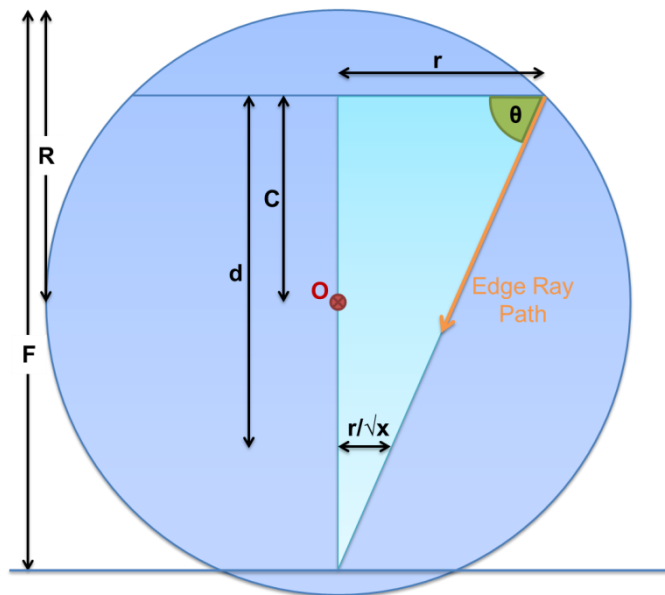


FIGURE 3.27: EDGE RAY CASE ANALYSIS SCHEMATIC

The edge ray case analysis is depicted in Figure 3.27, where  $O$  and  $R$  are the origin and radius of spherical symmetry of the convex lens face, respectively.  $C$  is the extent of curvature,  $r$  the lens front radius,  $F$  the focal length,  $d$  the distance to the receiver and  $x$  the concentration ratio.

The focal length,  $F$ , here depends on the lens orientation. The edge ray case analysis assumes an input edge ray of normal incidence. Lens orientation for concentration purposes is considered two-fold, as depicted in Figure 3.28.

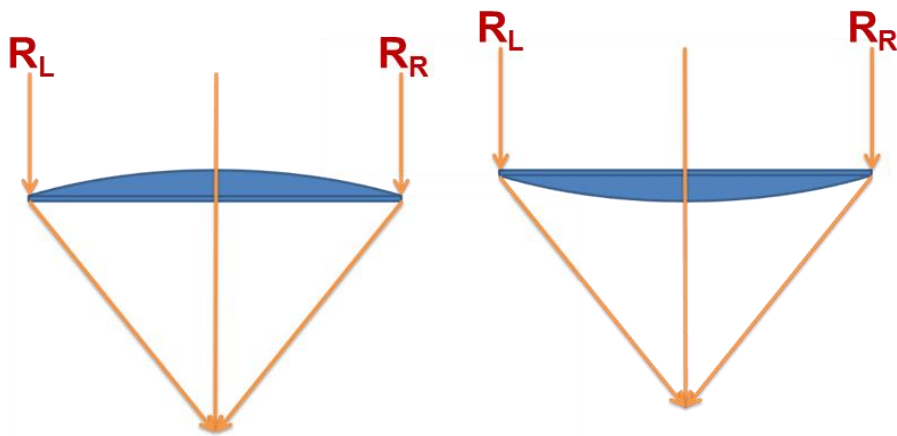


FIGURE 3.28: TWO-FOLD PLANO-CONVEX LENS FOCAL POINT CALCULATION WITH EDGE RAY DEPICTION

Figure 3.28 depicts the edge ray focal point calculation procedure with the extreme edge rays,  $R_L$  and  $R_R$  for both convex primary and planar primary orientations (left and right, respectively).

The focal length of the lens differs depending on chosen orientation. With the primary interface as the convex surface, incident normal rays undergo two directional changes at the boundary interfaces. By placing the planar surface at the primary interface this is reduced to a single directional change and the resultant focal length is thus reduced.

### Convex Surface Primary

With the convex surface as the primary interface, normally incident edge rays are refracted at both lens boundaries. Refraction at material interfaces occurs according to Equation 3.2: Law of Refraction.

For the entry ray in the example lens the primary angular change at the convex lens front surface is found as:

$$\theta_2 = \sin^{-1} \left( \frac{\sin \frac{\pi}{6}}{1.49} \right) \sim 0.3422^c$$

The secondary angular change at the planar lens back surface is then found as:

$$\theta_2 = \sin^{-1} \left( 1.49 \sin \left( \frac{\pi}{6} - 0.3422 \right) \right) \sim 0.2721^c$$

Thus the projected 2D Cartesian exit ray vectors is found as:

$$R_L = \begin{bmatrix} \sin(0.2721) \\ -\cos(0.2721) \end{bmatrix} = \begin{bmatrix} 0.269 \\ -0.963 \end{bmatrix}$$

$$\mathbf{R}_R = \begin{bmatrix} -\sin(0.2721) \\ -\cos(0.2721) \end{bmatrix} = \begin{bmatrix} -0.269 \\ -0.963 \end{bmatrix}$$

Where  $\mathbf{R}_L$  and  $\mathbf{R}_R$  are the left-most and right-most exit rays according to Figure 3.28, respectively

The focal point of the lens is then considered as the point of intersection of the edge rays hence is found by symmetry as:

$$\mathbf{P} = \begin{bmatrix} 0 \\ \frac{10}{0.269} \times 0.963 \end{bmatrix} = \begin{bmatrix} 0 \\ 35.8 \end{bmatrix}$$

Thus the lens focal length,  $F$ , is found by this analysis to be 35.8cm from the lens back. Calculated from the principle point of the lens this would be  $F = 35.8 + \frac{R-D}{n} = 37.6\text{cm}$ .

### Planar Surface Primary

With the planar surface as the primary interface, normally incident edge rays undergo directional change at the lens exit interface only. This directional change for the investigative lens design described above is found as:

$$\theta_2 = \sin^{-1} \left( 1.49 \sin \frac{\pi}{6} \right) = 0.8405^c$$

Hence the projected Cartesian exit ray vectors are calculated as:

$$\mathbf{R}_L = \begin{bmatrix} \sin \left( 0.8405 - \frac{\pi}{6} \right) \\ -\cos \left( 0.8405 - \frac{\pi}{6} \right) \end{bmatrix} = \begin{bmatrix} 0.312 \\ -0.951 \end{bmatrix}$$

$$\mathbf{R}_R = \begin{bmatrix} -\sin \left( 0.8405 - \frac{\pi}{6} \right) \\ -\cos \left( 0.8405 - \frac{\pi}{6} \right) \end{bmatrix} = \begin{bmatrix} -0.312 \\ -0.951 \end{bmatrix}$$

The focal point of the lens is then considered as the point of intersection of the edge rays hence is found by symmetry as:

$$\mathbf{P} = \begin{bmatrix} 0 \\ \frac{10}{0.312} \times 0.951 \end{bmatrix} = \begin{bmatrix} 0 \\ 30.5 \end{bmatrix}$$

Thus the lens focal length,  $F$ , is found by this analysis to be 30.5cm from the planar lens surface. For consistency this may be expressed as the focal length from the pinnacle lens front point according to  $F - \frac{R-C}{n} = 30.5 - \frac{20-17.3205}{1.49} = 28.7\text{cm}$ .

### 3.3.3.3. Focal Point Calculation Summary

The various focal point calculation methods presented above vary greatly for a plano-convex lens design subtending a radial half-angle of  $\frac{\pi^c}{6}$  to the origin of spherical symmetry. As the subtended radial half angle of the lens tends to zero so does the spread of these values. This is another interpretation of the condition of validity lensmaker's equation - being that the lens be 'thin'.

In reality, a singular measurement for the focal length of a lens is somewhat of a misnomer. The phenomenon known as spherical aberration causes a spread of the focal point that is dependent on the incident ray position on the lens front. The edge ray calculation procedure therefore indicates an extremity – the near-point focal length – rather than a useful parameter for optical system design. Figure 3.29, Figure 3.30, Figure 3.31 and Figure 3.32 demonstrate spherical aberration for the convex and planar primary surface orientations, respectively.

#### Convex Surface Primary

With the convex surface as the primary interface, the spread of the focal point is found between the extremes determined by the edge ray case and the lensmaker's equation. This amounts to approximately 3.2cm of longitudinal spherical aberration.

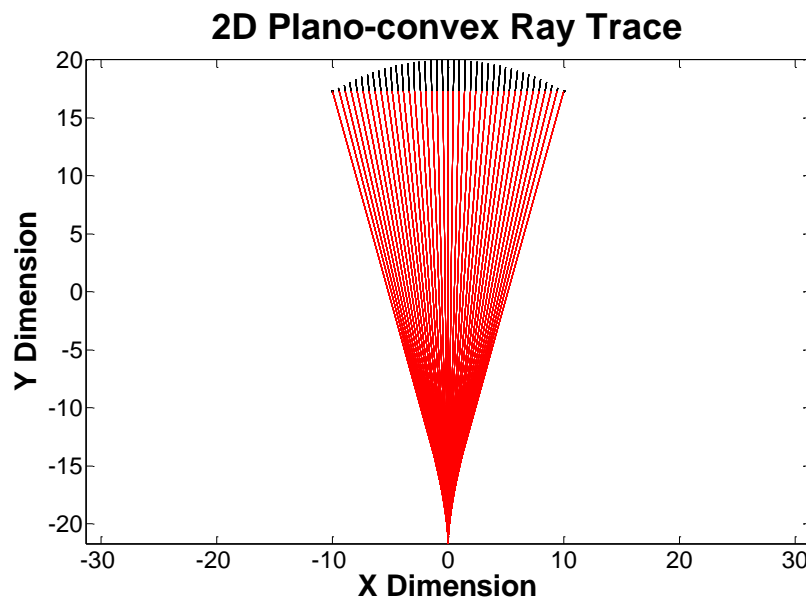


FIGURE 3.29: 2D RAY TRACE DIAGRAM OF AN IDEAL PLANO-CONVEX LENS WITH THE CONVEX SURFACE AS PRIMARY

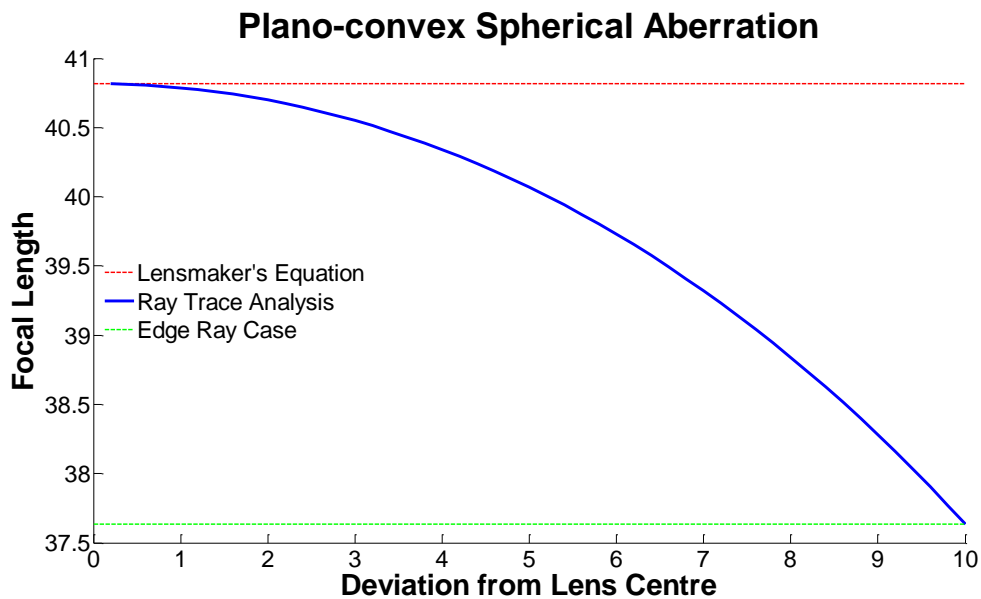


FIGURE 3.30: FOCAL LENGTH BY INTERSECTING RAYS AS A FUNCTION OF RADIAL DEVIATION FROM LENS CENTRE FOR AN IDEAL PLANO-CONVEX LENS WITH THE CONVEX SURFACE AS PRIMARY

### Planar Surface Primary

With the planar surface as the primary interface, the spread of the focal point is greater than the spread of the extremes as the far point focal distance from the lens centre is greater than that given by the lensmaker's equation. The total spread for the planar surface primary orientated lens is far greater than that of the convex surface primary orientated lens. The longitudinal spherical aberration here is approximately 13cm, which is about 4 times greater than that of the convex surface primary orientated lens.

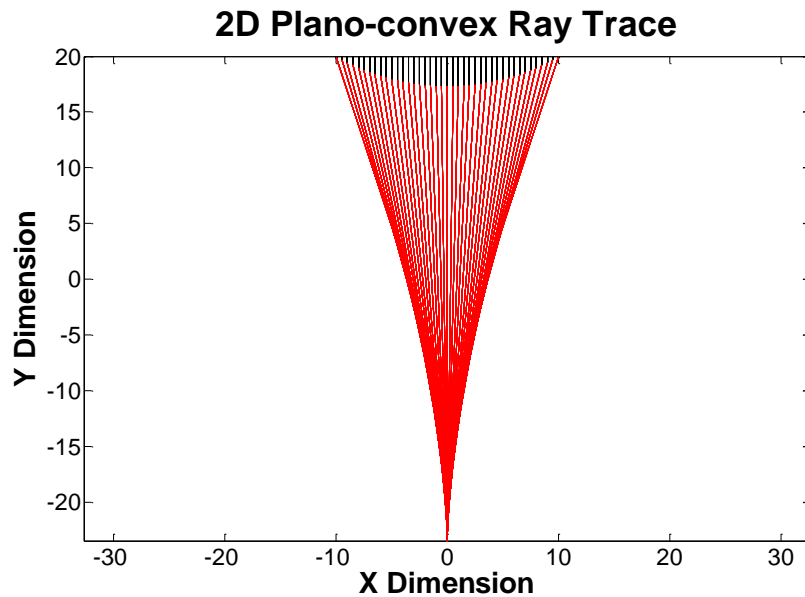


FIGURE 3.31: 2D RAY TRACE DIAGRAM OF AN IDEAL PLANO-CONVEX LENS WITH THE PLANAR SURFACE AS PRIMARY

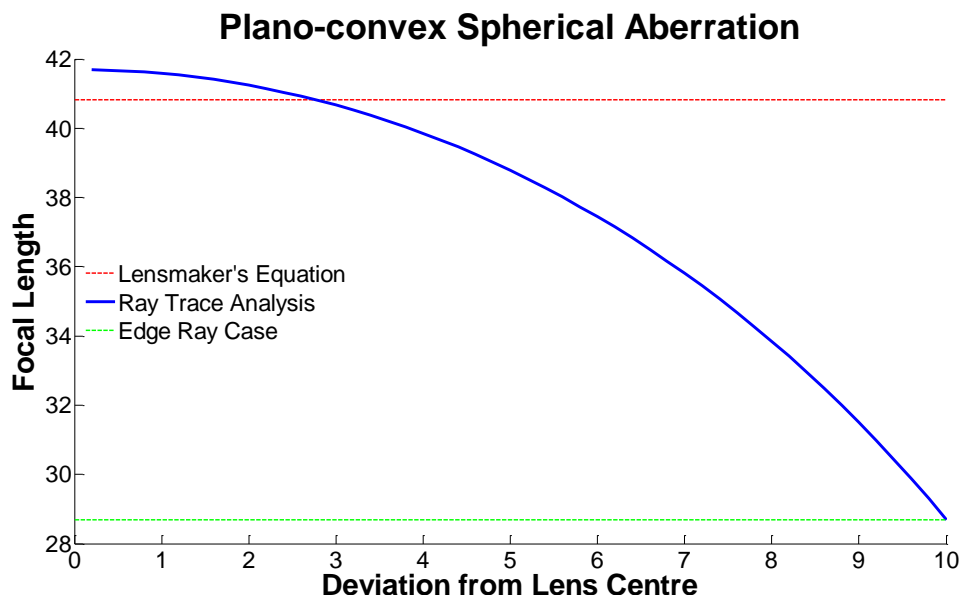


FIGURE 3.32: FOCAL LENGTH BY INTERSECTING RAYS AS A FUNCTION OF RADIAL DEVIATION FROM LENS CENTRE FOR AN IDEAL PLANO-CONVEX LENS WITH THE PLANAR SURFACE AS PRIMARY

### 3.4. The Fresnel Lens

By far the most prolific primary concentration device in HCPV today is the Fresnel lens. The main drivers for this are low cost, high transmission and material reduction.

### 3.4.1. Description

#### 3.4.1.1. Parametric Description

The Fresnel lens is derived as a material reduction of the plano-convex lens. Consider a plano-convex lens split into an arbitrary number of circular facets. The Fresnel lens is obtained by minimising each facet so that only the facet angle protrudes from the lens back substrate.

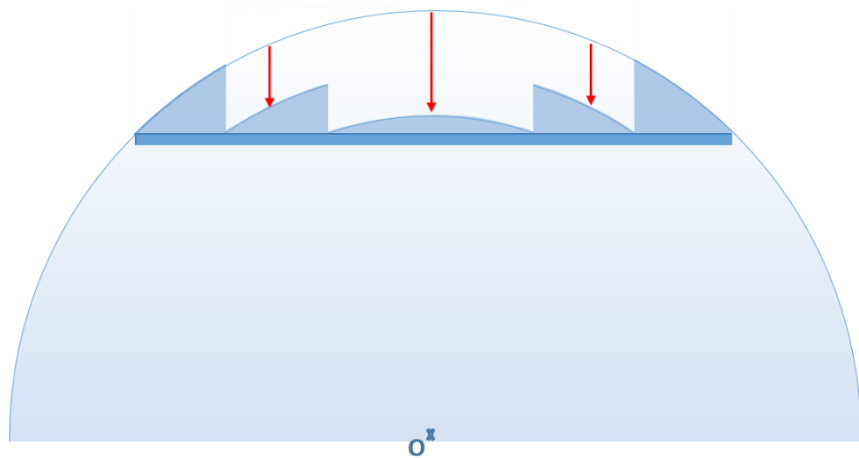


FIGURE 3.33: THREE-FACETED FRESNEL REDUCTION OF PLANO-CONVEX LENS SCHEMATIC

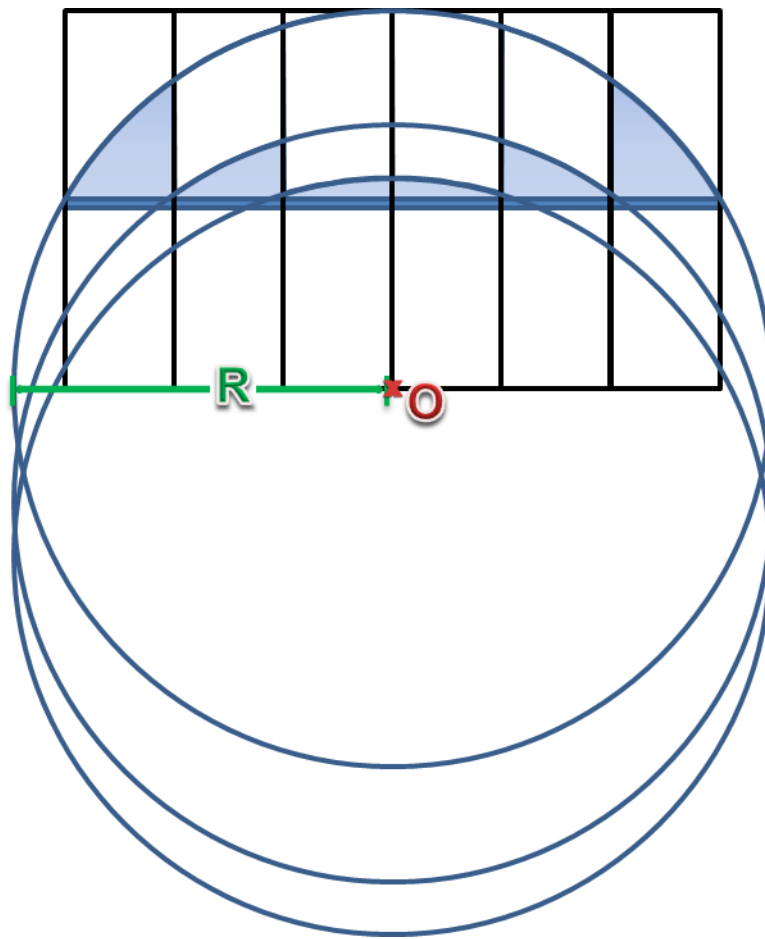


FIGURE 3.34: THREE-FACET FRESNEL REDUCTION GUIDELINES

A Fresnel lens of a given number of facets can be derived algorithmically from the plano-convex. Herein it is done so assuming equal facet radii (see Figure 3.33 and Figure 3.34).

### 3.4.1.2. Volume

The volume of the Fresnel lens is found as the volume of the cylindrical substrate section plus the volume of each facet. The volume of the cylindrical substrate is trivial (see Equation 3.18).

This total volume of the Fresnel facets can be calculated as an iterative set of integral equations according to:

$$\begin{aligned}
V &= \sum_{i=1}^{i=n} 4 \int_C^{R_i} \int_{r_i}^{\sqrt{R_i^2 - z^2}} \int_0^{\sqrt{R_i^2 - y^2 - z^2}} 1 dx dy dz \\
&= \pi \sum_{i=1}^{i=n} \frac{1}{3} \left( C^3 + \left( \left( \frac{\sqrt{R^2 - C^2}}{n} i \right)^2 + C^2 - \left( \frac{\sqrt{R^2 - C^2}}{n} (i-1) \right)^2 \right)^2 \right) \\
&\quad - \left( \left( \frac{\sqrt{R^2 - C^2}}{n} i \right)^2 + C^2 \right) \left( C + \sqrt{\left( \frac{\sqrt{R^2 - C^2}}{n} i \right)^2 + C^2 - \left( \frac{\sqrt{R^2 - C^2}}{n} (i-1) \right)^2} \right) \\
&\quad - \left( \sqrt{\left( \frac{\sqrt{R^2 - C^2}}{n} i \right)^2 + C^2 - \left( \frac{\sqrt{R^2 - C^2}}{n} (i-1) \right)^2} - C \right) \left( \frac{\sqrt{R^2 - C^2}}{n} (i-1) \right)^2
\end{aligned}$$

EQUATION 3.22

Where  $V$  is the volume of the Fresnel lens,  $R_i$  the radius of the spherical shell of the  $i^{\text{th}}$  facet,  $r_i$  the radial extent of the cylindrical wall boundary of the  $i^{\text{th}}$  facet,  $C$  the extent of curvature of the Fresnel lens and  $n$  the number of facets in the Fresnel lens

For the derivation of this please see section 9.1.2, ‘The Fresnel Lens’.

### 3.4.2. Use in CPV

According to the optical dictum ‘Fresnel and plano-convex lenses behave similarly with paraxial light’. In truth the Fresnel lens is associated with a loss in image quality (distortion) but this is conventionally considered insignificant in the context of CPV as the principle system input is power rather than image quality. However, it is understood that inhomogeneity and chromatic aberration are indecorous phenomena in CPV[80, 81] but exactly quite how these lenses differ in these areas is not well understood.

The major driving force behind CPV optics is an economic one, offsetting the high cost multi-junction solar cells with relatively cheap optical systems, hence costs need be kept low. The inherent material reduction in the Fresnel lens aids the economic argument by reducing tracker load and consequentially cost. A further benefit to the material reduction is the resultant increase in optical transmission by traversal path length reduction – the very principle of the Fresnel lens design.

### 3.4.3. Focal Length Calculation

The design of the Fresnel lens is such that incident edge rays undergo the same directional changes as in the plano-convex. Therefore, the focal point calculation procedures by the lensmakers's and edge ray methods are similar (see 3.3.3.1 Lensmaker's Equation and 3.3.3.2 Edge Ray Case Analysis).

The 2D ray trace analysis, however, is somewhat different. In this case, the single nominal value for the focal length of a Fresnel lens is more misleading. The edge ray calculation procedure still represents an extremity – the near-point focal length – rather than a useful parameter for optical system design. The lensmaker's focal length, however, is an arbitrary value in this case. Figure 3.35, Figure 3.36, Figure 3.37 and Figure 3.38 demonstrate spherical aberration for the convex and planar primary surface orientations, respectively.

#### 3.4.3.1. Focal Point Calculation Summary

##### Convex Surface Primary

With the convex surface as the primary interface, the spread of the focal point is found between the extremes determined by the edge ray case and the lensmaker's equation. This amounts to approximately 4.8cm of longitudinal spherical aberration.

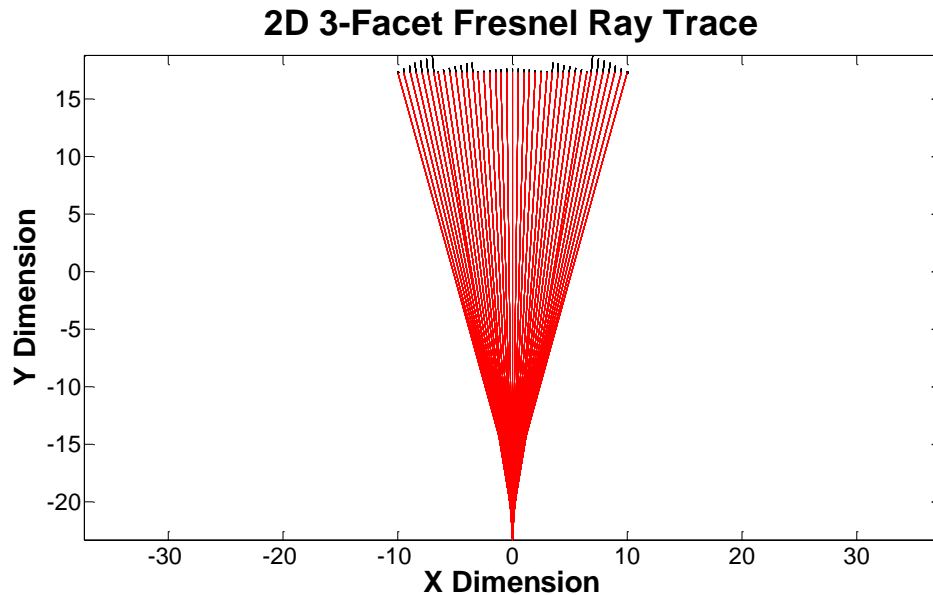


FIGURE 3.35: 2D RAY TRACE DIAGRAM OF AN IDEAL 3-FACET FRESNEL LENS WITH THE CONVEX SURFACE AS PRIMARY

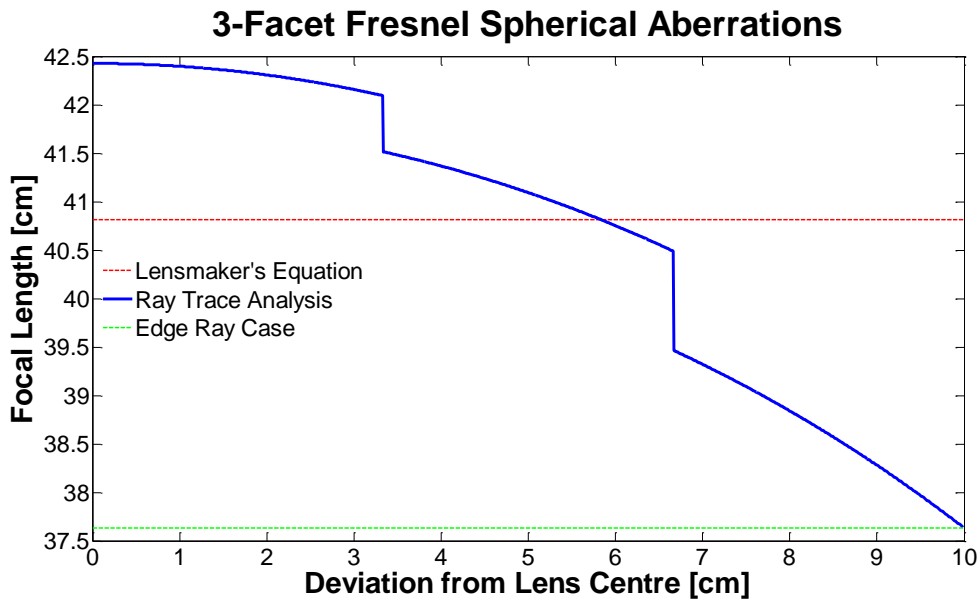


FIGURE 3.36: FOCAL LENGTH BY INTERSECTING RAYS AS A FUNCTION OF RADIAL DEVIATION FROM LENS CENTRE FOR AN IDEAL 3-FACET FRESNEL LENS WITH THE CONVEX SURFACE AS PRIMARY

#### Planar Surface Primary

With the planar surface as the primary interface, the spread of the focal point is greater than the spread of the extremes as the far point focal distance from the lens centre is greater than that given by the lensmaker's equation. The total spread for the planar surface primary orientated lens is greater than that of the convex surface primary orientated lens. The longitudinal spherical aberration here is approximately 6.4cm, which is about 1.3 times greater than that of the convex surface primary orientated lens.

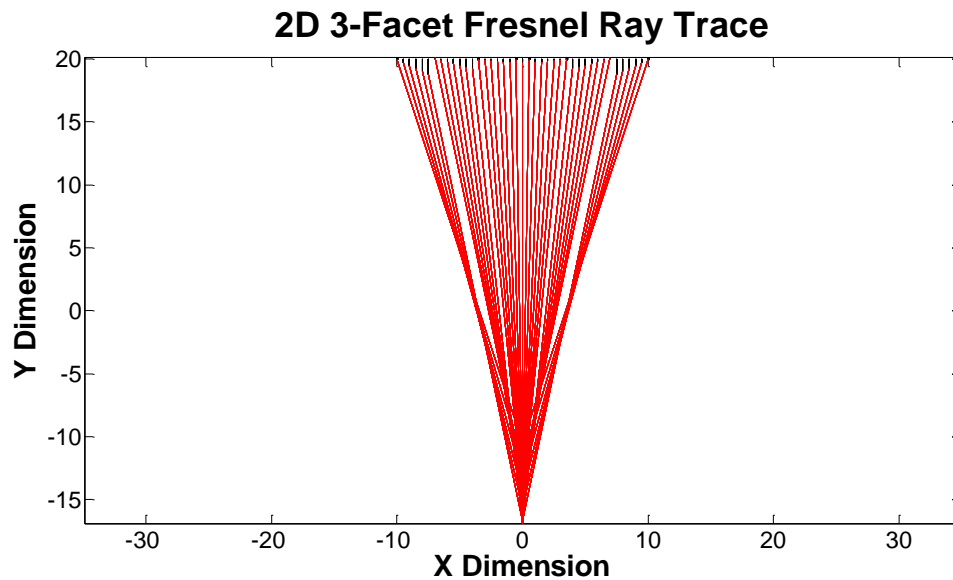


FIGURE 3.37: 2D RAY TRACE DIAGRAM OF AN IDEAL 3-FACET FRESNEL LENS WITH THE PLANAR SURFACE AS PRIMARY

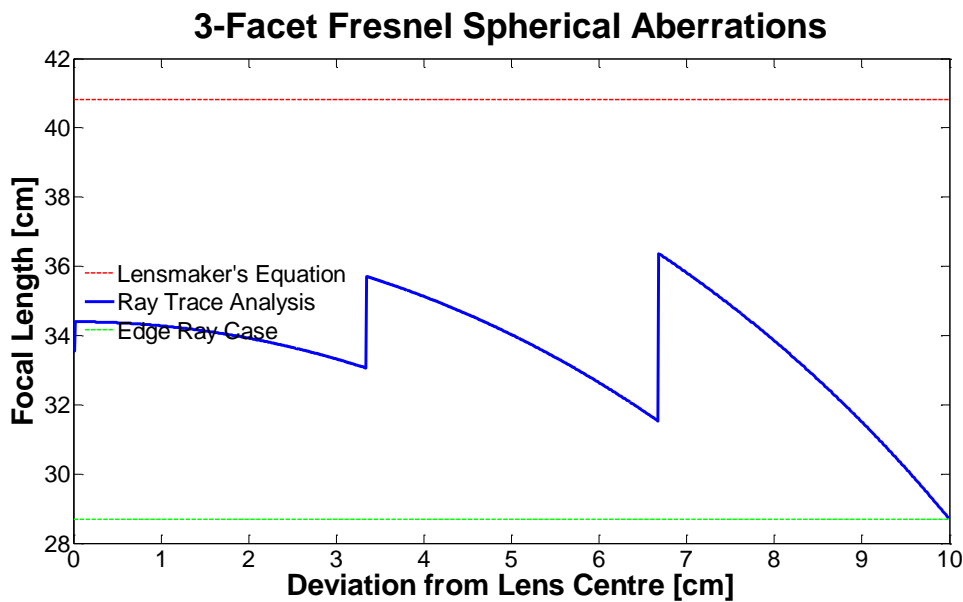


FIGURE 3.38: FOCAL LENGTH BY INTERSECTING RAYS AS A FUNCTION OF RADIAL DEVIATION FROM LENS CENTRE FOR AN IDEAL 3-FACET FRESNEL LENS WITH THE PLANAR SURFACE AS PRIMARY

### 3.5. Modelling

Modelling the transfer of incident solar energy through a given lens can be achieved by ray tracing. In ray tracing the distribution of incident insolation is considered as an image which is converted into directional rays incident on the lens surface. The traversal of rays through the lens is calculated by means of geometric optics, as governed by the principle of least time. Standard ray tracing practice operates under the assumption that the media traversal path lengths are far greater than the wavelength of the light ray hence is ignorant of such phenomena as diffraction and interference.

Firstly, a reference frame must be established so that all optical components can be placed relative to each other.

#### 3.5.1. Reference Frame

The reference frame is here set such that the ideal lens is positioned along the y-axis, as displayed in Figure 3.39.

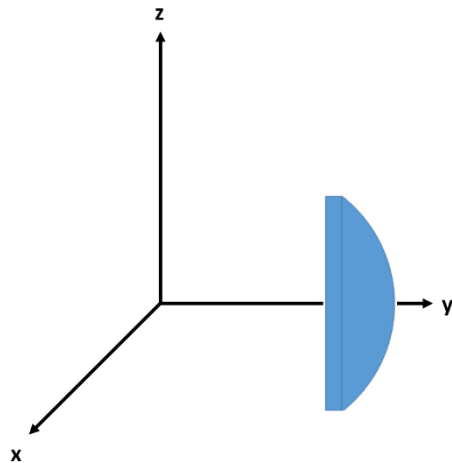


FIGURE 3.39: CARTESIAN REFERENCE FRAME WITH A PLANO-CONVEX LENS

Although a Cartesian reference frame is useful for most purposes it is necessary to introduce a spherical polar reference frame as angular descriptions of lens orientation are widespread, intuitive and perhaps more elegant than Cartesian vector descriptions. The spherical polar equivalent terms are displayed in Figure 3.40.

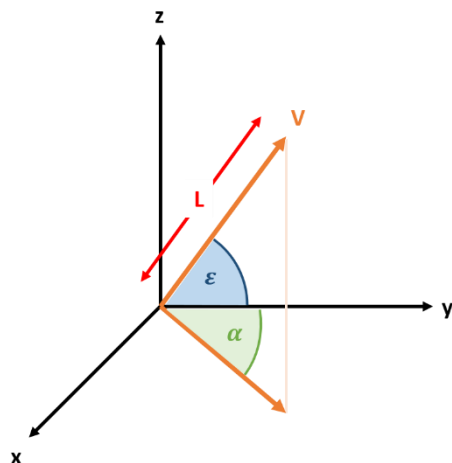


FIGURE 3.40: CARTESIAN AND SPHERICAL POLAR REFERENCE FRAMES

The Cartesian coordinate set  $\langle x, y, z \rangle$  has a spherical polar equivalent set  $\langle \alpha, \varepsilon, L \rangle$ .

- Azimuth,  $\alpha$ , is the angle towards the positive x-axis from the positive y-axis
- Elevation,  $\varepsilon$ , is the angle towards the positive z-axis from the x-y plane
- Length,  $L$ , is the magnitude of vector  $\mathbf{V}$

Mathematically these equivalences are defined as:

$$\begin{bmatrix} x \\ y \\ z \end{bmatrix} = \begin{bmatrix} L \sin \alpha \cos \varepsilon \\ L \cos \alpha \cos \varepsilon \\ L \sin \varepsilon \end{bmatrix}$$

EQUATION 3.23

$$\begin{bmatrix} \alpha \\ \varepsilon \\ L \end{bmatrix} = \begin{bmatrix} \tan^{-1}\left(\frac{x}{y}\right) \\ \sin^{-1}\left(\frac{z}{L}\right) \\ \sqrt{x^2 + y^2 + z^2} \end{bmatrix}$$

EQUATION 3.24

Cartesian vectors will be used here to describe component positioning and displacement errors whereas spherical polar forms will be used to describe component orientation errors.

### 3.5.2. Lens Front Mesh Generation

Consider the lens front surface as a finite set of area elements pointing in the general direction of the sky. Each lens front element ‘sees’ the sky. To model insolation transfer through the lens, the sky is translated to an image that projects a set of rays. These rays are traced through the lens at each surface element, forming a discrete set of intersections with a given surface of interest. The illumination profile at this surface is then calculated with some resolution. The resolution is variable, pertaining to the area or pixel size over which the incident rays are summated. However, the resolution of the illumination profile is itself governed by the limitations of geometric optics (see 3.1.1 Geometric Optics) and thus must be much larger than that of the wavelength of light considered. The set of finite area elements on the lens front is here termed a ‘lens front mesh’.

#### 3.5.2.1. The Ideal Lens

For a lens in the ideal position the placement is such that the lens normal,  $\mathbf{N}$ , is equivalent to the unit vector in the y-direction,  $\hat{\mathbf{j}}$ , and the centre of spherical symmetry,  $\mathbf{O}$ , is at the origin of the x-z plane with an arbitrary y-coefficient,  $Y_0$ , that is focal length dependent.

$$\mathbf{N} = \begin{bmatrix} 0 \\ 1 \\ 0 \end{bmatrix}$$

EQUATION 3.25

$$\mathbf{O} = \begin{bmatrix} 0 \\ Y_0 \\ 0 \end{bmatrix}$$

EQUATION 3.26

Where  $Y_0$  is an arbitrary value dependent on the lens focal length and optical system design

Independent of primary surface orientation, when viewed from the anti-normal, the lens front is a circle in the x-z plane with radius  $r$ :

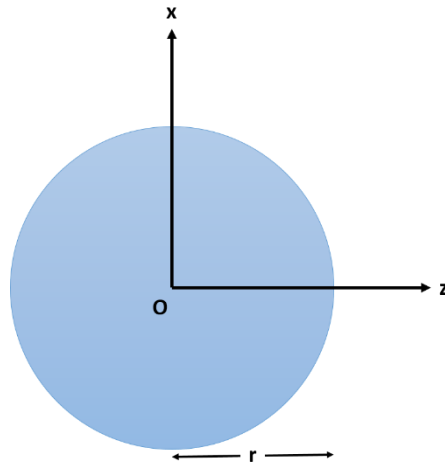


FIGURE 3.41: THE PLANO-CONVEX LENS FRONT FROM THE ANTI-NORMAL PERSPECTIVE

Where  $O$  is the origin of spherical symmetry and  $r$  the lens front radius

A homogenously distributed random mesh over the lens front can be obtained through the calculation of many random  $(x, z)$  points according to:

$$\text{Angle} = 2\pi \times \text{Random}_1$$

EQUATION 3.27

$$\text{Length} = r\sqrt{\text{Random}_2}$$

EQUATION 3.28

$$\begin{bmatrix} x \\ z \end{bmatrix} = \begin{bmatrix} \text{Length} \times \cos(\text{Angle}) \\ \text{Length} \times \sin(\text{Angle}) \end{bmatrix}$$

EQUATION 3.29

Where  $\text{Random}_1$  and  $\text{Random}_2$  are independently generated random numbers between 0 and 1  
and  $r$  is the lens front radius

### The Ideal Plano-convex Lens Front Mesh

Lens front mesh points for an ideally positioned convex primary surface orientation plano-convex lens are derived from the equation of a sphere as:

$$y_{\text{convex}} = \sqrt{R^2 - x^2 - z^2} + Y_0$$

EQUATION 3.30

Where  $x$  and  $z$  are found on the lens front and thus bound by:

$$x^2 + z^2 < r^2$$

EQUATION 3.31

For an ideally positioned planar primary surface orientation plano-convex lens the front surface is bound by an x-z plane. Thus the y component for any lens front mesh point is:

$$y_{planar} = Y_0 - D$$

EQUATION 3.32

The extension to mesh grid point vectors for the convex primary surface orientated lens by Equation 3.30 is then:

$$\begin{bmatrix} x \\ y \\ z \end{bmatrix} = \begin{bmatrix} Length \times \cos(Angle) \\ \sqrt{R^2 - x^2 - z^2} + Y_0 \\ Length \times \sin(Angle) \end{bmatrix}$$

EQUATION 3.33

and for the planar surface primary oriented lens by Equation 3.32:

$$\begin{bmatrix} x \\ y \\ z \end{bmatrix} = \begin{bmatrix} Length \times \cos(Angle) \\ Y_0 - D \\ Length \times \sin(Angle) \end{bmatrix}$$

EQUATION 3.34

Figure 3.42 shows the ideally positioned plano-convex lens front mapped with 10,000 mesh grid points.

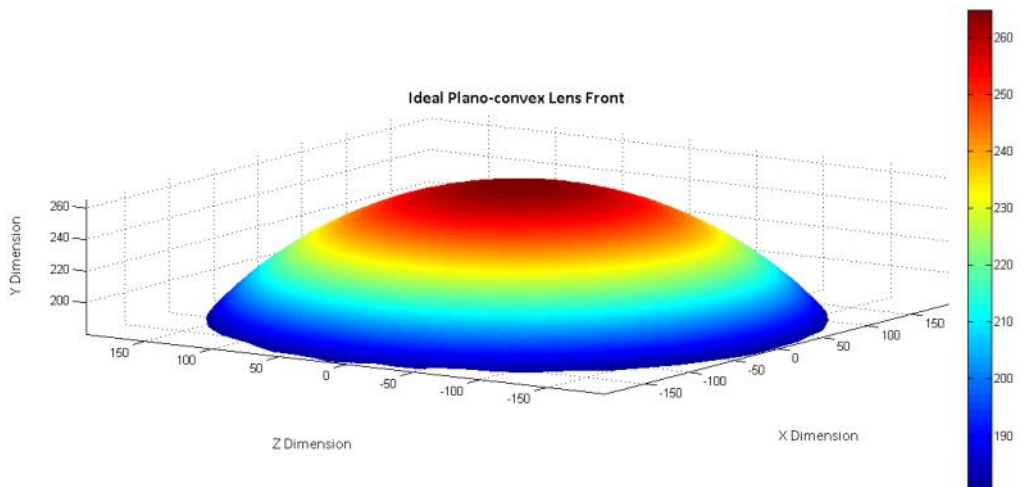


FIGURE 3.42: IDEAL PLANO-CONVEX LENS FRONT MESH GRID. RESOLUTION = 10,000

### The Ideal Fresnel Lens Front Mesh

Given that the external facets of the Fresnel lens are confined to the same spherical shell as the plano-convex lens front, the initial stages in lens front mesh calculation are similar. The y-dimension coordinate for each mesh grid point is then a function of the Fresnel facet index.

The Fresnel facet front radius,  $\rho$ , is calculated by:

$$\rho = \frac{r}{n}$$

EQUATION 3.35

For ease of reference the facets are indexed incrementally from centre to edge as depicted in Figure 3.43 and Figure 3.44.

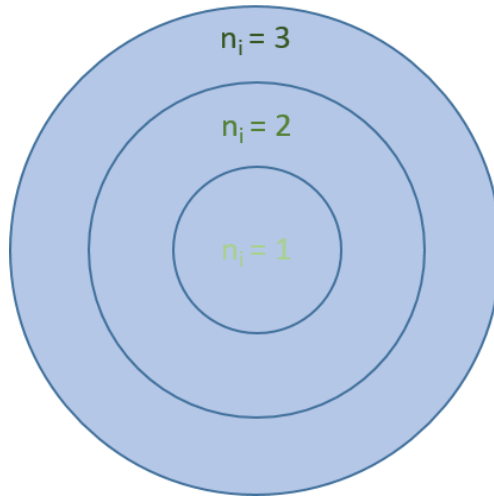


FIGURE 3.43: FRESNEL FACET INDEX NOTATION

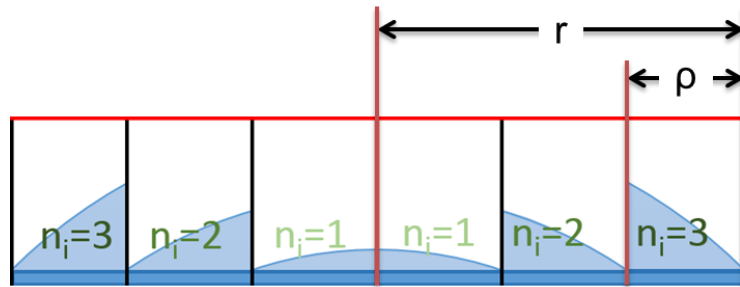


FIGURE 3.44: FRESNEL FACET INDEX SCHEMATIC

The facet index of a given  $(x, z)$  mesh point is determined by:

$$n_i = \text{Round} \left( \frac{\sqrt{x^2 + z^2}}{\rho} + 0.5 \right)$$

EQUATION 3.36

Each facet is a spherical section of constant radius. The radius of the outermost facet is equivalent to that of the plano-convex spherical shell. The facet radii reduce from outer to inner. The facet shell radius y-parameter reduction for each section is calculated in the ideal case as:

$$P = R - \left( \sqrt{R^2 - (n_i \rho)^2} - C \right)$$

EQUATION 3.37

Where  $P$  is the facet shell radius y-parameter reduction,  $R$  the outer shell plano-convex radius,  $n_i$  the facet index,  $\rho$  the Fresnel facet front radius &  $C$  the extent of curvature of the outer spherical shell

From Pythagoras the facet shell radius,  $F$ , is given by:

$$F = \sqrt{(n_i\rho)^2 + C^2}$$

EQUATION 3.38

From Equation 3.30 and Equation 3.37, the 3D lens front mesh point vector is found as:

$$\begin{bmatrix} x \\ y \\ z \end{bmatrix} = \begin{bmatrix} \text{Length} \times \cos(\text{Angle}) \\ \sqrt{R^2 - x^2 - z^2} + Y_0 - \left( \sqrt{R^2 - (n_i\rho)^2} - C \right) \\ \text{Length} \times \sin(\text{Angle}) \end{bmatrix}$$

$$= \begin{bmatrix} \text{Length} \times \cos(\text{Angle}) \\ \sqrt{R^2 - x^2 - z^2} + Y_0 - \left( \sqrt{R^2 - \text{Round} \left( \frac{\text{Length} \times n}{r} + 0.5 \right) \left( \frac{r}{n} \right)^2} - C \right) \\ \text{Length} \times \sin(\text{Angle}) \end{bmatrix}$$

EQUATION 3.39

Figure 3.45 shows a mapped graph of an ideally positioned 8 facet Fresnel lens front with 10,000 mesh grid points:

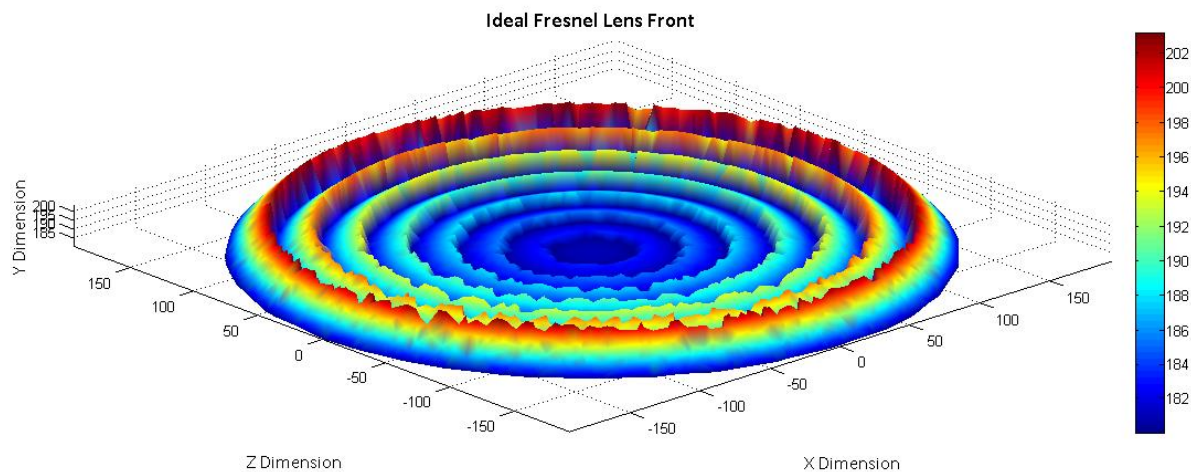


FIGURE 3.45: IDEALLY ORIENTED CONVEX FRESNEL LENS FRONT

As the surface of the Fresnel lens is discontinuous, the resolution features are noticeable in the surface plot. Given current computational restrictions a surface mesh resolution of approximately 10,000 points is realistic. The granularity of Figure 3.45 serves to highlight resolution-dependent issues in CPV simulation.

### 3.5.2.2. The General Lens

The general lens is positioned with placement and orientation errors. The actual placement of a lens relative to the ideal position can be described with two parameters.

- Placement Error
- Orientation Error

Placement error is here defined as a Cartesian vector describing the offset of a reference pivot point on the lens.

With no orientation error the placement error describes the offset of every lens point. For a misoriented lens, the placement error vector varies for each lens point as a function of the misorientation. A reference point on the lens must be chosen as a pivotal point about which the misorientation occurs.

Orientation error is defined as a spherical polar angle pair describing the offset of the lens normal.

Together with the lens parameters, the placement and orientation errors are used to define the position of all points on the erroneously positioned lens.

For consistency with a variety of lens types, specifically the plano-convex and Fresnel lenses, the reference point is chosen as the central point on the planar surface, as depicted in Figure 3.46. This reference point is chosen as it represents a real, physical point on all lenses with a planar back surface.

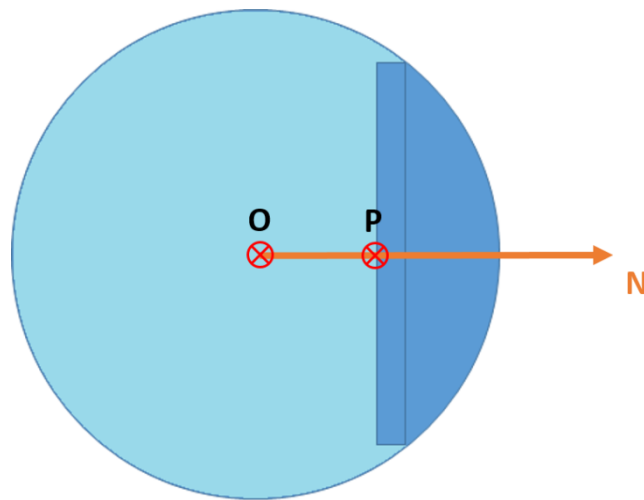


FIGURE 3.46: LENS ERROR REFERENCE POINT

Placement error is given in terms of x, y and z errors as a Cartesian vector. The placement error vector,  $\Delta$ , is applied to the reference point. According to the above definition, all lens points deviate from their misoriented (rotated about point **P**) position by the placement error vector,  $\Delta$ :

$$\Delta = \begin{bmatrix} \delta x \\ \delta y \\ \delta z \end{bmatrix}$$

EQUATION 3.40

Orientation error is given in terms of azimuth and elevation error. The orientation error has the effect of rotating the lens normal. Hence, from Equation 3.23, the general lens unit normal is defined by:

$$N = \begin{bmatrix} \sin \alpha \cos \varepsilon \\ \cos \alpha \cos \varepsilon \\ \sin \varepsilon \end{bmatrix}$$

EQUATION 3.41

The origin of spherical symmetry for the outer shell of a general lens is derived as:

$$O = O_0 + \Delta + D(\hat{j} - N)$$

EQUATION 3.42

Where  $O_0$  is the desired origin of spherical symmetry,  $\Delta$  the placement error vector,  $R$  the radius of spherical symmetry,  $\hat{j}$  the unit vector in the y-direction and  $N$  the general lens normal

From the perspective of the lens anti-normal the erroneously positioned lens back planar surface is a circle in the plane  $P_{LB}$  with radius  $r$ . Where the plane  $P_{LB}$  is defined as:

$$N \cdot \begin{bmatrix} x \\ y \\ z \end{bmatrix} = N \cdot (O_0 + \Delta)$$

EQUATION 3.43

The general lens front can be considered as the ideal lens front rotated about the reference pivotal point,  $P$ , as demonstrated in Figure 3.47.

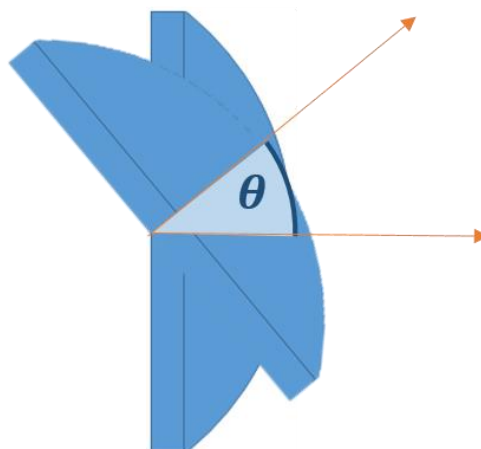


FIGURE 3.47: LENS ROTATION ABOUT THE LENS ERROR REFERENCE POINT BY THE ANGLE,  $\theta$

This translation is achieved by first rotating the ideal lens front within its spherical shell then adding a reference point correction vector,  $\mathbf{V}$ , as depicted in Figure 3.47. The addition of  $\mathbf{V}$  to all rotated lens points corrects the lens position for rotation about the reference point.

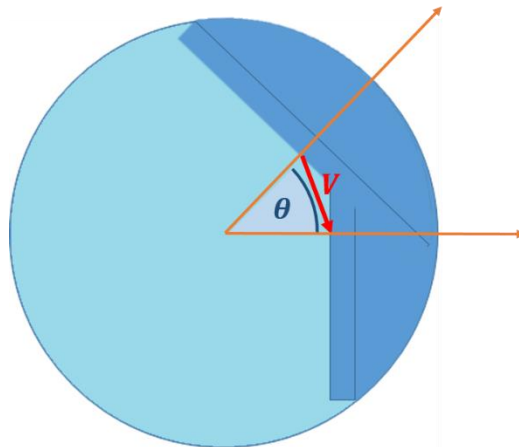


FIGURE 3.48: SPHERICAL SHELL LENS ROTATION AND LENS ERROR REFERENCE POINT CONSISTENCY ADJUSTMENT VECTOR

Rotation within the spherical shell can itself be thought of as a 2-part process, separating out the azimuth and elevation rotations.

The calculation of the general lens front mesh can thus be considered a 4 part process:

1. Generate Ideal Lens Front Mesh
2. Rotate for Azimuth
3. Rotate for Elevation
4. Correct for Pivotal Point Consistency

Step one is given in the above section (3.5.2 Lens Front Mesh Generation). Steps 2-4 are given below.

Rotation for azimuth error occurs in the x-y plane (see 3.5.1 Reference Frame). Given that a positive azimuth angle here corresponds to a clockwise rotation (from positive y to positive x) the rotation matrix corresponding to azimuth rotation is defined as:

$$R_\alpha = \begin{bmatrix} \cos(\alpha) & \sin(\alpha) & 0 \\ -\sin(\alpha) & \cos(\alpha) & 0 \\ 0 & 0 & 1 \end{bmatrix}$$

EQUATION 3.44

Where  $\alpha$  is the angle of azimuth rotation

Rotation for elevation occurs about the normal vector,  $\mathbf{N}$ , to the point of rotation, where that normal vector originates at the origin,  $\mathbf{O}$ . The rotation occurs in the plane:

$$\mathbf{N} \cdot (\mathbf{P}_P - \mathbf{O}) = \mathbf{N} \cdot \mathbf{P}_P = 0$$

EQUATION 3.45

Where  $\mathbf{P}_P$  is any point in the plane

Correction for lens error reference point consistency is achieved through simple vector addition. It can be derived from Figure 3.48 that the pinnacle point correction vector,  $\mathbf{V}$ , is equivalent to the lens depth,  $D$ , multiplied by the vector obtained by deducting the unit vector rotated lens normal,  $\mathbf{N}$ , from the ideal lens normal,  $\hat{\mathbf{j}}$ :

$$\mathbf{V} = D(\hat{\mathbf{j}} - \mathbf{N})$$

EQUATION 3.46

From Equation 3.41:

$$\mathbf{V} = D(\hat{\mathbf{j}} - \mathbf{N}) = D \left( \begin{bmatrix} 0 \\ 1 \\ 0 \end{bmatrix} - \begin{bmatrix} \sin \alpha \cos \varepsilon \\ \cos \alpha \cos \varepsilon \\ \sin \varepsilon \end{bmatrix} \right) = D \begin{bmatrix} \sin \alpha \cos \varepsilon \\ 1 - \cos \alpha \cos \varepsilon \\ \sin \varepsilon \end{bmatrix}$$

EQUATION 3.47

In the following section, examples of the above process applied to the plano-convex and Fresnel lenses are presented. Calculation of the general, optically misaligned lens front mesh is necessary for the investigation of component misalignment issues – an area of CPV performance modelling that is often overlooked.

### The General Plano-convex Lens Front

Figure 3.49 shows an erroneously (optically misaligned) positioned plano-convex lens front mapped with 10,000 mesh grid points. The errors in this lens position are in orientation:  $-10^\circ$  in azimuth and  $+5^\circ$  in elevation.

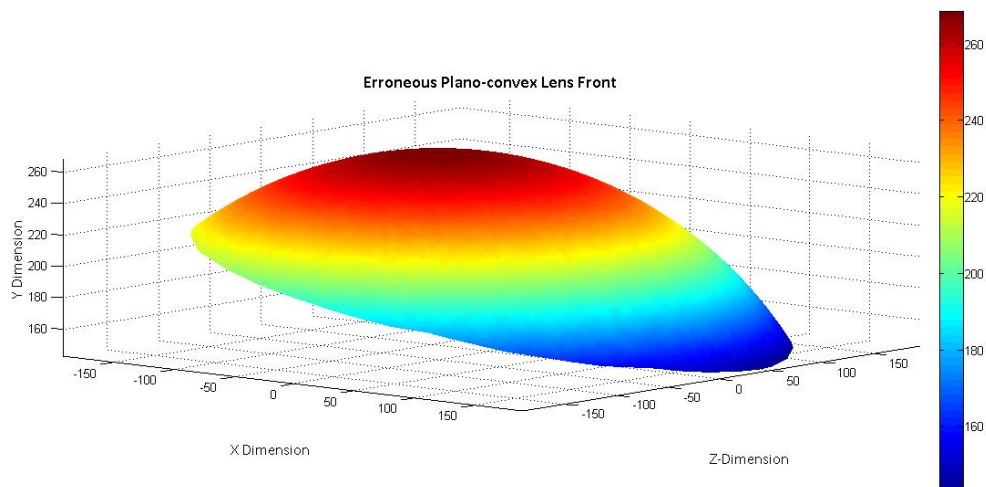


FIGURE 3.49: PLANO-CONVEX LENS FRONT MESH WITH ORIENTATION ERRORS OF  $10^\circ$  IN AZIMUTH AND  $5^\circ$  IN ELEVATION. RESOLUTION = 10,000

### The General Fresnel Lens Front

An erroneously positioned Fresnel lens is shown in Figure 3.50

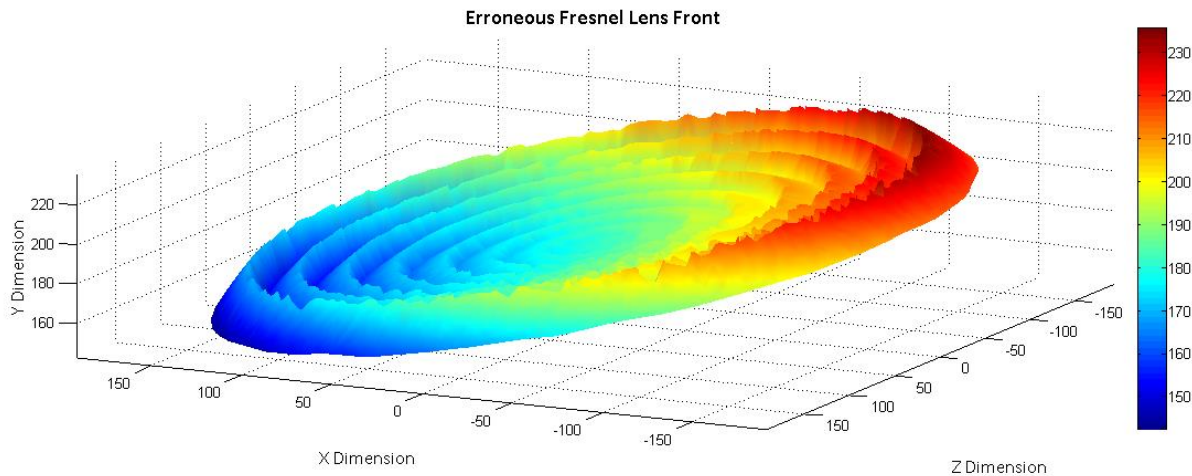


FIGURE 3.50: ERRONEOUS ORIENTED CONVEX FRESNEL LENS FRONT

The convex Fresnel lens front depicted in Figure 3.50 is an 8 facet lens front generated with 10,000 random homogeneously distributed mesh grid points. The errors in this lens position are in orientation: +10° in azimuth and +5° in elevation.

### 3.5.3. Ray Trace Traversal

#### 3.5.3.1. Input Rays

Each point on the generated lens mesh is subject to a set of incident rays. The incident rays are those derived from the incident solar profile, described in 2 Input, and generated by the processes divulged therein.

To allow for the consideration of spectral effects, a ray here has a vector origin, vector direction, scalar intensity and scalar wavelength. For the purpose of incident solar image conversion an ‘input ray’ is introduced as a reduced ray form. This input ray has only vector direction, scalar intensity and scalar wavelength. The conversion from an incident solar profile to an input ray set is obtained simply by means of coordinate system transposition and mirroring. The input image sky patch locations are given in terms of azimuth and elevation coordinates. These are readily converted into Cartesian directional vectors by Equation 3.23. However, due to the chosen reference frame and mirrored projection incidence, the directional vector components are mirrored. Thus the input ray direction vector,  $\mathbf{R}$ , is obtained as:

$$\mathbf{R} = \begin{bmatrix} -\sin \alpha \cos \varepsilon \\ -\cos \alpha \cos \varepsilon \\ -\sin \varepsilon \end{bmatrix}$$

EQUATION 3.48

The incident solar profile is then converted to input rays by Equation 3.48. The image points for conversion can then be defined either by some deterministic method or by the homogeneous random mesh grid method given by Equation 3.27, Equation 3.28 and Equation 3.29.

### Primary Trace Phase

The primary trace phase rays are created at the lens front interface. Each lens front mesh grid point is considered an origin for an input ray set. The ray intensity is reduced from the sky patch intensity according to the Fresnel equations (see Equation 3.13, Equation 3.14 and Equation 3.15) and the ray direction calculated according to the law of refraction (as derived from the principle of least time in 3.1.1.2 Law of Refraction). The process is similar for both plano-convex and Fresnel lenses with the major difference being the facet dependent computation of surface normal vectors in the Fresnel lens. The ray trace procedures then differ, largely in complexity, for the plano-convex and Fresnel lenses. The ray trace procedures as divulged hereafter are valid for any arbitrary ray entering the defined lens front.

#### 3.5.3.2. Plano-convex Lens Ray Tracing

A high level ray trace model flowchart for the plano-convex lens with a convex primary surface orientation is presented in Figure 3.51.

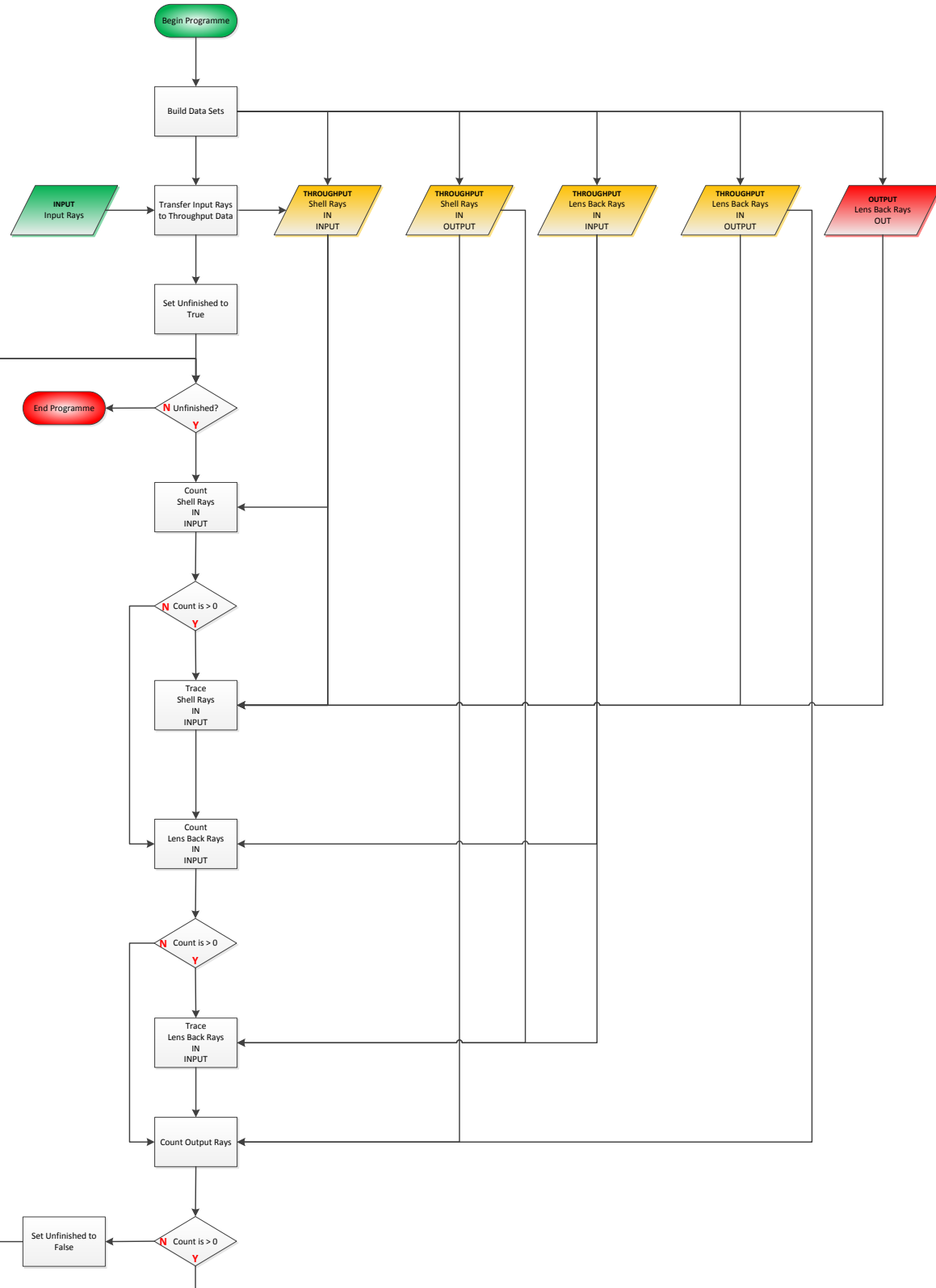


FIGURE 3.51: PLANO-CONVEX LENS WITH CONVEX PRIMARY SURFACE ORIENTATION RAY TRACE FLOWCHART

The data blocks in Figure 3.51 are split into 3 categories: **input**, **output** and **throughput**. Input refers to the primary trace phase rays defined above; output to the rays leaving the lens through the lens back; and throughput to rays traversing the lens with a lens-surface-bound origin. The throughput rays

are subdivided into 4 categories, those originating on the convex shell surface and those originating on the planar back surface, with input and output variations of each. The input rays being those moving into the lens and the output rays those moving out of the lens. Each category forms a different geometric problem and is hence treated individually. These internal datasets are updated throughout the simulation in real time as ray paths are calculated.

### Spherical Shell Rays

The **input** rays of Figure 3.51 are incident on the convex surface. These rays are useful if they trace through to the planar lens back, otherwise they are considered as lost to the environment. Once the point of intersection with the lens back plane is determined the directional change is calculated and a new ray born accordingly. The new ray is either a reflected ray that traverses through the lens and is thus added to the throughput dataset or a refracted ray that leaves the lens and is thus considered as an output exit ray. The calculation procedure is depicted schematically in Figure 3.52 and as a lower level flowchart in Figure 3.53.

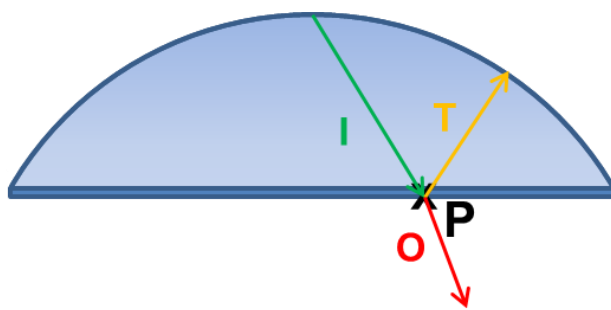


FIGURE 3.52: PLANO-CONVEX INPUT RAYS TRACE SCHEMATIC

Figure 3.52 shows the input shell ray, **I**, extended to a point of intersection at the lens back plane, **P**, if **P** is in the lens the directional change at **P** is calculated. If the ray is reflected, **T**, it remains in the lens and is thus added to the throughput category. If the ray is refracted, **O**, it leaves the lens towards the solar cell and is thus added to the output category. This process is further divulged in Figure 3.53.

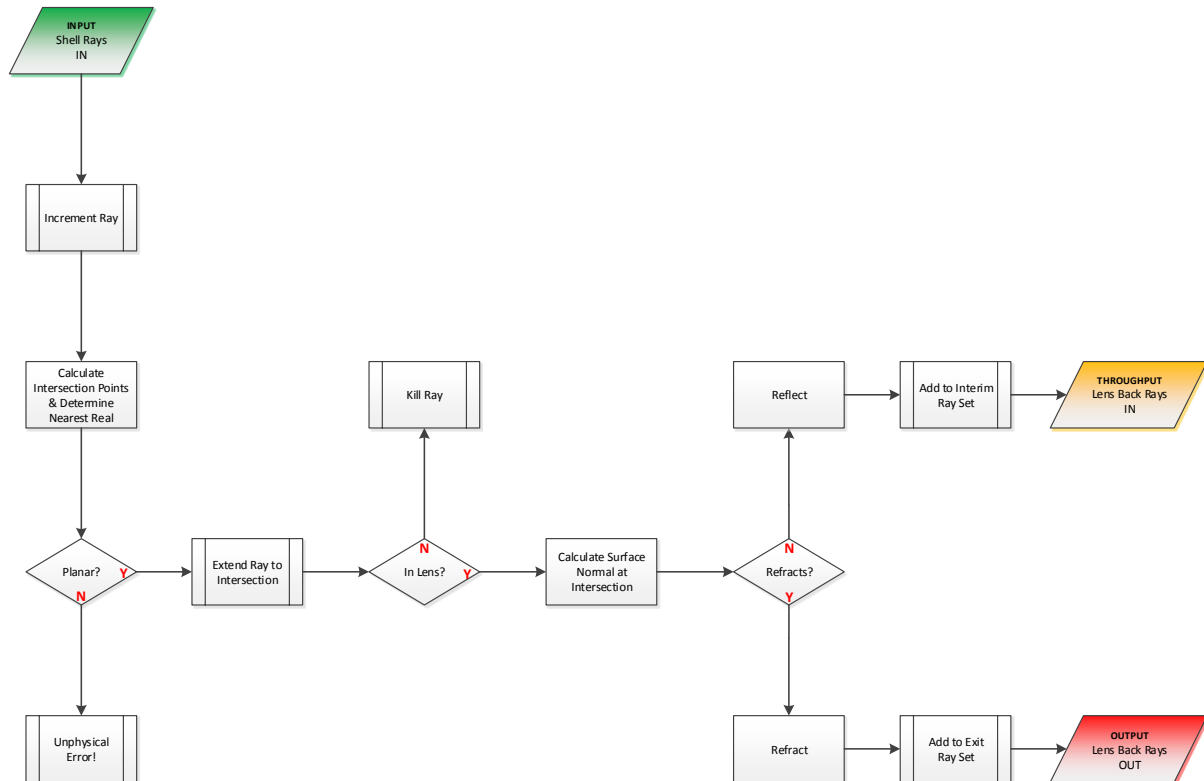


FIGURE 3.53: PLANO-CONVEX LENS WITH CONVEX PRIMARY SURFACE INPUT RAYS RAY TRACE FLOWCHART

This procedure runs until the input rays are exhausted.

### Planar Lens Back Rays

The throughput rays are then traced as per Figure 3.54 and Figure 3.55.

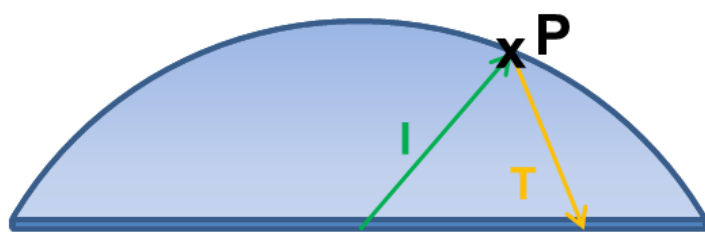


FIGURE 3.54: LENS BACK RAY INWARD THROUGHPUT RAY TRACE SCHEMATIC

Figure 3.54 shows the input lens back inward ray, **I**, extended to a point of intersection at the lens spherical shell surface, **P**. If the ray is reflected here, **T**, it remains in the lens and is thus added to the throughput category as an inward shell ray. If the ray is refracted it leaves the lens towards the Sun and thus is considered lost to the environment. This process is further divulged in Figure 3.55.

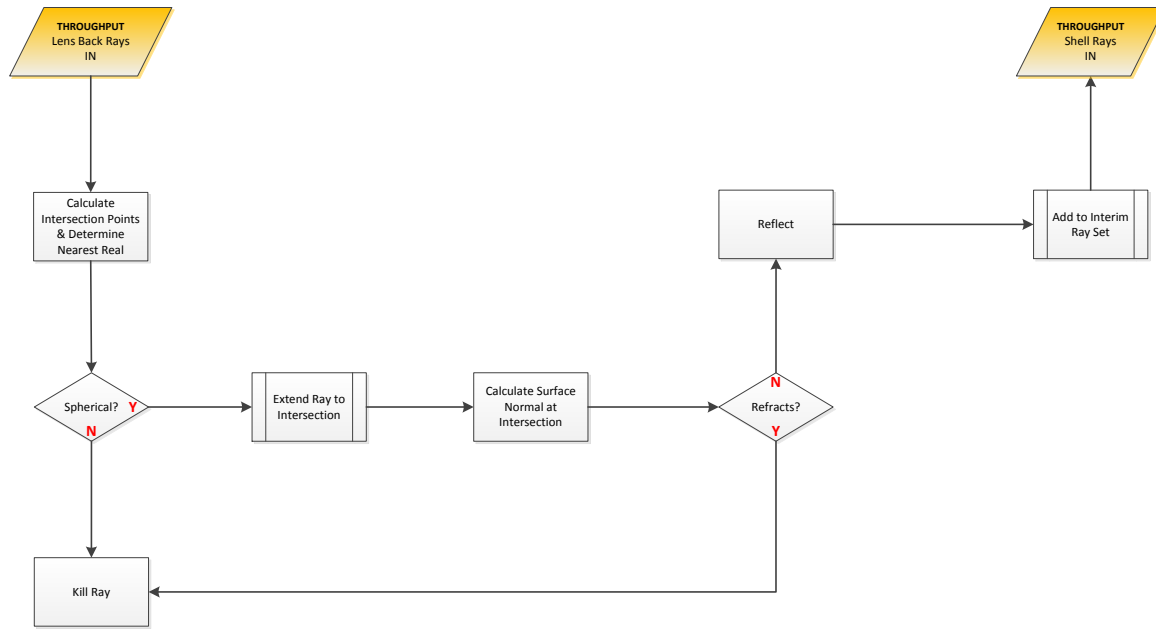


FIGURE 3.55: RAY TRACE FLOWCHART FOR INWARD LENS BACK THROUGHPUT RAYS IN THE PLANO-CONVEX LENS TRACE PROCEDURE

Once this procedure is complete, the overarching trace programme (see Figure 3.51) checks for further throughput rays and reruns. The trace is complete when all remaining rays are output rays.

### 3.5.3.3. Fresnel Lens Ray Tracing

Due to the added complexity of facets, the Fresnel lens ray trace procedure is more complex. The high level ray trace traversal model for the Fresnel lens with a convex primary surface orientation is shown in Figure 3.56.

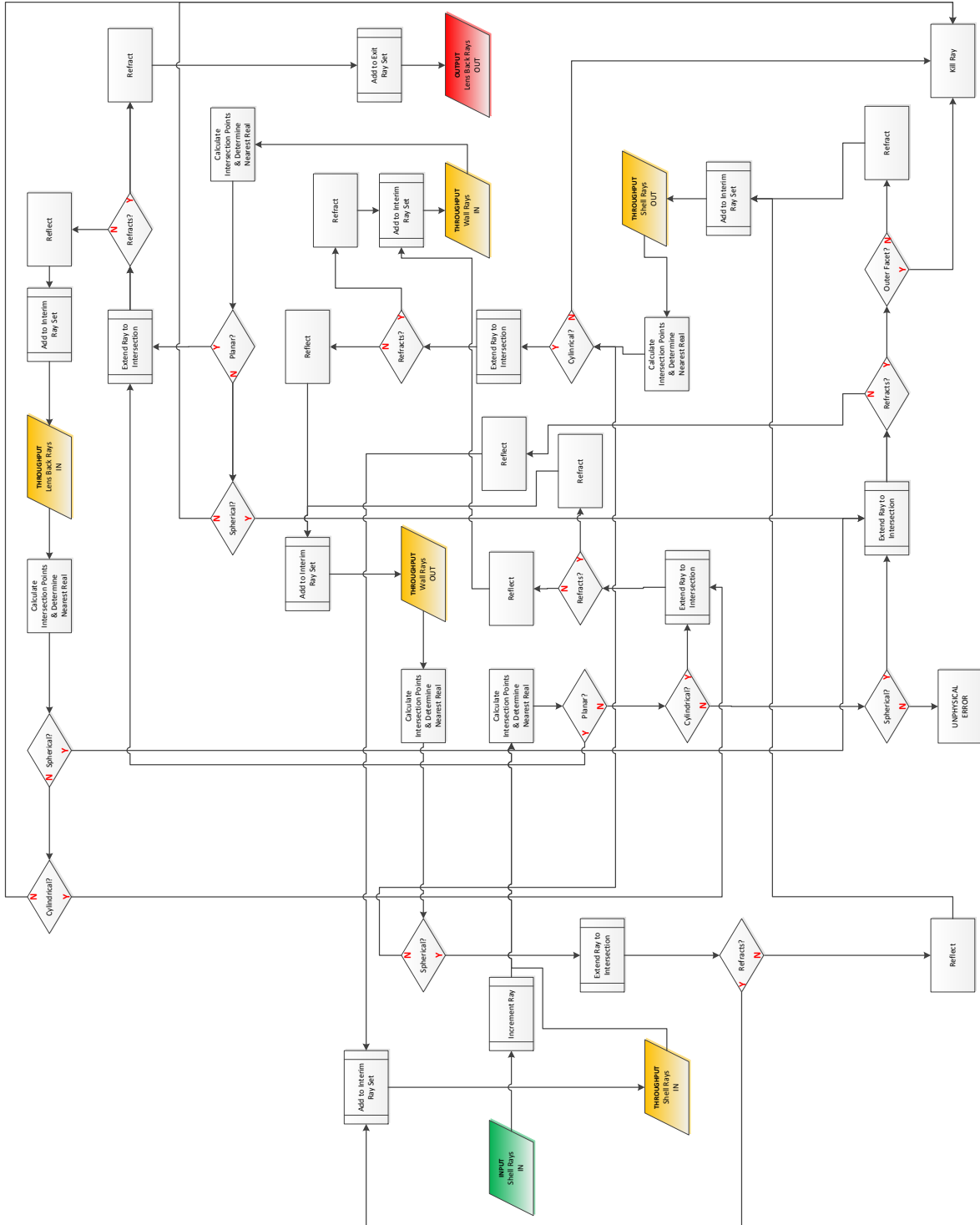


FIGURE 3.56: HIGH LEVEL FRESNEL RAY TRACE PROCEDURE SCHEMATIC

The data blocks in Figure 3.56 are split into 3 categories: **input**, **output** and **throughput**. Input refers to the primary trace phase rays defined above; output to the rays leaving the lens through the lens back; and throughput to rays traversing the lens with a lens surface bound origin. The throughput rays are subdivided into 6 categories, those originating on the convex shell surface, those originating on the planar back surface and those originating on the inner facet cylindrical walls; with input and output

variations of each. Each category forms a different geometric problem and is hence treated individually. These internal datasets are updated throughout the simulation in real time as ray paths are calculated.

### Spherical Shell Rays

The Fresnel facet shell ray problem is depicted in Figure 3.57.

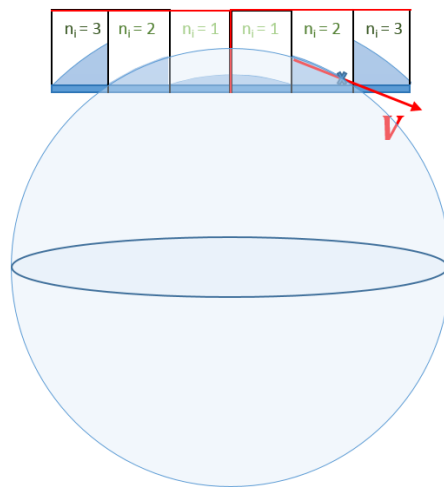


FIGURE 3.57: FRESNEL FACET SHELL RAY PROBLEM SCHEMATIC

The **input** rays of Figure 3.56 are incident on the convex surface of a Fresnel facet. These rays are useful at the next iteration if they trace through to the planar lens back and out of the lens, otherwise they are added to a throughput dataset. The intersection of a given **input** ray is either found with the planar lens back, the inner facet cylindrical wall, or the facet spherical shell housing, ordered respective of probability. The calculation procedure for determination of the intersection type and dataset allocation is depicted schematically in Figure 3.58 and as a lower level flowchart in Figure 3.59.

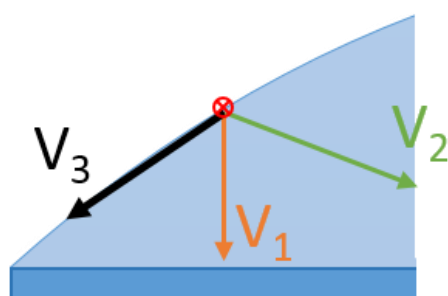


FIGURE 3.58: FRESNEL INPUT RAYS TRACE SCHEMATIC

Figure 3.58 shows three variations of the input shell ray, **I** ( $V_1$ ,  $V_2$  &  $V_3$ ), extended to points of intersection at the lens back plane, the cylindrical inner facet wall and the facet spherical shell housing, respectively. These intersection points are checked in order of probability and checked for refraction. If the ray is refracted, the reflected portion is ignored (no longer ray traced) and the refracted ray,

inclusive of reflection losses from the Fresnel equations and absorption losses from the material traversal, is passed to the appropriate throughput dataset. Only if the ray is refracted out of the lens back is it considered an **output** ray. This process is further divulged in Figure 3.59.

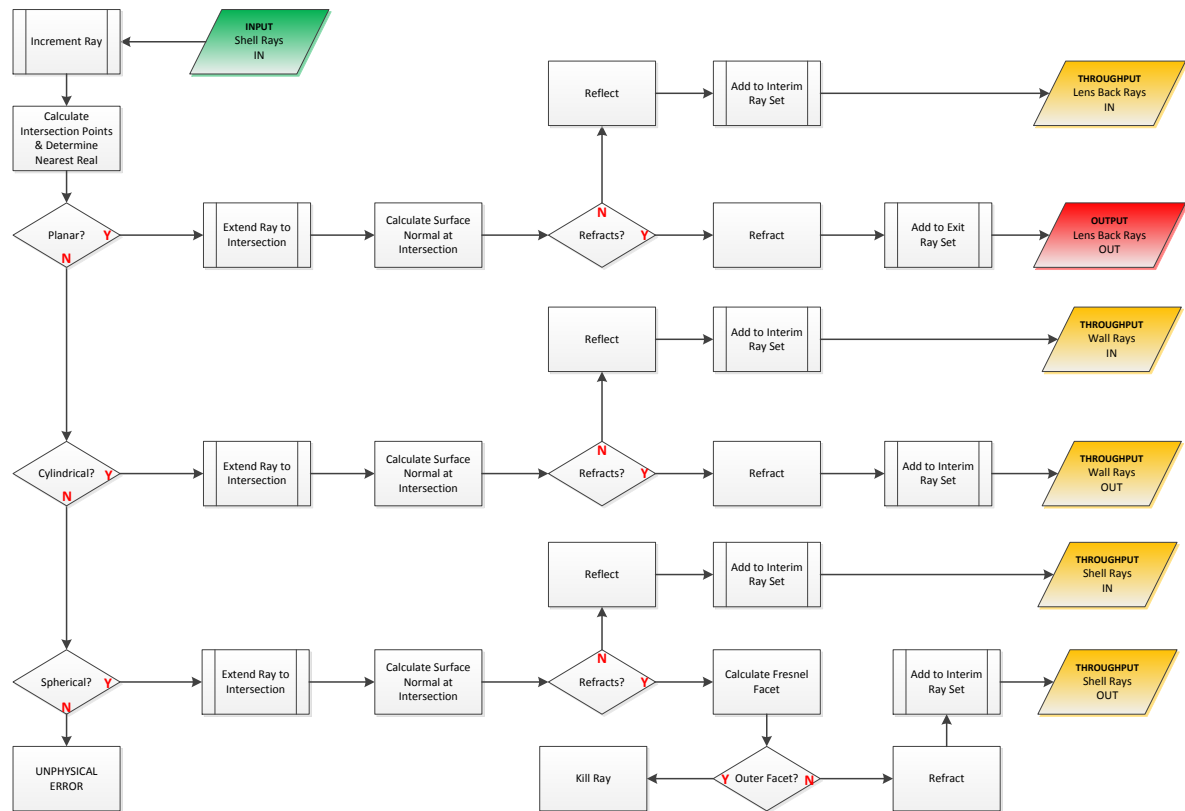


FIGURE 3.59: FRESNEL LENS WITH FACET-BOUND CONVEX PRIMARY SURFACE INPUT RAYS RAY TRACE FLOWCHART

Given the nature of the Fresnel lens structure, another shell ray case needs to be considered. This case is referred to as spherical shell out rays and is depicted schematically in Figure 3.60 and as a lower level flowchart in Figure 3.61.

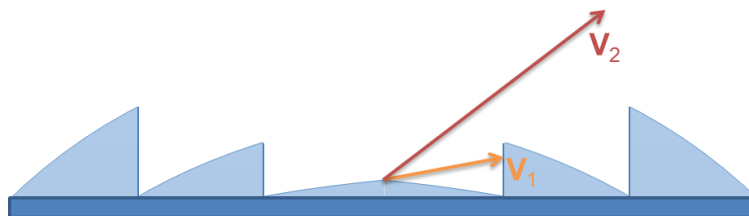


FIGURE 3.60: FRESNEL SHELL RAYS OUT TRACE SCHEMATIC

Figure 3.60 shows two variations of the shell out ray,  $V_1$  &  $V_2$ , one extended to a point of intersection with a cylindrical inner facet wall and the other leaving the lens and lost to the environment, respectively. These possibilities are checked in order of probability and the first for refraction. If the ray is refracted, the reflected portion is ignored and the refracted ray, inclusive of reflection losses

from the Fresnel equations and absorption losses from the material traversal, is passed to the appropriate throughput dataset. This process is further divulged in Figure 3.61.

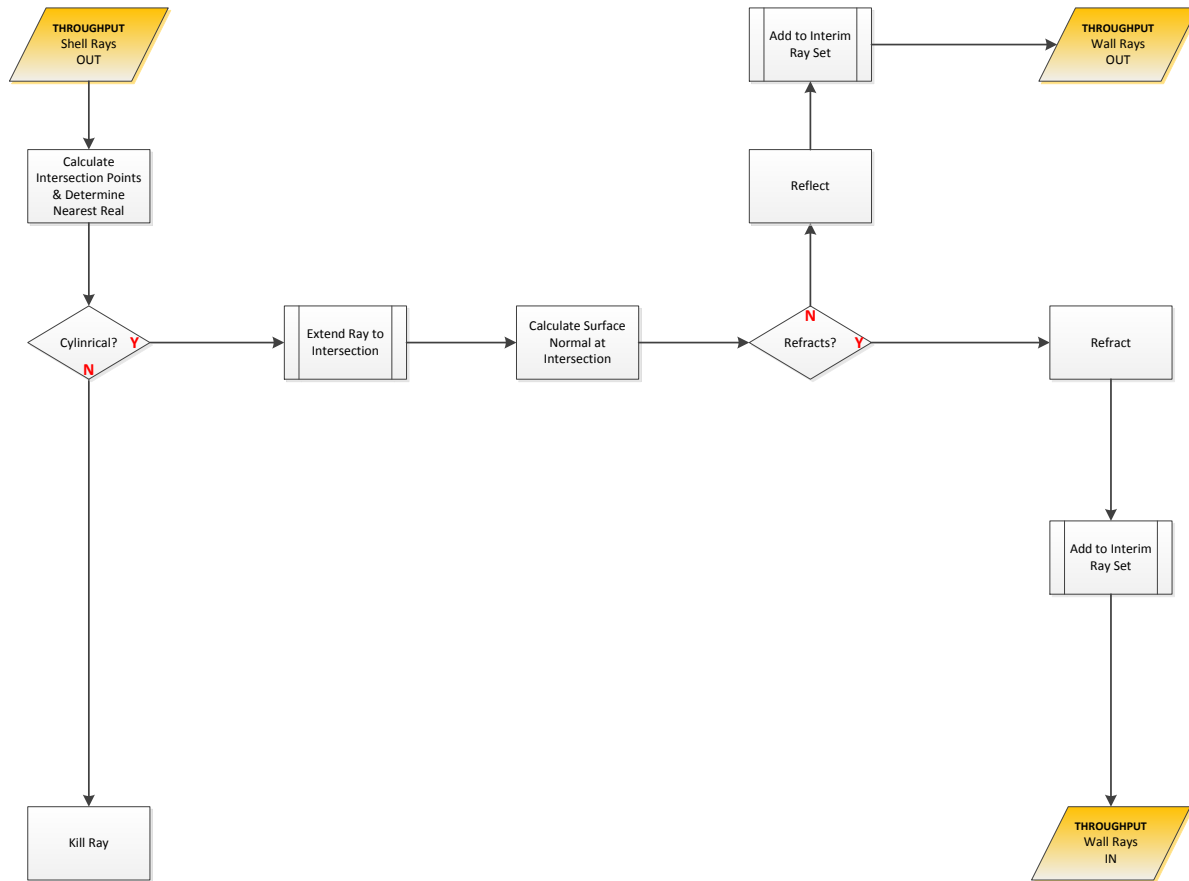


FIGURE 3.61: FRESNEL LENS WITH FACET-BOUND SHELL RAYS OUT RAY TRACE FLOWCHART

### Planar Lens Back Rays

The planar lens back ray calculation procedure is depicted schematically in Figure 3.62 and as a lower level flowchart in Figure 3.63.

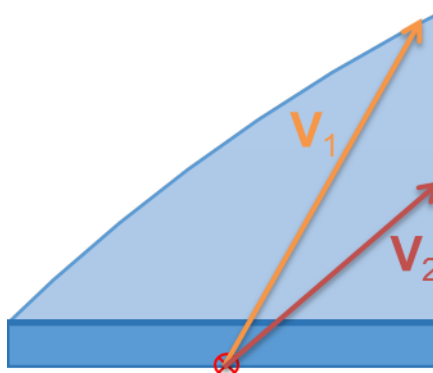


FIGURE 3.62: FRESNEL LENS BACK IN RAYS TRACE SCHEMATIC

Figure 3.62 shows two variations of the lens back reflected rays,  $V_1$  &  $V_2$ , extended to points of intersection at the facet spherical shell housing and the cylindrical inner facet wall, respectively. These intersection points are checked for refraction. If the ray is refracted, the reflected portion is ignored and the refracted ray, inclusive of reflection losses from the Fresnel equations and absorption losses from the material traversal, is passed to the appropriate throughput dataset. This process is further detailed in Figure 3.63.

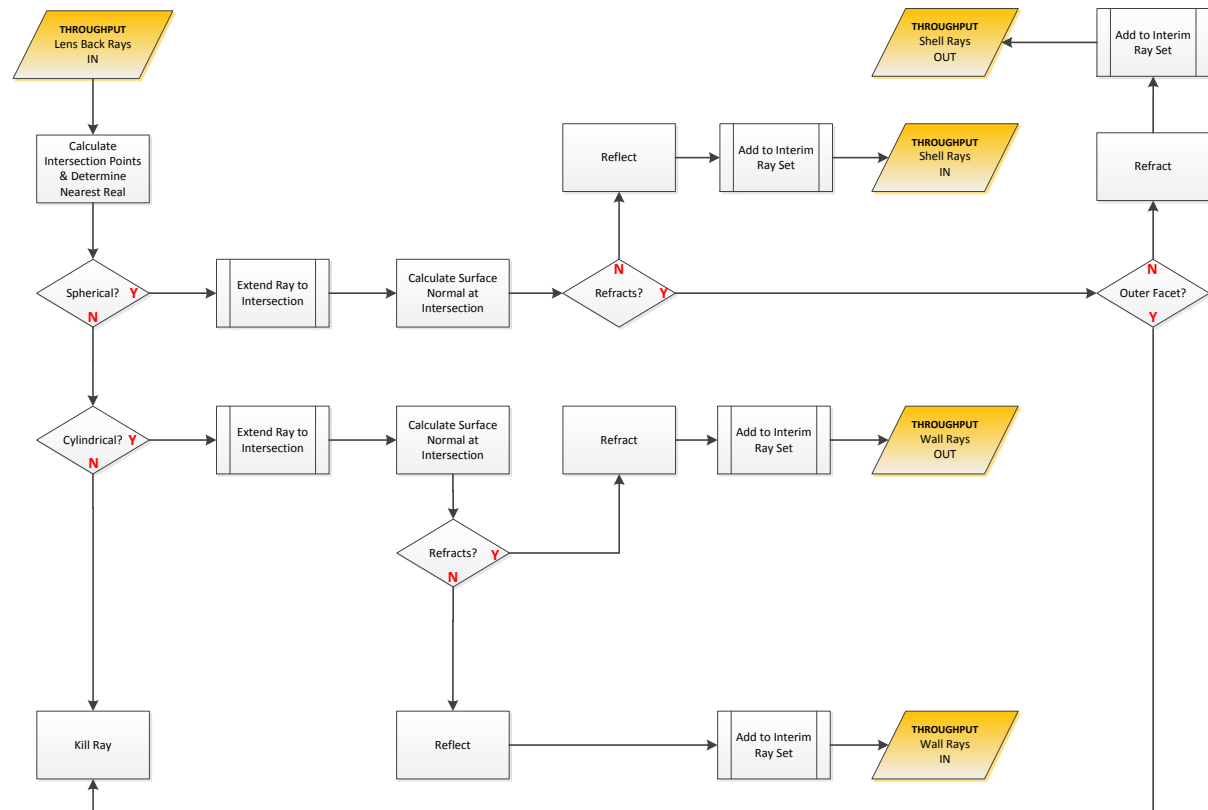


FIGURE 3.63: FRESNEL LENS WITH FACET-BOUND LENS BACK RAYS IN RAY TRACE FLOWCHART

### Cylindrical Wall Rays

The Fresnel facet cylindrical wall ray problem is depicted in Figure 3.64.

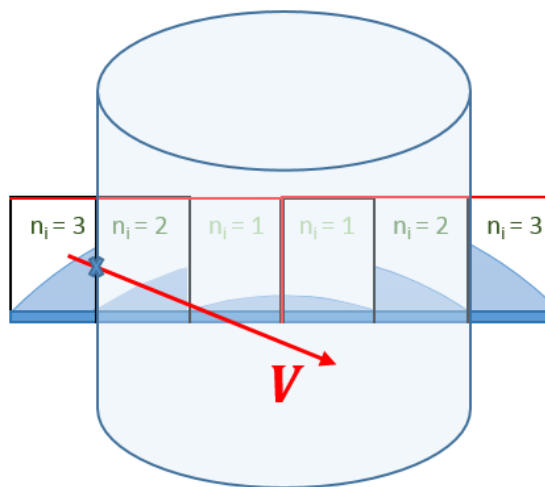


FIGURE 3.64: FRESNEL FACET CYLINDRICAL WALL RAY PROBLEM SCHEMATIC

The facet cylindrical wall problem is split into two separable scenarios, wall rays moving inward with a lens facet and walls rays moving outward from a lens facet. The most probable scenario is the inward wall rays. The wall rays in calculation procedure is depicted schematically in Figure 3.65 and as a lower level flowchart in Figure 3.66.

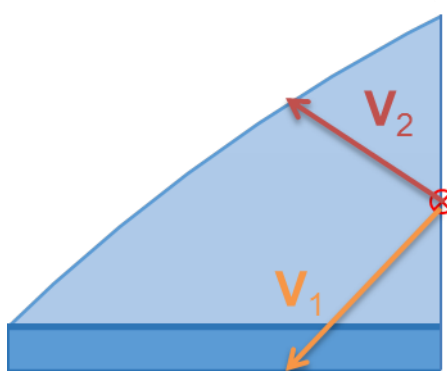


FIGURE 3.65: FRESNEL LENS WALL IN RAYS TRACE SCHEMATIC

Figure 3.65 shows two variations of the cylindrical wall in rays,  $V_1$  &  $V_2$ , extended to points of intersection at the planar lens back surface and the facet spherical shell housing, respectively. These intersection points are checked for refraction. If the ray is refracted, the reflected portion is ignored and the refracted ray, inclusive of reflection losses from the Fresnel equations and absorption losses from the material traversal, is passed to the appropriate throughput dataset. This process is further detailed in Figure 3.66.

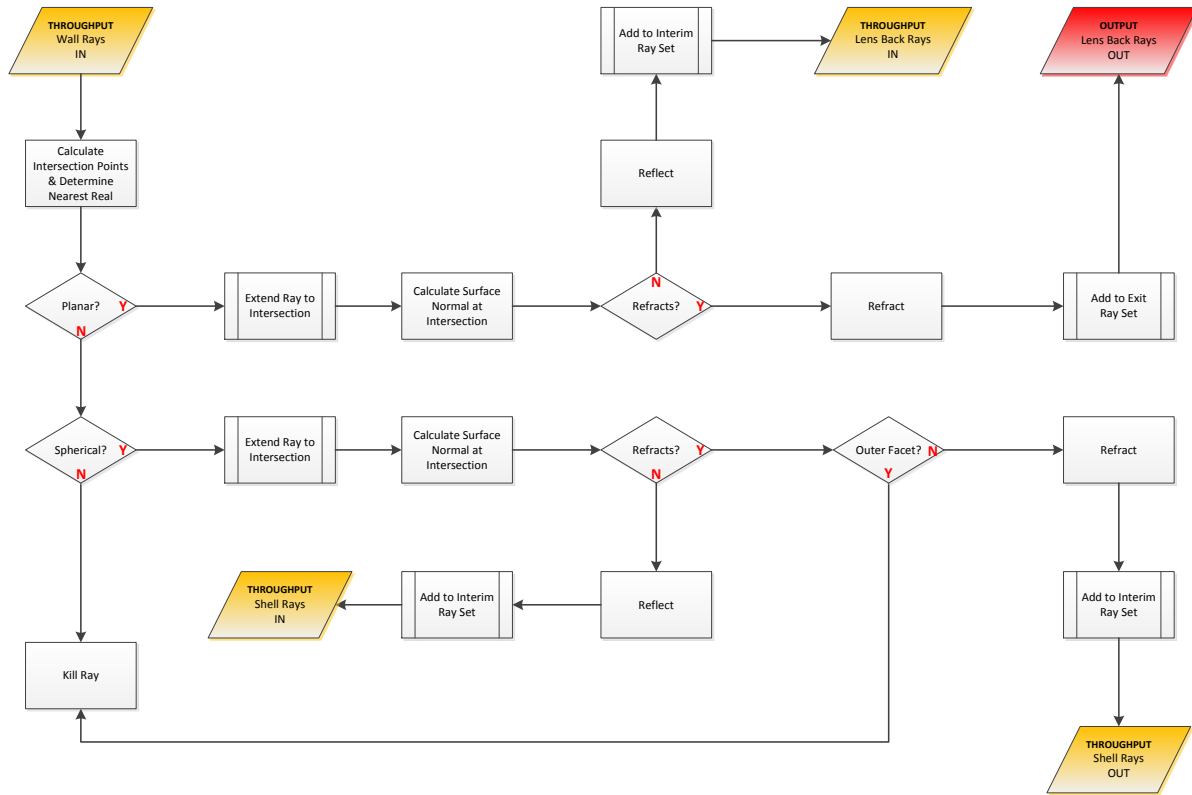


FIGURE 3.66: FRESNEL LENS WITH FACET-BOUND WALL RAYS IN RAY TRACE FLOWCHART

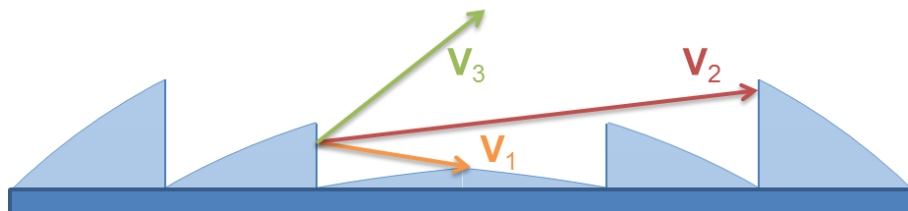


FIGURE 3.67: FRESNEL LENS WALL OUT RAYS TRACE SCHEMATIC

Figure 3.67 shows three variations of the cylindrical wall out rays,  $V_1$ ,  $V_2$  &  $V_3$ , extended to points of intersection at the facet spherical shell housing, the inner facet cylindrical wall and lost to the environment, respectively. These intersection points are checked for refraction. If the ray is refracted, the reflected portion is ignored and the refracted ray, inclusive of reflection losses from the Fresnel equations and absorption losses from the material traversal, is passed to the appropriate throughput dataset. In this case, independent of intersection type, the next ray iteration remains in the lens as throughput. This process is further illustrated in Figure 3.68.

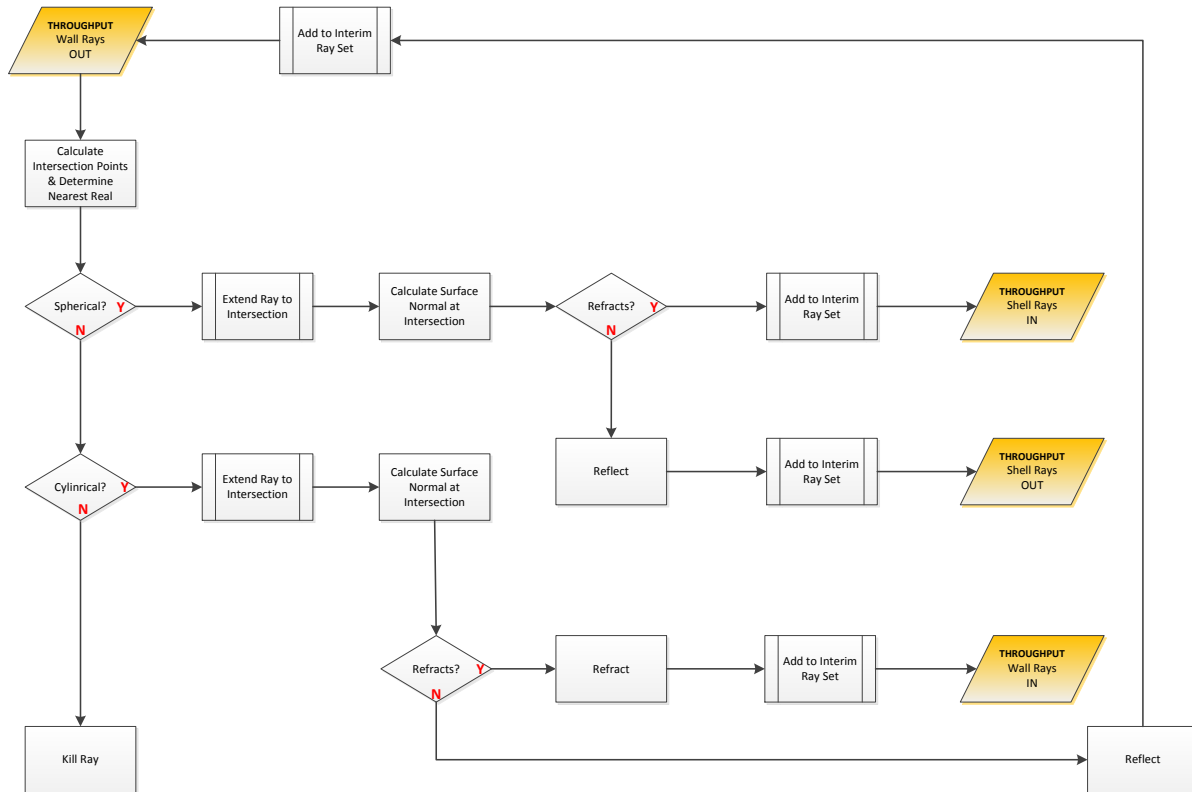


FIGURE 3.68: FRESNEL LENS WITH FACET-BOUND WALL RAYS OUT RAY TRACE FLOWCHART

### 3.5.3.4. Ray Directional Changes – A Note on Optimisation

Directional changes for rays need to be calculated at every material interface. The directional changes occur in a 2D plane according to the law of refraction (see Equation 3.2). However, the plane is specific to each point of intersection and is thus arbitrary in the context of the simulation. The direction change can be considered as a rotation in this arbitrary plane. Vector rotations in arbitrary planes are commonly calculated as a five step process of matrix operations. However, given the number of directional change calculations required in this work, the five step process proved time-inefficient, as over 20,000,000,000 matrix operations were performed on average for each simulation run. Given the inefficiency of the process, an optimisation was calculated. The optimised directional change procedure used a single matrix operation for the rotation of a vector about an arbitrary axis by an arbitrary angle:

$$M(V, \theta) = \begin{bmatrix} \frac{V_x^2 + (V_y^2 + V_z^2) \cos \theta}{|V|^2} & \frac{V_x V_y (1 - \cos \theta)}{|V|^2} - \frac{V_z \sin \theta}{|V|} & \frac{V_x V_z (1 - \cos \theta)}{|V|^2} + \frac{V_y \sin \theta}{|V|} \\ \frac{V_x V_y (1 - \cos \theta)}{|V|^2} + \frac{V_z \sin \theta}{|V|} & \frac{V_y^2 + (V_x^2 + V_z^2) \cos \theta}{|V|^2} & \frac{V_y V_z (1 - \cos \theta)}{|V|^2} - \frac{V_x \sin \theta}{|V|} \\ \frac{V_x V_z (1 - \cos \theta)}{|V|^2} - \frac{V_y \sin \theta}{|V|} & \frac{V_y V_z (1 - \cos \theta)}{|V|^2} + \frac{V_x \sin \theta}{|V|} & \frac{V_z^2 + (V_x^2 + V_y^2) \cos \theta}{|V|^2} \end{bmatrix}$$

EQUATION 3.49

This reduced the number of required matrix operations by a factor of 5. For the derivation of this arbitrary rotation matrix and an explanation of the variable definitions, please see section 9.2, ‘Rotation Matrix Derivation’.

## 3.6. Results

The models and reduced variable systems as described above have been used to generate system behaviour information and banded illumination profiles. Example results are presented here both singularly for specific analysis and contextually for the consideration of system level effects.

### 3.6.1. Lens Volumes

Variations in Fresnel lens volume as calculated by Equation 3.22 are shown in Figure 3.69.

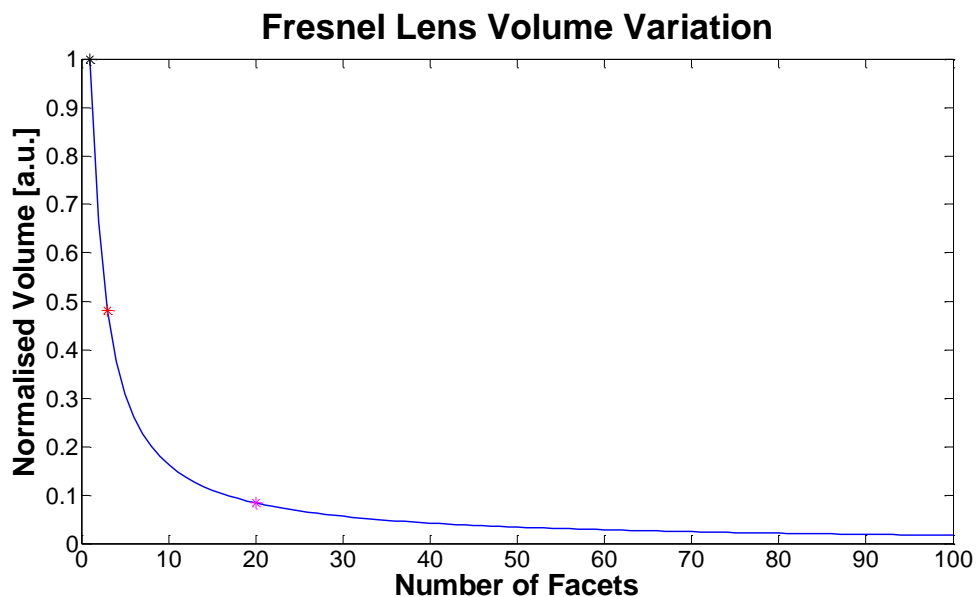


FIGURE 3.69: FRESNEL LENS VOLUME VERSUS NUMBER OF FACETS FOR A GIVEN SHELL RESTRICTION ANGLE

Figure 3.69 shows the normalised variation of Fresnel volume for the example lens given in section 3.3.3, ‘Focal Point Calculation’ i.e. a radial half angle restriction of  $\frac{\pi^c}{6}$ . The single facet, three facet and 20 facet Fresnel lens volumes are highlighted for reference as they are used as examples within this chapter. The actual volume variation changes slightly with angular restriction, this variation is shown in Figure 3.70.

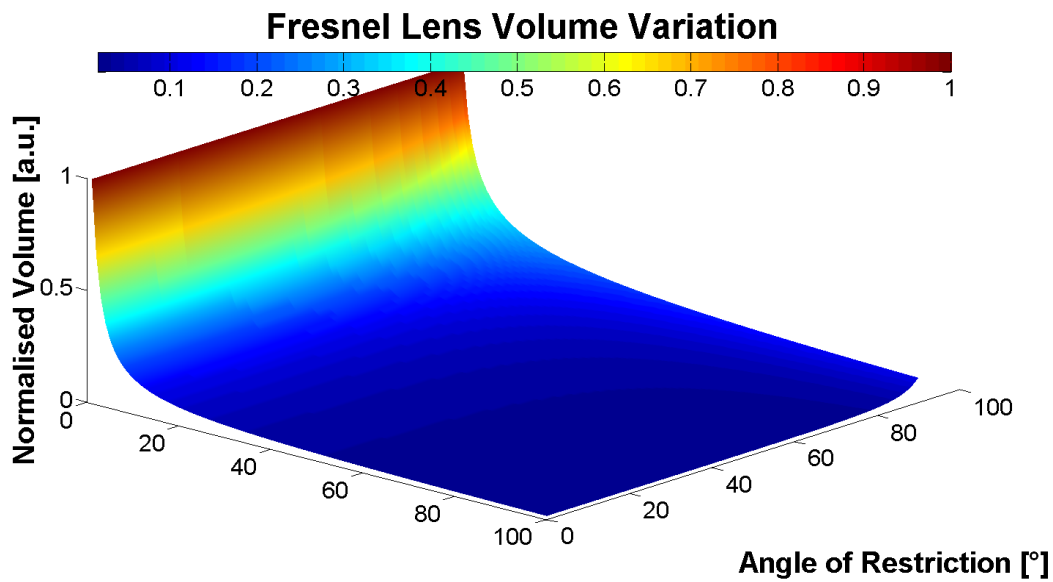


FIGURE 3.70: FRESNEL LENS VOLUME VARIATION VERSUS NUMBER OF FACETS VS SHELL RESTRICTION ANGLE

Figure 3.70 shows a slight angular dependence on angle of restriction in the normalised lens volume versus number of facets relationship. As the angle of restriction is increased the volume reduction with facets is initially somewhat more sudden and then more gradual. This is related directly to gradient of the convex shell.

### 3.6.2. Banded Irradiation Variations

It is suggested herein that a satisfactory number of spectral bands be defined as a spectral resolution in optical simulations and that at minimum this should correspond to the number of active junctions of the solar cell under investigation. This allows for an active junction specific investigation into the effects of chromatic aberration on cell illumination profiles. The test case used here is an approximated triple junction cell banding using the spectral bands: 280-680, 680-880 and 880-1880nm.

Due to spectral dependency on air mass, the apportioned central solar and circumsolar beam contributions vary as shown in Figure 3.71.

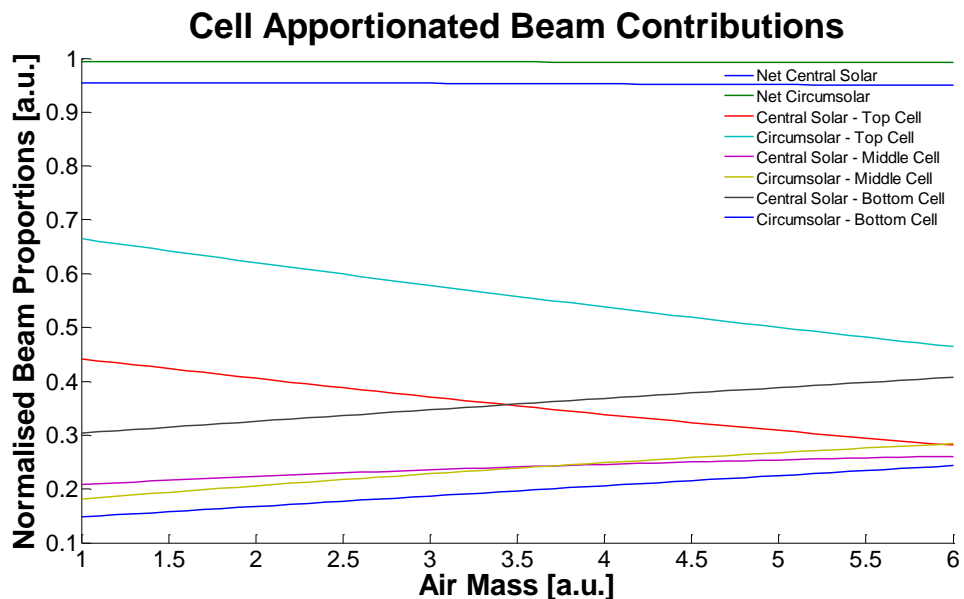


FIGURE 3.71: BEAM CONTRIBUTION VARIATIONS WITH AIR MASS

Figure 3.71 shows a large variation of air mass dependencies on normalised cell apportioned beam contributions for the central solar and circumsolar regions. The calculation of actual incident proportion is then a function of CSR, as shown in Figure 3.72, Figure 3.73 and Figure 3.74.

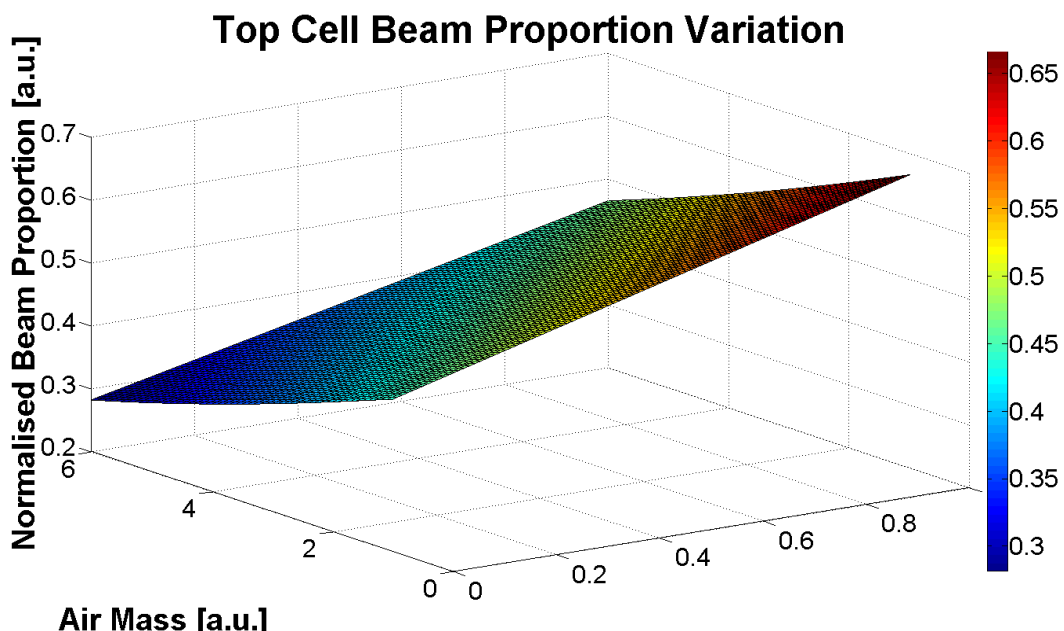


FIGURE 3.72: TOP CELL (280-680NM BAND) BEAM PROPORTION VARIATION VERSUS AIR MASS VERSUS CSR

Figure 3.72 shows an increase in top cell beam proportion from low CSR and high air mass to high CSR and low air mass.

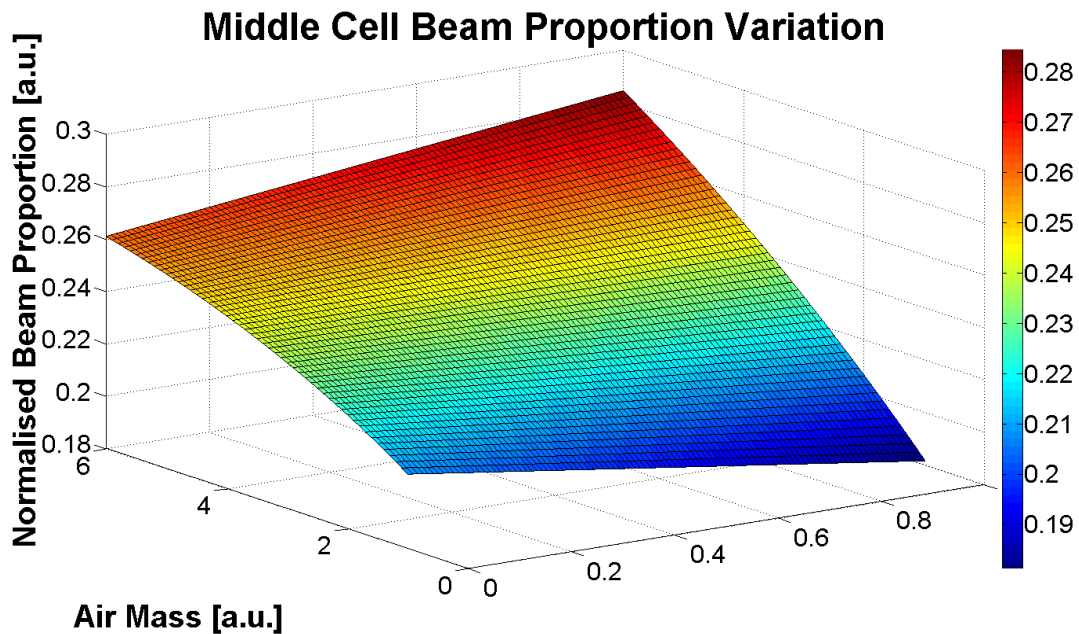


FIGURE 3.73: MIDDLE CELL (680-880NM BAND) BEAM PROPORTION VARIATION VERSUS AIR MASS VERSUS CSR

Figure 3.73 shows an increase in middle cell beam proportion from low CSR and low air mass to high CSR and high air mass.

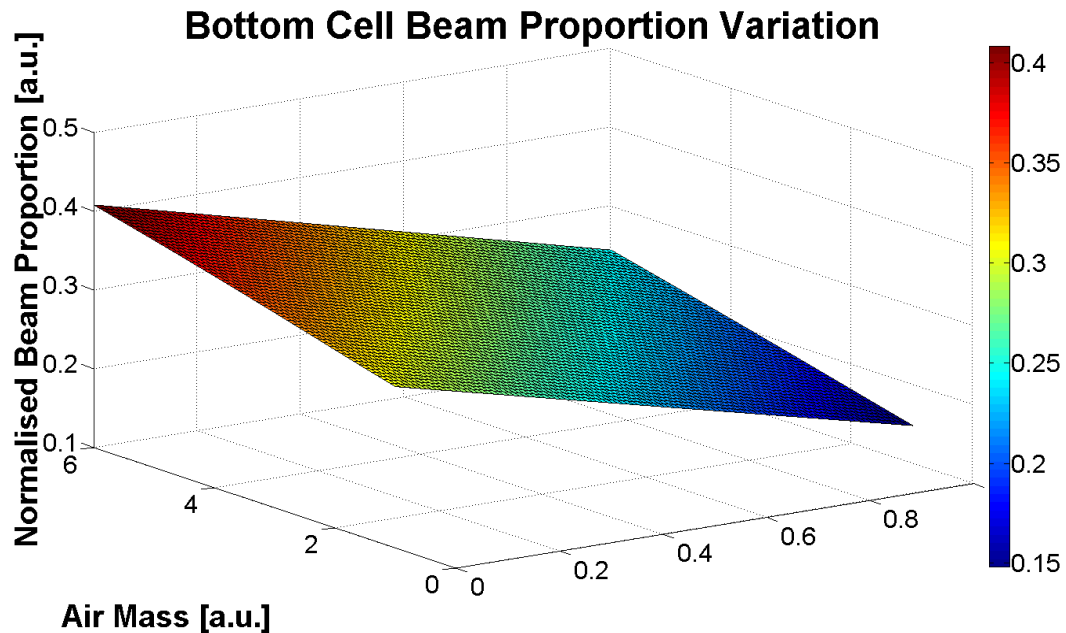


FIGURE 3.74: BOTTOM CELL (880-1880NM BAND) BEAM PROPORTION VARIATION VERSUS AIR MASS VERSUS CSR

Figure 3.74 shows an increase in bottom cell beam proportion from high CSR and low air mass to low CSR and high air mass.

Figure 3.72, Figure 3.73 and Figure 3.74 explicitly show different dependencies for the active junction spectral band region beam proportions on air mass and circumsolar ratio. These variations are

significant and ought to be considered in CPV system modelling as they are directly related to MJ cell performance by current limiting and chromatic aberration.

### 3.6.3. 2D Modelling Illumination Profiles

Illumination profiles resulting from 2D lens models and the Sun traces for the point source, pillbox and extended light source Sun are here presented. Chromatic aberration effects are investigated by means of split spectral analysis by active cell junction band. The AM1.5 DNI spectrum is used throughout for illustration. Full DNI and whole cell DNI differ due to the spectral content of the DNI irradiation. The full spectrum (280-4000nm) net irradiance amounts to 911W/m<sup>2</sup>, whereas the example whole cell spectrum net irradiance (280-1880nm) amounts to just 870W/m<sup>2</sup>. This is as produced by SMARTs which has a default near zero CSR. In reality this total cell apportioned irradiance changes with CSR. With a CSR of 0.3, for example, the whole cell spectrum net irradiance increases to 875 W/m<sup>2</sup>, an increase of approximately 0.6% on the zero CSR irradiance value.

#### 3.6.3.1. Point Source Sun Traces

The following illumination profiles are those that result from modelling the Sun as a point source. For a detailed overview of the point source Sun see section 2.2.1, ‘The Point Source Sun’.

##### Plano-convex Lens

The plano-convex lens simulated here is a soda-lime glass plano-convex lens. See section 3.2.4, ‘CPV Material Properties Overview’ for the banded material property data. The illumination profile here is calculated at the reference focal plane that is determined from the lensmaker’s equation using the nominal refractive index of soda-lime glass (the 589nm reference) which is approximately 1.562. All profiles are shown as traced to this plane.

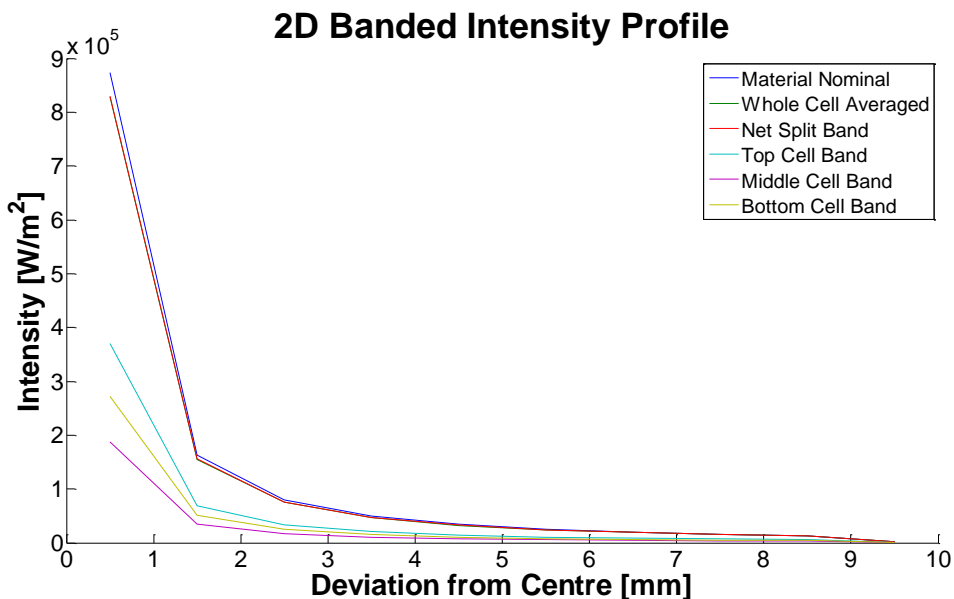


FIGURE 3.75: 2D BANDED INTENSITY ILLUMINATION PROFILE POINT SOURCE TRACE FOR A PLANO-CONVEX LENS

The banded optical efficiencies of the nominal material, whole cell averaged, top cell banded, middle cell banded and bottom cell banded calculations are: 38.1, 38.0, 37.9, 38.1 and 38.3%, respectively. Which amounts to a maximal absolute optical efficiency variation of approximately 0.4% and a maximal relative optical efficiency variation of around 1%.

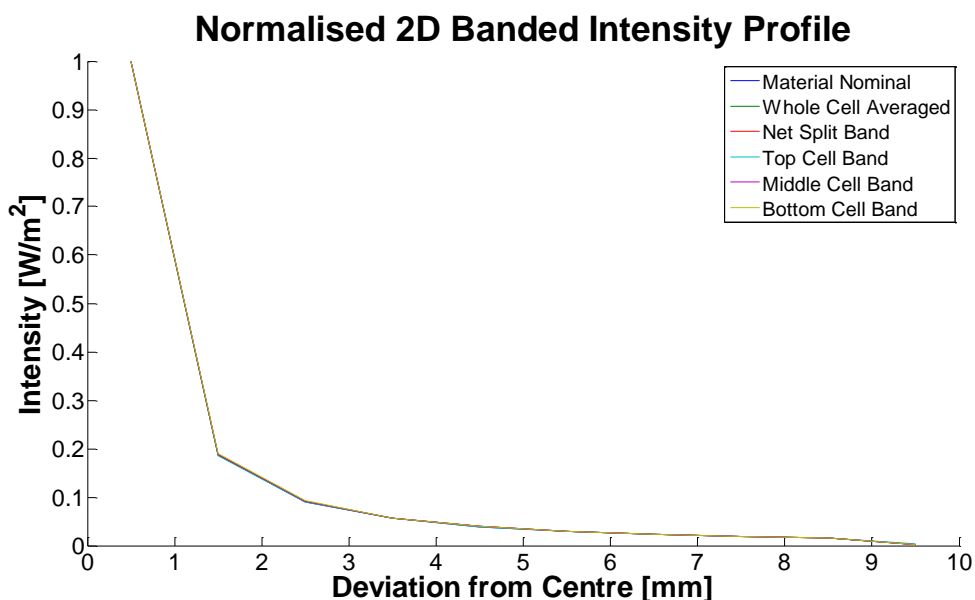


FIGURE 3.76: NORMALISED 2D BANDED INTENSITY ILLUMINATION PROFILE POINT SOURCE TRACE FOR A PLANO-CONVEX LENS

The normalised banded intensity profiles shown in Figure 3.76 show very little variation. The chromatic aberration effects of this trace are therefore negligible.

### 3 Facet Fresnel Lenses

The Fresnel lens simulated here is a PMMA Fresnel lens with 3 facets. See section 3.2.4, ‘CPV Material Properties Overview’ for the banded material property data. The illumination profile here is calculated at the reference focal plane that is determined from the lensmaker’s equation using the nominal refractive index of PMMA (the 589nm reference) which is approximately 1.470. All profiles are shown as traced to this plane.

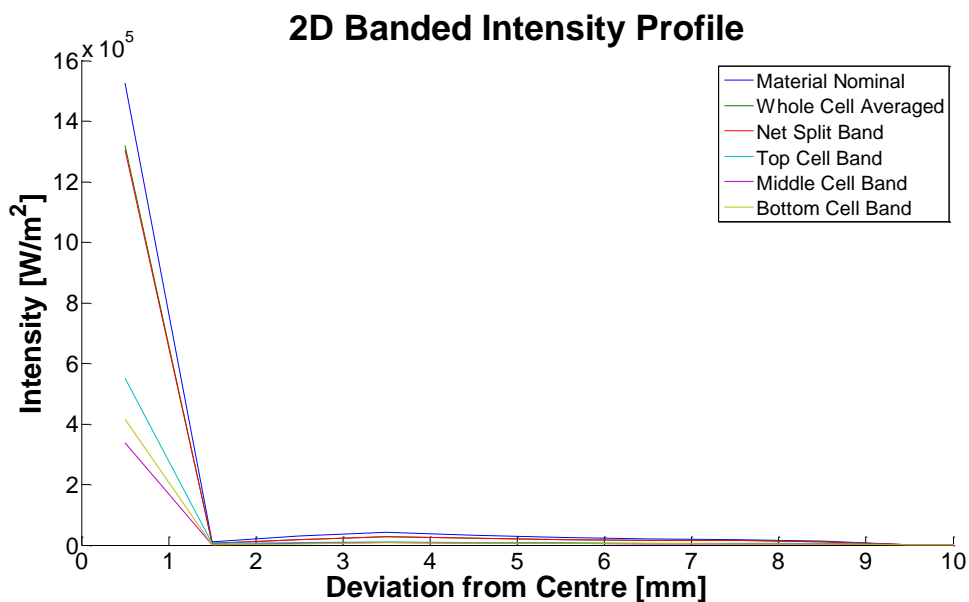


FIGURE 3.77: 2D BANDED INTENSITY ILLUMINATION PROFILE POINT SOURCE TRACE FOR A THREE-FACET FRESNEL LENS

The banded optical efficiencies of the nominal material, whole cell averaged, top cell banded, middle cell banded and bottom cell banded calculations are: 37.2, 31.4, 29.6, 37.4 and 28.7%, respectively. Which amounts to a maximal absolute optical efficiency variation of approximately 8.7% and a maximal relative optical efficiency variation of around 30%.

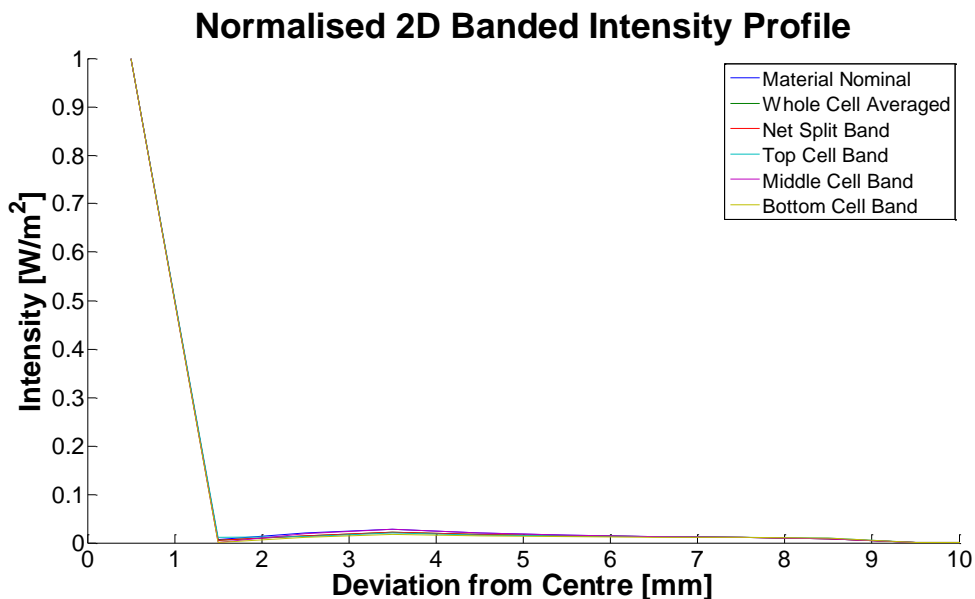


FIGURE 3.78: NORMALISED 2D BANDED INTENSITY ILLUMINATION PROFILE POINT SOURCE TRACE FOR A THREE-FACET FRESNEL LENS

Figure 3.78 shows small variations in the normalised 2D banded intensities profiles as traced through the 3 facet Fresnel lens. These variations are a direct consequence of chromatic aberration. The main driver for these variations is the significant variation of the absorptivity of PMMA over the useful spectrum. This variation results in spectrally dependent inhomogeneities.

### 20 Facet Fresnel Lens

The Fresnel lens simulated here is a PMMA Fresnel lens with 20 facets. See section 3.2.4, ‘CPV Material Properties Overview’ for the banded material property data. The illumination profile here is calculated at the reference focal plane that is determined from the lensmaker’s equation using the nominal refractive index of PMMA (the 589nm reference) which is approximately 1.470. All profiles are shown as traced to this plane.

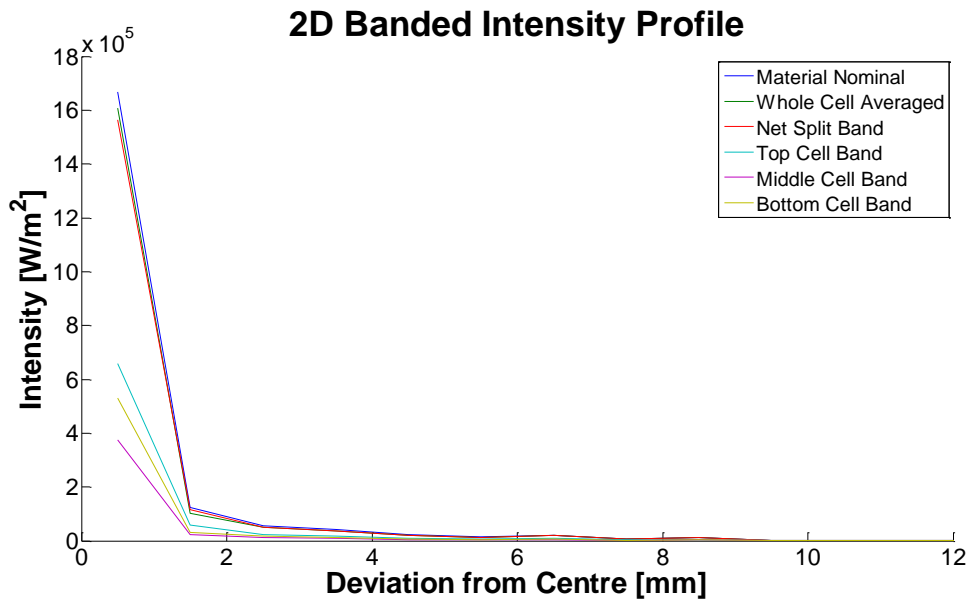


FIGURE 3.79: 2D BANDED INTENSITY ILLUMINATION PROFILE POINT SOURCE TRACE FOR A TWENTY-FACET FRESNEL LENS

The banded optical efficiencies of the nominal material, whole cell averaged, top cell banded, middle cell banded and bottom cell banded calculations are: 40.9, 39.8, 39.2, 41.1 and 39.5%, respectively. Which amounts to a maximal absolute optical efficiency variation of approximately 1.9% and a maximal relative optical efficiency variation of around 5%.

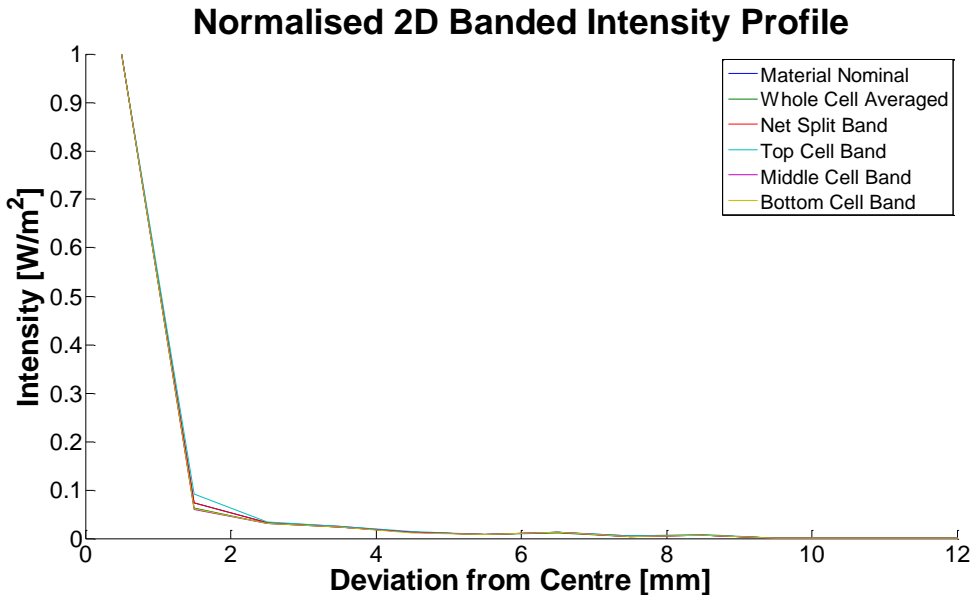


FIGURE 3.80: NORMALISED 2D BANDED INTENSITY ILLUMINATION PROFILE POINT SOURCE TRACE FOR A TWENTY-FACET FRESNEL LENS

Figure 3.80 shows small variations in the normalised 2D banded intensities profiles as traced through the 20 facet fresnel lens. These variations are a direct consequence of chromatic aberration. The main driver for these variations is the significant variation of the absorptivity of PMMA over the useful spectrum. This variation results in spectrally dependent inhomogeneities. The region of intensity

deviation is less widespread here than in the 3 facet Fresnel trace. This is a result of the significant reduction of central facet thicknesses and thus the relative insignificance of the absorption of the rays whence cast.

### 3.6.3.2. Pillbox Source Sun Traces

#### Plano-Convex Lens

The plano-convex lens simulated here is a soda-lime glass plano-convex lens. See section 3.2.4, 'CPV Material Properties Overview' for the banded material property data. The illumination profile here is calculated at the reference focal plane that is determined from the lensmaker's equation using the nominal refractive index of soda-lime glass (the 589nm reference) which is approximately 1.562. All profiles are shown as traced to this plane.

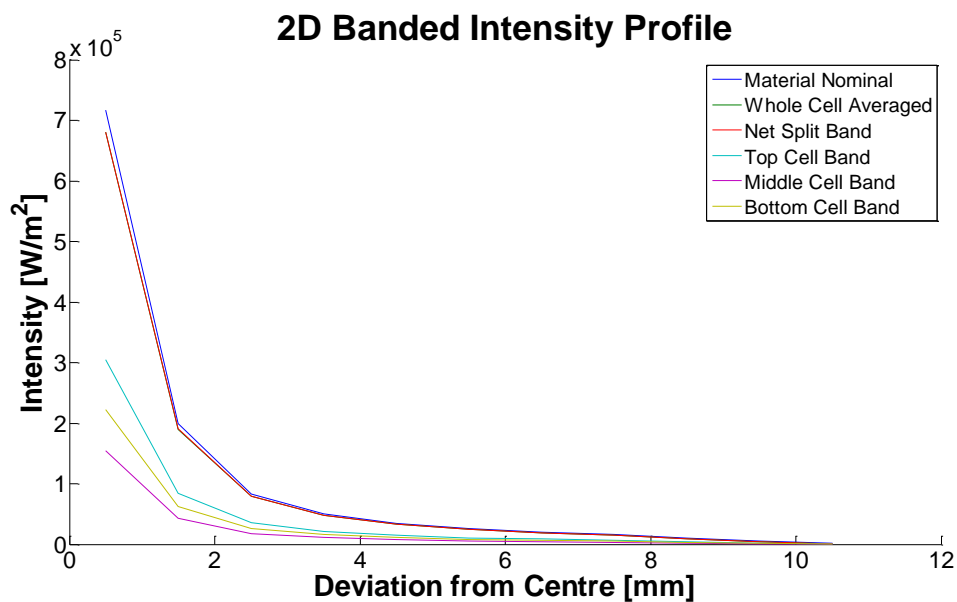


FIGURE 3.81: 2D BANDED INTENSITY ILLUMINATION PROFILE PILLBOX SOURCE TRACE FOR A PLANO-CONVEX LENS

The banded optical efficiencies of the nominal material, whole cell averaged, top cell banded, middle cell banded and bottom cell banded calculations are: 38.1, 38.0, 37.9, 38.1 and 38.3%, respectively. Which amounts to a maximal absolute optical efficiency variation of approximately 0.4% and a maximal relative optical efficiency variation of around 1%. The efficiencies here are very similar (the same to the nearest 0.1%) to those found in the point source Sun trace. The resultant distribution, however, is notably different. The peak irradiance value is less than in the pillbox trace and the spread is greater. Intensity values away from the profile centre are greater in the pillbox Sun trace than those in the point source Sun trace. Thus, the profile homogeneity is greater in the pillbox trace but the power losses due to deviation restriction (or solar cell size) are greater.

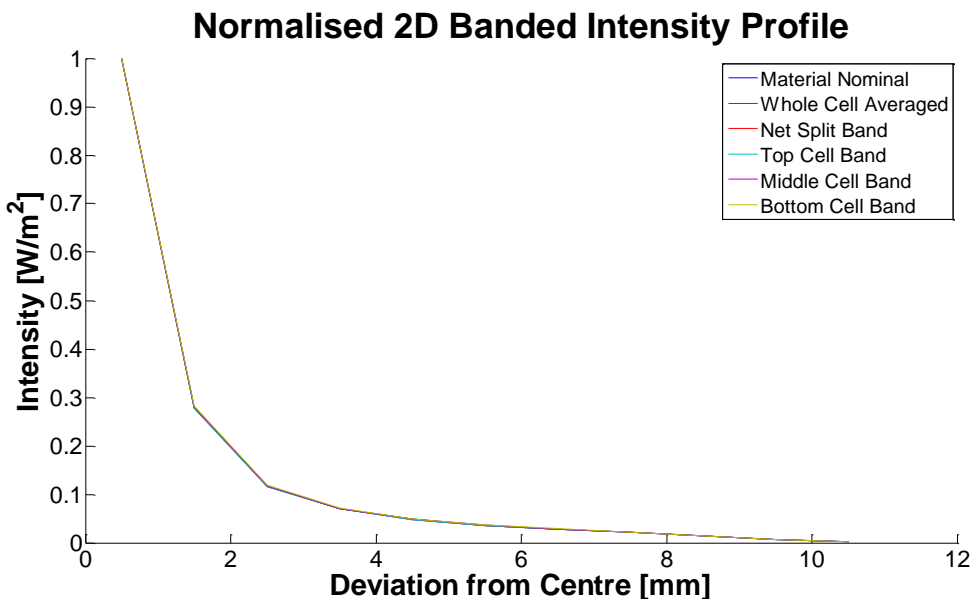


FIGURE 3.82: NORMALISED 2D BANDED INTENSITY ILLUMINATION PROFILE PILLBOX SOURCE TRACE FOR A PLANO-CONVEX LENS

The normalised banded intensity profiles shown in Figure 3.82 show very little variation. The chromatic aberration effects of this trace are therefore negligible.

### 3 Facet Fresnel Lens

The Fresnel lens simulated here is a PMMA Fresnel lens with 3 facets. See section 3.2.4, ‘CPV Material Properties Overview’ for the banded material property data. The illumination profile here is calculated at the reference focal plane that is determined from the lensmaker’s equation using the nominal refractive index of PMMA (the 589nm reference) which is approximately 1.470. All profiles are shown as traced to this plane.

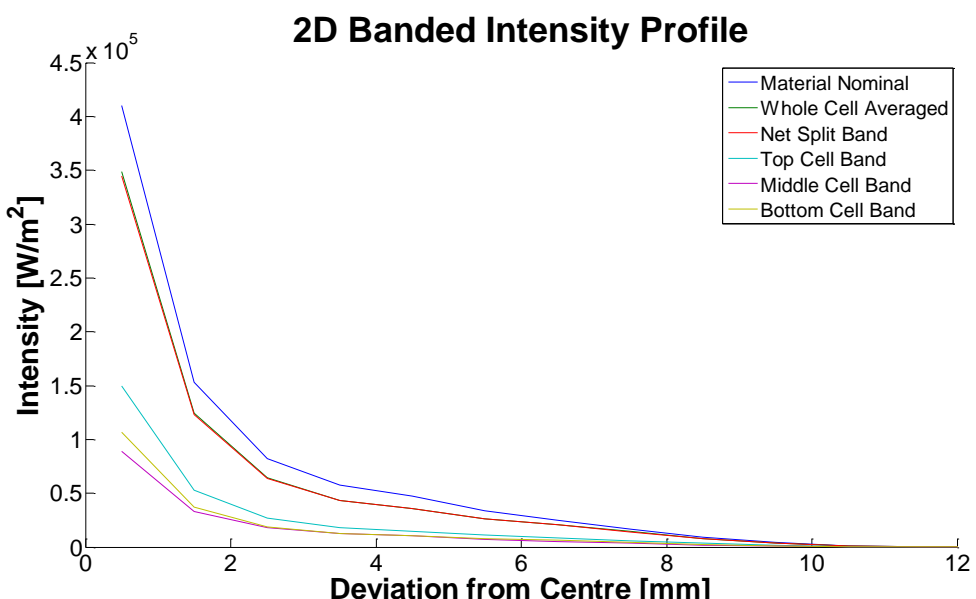


FIGURE 3.83: 2D BANDED INTENSITY ILLUMINATION PROFILE PILLBOX SOURCE TRACE FOR A THREE-FACET FRESNEL LENS

The banded optical efficiencies of the nominal material, whole cell averaged, top cell banded, middle cell banded and bottom cell banded calculations are: 37.2, 31.4, 29.6, 37.4 and 28.7%, respectively. Which amounts to a maximal absolute optical efficiency variation of approximately 8.7% and a maximal relative optical efficiency variation of around 30%. The efficiencies here are very similar (the same to the nearest 0.1%) to those found in the point source trace. The resultant distribution, however, is notably different. The peak irradiance value is far less than that in the pillbox trace and the spread is greater. Intensity values away from the profile centre are greater in the pillbox Sun trace than those in the point source Sun trace. Thus, the profile homogeneity is greater in the pillbox trace but the power losses due to deviation restriction (or solar cell size) are greater.

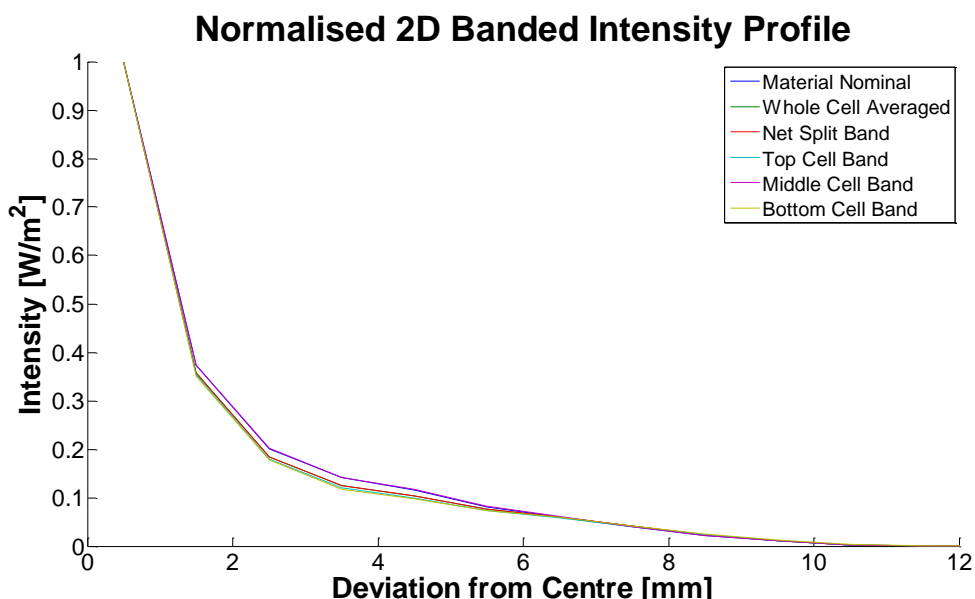


FIGURE 3.84: NORMALISED 2D BANDED INTENSITY ILLUMINATION PROFILE PILLBOX SOURCE TRACE FOR A THREE-FACET FRESNEL LENS

Figure 3.84 shows significant variations in the normalised 2D banded intensities profiles as traced through the Fresnel lens from the pillbox source. These variations are a direct consequence of chromatic aberration. The main driver for these variations is the significant variation of the absorptivity of PMMA over the useful spectrum. This variation results in spectrally dependent inhomogeneities. The variation is greater here than in the point source evaluation due to the angular dependence of the phenomenon.

## 20 Facet Fresnel Lens

The Fresnel lens simulated here is a PMMA Fresnel lens with 20 facets. See section 3.2.4, 'CPV Material Properties Overview' for the banded material property data. The illumination profile here is calculated at the reference focal plane that is determined from the lensmaker's equation using the nominal

refractive index of PMMA (the 589nm reference) which is approximately 1.470. All profiles are shown as traced to this plane.

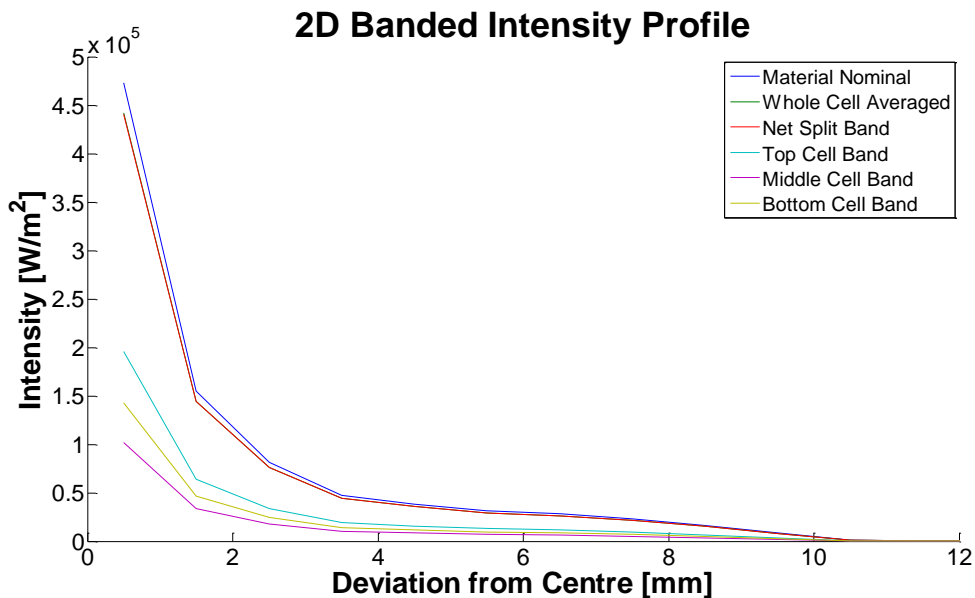


FIGURE 3.85: 2D BANDED INTENSITY ILLUMINATION PROFILE PILLBOX SOURCE TRACE FOR A TWENTY-FACET FRESNEL LENS

The banded optical efficiencies of the nominal material, whole cell averaged, top cell banded, middle cell banded and bottom cell banded calculations are: 40.9, 39.8, 39.2, 41.1 and 39.5%, respectively. Which amounts to a maximal absolute optical efficiency variation of approximately 1.9% and a maximal relative optical efficiency variation of around 5%.

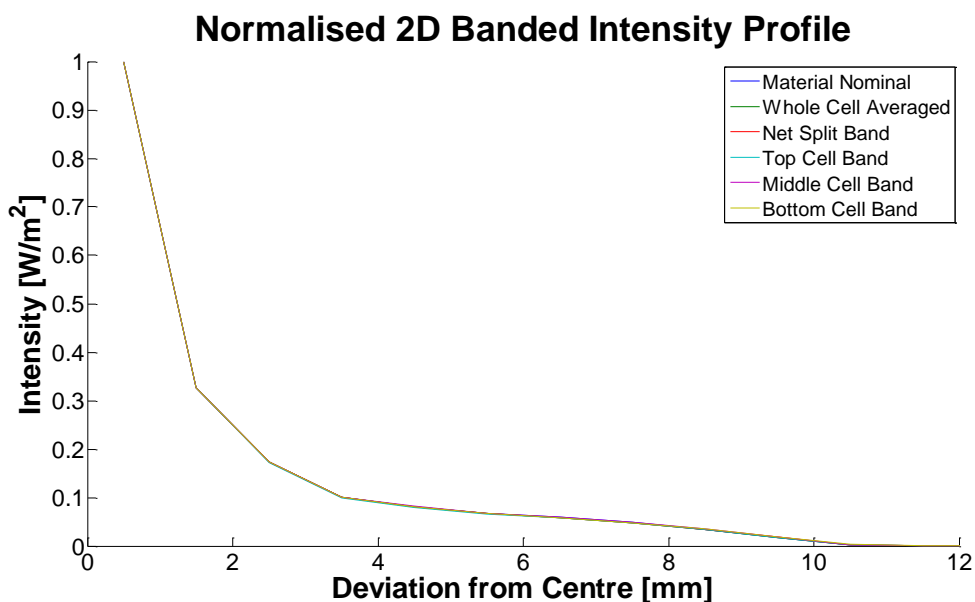


FIGURE 3.86: NORMALISED 2D BANDED INTENSITY ILLUMINATION PROFILE PILLBOX SOURCE TRACE FOR A TWENTY-FACET FRESNEL LENS

The normalised banded intensity profiles shown in Figure 3.86 show very little variation. The chromatic aberration effects of this trace are therefore negligible.

### 3.6.3.3. Extended Light Source Sun Traces

The extended light source Sun traces here use an example CSR of 0.27.

#### Plano-Convex Lens

The plano-convex lens simulated here is a soda-lime glass plano-convex lens. See section 3.2.4, ‘CPV Material Properties Overview’ for the banded material property data. The illumination profile here is calculated at the reference focal plane that is determined from the lensmaker’s equation using the nominal refractive index of soda-lime glass (the 589nm reference) which is approximately 1.562. All profiles are shown as traced to this plane.

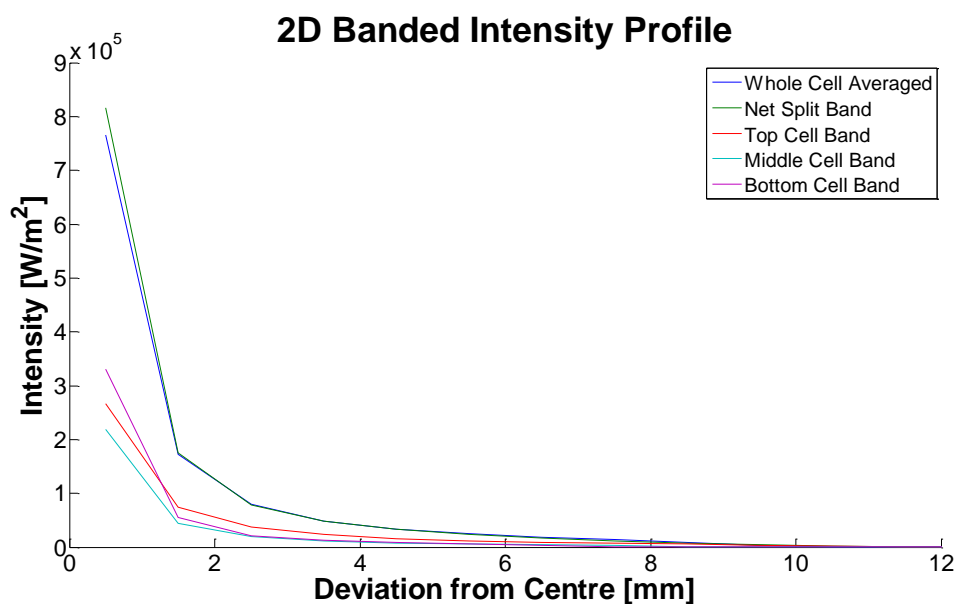


FIGURE 3.87: 2D BANDED INTENSITY ILLUMINATION PROFILE EXTENDED LIGHT SOURCE TRACE FOR A PLANO-CONVEX LENS

The banded optical efficiencies of the nominal material, whole cell averaged, top cell banded, middle cell banded, bottom cell banded and net cell banded calculations are: 38.1, 38.0, 38.0, 38.1, 38.2 and 38.0%, respectively. Which amounts to a maximal absolute optical efficiency variation of approximately 0.2% and a maximal relative optical efficiency variation of around 1%. The efficiencies here are similar to those found in the point source and pillbox Sun traces, though absolute variations of approximately 0.1% are found. The resultant distribution, however, is notably different. The peak irradiance value is less here than in the point source Sun trace and greater than in the pillbox Sun trace. The spread is greater here than in both. Overall, the profile homogeneity is greater here than in the pillbox and point source traces but the power losses due to deviation restriction (or solar cell size) are greater. Moreover, a difference can now be seen between the whole cell averaged and net split spectral band profiles that compounds the importance of spectral resolution in CPV optical modelling.

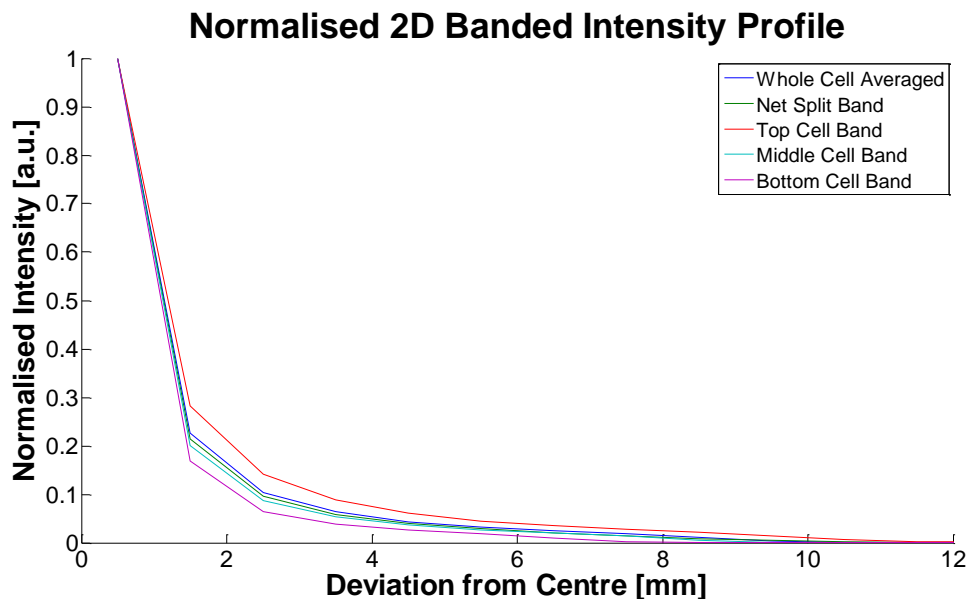


FIGURE 3.88: NORMALISED 2D BANDED INTENSITY ILLUMINATION PROFILE EXTENDED LIGHT SOURCE TRACE FOR A PLANO-CONVEX LENS

The normalised banded intensity profiles shown in Figure 3.88 show significant variation. The chromatic aberration effects of this trace are therefore non-negligible and worthy of consideration in CPV optical system modelling. These variations are not accounted for in the point source or pillbox Sun traces.

### 3 Facet Fresnel Lens

The Fresnel lens simulated here is a PMMA Fresnel lens with 3 facets. See section 3.2.4, ‘CPV Material Properties Overview’ for the banded material property data. The illumination profile here is calculated at the reference focal plane that is determined from the lensmaker’s equation using the nominal refractive index of PMMA (the 589nm reference) which is approximately 1.470. All profiles are shown as traced to this plane.

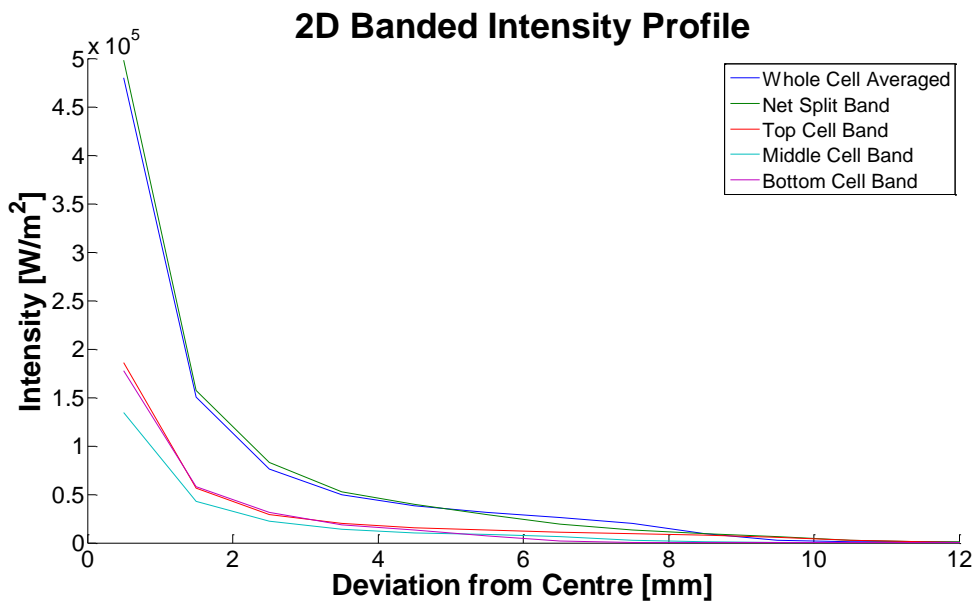


FIGURE 3.89: 2D BANDED INTENSITY ILLUMINATION PROFILE EXTENDED LIGHT SOURCE TRACE FOR A THREE-FACET FRESNEL LENS

The banded optical efficiencies of the nominal material, whole cell averaged, top cell banded, middle cell banded, bottom cell banded and net cell banded calculations are: 37.2, 31.4, 29.7, 37.4, 28.6 and 31.2%, respectively. Which amounts to a maximal absolute optical efficiency variation of approximately 8.8% and a maximal relative optical efficiency variation of around 30%. The efficiencies here are similar to those found in the point source and pillbox Sun traces, though absolute variations of approximately 0.1% are found. The resultant distribution, however, is notably different. The peak irradiance value is less here than in the point source Sun trace and greater than in the pillbox Sun trace. The spread is greater here than in both. Overall, the profile homogeneity is greater here than in the pillbox and point source traces but the power losses due to deviation restriction (or solar cell size) are greater. Moreover, a difference can now be seen between the whole cell averaged and net split band profiles that compounds the importance of spectral resolution in CPV optical modelling.

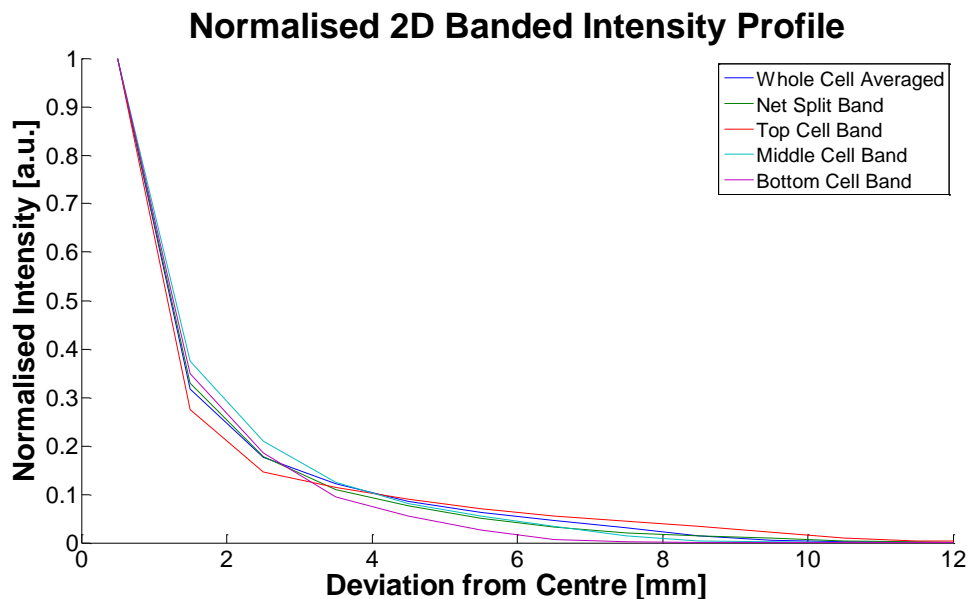


FIGURE 3.90: NORMALISED 2D BANDED INTENSITY ILLUMINATION PROFILE EXTENDED LIGHT SOURCE TRACE FOR A THREE-FACET FRESNEL LENS

The normalised banded intensity profiles shown in Figure 3.90 show significant variation. The chromatic aberration effects of this trace are therefore non-negligible and worthy of consideration in CPV optical system modelling. These variations are not accounted for in the point source or pillbox Sun traces.

#### 20 Facet Fresnel Lens

The Fresnel lens simulated here is a PMMA Fresnel lens with 20 facets. See section 3.2.4, ‘CPV Material Properties Overview’ for the banded material property data. The illumination profile here is calculated at the reference focal plane that is determined from the lensmaker’s equation using the nominal refractive index of PMMA (the 589nm reference) which is approximately 1.470. All profiles are shown as traced to this plane.

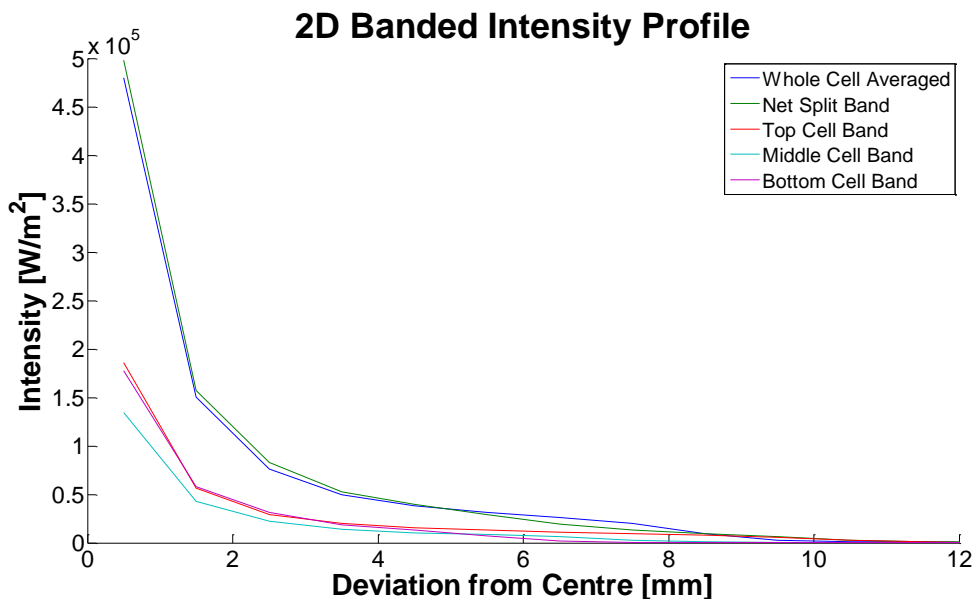


FIGURE 3.91: 2D BANDED INTENSITY ILLUMINATION PROFILE EXTENDED LIGHT SOURCE TRACE FOR A TWENTY-FACET FRESNEL LENS

The banded optical efficiencies of the nominal material, whole cell averaged, top cell banded, middle cell banded and bottom cell banded calculations are: 40.9, 39.9, 39.3, 41.1, 39.4 and 39.7%, respectively. Which amounts to a maximal absolute optical efficiency variation of approximately 1.8% and a maximal relative optical efficiency variation of around 5%. The efficiencies here are similar to those found in the point source and pillbox Sun traces, though absolute variations of approximately 0.1% are found. The resultant distribution, however, is notably different. The peak irradiance value is less here than in the point source Sun trace and greater than in the pillbox Sun trace. The spread is greater here than in both. Moreover, a difference can now be seen between the whole cell averaged and net split band profiles that compounds the importance of spectral resolution in CPV optical modelling. Furthermore, the variation in normalised profile is particularly significant in this trace.

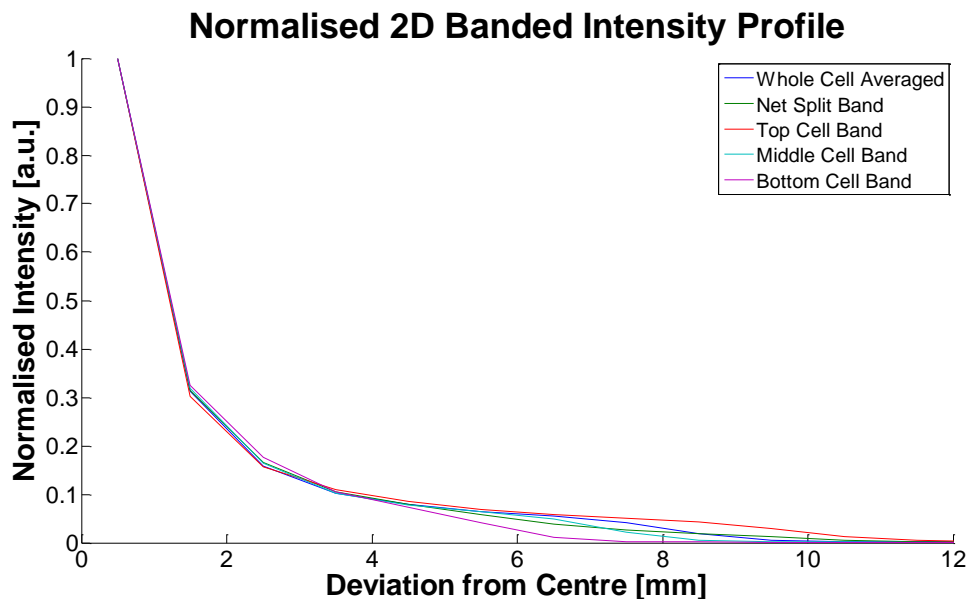


FIGURE 3.92: NORMALISED 2D BANDED INTENSITY ILLUMINATION PROFILE EXTENDED LIGHT SOURCE TRACE FOR A TWENTY-FACET FRESNEL LENS

The active cell junction apportioned absolute and normalised intensity profiles for the extended light source Sun are clearly significantly different than those generated by the pillbox and point source Sun traces. In particular, as evidenced by the normalised profiles, the spread of irradiation is much different in each of the active cell bands. Thus, differences in irradiation inhomogeneities are identified by this technique and ignored elsewhere.

A Fresnel lens with a low number of facets shows significant normalised intensity variations over the full spread of the image. The near centre variations in these lenses result from path length variations and the associated variations in absorption losses. The variations in intensity further from the centre can be attributed to reflections off the inner facet walls, which are typically more numerous in the circumsolar region than the central solar region. As the number of facets in the Fresnel lens is increased, the near centre variations reduce because of the reduction in lens thickness whereas the variations further from the centre increase due to an increase in facet wall reflections.

#### 3.6.4. 3D Modelling Illumination Profiles

2D traces, such as those presented above, are limited in that the investigation of tracking and misalignment errors are confined to a single dimension. For more informative ray trace information, specifically non-ideal tracking traces and component placement errors, 3D tracing must be used. Example 3D traces from the above model (see section 3.5, ‘Modelling’) are given below.

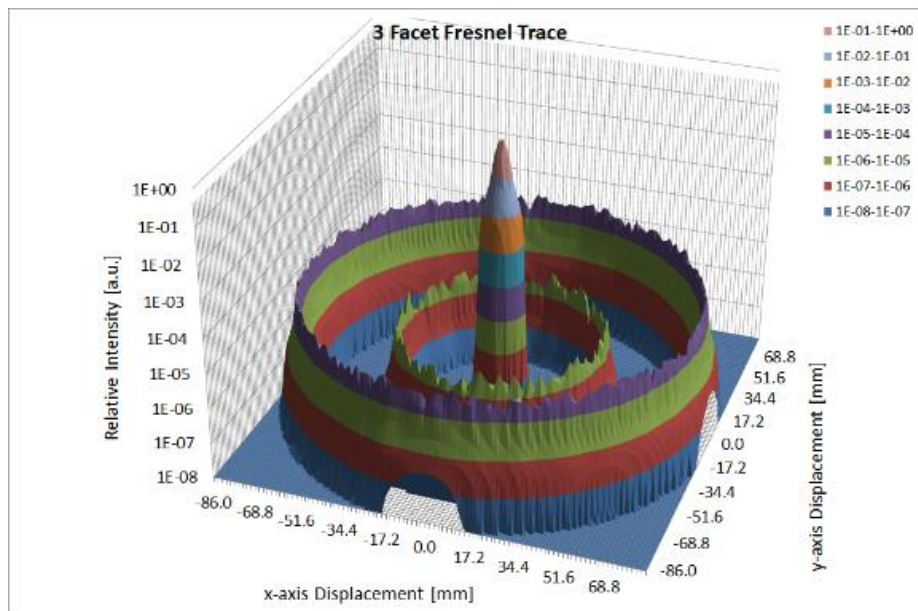


FIGURE 3.93: 3 FACET FRESNEL LENS RAY TRACED PLANE-RESTRICTED SURFACE ILLUMINATION PROFILE

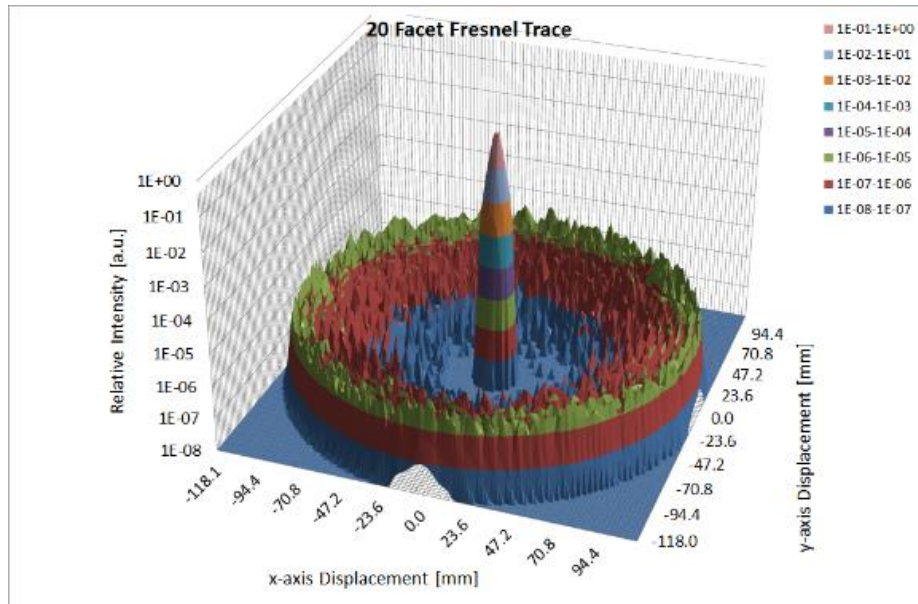


FIGURE 3.94: 20 FACET FRESNEL LENS RAY TRACED PLANE-RESTRICTED SURFACE ILLUMINATION PROFILE

Figure 3.93 and Figure 3.94 show the illumination profile found at the focal plane of an example 3 facet Fresnel lens and 20 facet Fresnel lens, respectively. In both these traces illumination rings can be seen around the central profile. These rings result from reflections off inner facet walls. The number of rings here is one less than the number of Fresnel facets, 2 in Figure 3.93 and 19 in Figure 3.94. This is an artefact of the lens structure. It can also be seen that the intensity of the outer rings is greater than that of the inner rings. This is another artefact of the lens structure – that the height of the facet walls increases with distance from the lens centre. Should the simulation here have been run at a higher resolution, the rings in Figure 3.94 would be more visibly explicit.

### 3.7. Conclusions

A ray trace method has been developed and used to investigate example plano-convex and Fresnel lenses under the illumination of the various solar insolation models described in chapter 2, ‘Input’. For the effective spectral analysis of system components, common CPV optical component materials for the plano-convex and Fresnel lenses have been analysed. The optical properties of these components have been measured and a spectral weighting method applied for the banding of optical properties. As it is computationally expensive to perform simulations with both high spatial and spectral resolutions, the spectral banding method offers an elegant resolution reduction by averaging. It is suggested that the number of spectral bands used in simulation correspond to at least the number of junctions in the MJSC receiver. A triple junction example has been used here. Variations the optical components over these bands are found to be significant.

Optical analyses have been performed in spectral bands using weighted averaged material parameters. The examples presented herein partition the solar spectrum in 5 bands for comparison: 280-4000, 280-1880, 280-680, 680-880 and 880-1880. These bandings represent: the full solar spectrum, the whole triple junction solar cell active range, the triple junction top cell active range, the triple junction middle cell active range and the triple junction bottom cell active range, respectively. Spectrally banded optical analyses corresponding to these ranges show significant dependencies on air mass and CSR. The nature of these dependencies changes with each spectral band. These variations are significant. Banded beam proportion contributions can change by as much as 10% in absolute terms within the air mass range of 1 to 3. The importance of the inclusion such spectral variations in CPV system simulation has thus been further highlighted.

Two-dimensional ray trace investigations have been used to investigate the differences in illumination profile results for 3 specific lenses: a plano-convex lens, a 3 facet Fresnel lens and a 20 facet Fresnel lens. In the net power only analysis, the illumination profile variations seem simple: the greater the number of facets the greater the homogeneity and the wider the spread. The spectrally dependent variations, however, show a more complex picture. The plano-convex lens trace shows next to no variations in spectrally banded normalised intensity profiles for the point source and pillbox Sun traces. Small variations in the spectrally banded normalised intensity profiles for the Fresnel lenses are found, these result both from the large spectrally dependent variation of the absorption coefficient of PMMA and reflections off inner facet Fresnel walls. For the extended light source Sun traces, though, relatively large variations in the spectrally banded normalised intensity profiles for the plano-convex and Fresnel lenses are found. These result primarily from the circumsolar contribution, particularly the uneven spectrally banded distribution of the circumsolar irradiation. The Fresnel lens traces in

particular show an interesting phenomenon. The spectrally banded normalised intensity profiles are obviously different for the 3 facet and 20 facet Fresnel examples. Namely, this difference is that the near central illumination profile is more homogeneous in the higher faceted lens while the near edge illumination profile is less homogeneous. This is a direct consequence of the Fresnel structure. The higher faceted Fresnel lenses have the effect of homogenising the lens thickness – the greater the number of facets, the smaller the average thickness and the smaller the variation – thus absorption in the higher faceted lenses is reduced whilst image spread is increased due to inner facet reflections. The inner facet reflected rays have greater chromatic aberrations due to the increased material traversal in boundary interactions. In short, solar source description can have a significant impact on illumination profile, especially with respect to spectrally variant phenomena.

Three-dimensional ray trace simulations have also been used to investigate illumination profile variation with optical system specification. Example 3 facet and 20 facet Fresnel lens ray trace simulations have been presented. Illumination rings can be seen around the central profile in these traces. These rings result from reflections off inner facet walls. The number of rings is one less than the number of Fresnel facets. This is an artefact of the lens structure. It can also be seen that the intensity of the outer rings is greater than that of the inner rings. This is another artefact of the lens structure, deriving from the increase in height of the facet walls with distance from the lens centre.

In general, this chapter has further compounded the argument for the need for spatially and spectrally resolved insolation models as presented in chapter 2, ‘Input’. The use of spectrally banded optical analyses corresponding to the MJSC active junction ranges proved fruitful, as chromatic aberrations specific to each junction range were identified. These junction specific aberrations introduce differing inhomogeneities at each subcell and thus are a necessary consideration in CPV given the detrimental effects of subcell mismatch in MJSC performance.

# 4. Uncertainty

*the Realm of the Unknown*

## 4.1. Introduction

It is the role of Physics to describe the infinite in terms of the finite. This is achieved by constraining physical laws to closed systems bound by underlying assumptions that define the context of their predictions. Thus no system prediction is perfect and any real prediction has an associated uncertainty.

A predicted output is then a function of input with some associated uncertainty, this is often quoted in the form of:

$$O = f(I) \pm \Delta$$

EQUATION 4.1

*Where  $O$  is predicted output,  $I$  input and  $\Delta$  a measure of uncertainty*

In the technology industries, the term uncertainty most often pertains to technological performance and is commonly subdivided into two categories: measurement uncertainty and prediction uncertainty. Measurement uncertainty is often a direct consequence of the imperfections of measurement equipment an example of this is the classic 30cm ruler. It is difficult to be more accurate than estimation to the nearest mm when measuring with the 30cm ruler. Thus a length measurement made using this equipment may be quoted with uncertainty as:  $X \pm 0.5mm$ . Prediction uncertainties result from the uncertainties of both the input parameters to the prediction function and the uncertainties associated with the prediction function itself.

The last century has seen a dramatic rise in the use and development of technology and an associated increase in technological system complexities. Discussions of uncertainty and prediction in the published literature have risen alongside this.

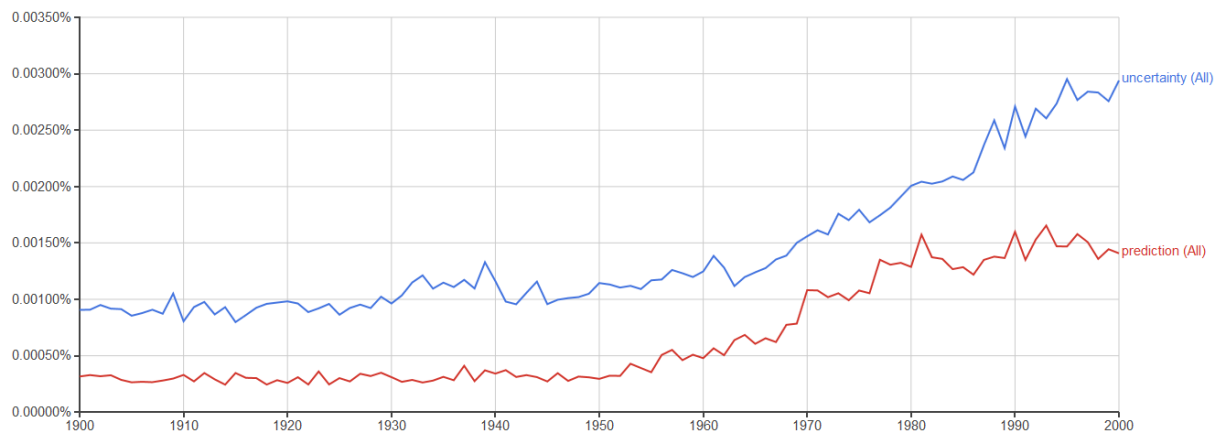


FIGURE 4.1: GOOGLE BOOKS NGRAM VIEWER SHOWING THE INCREASE OF UNCERTAINTY AND PREDICTION DISCUSSION IN THE TWENTIETH CENTURY FROM THE BRITISH ENGLISH CORPUS

This chapter serves as an investigation of uncertainty in the context of CPV and examines the associated ramifications of these uncertainties through the CPV system.

#### 4.1.1. Production Uncertainties

Production uncertainties are effectively those uncertainties in production that derive from measurement uncertainty. When manufacturing components, an ideal design is set as the base of construction and an attempt at making the ideal component is made. In reality the ideal component is never achieved and resultant components are accepted or rejected based on accepted limits of tolerance. Tolerance limits are an accepted compromise between the desired, ideal, product and the resultant product. The compromise is itself the result of an often complex relationship between system requirements, manufacturing method and cost.

The CPV system is a complex design of multiple interacting parts. There are several components for which production tolerances can have an effect on system yields. The typical CPV system is shown schematically in Figure 4.2.

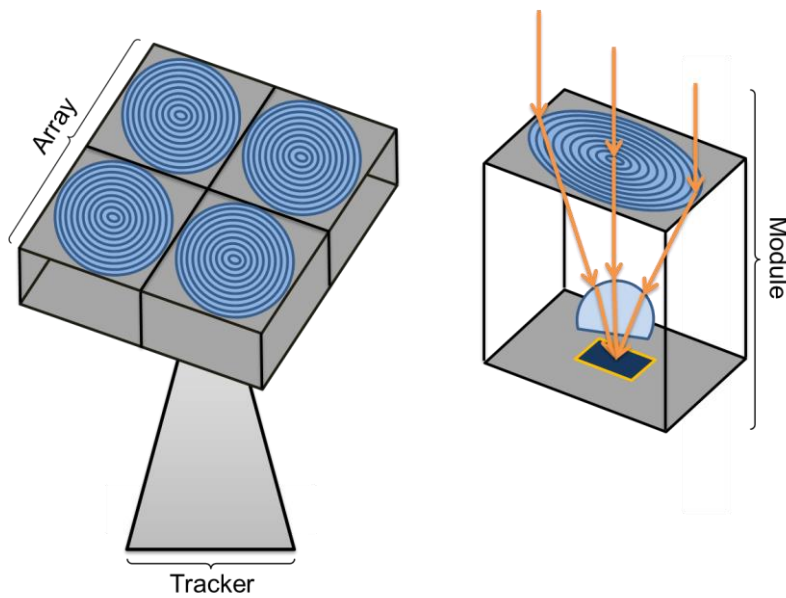


FIGURE 4.2: CPV SYSTEM SCHEMATIC

The typical CPV system consists of a high efficiency, multi-junction solar cell mounted in a module frame beneath an optical concentration system. The optical concentration system typically consists of both primary and secondary optical concentration stages that are also mounted to the module frame. The assembled modules are then placed in an array frame which is situated atop a solar tracking system. The production tolerances of all these parts play a role in CPV system performance and prediction uncertainties. Those discussed here are lens parameters and frames.

#### 4.1.1.1. Lenses

The optics industry, as many industries, uses graded standards of production tolerance such as: commercial, precision and high precision. Due to the very argument for its economic viability, the CPV industry is financially restricted in terms of investment in optical systems. The optical systems of CPV are used to offset the material cost of high efficiency solar cells by the concentration of sunlight. As, such the economic argument for CPV systems determines that low-cost, commercial grade optics be used in these systems. The reduction of tolerance and cost of product are exponentially related.

#### Parameter Variation

It is important to identify key parameters of a product for tolerance levels. The typical CPV module, as shown in Figure 4.2, comprises a frame in which a primary concentration device, a secondary concentration device and a solar cell are mounted relative to each other. The lenses themselves are designed using mathematical principles and formulae that describe a perfect shape. System simulations are most often performed using these perfect mathematical models of these lenses. The actual lenses used in the real in-field systems are bound to forms governed by a combination of the

mathematical design principles and the production uncertainties. The inaccuracies in the production of these lenses will then have an effect of deviating the actual system performance from the simulated, idealised system performance.

Typical commercial grade production uncertainties associated with key plano-convex lens parameters[82, 83] are given in Table 4.1.

TABLE 4.1: COMMERCIAL GRADE PLANO-CONVEX LENS PARAMETER UNCERTAINTIES

Parameter	Typical Tolerances
Diameter	$\pm 0.1\text{mm}$
Central Thickness	$\pm 0.2\text{mm}$
Focal Length	$\pm 4\%$
Surface Quality	60-40 (scratch-dig)

The industry standard definition of surface quality is the ‘scratch-dig’ specification. A scratch is defined as any mark or surface tear whereas a dig is surface rough spot such as a pit or a bubble. These defect sizes are most often measured by an optical comparator. The first number of the scratch dig specification indicates the maximum scratch length in microns. The second number in the scratch dig specification indicates the maximum dig diameter in tens of microns. There are a variety of surface standards for optical elements[84, 85], these are beyond the scope of this document but ought to be noted as they govern the uncertainties associated with the lenses available for CPV optical systems.

Fresnel lens tolerance information is much more difficult to find. Diameter variations of  $\pm 0.2\text{mm}$  are commonplace and focal length variations are found typically as  $\pm 1\%$ . Surface errors in the Fresnel lens are limited by the manufacturing technique, injection moulding. The limiting factors in this technique are the mould accuracy and the material annealing process. The resultant errors are assumed to be in the nanometre to micrometre range and thus are not investigable by ray tracing means.

Given that the model presented in 3.5, ‘Modelling’ uses real physical values as an input, the virtual parameter tolerances such as focal length variations will be ignored here. Main focus will be given to physical tolerance parameters, namely: diameter, thickness and surface quality.

### Deformation

A further point of significance for the Fresnel lens uncertainties is deformation. Fresnel lens deformation occurs in both the short and long terms. Long term Fresnel lens deformation occurs mostly in the form of drooping in the unsupported lens area. Short term deformations however are dynamic deformations that result predominantly from thermal expansions within the lens structure. Both PMMA and silicone-on-glass (SOG) lenses have been shown to reduce in optical efficiency typically by around 1-2% at various terrestrial locations as a result of thermal effects[86]. The study showed that SOG glass generally suffers greater efficiency reductions.

The optical efficiency variations with temperature are related to a combination of the temperature dependence of refractive index[87, 88] and the effects of the varying magnitudes of thermal expansion coefficients for the lens materials, particularly within the SOG Fresnel lenses[89, 90]. Fresnel lens designs to mitigate these effects have been proposed[91, 92] but are not commonplace in the industry.

#### 4.1.1.2. System Frames

Frames play a large part in the accuracy of component mounting. Within CPV systems the major framing components are the array and module frames.

##### The Array Frame

The array frame is the CPV system component that is directly mounted to the solar tracker. The array frame houses the CPV modules. The number of modules in the array and the array size vary dramatically over the wide scope of system designs. The frame material is typically aluminium. Typical CPV module density is approximately  $25\text{kg/m}^2$ .

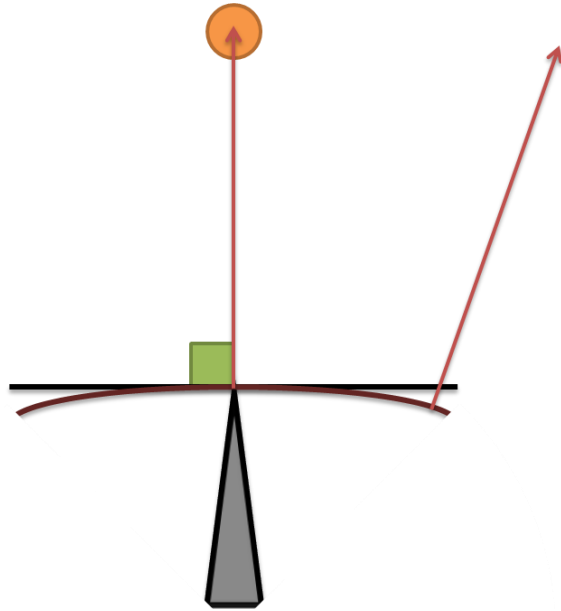


FIGURE 4.3: ARRAY FLEX UNDER MATERIAL LOAD SCHEMATIC

Particularly large frames inevitably suffer from flexing. Flexing is typically the result of load deflections. Load deflections result from pivoting, mounted load (gravitational bending) and wind loading. Array frame flexing is depicted in Figure 4.3 and can be analysed as cantilevered beam deflection which is governed by 3<sup>rd</sup> and 4<sup>th</sup> order differential equations according to:

$$\Delta y = -\frac{Wx^2}{24EI} (6l^2 - 4lx + x^2)$$

EQUATION 4.2

$$\Delta \theta = -\frac{Wx}{6EI} (3l^2 - 3lx + x^2)$$

EQUATION 4.3

Where  $\Delta y$  is the beam deflection in the y-axis,  $\Delta \theta$  is the angular beam deflection from normal,  $W$  the total load on the beam in Newtons,  $E$  the modulus of elasticity,  $I$  the moment of inertia,  $l$  the length of the beam and  $x$  the deviation from the pivot point

The maximum deflections are then derived as:

$$\Delta y_{max} = \frac{Wl^4}{8EI}$$

EQUATION 4.4

$$\Delta \theta_{max} = \frac{Wl^3}{6EI}$$

EQUATION 4.5

The moment of inertia for a beam is defined as:

$$I = \frac{lh^3}{12}$$

EQUATION 4.6

Where  $I$  is the moment of inertia of the beam and  $h$  the beam height which is the beam dimension along the axis of deflection

The modulus of elasticity for aluminium is approximately 70GPa, this compares with approximately 200GPa for steel. Example deflections across a 2m by 0.1m beam of aluminium with a load force of 2kN are shown in Figure 4.4.

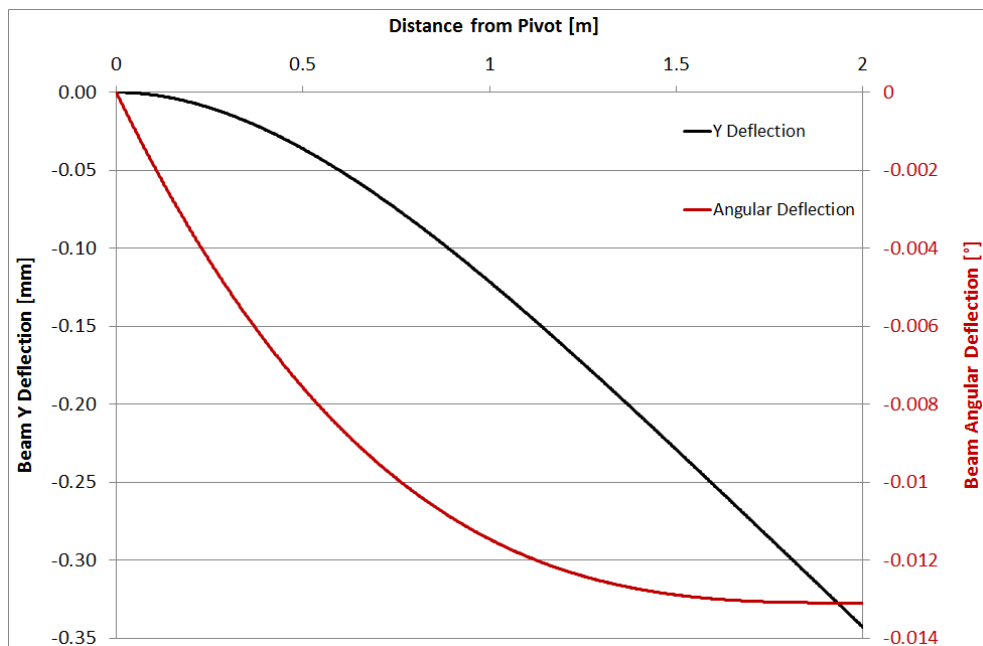


FIGURE 4.4: EXAMPLE ALUMINIUM BEAM DEFLECTIONS

The example aluminium beam deflections in Figure 4.4 show a maximum nominal load angular deflection of approximately 0.013°. This will vary with dynamic load variation from wind forces.

As an approximation, wind force can be calculated from the drag equation of fluid dynamics according to:

$$F_D = \rho v^2 C_D A$$

EQUATION 4.7

Where  $F_D$  is drag force,  $\rho$  is the mass density of the fluid,  $v$  the speed of the object through the liquid,  $C_D$  the drag coefficient of the object and  $A$  the area of the object as projected perpendicular to the direction of travel

An approximation to the drag force on a CPV array is provided here using Equation 4.7. A cuboidal array of dimensions 3m by 3m by 0.1m was used as an example. The drag coefficient was set to 1,

which is the approximate drag coefficient for a cuboid. The mass density of air varies with temperature. The value of 1.2, corresponding to an air temperature of 20°C, was used here. Figure 4.5 shows the relationship of the drag force on the array with wind speed and angle to the wind from normal. The area was calculated as the orthogonal projection of the array cuboid perpendicular to the wind direction.

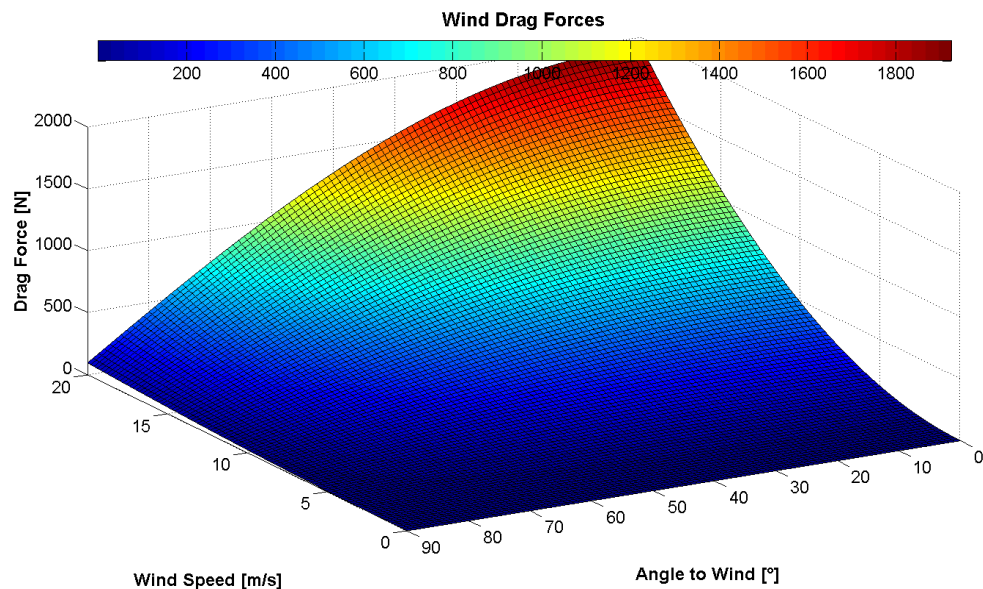


FIGURE 4.5: EXAMPLE WIND DRAG FORCES ON CPV ARRAY AS CALCULATED BY THE DRAG EQUATION

Figure 4.5 shows the variation of drag force with wind speed and direction for wind speeds up to 20m/s. Maximal loads for the example are found as approximately 2kN. This is at the wind speed of 20m/s which is described on the Beaufort scale as '8 – Gale' and is associated with a double red warning flag. Wind speeds of 13.8m/s however are described as '6 – Strong Breeze' and are not uncommon in normal operating conditions.

The above example serves well as a demonstration of the load force effects of wind. However, wind loading is a complicated science. There are a variety of methods for calculating wind loading. An alternative example is the American Society of Civil Engineers standard, ASCE 7[93] , which offers the following equation:

$$q = 0.00256K_zK_{zt}K_dV^2$$

EQUATION 4.8

Where  $q$  denotes the effective velocity pressure,  $K_z$  the exposure velocity pressure coefficient – a reflection of wind speed variation with height and terrain roughness,  $K_{zt}$  the topographic factor accounting for wind speed variation with hills and valleys,  $K_d$  the directionality factor and  $V$  the basic wind speed referenced at 33ft above ground

Reference tables are offered for the appropriate determination of these coefficients. This is one current standard for the determination of appropriate reinforcement requirements for free-standing structures.

Whatever the mechanism, array frame flexing causes distributed optical misalignments within the module housing units. Thus, in the context of optical system performance uncertainties, array frame flexing can be considered equivalent to distributed solar tracking error. In the ideal tracking case, the pivotal point of the array fame will be in optical normality with the solar centre. Material flexing over the frame area results in inherent pointing errors for individual modules. These distributed misalignments can be calculated from Equation 4.3.

### The Module Frame

The module frame acts as a component housing unit for the optical concentration and energy conversion components of the CPV system. Errors in frame build thus result in optical misalignments. These misalignments can be analysed by 2-dimensional ray tracing if they occur only in 1 dimension. For example, if all alignment errors occur in the x-y plane where the x-y plane is the plane in which elevation rotation occurs, the effects of the component misalignment and elevation tracking error may be investigated in 2D. In reality though, these errors are 3-dimensional and 3D ray tracing is required to correctly assess their effects.

The alignment of the module housed components relative to one another is key for system performance. The design specification of a CPV system stipulates component positioning such that, when the module housed components are correctly internally aligned and the module itself is correctly aligned with the Sun, the solar cell at the base of the module is illuminated with the intensity peak of an illumination profile at its centre. Misalignments of the components shift the illumination profile over the receiver. As well as efficiency reduction by reflection, asymmetric receiver illumination reduces the thermal management capabilities of the system.

Typical commercial extruded aluminium component tolerances are given in Table 4.2

TABLE 4.2: COMMERCIAL GRADE EXTRUDED ALUMINIUM TYPICAL TOLERANCES

Parameter	Typical Tolerances
Angles	$\pm 2^\circ$
Straightness	$\pm 0.3\text{mm per foot}$ ( $\sim 0.1\%$ )
Twist	$\pm 0.5^\circ$ per foot

---

<b>Length</b>	$\pm 1.5\text{mm}$
---------------	--------------------

---

The effective context of these production tolerances changes with module housing design. Although module frame designs vary from system to system, the basic form is similar – a box with a solar cell at the base and a lens at the top, supported by the box walls. An example module model is given in Figure 4.6.

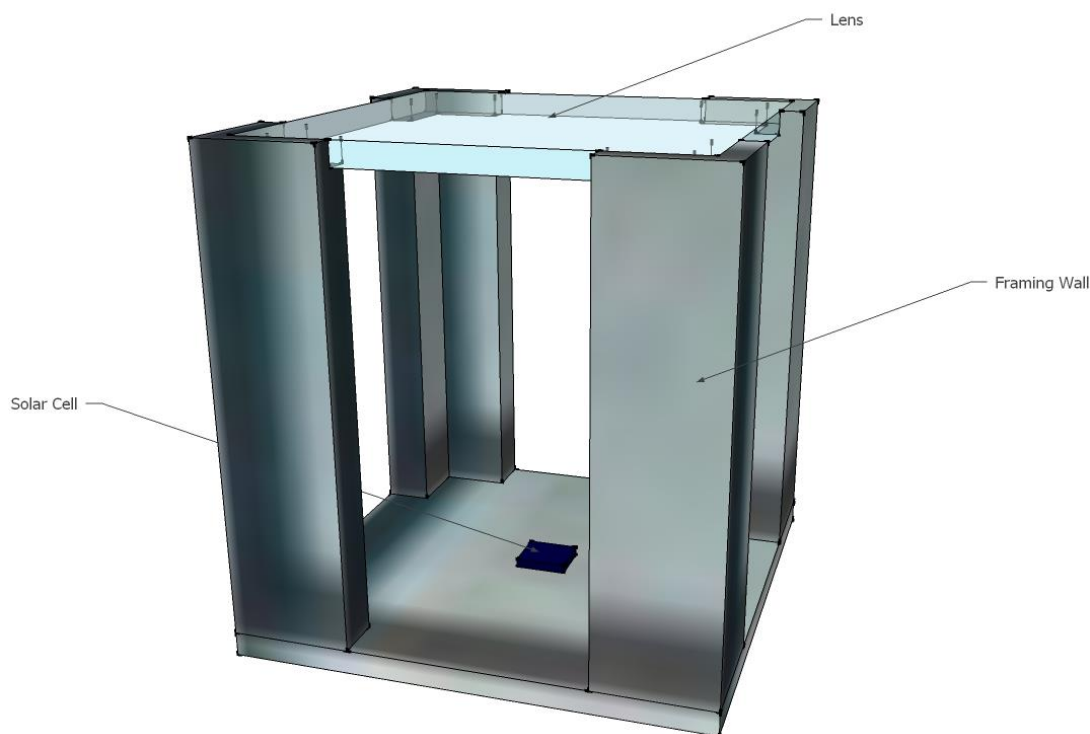


FIGURE 4.6: MODULE FRAME MODEL EXAMPLE

It can be seen from the module model example in Figure 4.6 that frame component tolerances may affect optical alignment and thus system performance. The module frame of Figure 4.6 is provided as an example primarily to investigate issues with the lens mounting structure. In reality there will be more components to the CPV module, such as: a secondary concentration device and a heat sink.

#### 4.1.2. Operational Uncertainties

Operational uncertainties are effectively those uncertainties in operation that derive from prediction uncertainty. The largest prediction uncertainty in any renewable energy technology is almost exclusively environmental or weather forecasting.

Beyond this, operational uncertainties occur in all dynamic components of an energy conversion system. The dynamic components of CPV systems considered here are solar tracking systems and balance of system side components.

#### 4.1.2.1. Sun Tracking

As demonstrated in chapter 2, ‘Input’, solar tracking errors can have a significant effect on system performance. Maintaining optical normality with the Sun can prove difficult, especially for large arrays in areas of high wind.

The earliest reference to solar tracking in photovoltaic related literature appears to be in 1963[94]. In flat-plate PV systems, the use of solar tracking has been shown to improve energy harvests by over 30% and accordingly, for a given energy requirement, reduce the number of required PV modules by 30%[95, 96]. Thus the interest in solar tracking systems for PV energy conversion was heightened. Further to this interest, the calculation of Sun path trajectory has been used to find location dependent optimal orientations and sizing of static PV and solar thermal systems[97-100]. There have been extensive studies of performance comparisons of static, single-axis tracked and dual-axis tracked using both meteorological and in-field performance data[101].

A variety of solar tracking system designs exist. Loosely these designs can be sub divided into two categories: closed-loop and open-loop.

##### Closed-loop Tracking Systems

Closed-loop solar tracking systems employ electrical feedback systems to constantly assess the pointing error with the Sun and provide alignment correction signals to the controllers. Pointing error in such systems is commonly analysed by means of distributed well calibrated reference cells. The system is then considered as perfectly aligned when the sensors return the same output. A difference in sensor outputs results in an alignment correction signal attempting to balance the sensor outputs. An example multi-sensor system is shown schematically in Figure 4.7.

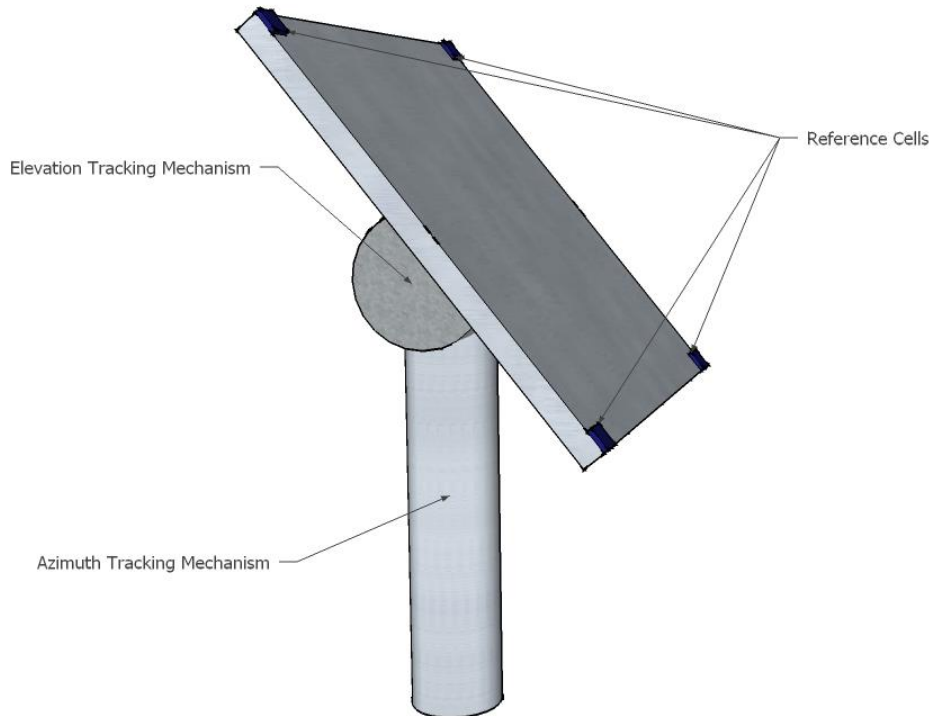


FIGURE 4.7: TRACKER WITH REFERENCE CELL SCHEMATIC

The reference cells of Figure 4.7 provide positional adjustment signals to the azimuth and elevation tracking mechanisms. This is a schematic representation only. In practice reference cells are rarely placed at such extremes, although four cell reference systems do exist[102].

The reference cell pointing adjustment feedback system cannot be the sole driver for solar tracking. The reference cell system alone will search the sky for the brightest spot and then follow the brightest spot through the sky. It may at first seem logical that the brightest spot in the sky is the Sun, but there are many occasions, for example in partial cloud cover, when the brightest part of the sky is elsewhere. Focussing in on the brightest part of the sky may then on occasions be detrimental to system performance. Thus, a combination of algorithmic determination of predicted solar position (often by ephemeris referencing) and reference cell positional correction is used. The combination of these mechanisms is often used by first approximating the Suns location and then restricting the positional correction to an angular range about the approximation, as depicted in Figure 4.8.

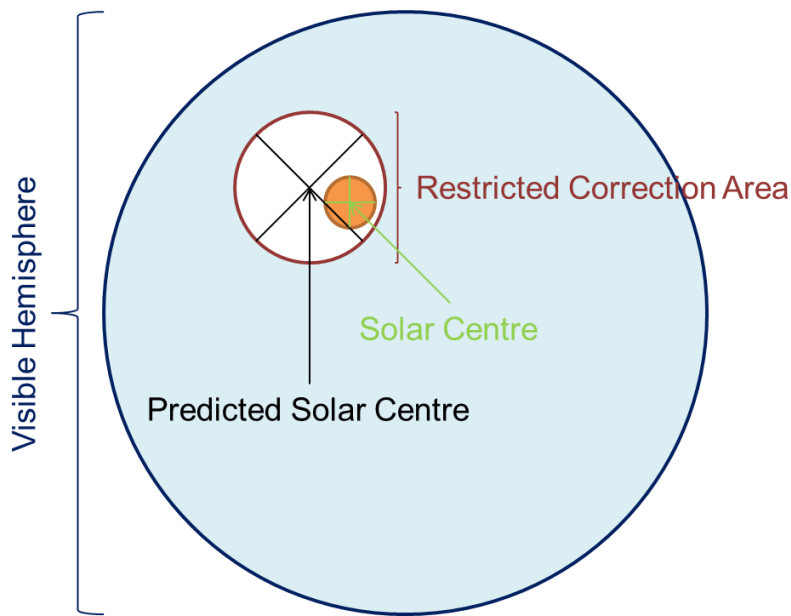


FIGURE 4.8: SOLAR TRACKING RESTRICTED POSITIONAL ADJUSTMENT SCHEMATIC

Figure 4.8 demonstrates the ephemeris base and controller correction method for closed loop solar tracking systems. Examples of the controller corrected tracking as compared to the predicted Sun position only tracking can be found in the literature[103].

### Open-loop Solar Tracking Systems

The open-loop tracking system uses only the algorithmic estimation of the solar position with no mechanism for positional correction. Solar position algorithms (SPAs) are able to predict the relative location of the Sun with great accuracy[16, 18, 19]. The SPA of Reda & Andreas has been shown to be accurate in the prediction of solar azimuth and zenith to  $\pm 0.0003^\circ$ .

Although the accuracy of the SPAs today are extremely high, open-loop solar tracking systems require particularly accurate installation and setup procedures in order to realise this accuracy in performance. Beyond this, solar alignment is constantly affected by factors such as thermal expansion in tracking system mounting materials. In reality, the accuracy of open-loop solar tracking systems is limited by factors other than the accuracy of the SPAs.

Open-loop solar tracking systems use fewer components than closed-loop solar tracking systems and are less complex in the principles of their operation. These systems are thus less expensive than their closed-loop counterparts although their accuracy is also less.

### Solar Tracking Accuracies

Although it is possible to find solar tracking systems with very low operational uncertainties, for the most part it is not economically viable to use these trackers in CPV systems due to the resultant

increases in the system levelised cost of energy (LCOE). Hence a compromise between tracker cost and tracker accuracy must be made. CPV trackers account for about 20% of the overall CPV system cost[104]. A common accuracy quotation for a CPV solar tracking system is  $\pm 0.1^\circ$  though in reality this may vary somewhat due to calibration issues and wind loading. This variation introduces much complexity into the uncertainty analysis of CPV system performance.

Solar tracker accuracies are often quoted in terms of the algorithmic and mechanical capability of the systems. In reality, the actual in-field tracker performances differ substantially from the nameplate accuracies[105], sometimes pushing the boundaries of optical misalignment tolerances and specifications. The difference in nameplate tracker accuracies and actual tracker performance is partly due to wind loading. Due to a  $v^2$  proportionality (see Equation 4.7), high wind speeds can significantly increase solar tracking errors. Test studies of tracking error variation with wind speed have shown tracking error increases of factors of five for high but occurring wind speeds[106]. Moreover, calibration has been shown to have a significant effect on tracking accuracy[107], causing seasonal variations in the tracker error distributions[108]. Solar tracking errors and wind loading should therefore be considered in CPV system modelling and performance uncertainties. Forces on CPV systems as induced by wind loading are explored in section 4.4, ‘Sun Tracking – Wind Loading’.

#### 4.1.2.2. System Effects

In this context, system effects refer to those effects beyond the module performance. A solar module outputs electrical power which can be captured and used as energy. The power production to energy capture phase is termed the system phase. Inevitably, as no system component has 100% efficiency, the energy produced by a CPV system is less than that produced by the CPV modules. These losses are termed system losses. System losses are an important part of CPV system analysis, balance of system (BOS) costs currently account for about 40% of the overall CPV system cost[104]. This figure is similar to that of flat-plate PV. BOS uncertainties are beyond the scope of this chapter. An overview is given here for reference.

The key areas of system design are: maximum power point tracking, interconnection structure, and DC to AC conversion.

##### Maximum Power Point Tracking

A maximum power point tracker (MPPT) is a system component specific to solar photovoltaics and is required due to complex and variant nature of PV electrical output. The power output of a solar cell is non-linear. A solar cell produces a current-voltage (I-V) curve that is dependent on a variety of factors affecting both current and voltage such as incident power and cell temperature. The MPPT analyses

the IV curve of the solar module in real time and applies the optimal resistive load for maximum power extraction. The current standard method for MPPT operation is by means of the hill climbing algorithm. The hill climbing algorithm is essentially a search function that incrementally sweeps an IV curve in search of the maximum power point. A variety of hill climbing algorithms exist with variable step methods being the most efficient[109].

By definition, real time search algorithms have to constantly change their point of operation to identify changes in the maximum power point and thus spend much time offset from the maximum power point in oscillation. Furthermore, the performance of MPPT tracker can be significantly affected by noise[110]. MPPT efficiencies are thus recognised as an issue in PV systems. Methods for MPPT efficiency measurement have been published in some detail[111-113]. Reported values of MPPT efficiencies are typically in the range of 90-99%. In general, CPV systems should suffer reduced MPPT tracking errors since the IV curve will be more constant than an untracked array. However, the performance of MPPT systems in HCPV systems operating under wind load is an exception to this, as the relative movement of the Sun from the rapidly induced tracking errors in small input aperture optical systems can alter the cell IV curve.

It is commonplace for MPPT systems to be merged with the inverter (see [114]) into an integrated unit.

### Cell & Module Interconnection Structures

The behaviour of electrical components is dependent on their circuit placement. In power generating devices such as PV modules, series connections result in voltage summing whereas parallel connections result in current summing. The interconnection of PV cells and modules thus determines the power transfer of the PV system. Cell interconnection losses are discussed, for example, in [115].

High voltage transfer of electricity is preferable due to the phenomenon of resistive heating. Resistive heating refers to the heating of a conducting material that result from the passage of electrical current through that material. Resistive heating effects are proportional to the square of the current according to:

$$Q \propto I^2 R$$

EQUATION 4.9

Heating a material requires energy thus high current electricity transfer results in energy losses. High voltages are obtained from PV systems by the series connection of cells and modules. Series connections of dynamic power generators, however, can cause problematic losses in net output

power due to the behaviour of electrical circuits. Namely, that the net power of a string of series connected power generating devices is limited by the minimum current according to:

$$P = I_{min} \sum V$$

EQUATION 4.10

In practice, module series connections are often organised in order to satisfy inverter specifications, thus voltages are limited by the inverter specifications.

### DC to AC Conversion

Solar cells produce electricity in the direct current (DC) form. The electricity grid operates using alternating current (AC). One of the primary reasons for this is the ease of high voltage conversion by transformers that allow for more efficient energy transfer by reduced resistive heating (see Equation 4.9). Grid connected PV systems require a conversion from DC to AC in order to feed the electricity they generate into the grid.

Inverter efficiencies tend to be listed on manufacture data sheets at around 92-95%, although inverter testing suggests that these are efficiencies at near optimal operating conditions[116].

There exist designs whereby the MPPT and the inverter are merged with the tracking controller into a single unit – the mechanical maximum power point tracker (MPPTm)[114].

#### 4.1.3. Synopsis

Although a CPV system is designed according to strict mathematical principles, in practice, the production quality of these systems is limited by the accuracies of the manufacturing process. This is a particularly sensitive issue for CPV, as the economic argument for the technology relies on the use of inexpensive optical components to offset the material cost of multi-junction solar cell. Example manufacturing tolerance levels have been quoted here. The extent to which the limitations of the production processes affect the performance is currently not well understood.

This chapter serves to investigate the effects of production tolerance levels by the optical analysis of example systems, both ideal and manufactured according to some production errors. A process of high resolution wind loading force variation is also introduced to highlight the chaotic nature of tracking uncertainty.

## 4.2. Lens Parameter Variation Effects

The effects of lens parameter variation on receiver illumination profiles are analysed here.

#### 4.2.1. Material Boundary Interface

The material boundary interfaces are the principle regions of interaction and thus the most important aspects of the lens. These interfaces determine the reflection losses and directional changes of incident light.

Material boundaries are typically described as a mathematically perfect shape. For the convex lens front of the plano-convex lens this shape is a spherical segment, as described by:

$$(x - x_0)^2 + (y - y_0)^2 + (z - z_0)^2 = r^2$$

EQUATION 4.11

No manufacturing process is perfect and real boundary surfaces vary from these ideal forms. A schematic representation of this variation is given in Figure 4.9.

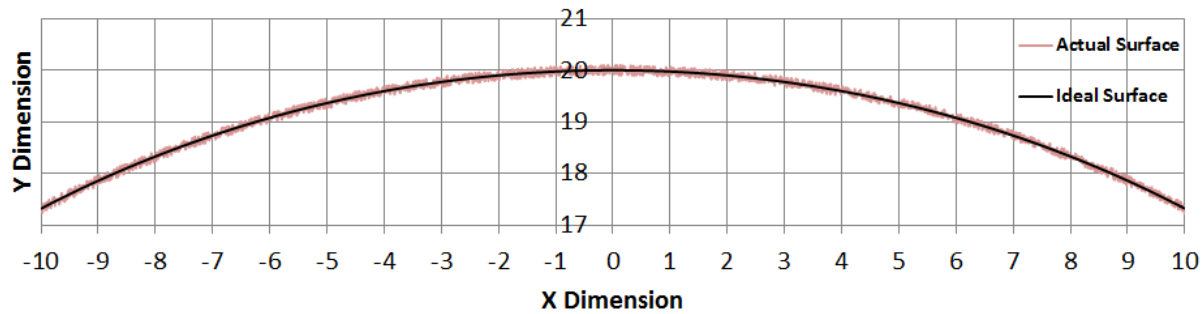


FIGURE 4.9: LENS FRONT SURFACE ROUGHNESS SCHEMATIC

For the most part, the random physical displacement of surface points from the ideal form in the form of roughness has a negligible effect on ray displacement. More significant is the deviation in curvature that results from surface inconsistencies. The curvature deviation alters the angle of contact of light with the surface, this alters the ray path by refraction. Geometrics optics is a tool limited to investigating media of dimensions much greater than the wavelength of light considered. Small variations of surface roughness (on the nm- $\mu$ m scale) are then ignored in ray trace simulations. However, generalised surface defects can be investigated by real changes in the physical positions of surface points. Purely angular variations in surface contact can be considered as surface tangent variations, where the real physical position of the surface intersection remains the same but a virtual, displaced, surface normal is considered. These errors can be imposed in ray tracing for a given lens front mesh point (see 3.5.2 Lens Front Mesh Generation) according to:

$$\theta = \cos^{-1} \left( \frac{|\mathbf{P}| |\mathbf{R}|}{\mathbf{P} \cdot \mathbf{R}} \right)$$

$$\mathbf{R} = \begin{pmatrix} R_x \\ R_y \\ R_z \end{pmatrix}$$

$$\mathbf{P} = \begin{pmatrix} P_x + \delta_x \\ P_y + \delta_y \\ P_z + \delta_z \end{pmatrix}$$

EQUATION 4.12

Where  $\theta$  is the angle between the incoming ray,  $\mathbf{R}$ , and the mesh grid point vector,  $\mathbf{P}$ ,  $\delta_x$  is a virtual error in the x-dimension (East-West plane),  $\delta_y$  a virtual error in the y-dimension (height) and  $\delta_z$  a virtual error in the z-dimension (North-South plane)

In real physical displacement considerations, the actual mesh point,  $\mathbf{P}$ , changes according to Equation 4.12. In angle-only changes the errors associated with  $\mathbf{P}$  are virtual, thus the angle between the incidents rays,  $\mathbf{R}$ , and the lens front mesh point,  $\mathbf{P}$ , changes according to the error set while the lens front intersection point remains at  $\mathbf{P}$ .

#### 4.2.2. 2D Lens Investigations

The typical MJSC for CPV purposes has a surface area of around 1cm by 1cm. A plano-convex lens for secondary concentration purposes will sit on the MJSC. An example plano-convex lens for operation with the typical 1cm by 1cm MJSC is a hemispherical lens with a diameter of twice the cell radius, similar to the ball lens of[117]. This example lens is depicted in Figure 4.10.

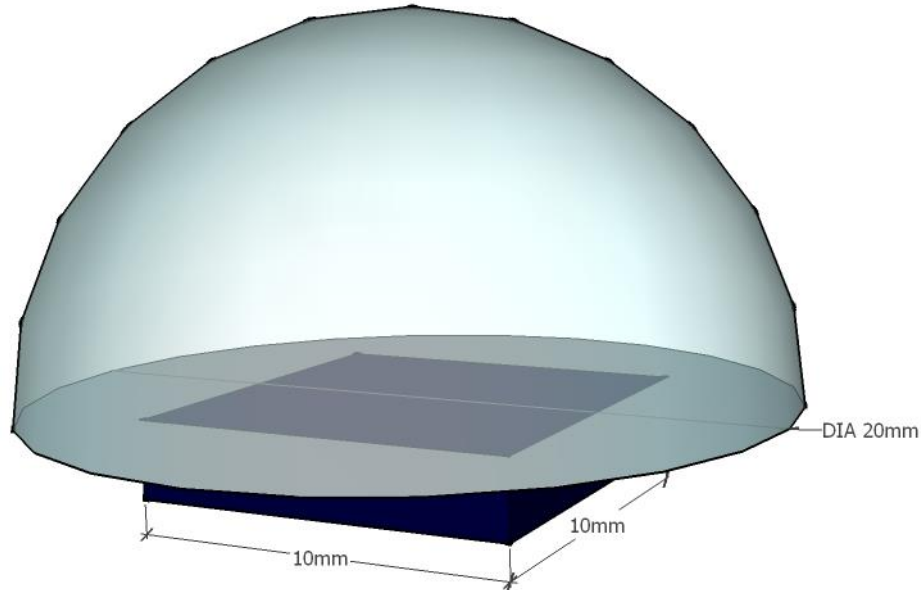


FIGURE 4.10: PLANO-CONVEX SECONDARY – EXAMPLE

The ideal lens shell for the example lens is then described by the 3 parameter set:

$$\begin{aligned} R &= \frac{10}{\sin \frac{\pi}{2}} = 10 \\ C &= \frac{10}{C} = 0 \\ D &= \frac{10}{\tan \frac{\pi}{2}} = 0 \end{aligned}$$

EQUATION 4.13

The diameter of the lens is then  $2R = 20\text{mm}$  and the central thickness of the lens is  $R - D = 10\text{mm}$ . This lens will here be investigated with extremes of diameter and central thickness tolerance allowances and the resultant variations in illumination profiles analysed. Typical production tolerances for the lens diameter and central thickness are 0.1 and 0.2mm, respectively.

The diameter tolerance can be investigated with respect to this example lens using a lens front radius of 10.05mm. The lens parameters then become:

$$\begin{aligned} R &= \frac{10}{\sin \frac{\pi}{2}} = 10.05 \\ C &= \frac{10}{C} = 0 \\ D &= \frac{10}{\tan \frac{\pi}{2}} = 0 \end{aligned}$$

EQUATION 4.14

The central thickness of this lens as induced by the diameter change is  $R - D = 10.05\text{mm}$ . Which is 0.05mm greater than the ideal central thickness – or ¼ of the production tolerance quotation. Thus

the maximal central thickness deviation here must be related to a change in geometric form of the lens shell. It shall here be assumed that the thickness error is linearly proportional to the distance from the lens edge such that:

$$\delta y = \frac{\Delta_y(R - |x|)}{R}$$

EQUATION 4.15

Where  $\delta y$  is the y-dimension error addition,  $\Delta_y$  the maximum error in the y-dimension beyond that induced naturally by the change in  $R$ ,  $r$  the lens front radius and  $x$  the distance from the lens centre

The ideal example lens described by Equation 4.13 and the erroneous lens of Equation 4.14 and Equation 4.15 with  $\Delta_y = 0.15\text{mm}$  are shown as diametric cross sections in Figure 4.11.

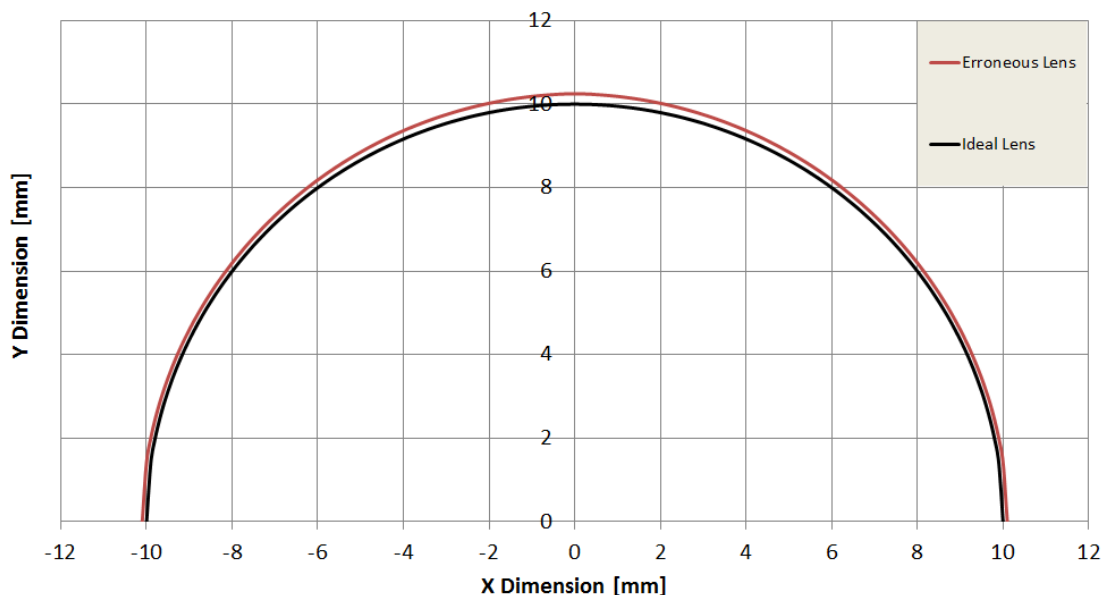


FIGURE 4.11: PLANO-CONVEX LENS FRONT ERROR EXAMPLE

The major variations in optical system behaviour result from changes in lens surface normal vectors. These changes affect the directional change of the incident light rays by refraction. The surface normals of the diametric cross-sections (see Figure 4.11) can be calculated as vectors perpendicular to the surface tangents, as found from the surface gradient. The surface gradients for the ideal and erroneous example lenses are calculated according to Equation 4.16 and Equation 4.17, respectively.

$$\frac{d}{dx} \left( \sqrt{R^2 - (x - x_0)^2} + y_0 \right) = \frac{x_0 - x}{\sqrt{R^2 - (x_0 - x)^2}} + y_0$$

EQUATION 4.16

$$\frac{d}{dx} \left( \sqrt{R^2 - (x - x_0)^2} + y_0 + \frac{\Delta_y(R - |x|)}{R} \right) = \frac{x_0 - x}{\sqrt{R^2 - (x_0 - x)^2}} + y_0 - \frac{x\Delta_y}{R|x|}$$

EQUATION 4.17

The surface normal vectors are then found as

$$\begin{aligned} & \begin{bmatrix} 0 & -1 \\ 1 & 0 \end{bmatrix} \begin{bmatrix} 1 \\ \frac{dy}{dx} \end{bmatrix}, x < 0 \\ & \begin{bmatrix} 0 \\ 1 \end{bmatrix}, x = 0 \\ & \begin{bmatrix} 0 & 1 \\ -1 & 0 \end{bmatrix} \begin{bmatrix} 1 \\ \frac{dy}{dx} \end{bmatrix}, x > 0 \end{aligned}$$

EQUATION 4.18

The variations in surface normals for the ideal and erroneous lens front are shown as a function of deviation from the lens centre,  $x$ , in Figure 4.12 and Figure 4.13.

### Lens Comparison - Surface Normal Vectors

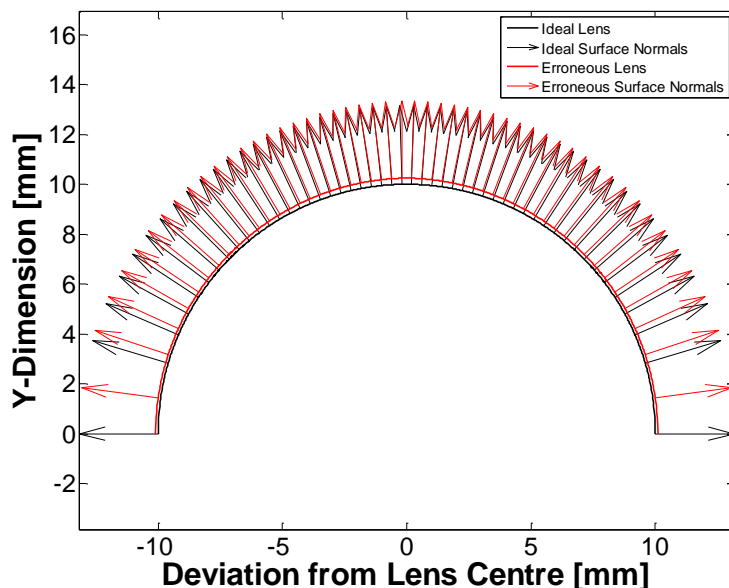


FIGURE 4.12: VARIATIONS IN SURFACE NORMAL VECTORS FOR THE IDEAL AND ERRONEOUS EXAMPLE PLANO-CONVEX LENSES

The angular deviations between the surface normal vectors at larger deviations from the lens centre are very large, around  $10^\circ$ , this angular deviation significantly reduces towards the lens centre. This is elaborated graphically in Figure 4.13.

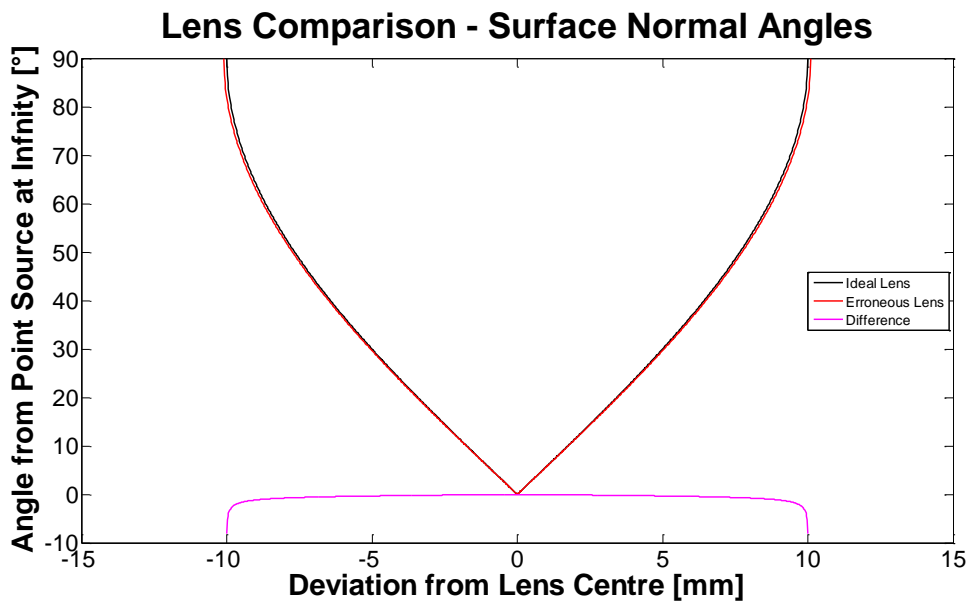


FIGURE 4.13: VARIATIONS IN SURFACE NORMAL ANGLES FOR THE IDEAL AND ERRONEOUS EXAMPLE PLANO-CONVEX LENSES

The effect that these surface deviations have on the resultant illumination profile is investigated here for the point source, pillbox and extended light source Sun source descriptions (see chapter 2, ‘Input’).

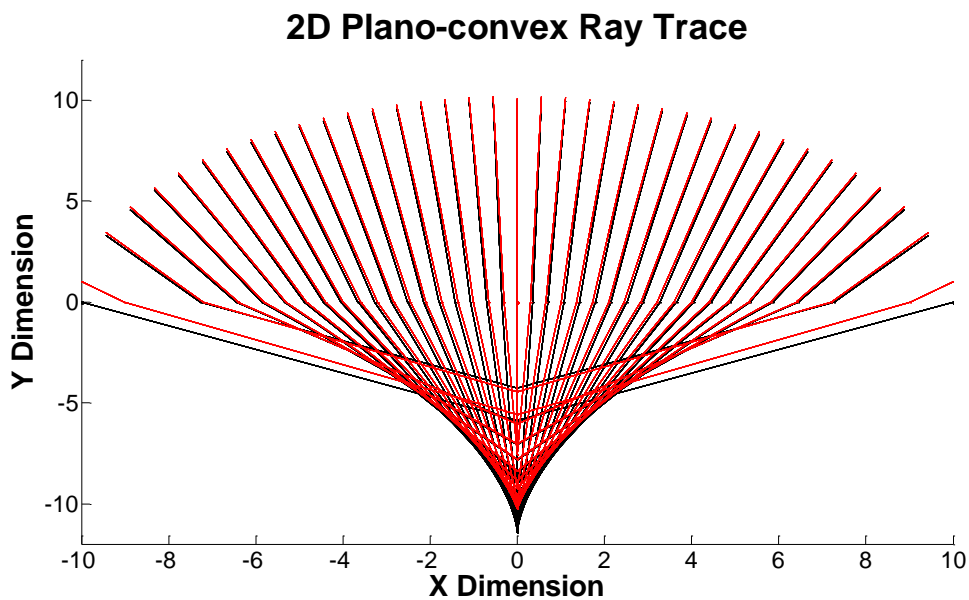


FIGURE 4.14: 2D RAY TRACE DIAGRAMS FOR THE EXAMPLE ORIGINAL LENS (BLACK) AND ERRONEOUS LENS (RED)

Figure 4.14 presents a comparison between the ray paths through the ideal and erroneous lenses at the same set of incident x-values. The ray paths reflect the path of light from a point source at infinity – i.e. the incident rays are modelled as the vector  $-\hat{j}$ . The directional changes resulting from the surface normal deviations of Figure 4.12 and Figure 4.13 are clearly visible. A linear shift in the crossover focal point of approximately 0.2mm is seen here. Figure 4.15, Figure 4.16 and Figure 4.17

show the differences in illumination profiles at the nominal 589nm lensmaker's focal plane for the point source, pillbox and extended light source Sun traces; respectively.

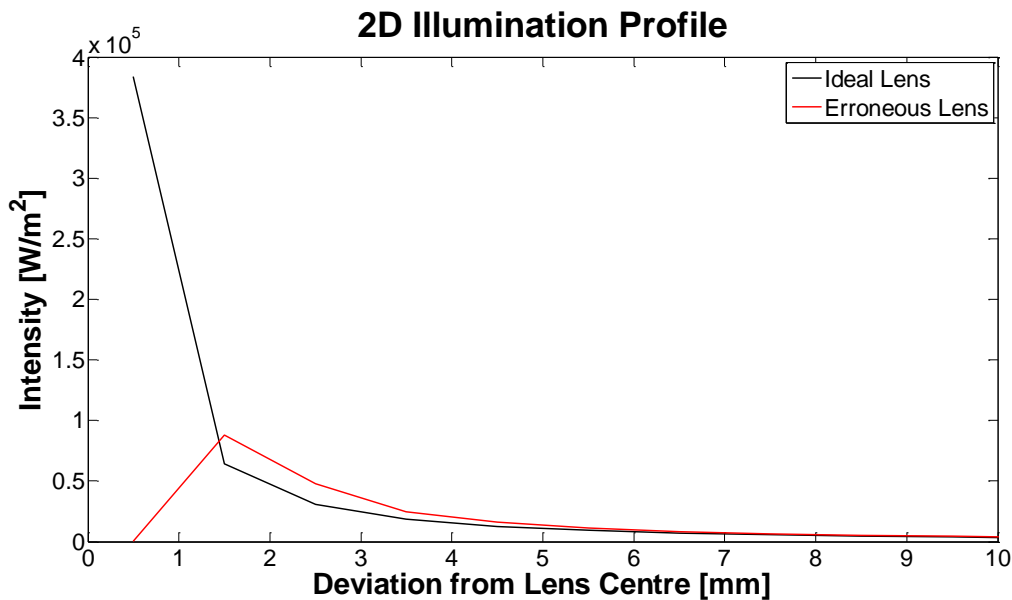


FIGURE 4.15: 2D POINT SOURCE ILLUMINATION PROFILES FOR THE EXAMPLE ORIGINAL LENS (BLACK) AND ERRONEOUS LENS (RED)

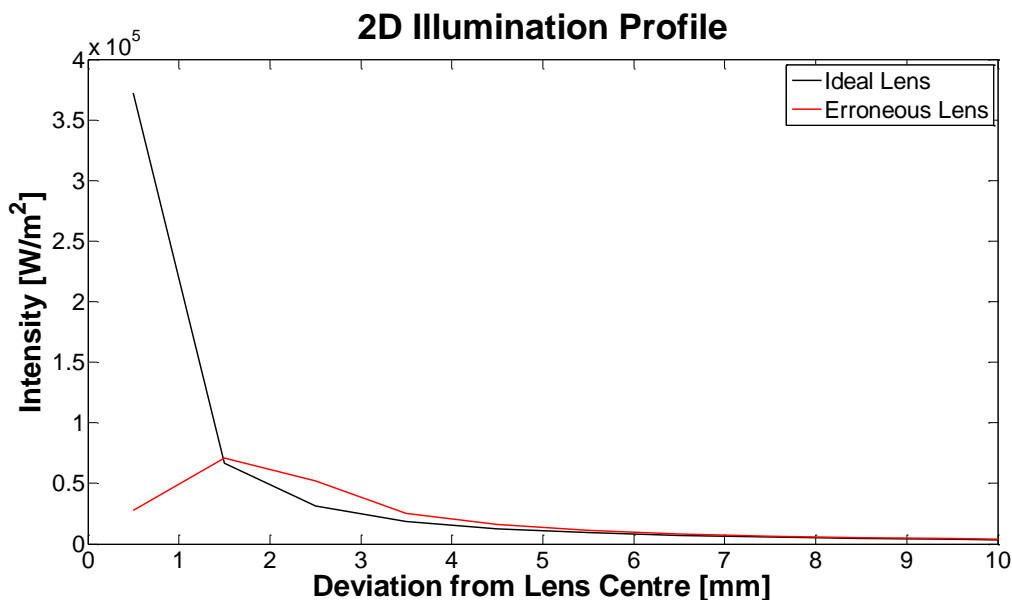


FIGURE 4.16: 2D PILLBOX ILLUMINATION PROFILES FOR THE EXAMPLE ORIGINAL LENS (BLACK) AND ERRONEOUS LENS (RED)

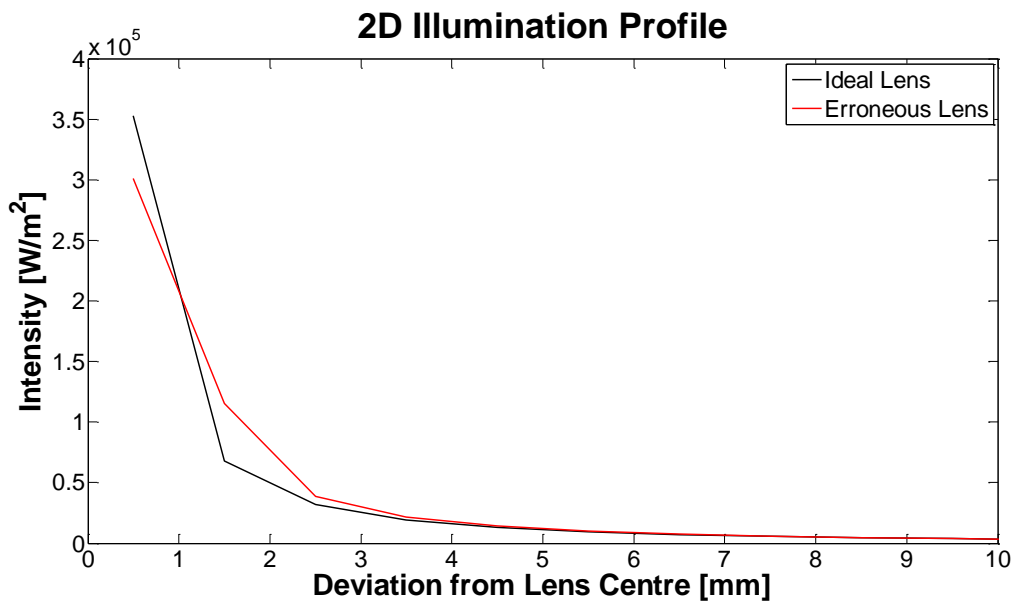


FIGURE 4.17: 2D EXTENDED LIGHT SOURCE ILLUMINATION PROFILES FOR THE EXAMPLE ORIGINAL LENS (BLACK) AND ERRONEOUS LENS (RED)

### 4.3. Framing Variation Effects

An example module frame is here used to illustrate the role of framing variation effects on system performance uncertainty. The example frame is designed to hold a 10cm by 10cm square PMMA Fresnel lens operating at a concentration of 100 Suns (100X). The manufacture tolerances outlined in Table 4.2 are then considered in terms of their effect on the optical misalignment of the lens in terms of deviation from the ideal placement and the associated changes in the solar cell illumination profile. In accordance with the optical modelling principles outlined in chapter 3, ‘Optics’, the misalignment is considered two-fold: Cartesian positional error and spherical polar orientation error.

A trivial, summative, approach to compounded uncertainties is taken here for illustration purposes. In reality all tolerance errors are correlated and interdependent. Although it is common good practice to consider uncertainties as probability density functions where deviations from an expected outcome are analysed as normal distributions, this is beyond the scope of this work.

#### 4.3.1. Example Frame Design

The minimum plano-convex shell lens radius for the example lens is then:

$$R_{pc\min} = \sqrt{5^2 + 5^2} \approx 7.07\text{cm}$$

A plano convex shell lens must then be defined such that:

$$R_{pc} > R_{pc\min}$$

The focal length for this minimum radius shell lens, as determined from the lensmaker's equation (Equation 3.20), is then calculated as:

$$l_f = \frac{R_{pc}}{(n - 1)} \approx 15.37\text{cm}$$

The corresponding focal distance for a given concentration factor can be calculated according to:

$$l_{fx} = l_f \left(1 - \frac{1}{\sqrt{X}}\right)$$

EQUATION 4.19

Where  $l_{fx}$  is the focal length at the desired concentration ratio,  $X$ , and  $l_f$  the lensmaker's focal length

The minimum focal length of the example concentration system is thus found as:

$$l_{fx} = 15.37 \left(1 - \frac{1}{\sqrt{100}}\right) \approx 13.83\text{cm}$$

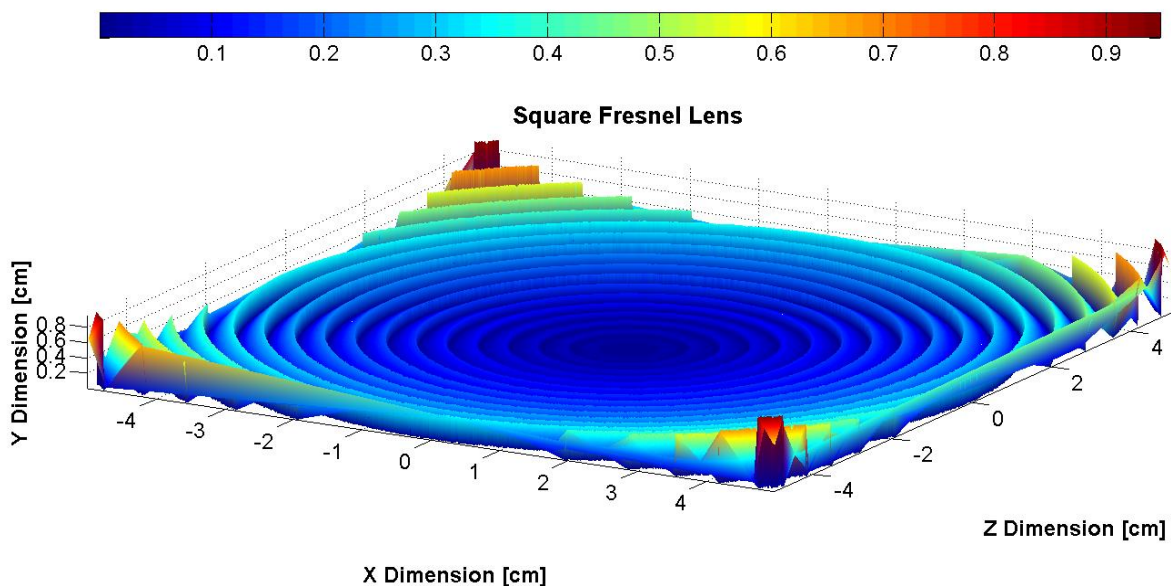
The use of the minimum radius plano-convex shell lens is impractical as it requires a subtended radial half angle of restriction (see 3.3.3, 'Focal Point Calculation') of  $\frac{\pi c}{2}$ , leading both to extreme chromatic aberration effects and a large maximum to minimum facet height ratio. The example system is thus designed to somewhat mitigate these complications by choosing a greater focal length. For simplicity a focal length of 15cm is chosen. The corresponding lensmaker's focal length is then found from Equation 4.19 as:

$$l_f = \frac{l_{fx}}{\left(1 - \frac{1}{\sqrt{X}}\right)} = \frac{15}{\left(1 - \frac{1}{\sqrt{100}}\right)} \approx 16.67\text{cm}$$

The plano-convex shell lens spherical radius is then calculated from the lensmaker's equation as:

$$R_{pc} = l_f(n - 1) = 16.67(1.46 - 1) \approx 7.67\text{cm}$$

The resultant square Fresnel lens is shown in Figure 4.18:

FIGURE 4.18: EXAMPLE 100CM<sup>2</sup> SQUARE FRESNEL LENS

This lens is housed in a module frame. The module frame of this example is based on the example of Figure 4.6, using the calculations outlined above. Manufacture tolerance levels and production uncertainties in the framing components will naturally displace the lens from the design-based optimal position and affect the system performance.

The normalised ideal illumination profile cast by the lens of Figure 4.18 is shown in Figure 4.19.

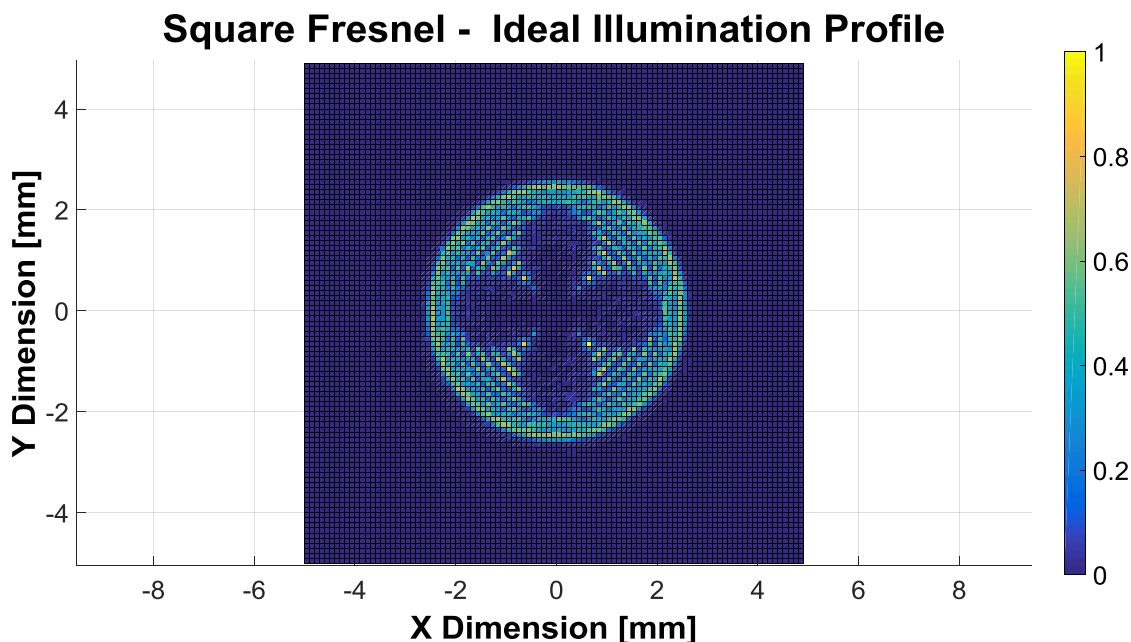


FIGURE 4.19: IDEAL SQUARE FRESNEL LENS NORMALISED 3D RAY TRACE CELL ILLUMINATION PROFILE

The central focal spot (or large illumination spread) seen in the illumination profile of Figure 4.19 highlights a problem with the edge ray design process outlined above. In order to better

approximate CPV cell illumination by near full illumination, the central spot (major intensity portion) of this image is scaled to occupy a larger portion of the cell. In practice, a similar effect can be achieved physically by adjusting the distance from the lens to the receiver plane. Optimisation of this distance beyond that found in the modelling is typically a laboratory based calibration procedure. The adjusted illumination profile is shown in Figure 4.20.

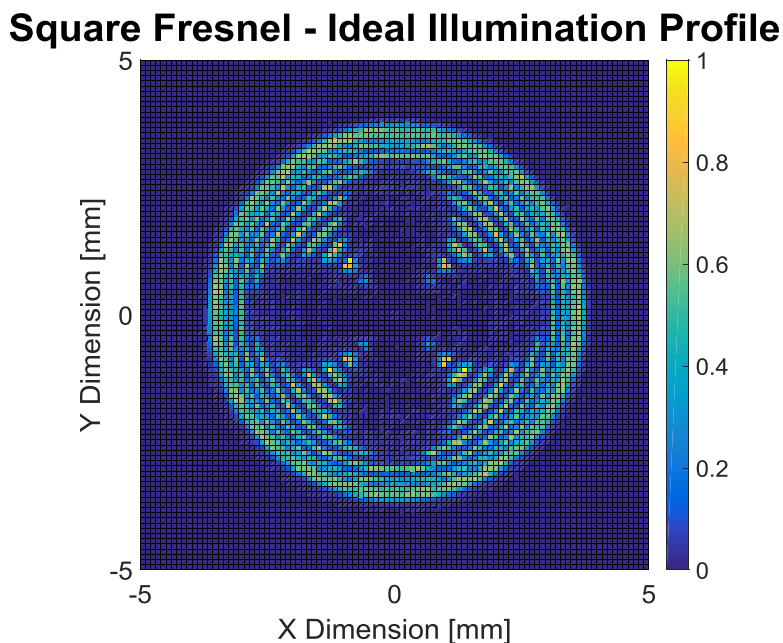


FIGURE 4.20: IDEAL SQUARE FRESNEL LENS NORMALISED 3D RAY TRACE CELL ILLUMINATION PROFILE – FOCUS ADJUSTED

The nature the illumination profile and the physical phenomena underlying its structure is further divulged after the presentation of the misaligned, non-ideal, equivalent (see Figure 4.25) in section 4.3.2, ‘Optical Misalignment’.

### 4.3.2. Optical Misalignment

The manufacture tolerance levels outlined in 4.1.1.2, ‘System Frames’ are here considered along with the resultant optical alignment errors. The lens position and orientation error vectors,  $\Delta$  and  $N$  are analysed as a function of the example tolerance errors of Table 4.2 such that:

$$\Delta = f(\alpha, \sigma, \tau) = \begin{bmatrix} \delta x \\ \delta y \\ \delta z \end{bmatrix}$$

EQUATION 4.20

$$N = f(\lambda) = \begin{bmatrix} \sin \alpha \cos \varepsilon \\ \cos \alpha \cos \varepsilon \\ \sin \varepsilon \end{bmatrix}$$

EQUATION 4.21

Where  $\alpha$  represents component angle errors,  $\sigma$  straightness errors,  $\tau$  twist errors and  $\lambda$  length errors

Framing component errors in relation to the example frame of Figure 4.6 are shown in Figure 4.21, Figure 4.22, Figure 4.23 and Figure 4.24. These examples demonstrate the errors of most significance in terms of effects on optical system behaviour.

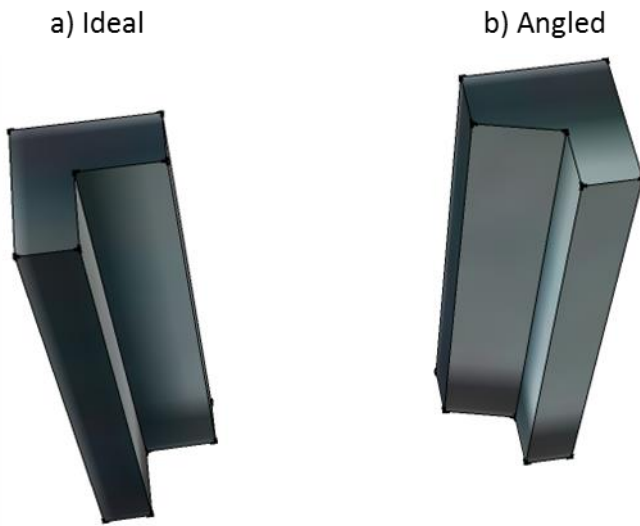


FIGURE 4.21: FRAME VARIATIONS – ANGLE ERROR SCHEMATIC

One angle of concern in the example frame is the right angle of the corner housing unit. For the test case example, the maximum stated tolerance of  $2^\circ$  is considered. This is analysed as two equal half angle errors of  $1^\circ$ . Lateral shifts in the  $x$  and  $z$  directions are then found as  $w \sin \theta$  thus the contribution to the lens placement error vector is then:

$$\Delta_\alpha = \begin{bmatrix} 2.5\text{mm} \times \sin 1^\circ \\ 0 \\ 2.5\text{mm} \times \sin 1^\circ \end{bmatrix} = \begin{bmatrix} 0.4 \\ 0 \\ 0.4 \end{bmatrix}$$

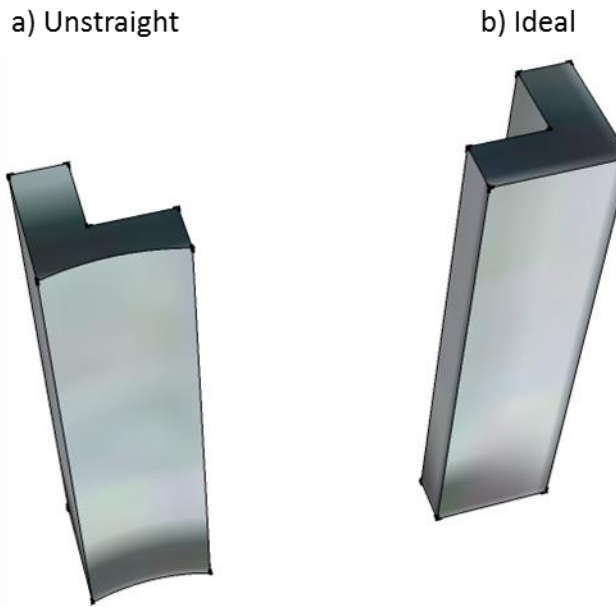


FIGURE 4.22: FRAME VARIATIONS – STRAIGHTNESS ERROR SCHEMATIC

The primary edges of concern in the example frame are the  $x$  and  $z$  back edges of the corner housing unit. For the test case example, the maximum stated tolerance of approximately 0.1% of edge length is considered. Lateral shifts in the  $x$  and  $z$  directions are then found as  $l/1000$  thus the contribution to the lens placement error vector is then:

$$\Delta_{\sigma} = \begin{bmatrix} 150\text{mm}/1000 \\ 0 \\ 150\text{mm}/1000 \end{bmatrix} = \begin{bmatrix} 0.15 \\ 0 \\ 0.15 \end{bmatrix}$$

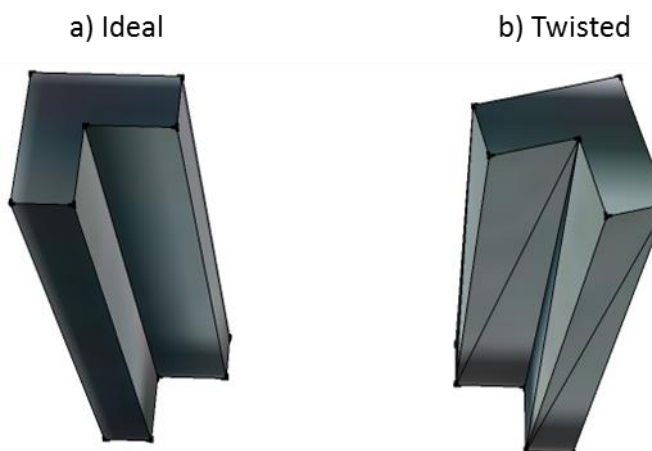


FIGURE 4.23: FRAME VARIATIONS – TWIST ERROR SCHEMATIC

The primary extrusion twist of concern in the example frame is the corner housing unit. For the test case example, the maximum stated tolerance of 0.5° per foot is considered. Lateral shift in the  $x$  and

$z$  directions are then estimated as  $w \sin(l \times 0.5^\circ / 304)$ . The contribution to the lens placement error vector is then:

$$\Delta_\tau = \begin{bmatrix} 2.5\text{mm} \sin(150\text{mm} \times 0.5^\circ / 304\text{mm}) \\ 0 \\ 2.5\text{mm} \sin(150\text{mm} \times 0.5^\circ / 304\text{mm}) \end{bmatrix} = \begin{bmatrix} 0.01 \\ 0 \\ 0.01 \end{bmatrix}$$

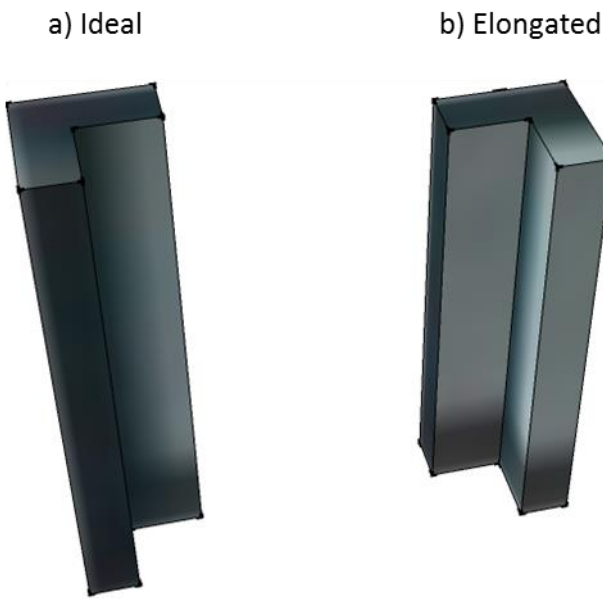


FIGURE 4.24: FRAME VARIATIONS – LENGTH ERROR SCHEMATIC

The primary extrusion length of concern in the example frame is the corner housing unit. For the test case example, the maximum stated tolerance of 1.5mm is considered. A single bar error is considered here, both vertical shift if the  $y$  direction at the lens centre and lens orientation error result. Vertical shift in the  $y$  direction is calculated as  $\lambda/2$ . Equal orientation errors in the azimuth and elevation

angles are assumed, these angles are then calculated as  $\sqrt{(\tan^{-1}(\lambda/\sqrt{2d^2}))^2/2}$ . The contributions to the lens placement and orientation error vectors are then:

$$\Delta_\lambda = \begin{bmatrix} 0 \\ 1.5\text{mm}/2 \\ 0 \end{bmatrix} = \begin{bmatrix} 0 \\ 0.75 \\ 0 \end{bmatrix}$$

$$N = \begin{bmatrix} \sin \sqrt{(\tan^{-1}(\lambda/\sqrt{2d^2}))^2/2} \cos \sqrt{(\tan^{-1}(\lambda/\sqrt{2d^2}))^2/2} \\ \cos \sqrt{(\tan^{-1}(\lambda/\sqrt{2d^2}))^2/2} \cos \sqrt{(\tan^{-1}(\lambda/\sqrt{2d^2}))^2/2} \\ \sin \sqrt{(\tan^{-1}(\lambda/\sqrt{2d^2}))^2/2} \end{bmatrix} \approx \begin{bmatrix} 0.008 \\ 0.999 \\ 0.008 \end{bmatrix}$$

This can be analysed as a uniaxial error of 0.61°.

The above case is expanded as using

$$\Delta = \Delta_\alpha + \Delta_\sigma + \Delta_\tau + \Delta_\lambda$$

$$\begin{pmatrix} \alpha \\ \tau \\ \sigma_w \\ \sigma_b \\ \lambda \end{pmatrix} \approx \begin{pmatrix} 2^\circ \\ 0.16^\circ \\ 0.025\text{mm} \\ 0.025\text{mm} \\ 0.1\text{mm} \end{pmatrix}$$

$$\Delta = \begin{bmatrix} \delta x \\ \delta y \\ \delta z \end{bmatrix} = \begin{bmatrix} 0.4 \\ 0 \\ 0.4 \end{bmatrix} + \begin{bmatrix} 0.1 \\ 0 \\ 0.1 \end{bmatrix} + \begin{bmatrix} 0.01 \\ 0 \\ 0.01 \end{bmatrix} + \begin{bmatrix} 0 \\ 0.75 \\ 0 \end{bmatrix} = \begin{bmatrix} 0.51 \\ 0.75 \\ 0.51 \end{bmatrix}$$

The  $\delta x$  and  $\delta z$  parameters cause a lateral shift in the illumination profile resulting directly from the lateral lens shift. The  $\delta y$  parameter causes image spread from ray divergence resulting from movement away from the focal point. The optical misalignment errors  $\delta\theta$  and  $\delta\varphi$  cause both lateral shift in the focal point from incident angle changes and biased image spread from ray divergence.

The erroneous solar cell illumination profile is presented for comparison with the ideal (see Figure 4.20) in Figure 4.25.

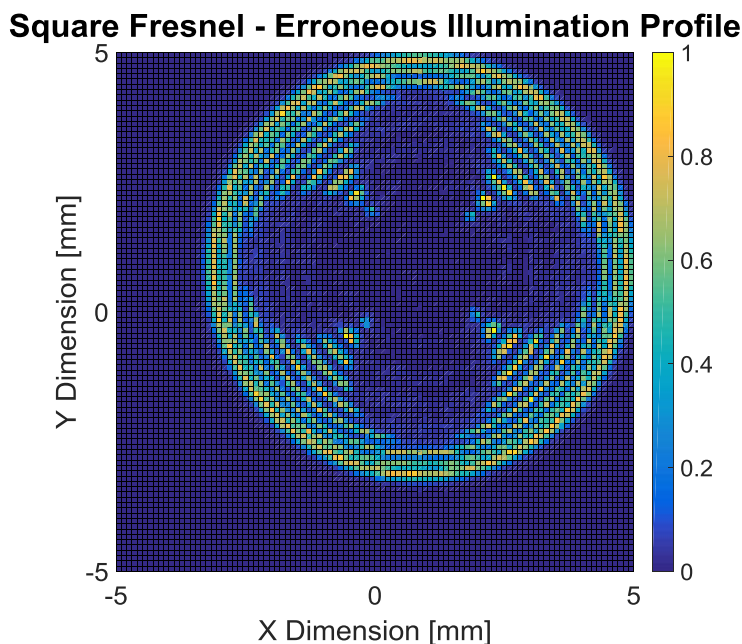


FIGURE 4.25: ERRONEOUS SQUARE FRESNEL LENS NORMALISED 3D RAY TRACE CELL ILLUMINATION PROFILE

The illumination pattern reflects the structure of the square Fresnel lens that was traversed by the incident light. Waves of intensity can be seen – these result from the facet reflections. There is also a ‘flowering’ effect that results from the aberrations of the lens, specifically the difference in refraction at the lens centre and the lens edges. In the square Fresnel lens, the major difference is found at the

square edges – hence the four pseudo-triangular intensity trails towards the centre of the illumination profile.

A significant difference between the ray traced illumination profiles of the ideal and erroneously aligned lenses can be seen. Namely, in the profile of the erroneously aligned lens:

- There is a linear shift in the central image point of approximately 0.85mm (approximately 0.6mm in each axis)
- There is a 20% increase in ring size
- There is a 15% reduction in maximum intensity

The effects of these differences on the electrical performance of the cell are investigated in the following chapter, 5, 'Electrical Output'.

#### 4.4. Sun Tracking – Wind Loading

Sun tracking misalignment resulting from wind loading is a complex problem. The complexity results mainly from the chaotic nature of wind. Although wind direction is often spoken of in terms of a nominal compass direction, it can be seen from high resolution data that the assertion of these nominal values is very much an oversimplification. Example solar days of wind speed and direction data are presented in Figure 4.26 and Figure 4.27.

Two example days are presented. There are major differences in the wind patterns found on these days, the average wind direction on July 25<sup>th</sup> 2014 is found as south-westerly, whereas the average wind direction of October 31<sup>st</sup> 2014 is northerly. The wind speeds on these days are also significantly different, with hourly averages of up to approximately four times greater found on October 31<sup>st</sup>.

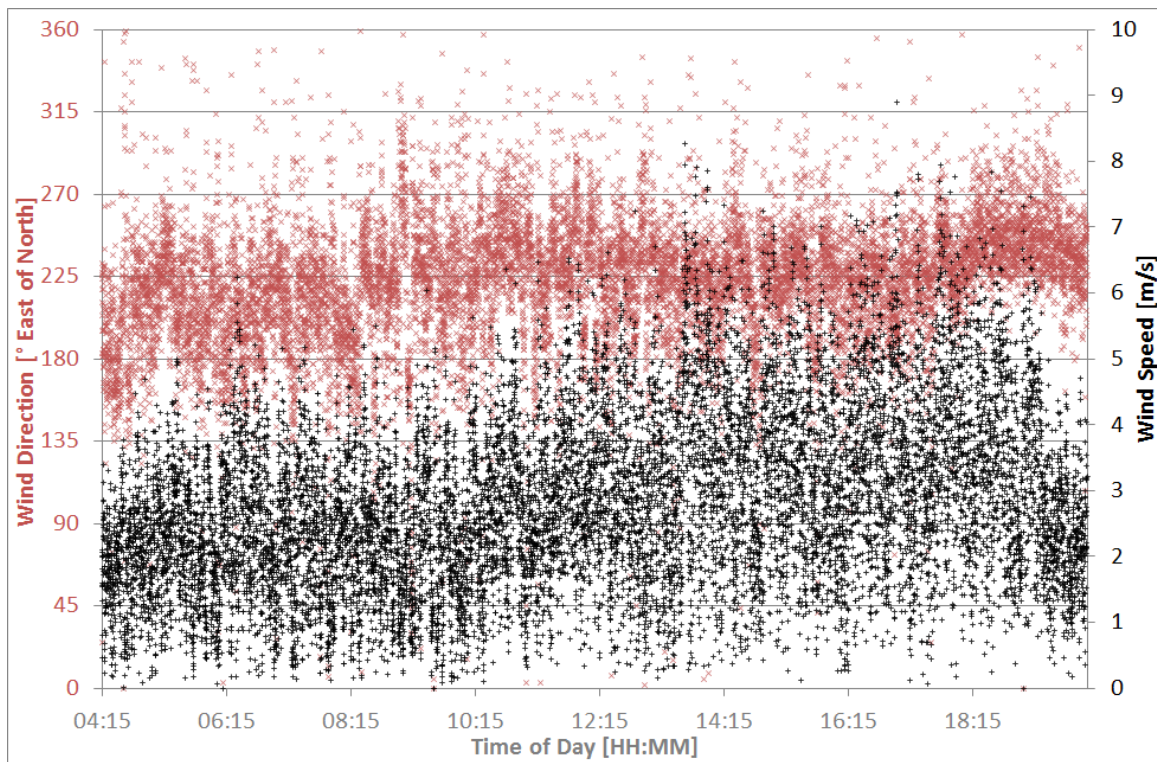


FIGURE 4.26: EXAMPLE WIND SPEED AND DATA AS MEASURED AT CREST ON JULY 25<sup>TH</sup> 2014 FROM SUNRISE TO SUNSET

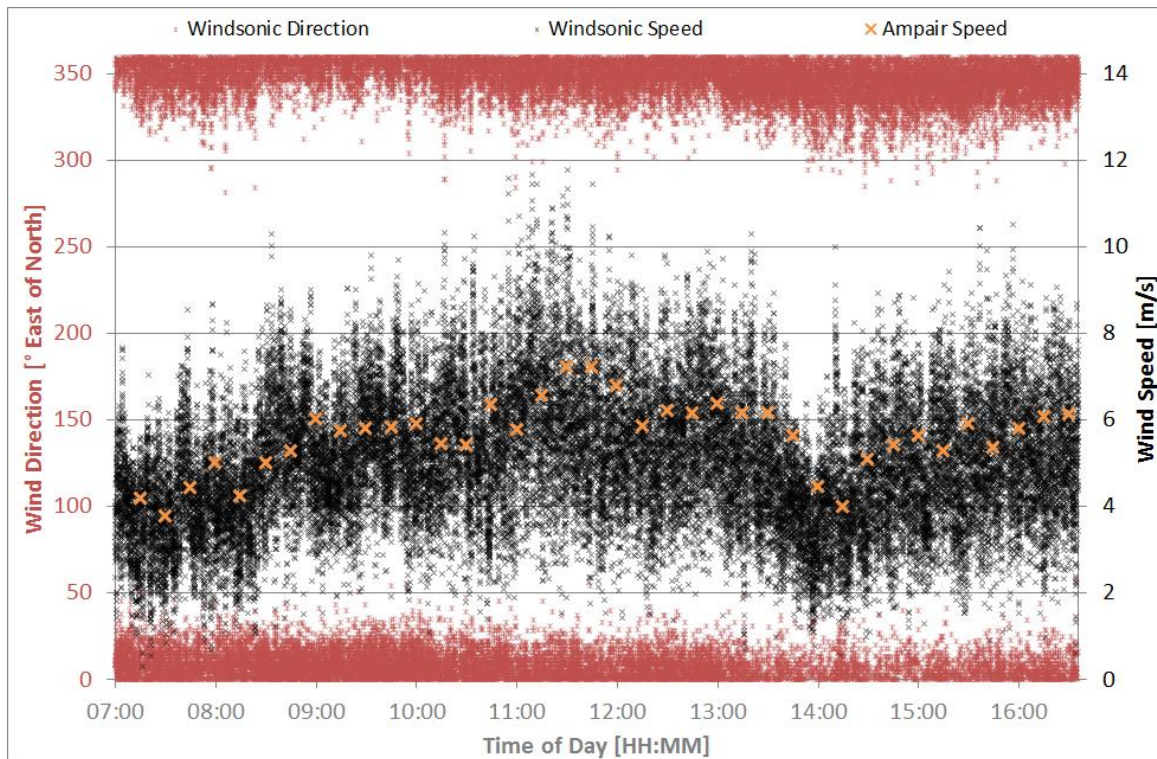


FIGURE 4.27: EXAMPLE WIND SPEED AND DATA AS MEASURED AT CREST ON OCTOBER 31<sup>ST</sup> 2014 FROM SUNRISE TO SUNSET

Figure 4.26 shows 2 second resolution wind speed and direction data from a Windsonic ultrasonic wind measurement device. Figure 4.27 shows the 2 second resolution ultrasonic wind speed and

direction data alongside 15 minute wind speed averages recorded with an Ampair wind turbine, for reference.

The force on the CPV module due to wind loading is not only related to wind force and direction but also to Sun tracking module orientation path. The Sun path diagrams for 25<sup>th</sup> July and 31<sup>st</sup> October 2014 are shown in Figure 4.28. The Sun position data was generated using the solar position algorithm (SPA) of Reda & Andreas[18, 19].

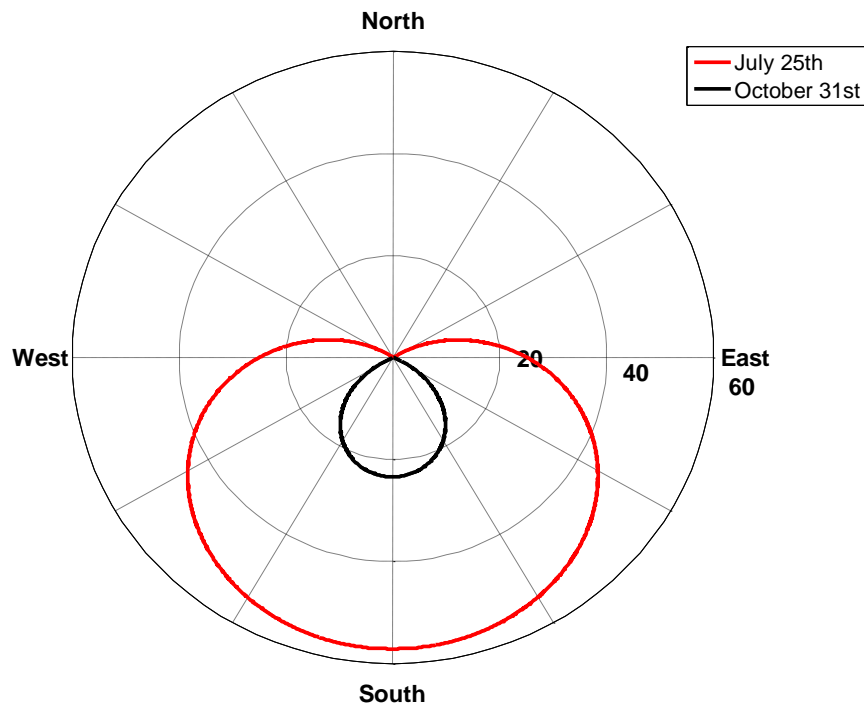


FIGURE 4.28: SUNPATH DIAGRAMS FOR JULY 25<sup>TH</sup> AND OCTOBER 31<sup>ST</sup> 2014

The force on the CPV module due to wind loading is calculated here assuming perfect solar tracking. Given the nature of the collected wind data, a further assumption, that there is no z/elevation-component to the wind direction, is made. It is recognised that this is not ideal, yet it is rare to find 3-dimensional wind direction data.

For consistency, the example CPV array used here is that used in section 4.1.1.2, ‘System Frames’ for wind load calculation examples, namely a cuboidal array of dimensions 3m by 3m by 0.1m. For each timestamp the projected area of the CPV array cuboid in the direction of the wind is calculated. To do this, the normal vectors projected from the 3 orthogonal cuboid faces are determined from the solar pointing vector according to:

$$\mathbf{N}_{fb} = \begin{pmatrix} \alpha \\ \varepsilon \end{pmatrix}$$

$$\mathbf{N}_{tb} = \begin{pmatrix} \alpha \\ \varepsilon + \frac{\pi}{2} \end{pmatrix}$$

$$\mathbf{N}_{lr} = \begin{pmatrix} \alpha + \frac{\pi}{2} \\ \varepsilon \end{pmatrix}$$

Where  $\alpha$  is the solar azimuth,  $\varepsilon$  the solar elevation,  $\mathbf{N}_{fb}$  the array front-back normal vector,  $\mathbf{N}_{tb}$  the array top-bottom normal vector and  $\mathbf{N}_{lr}$  the array left-right normal vector

The area projection factors of the cuboid faces are then found from the dot product of the face normal vectors with the wind direction vector. The projected area is then the sum of the products of the true face areas and their respective projection factors. The 3 face reduction argument is sufficient due to the geometric symmetry of the situation, as the maximal number of visible cuboid faces from any perspective is 3. Thus this method is particularly efficient as it avoids redundant calculations. An example perspective view of a cuboid is given in Figure 4.29 for reference.

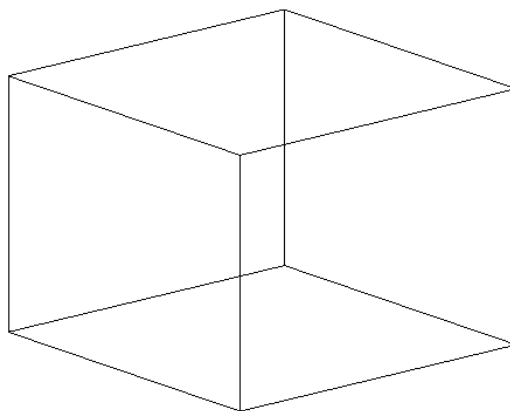
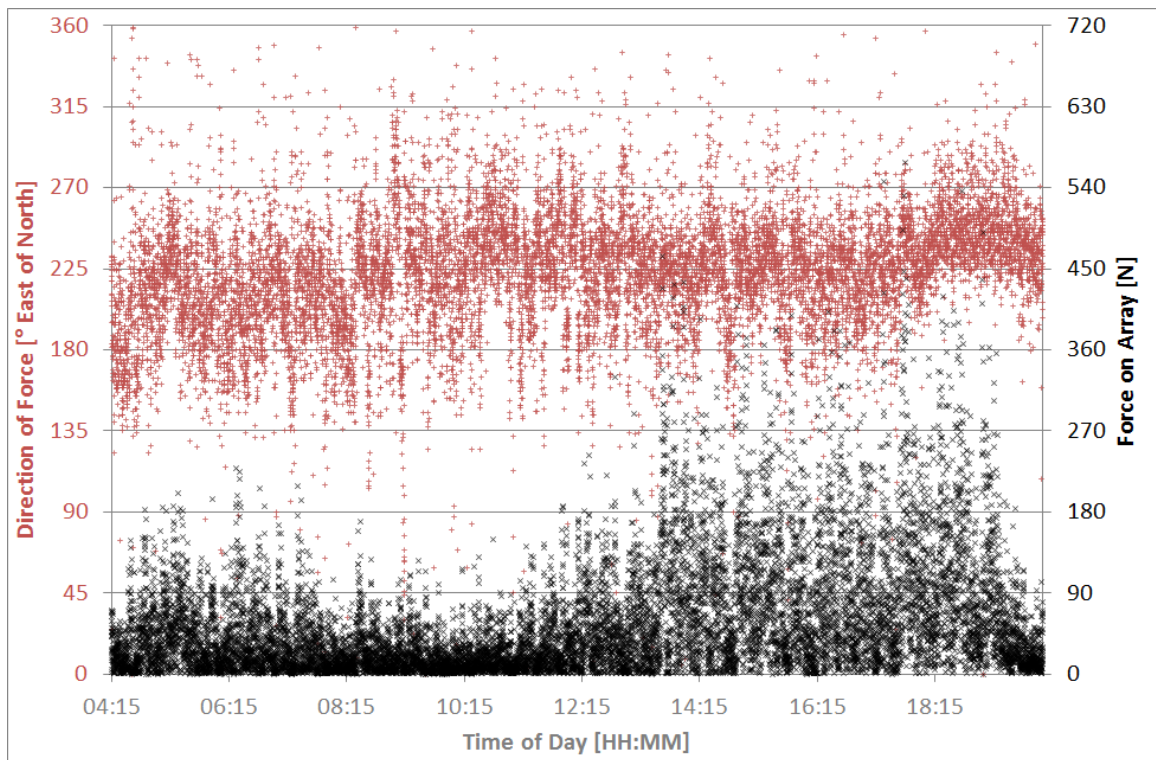
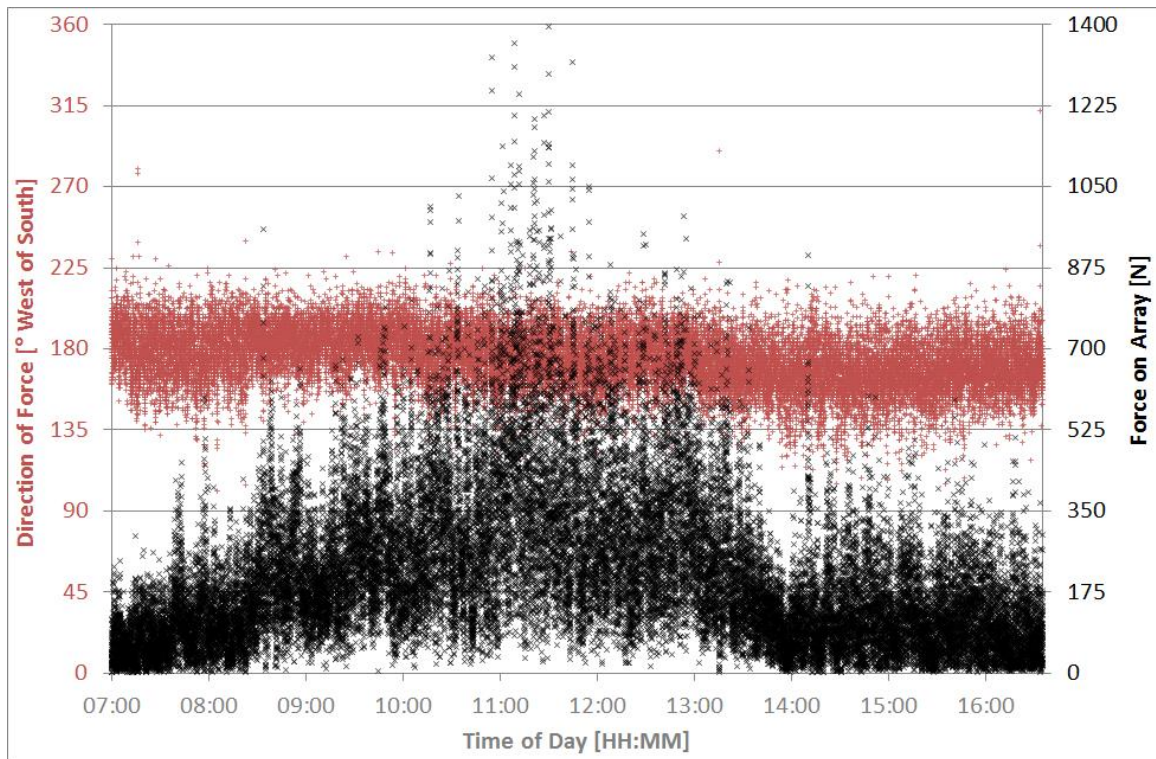


FIGURE 4.29: EXAMPLE PERSPECTIVE OF CUBOID DEMONSTRATING THE 3-FACE PROJECTION PHENOMENON

The wind loading force on the array is then calculated according to Equation 4.7. The wind loading forces on the example array throughout solar days of July 25<sup>th</sup> and October 31<sup>st</sup> 2014 are shown in Figure 4.30 and Figure 4.31.

FIGURE 4.30: CALCULATED WIND LOADING FORCE ON EXAMPLE CPV ARRAY ON JULY 25<sup>TH</sup> 2014FIGURE 4.31: CALCULATED WIND LOADING FORCE ON EXAMPLE CPV ARRAY ON OCTOBER 31<sup>ST</sup> 2014

Significant differences in wind loading forces can be seen between the two example days. The maximum wind loading force on the example CPV system on July 25<sup>th</sup> is found towards the end of the day as approximately 570N. On October 31<sup>st</sup>, the maximum wind loading force is found as

approximately 1400N, around 250% greater. In both examples there is a rise in average load force as the array tracking aligns near normal with the average wind direction. On July 25<sup>th</sup> this occurs toward the end of the solar day whereas on October 31<sup>st</sup> this occurs in the middle of the day. Similarly there are lulls in average load force that correspond to orthogonality of the array tracking with average wind direction.

## 4.5. Conclusions

This chapter has focussed on two major areas of uncertainty in CPV module manufacture, namely those uncertainties arising from manufacture tolerance levels in lens and framing component production. Tolerance errors were extracted from manufacturer datasheets and applied to the optical model presented in chapter 3, ‘Optics’. The results have shown that errors in the component manufacture process can significantly alter the performance of CPV optical systems and lead to notable variations in the illumination profile at the solar cell.

For an example plano-convex lens system, a 15% variation in maximum intensity value as well as a linear shift in focal point crossover of approximately 0.2mm were found between an ideal and erroneously manufactured lens, although the optical efficiency remained the same. In an example system using a square Fresnel lens focussing light onto a 10mm by 10mm solar cell, a possible linear shift of the focal centre of the cell illumination profile of approximately 0.85mm was identified as a result of framing component manufacture error. The significance of these intensity variations on the electrical output of a solar cell is explored in the following chapter (see 5, ‘Electrical Output’).

Wind loading has previously been identified as a major source of solar tracking error in CPV systems[49, 105]. Given this, the loading force on an example 3m by 3m by 0.1m CPV system array was calculated using 2 second resolution wind data from the CREST measurement system by means of geometric analysis and fluid dynamics. The chaotic nature of the force variation was highlighted with forces of up to 1.4kN found. The strength and chaotic variation of these forces is illuminating and the method of deriving this information could well prove useful in the simulation of CPV systems.

# 5. Electrical Output

*the Numbers that Count*

## 5.1. Introduction

The motivation for all photovoltaic technologies is the renewable generation of electricity from the Sun. PV systems are built specifically for the generation of energy. Energy is a measure of power over time and is commonly expressed as:

$$E = \int_{t=0}^{t=n} P_t$$

*Where E is energy, P power and t time*

PV output power is a dynamic variable dependent on incident irradiation and system behaviour. The dynamic nature of incident insolation is discussed in some detail in chapter 2, ‘Input’, where a variety of insolation descriptions and models are compared. CPV system behaviour can be considered two-fold: optical concentration system behaviour and energy conversion system behaviour. Optical concentration systems are discussed in some detail in chapter 3, ‘Optics’ and their behavioural uncertainty explored somewhat in chapter 4, ‘Uncertainty’.

Electrical modelling allows for the prediction of device energy generation. These predictions are often given as annual energy harvest predictions and are a crucial consideration in investment negotiations for energy generation technologies. Furthermore, electrical performance models are a necessity in utility grid connection design. An example of modelled annual energy generation is given in Figure 5.1.

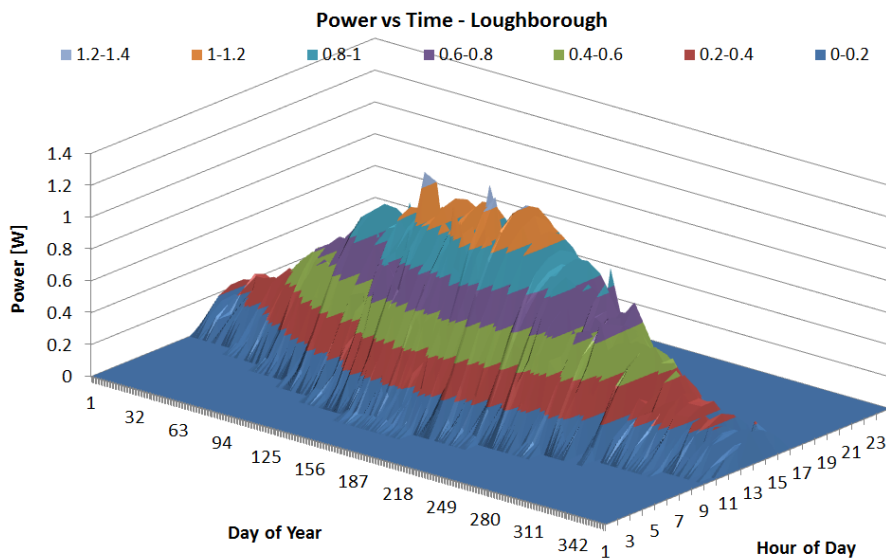


FIGURE 5.1: ANNUAL ENERGY GENERATION EXAMPLE – POWER OVER TIME FOR LOUGHBOROUGH, UK

Figure 5.1 shows the average hourly power generation for a  $64\text{cm}^2$  solar cell in Loughborough, UK, as modelled by an ideal diode. The ideal diode model is further explained in section 5.2.1, ‘1D Solar Cell Modelling’. Incident irradiance and ambient temperature data were taken from meteorological measurement site at CREST, Loughborough University, from 2011. The induced photocurrent was calculated using a typical crystalline silicon cell spectral response curve at an AM1.5 spectrum and weighted according to relative intensity. The energy estimate for this cell is approximately 1kWh per year. This is an overoptimistic model, but serves the purpose of illustration.

The conversion device of a photovoltaic system is termed the solar, or photovoltaic, cell. The solar cell is effectively a large area semiconductor diode that exploits the photovoltaic effect in its operation. The photovoltaic effect was reportedly first observed in 1839 by Edmund Becquerel, whilst the first realisation of its application to electrical energy production is attributed to C.E. Fritz in 1883[118], although conversion efficiencies stayed below the 1% mark for approximately the next 75 years. Today, officially tested record laboratory solar cell efficiencies have reached 44.7% for multi-junction devices, 27.6% for Silicon devices and 23.3% for thin film devices. There are a variety of emergent PV technologies, the most efficient of which having a 20.1% record[1].

This chapter serves as an investigation into the electrical behaviour of solar cells under the illumination profiles produced in chapter 4, ‘Uncertainty’.

### 5.1.1. Solar Cells

Today there exist a wide variety of solar cells, both commercially established and in research. The established, commercially available technologies are typically categorised as: silicon, thin film and

multi-junction technologies. Here solar cells will be considered simply as single-junction and multi-junction technologies, as multi-junction solar cells are the conversion technology of choice for CPV.

Firstly, a typical solar cell I-V curve is presented and the principle points identified for reference.

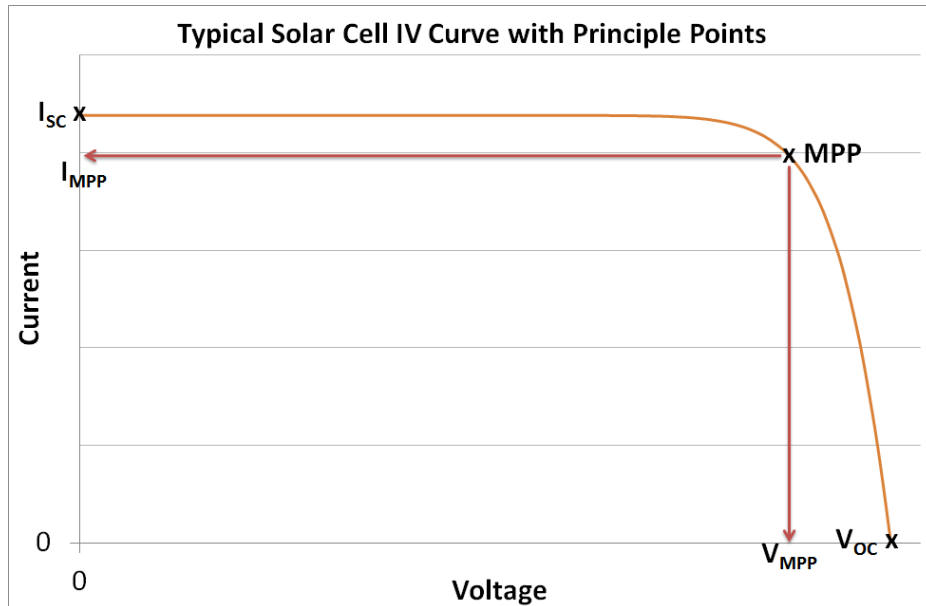


FIGURE 5.2: I-V CURVE SHOWING PRINCIPLE POINTS

Figure 5.2 shows a typical solar cell I-V curve with the principle points highlighted. These principle points are: The short-circuit current,  $I_{SC}$ , the open-circuit voltage,  $V_{OC}$  and the maximum power point,  $MPP$ . A further point of merit is derived from these points, the fill factor. The fill factor,  $FF$ , is considered a measure of quality of the solar cell and is found as:

$$FF = \frac{I_{MPP}V_{MPP}}{I_{SC}V_{OC}}$$

EQUATION 5.1

#### 5.1.1.1. Single-junction Solar Cells

The majority of commercially available terrestrial solar cells today are single-junction solar cells optimised to the AM1.5 spectrum. A brief discussion of silicon cell design considerations is given here, followed by an operational overview of single-junction solar cells.

#### Design Considerations

The principle feature of a solar cell is the p-n junction, of which the key parameter is the band gap energy. The band gap energy determines the both minimum amount of energy required for the promotion of an electron across the junction and the maximum amount of energy that can be extracted from a promoted electron. Beyond the p-n junction, there are a variety of design considerations in the manufacturing of a solar cell.

The thickness of a solar cell is typically found as hundreds of micrometres. The optimal thickness of a solar cell is a balance of absorption and current collection as well as practical considerations such as handling fragility and surface passivation requirements. Photon absorption is increased both by the application of anti-reflection coatings (ARCs), as discussed in section 3.2, ‘Material Properties’, and surface texturing for light trapping. Typical reductions in surface reflection achieved by these methods are from approximately 30% to approximately 10%.

The archetypal solar cell today is the silicon solar cell and has been since the 1940s. According to the Rutherford-Bohr model of the atom[119], silicon, in its pure form, contains 4 electrons in its outer shell. These are termed the valence electrons. In order to form a p-n junction and introduce an electric field to drive photogenerated electrons across the material, other elements are introduced to the silicon with fewer (n-type) or greater (p-type) electrons, termed valence electrons. This process is known as doping and the additional materials as dopants. Dopants are a design requirement of almost all solar cells. The front and back of the p-n junction are termed the emitter and base, respectively. Typically, phosphorus is the dopant for n-type silicon and boron the dopant for p-type silicon. The doping process tends to involve the application of a dopant material coating to the silicon wafer followed by placement in a furnace. Higher doping levels lead to a higher cell  $V_{OC}$  but also to crystal damage. Optimum doping levels are discussed in the literature[120, 121].

Given that the electrical resistivity of most active solar cell emitter materials is high (approximately  $2\text{k}\Omega\text{m}$  for silicon), the generated current is not effectively conducted away from the generation regions, so conducting grids are used to transport the current. These conducting grids, however, shade the emitter and thus reduce generated current. Optimisation of the emitter grid design is a topic of much discussion in the literature[122-124].

A major performance limitation in solar cell design is the loss of minority charge carriers by recombination[125]. There are several mechanisms for recombination such as: radiative recombination, Auger recombination[126] and Shockley Read Hall (SRH) recombination[127, 128]. The most common separation of recombination mechanisms is into diffuse and drift categories. Diffusive recombination is that that occurs in the bulk material of the cell (the quasi-neutral region) and drift that that occurs in the p-n junction (the depletion region). Minimising recombination in solar cells can be achieved by various methods, overviews of recombination and minimisation mechanisms in various solar cell technologies are given in[129-131].

## Operational Overview

In order to accelerate an electron from the emitter over the p-n junction, an incoming photon must have an energy of at least that of the band gap. The band gap is a material property that is optimised for terrestrial operation.

The characteristics of solar cell performance depend entirely on the nature of the illuminating source – the solar spectrum – because of this the performance of a solar cell ought to be quoted with a given spectrum. Commercialisation of any product is difficult to achieve without a set of standards that allow consumers to make comparisons between available technologies. Despite being an unrealistic indication of performance[132], in most circumstances, the AM1.5 spectrum is used for performance statistics.

A single-junction solar cell gap operates most efficiently with monochromatic light specific to its particular band gap. Due to the restrictions of a single band gap, only a set portion of the solar spectrum is utilised for energy conversion.

The solar spectrum is most commonly given as a wavelength intensity distribution, however for solid state considerations it is perhaps more intuitive to consider the solar spectrum as an energy distribution. Both representations of the AM1.5G solar spectrum are given in Figure 5.3 for reference.

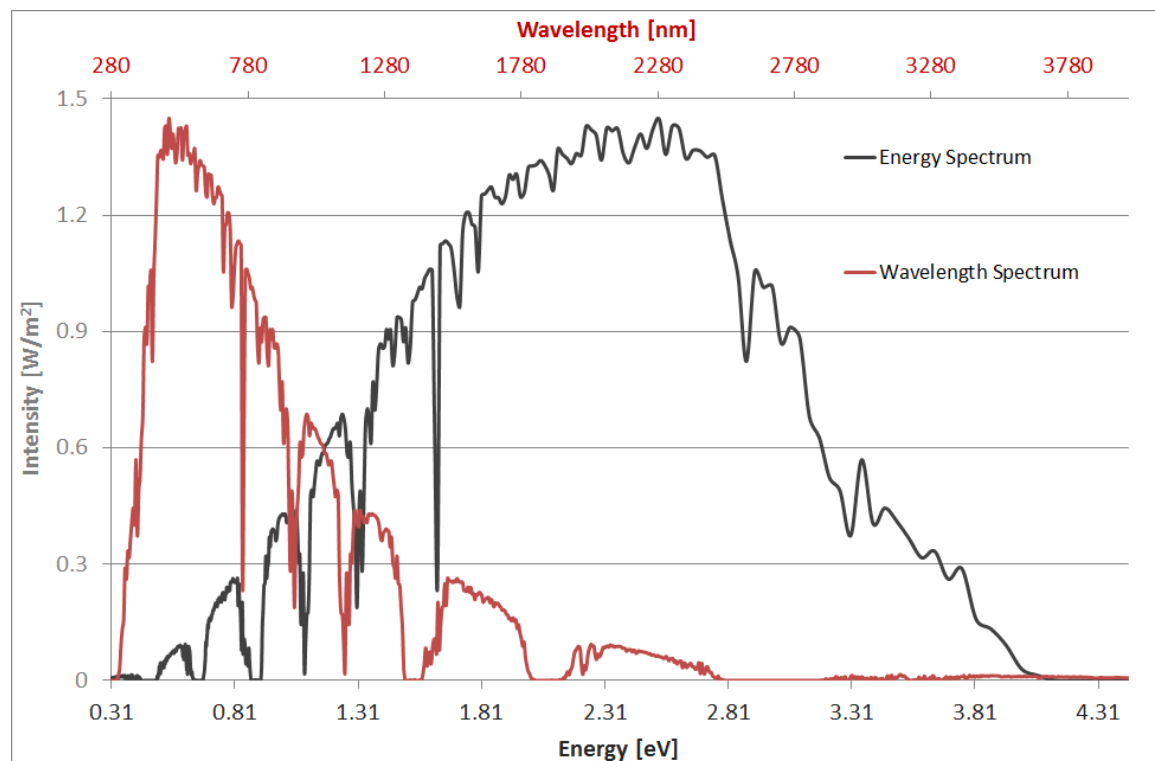


FIGURE 5.3: AM1.5G SOLAR SPECTRUM EXPRESSED AS INTENSITY OVER WAVELENGTH AND ENERGY

The maximal conversion portion of the solar spectrum for a typical, single-junction, silicon solar cell is shown in Figure 5.4.

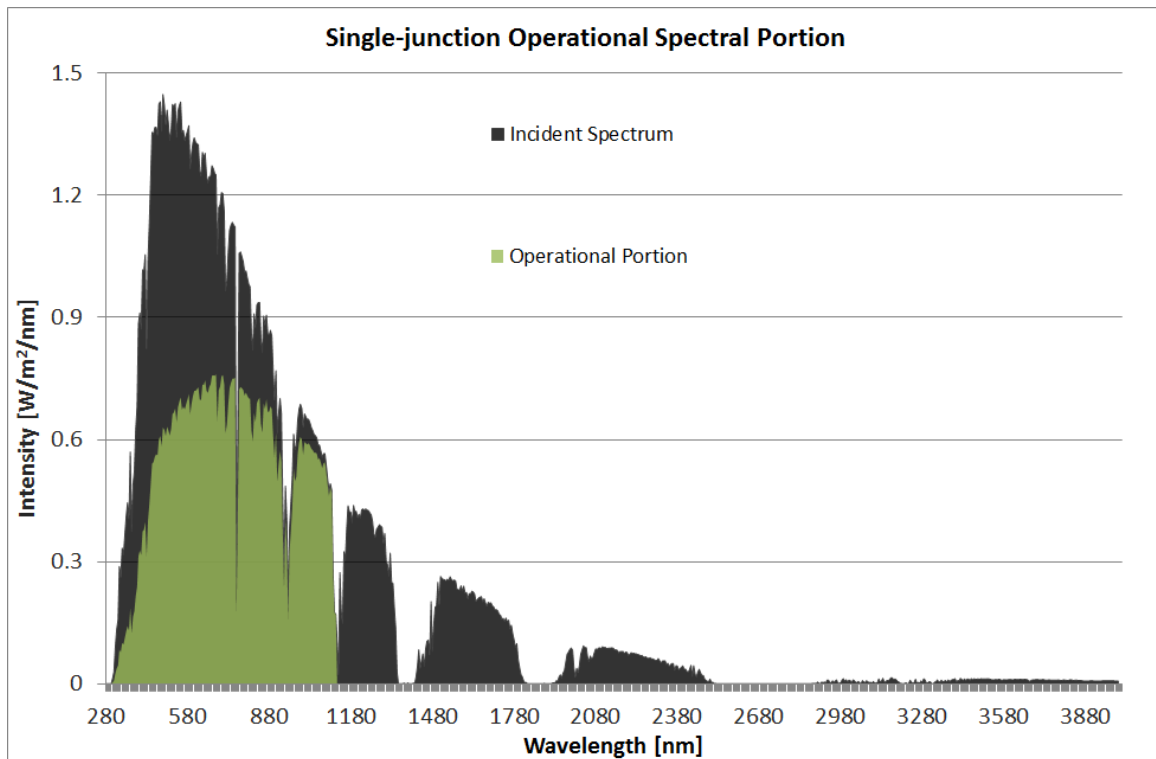


FIGURE 5.4: MAXIMUM OPERATIONAL PORTION OF THE AM1.5G SOLAR SPECTRUM FOR A SINGLE JUNCTION CELL WITH A 1.1eV BAND GAP

The above graph shows the maximum potential power extracted from the solar spectrum by a single band gap silicon cell with a 1.1eV band gap, a value typically seen in silicon cells. The band gap for this example cell is such that photons of wavelength greater than approximately 1100nm are energetically insufficient for electron excitation across it. Photons with wavelengths lower than the threshold can excite an electron across the band gap but the electrical energy generated by this excitation is limited by the band gap energy, hence the conversion efficiency drops with photon wavelengths below the threshold. The extra energy from the lower wavelength photons will likely generate heat through phononic interaction, increasing the temperature of the device and so further lowering the efficiency of the process[133]. In reality, there are extraction losses in the minority carrier collection process that diminish the energy available for conversion. A discussion of these loss mechanisms can be found in[134].

Band gap selection is an important process in cell production. The selection of a band gap is always a compromise considering the phenomena described above. The generally accepted optimal band gap for a single-junction solar cell under the spectrum from a black body at 6000K is: 1.31eV[135] whereas for the Air Mass 1.5 (AM1.5) spectrum, the optimal band gap is approximately 1.4eV.

Inherent in the single junction solar cell is an operational restriction that limits the conversion efficiency of the device. In the detailed balance argument presented in [136], the maximum efficiency of a single band gap converter is calculated as 32.5% under 1 Sun and 44.6% at maximum concentration under AM1.5 direct normal irradiance. However, under the same irradiance, the maximum efficiency of an infinite stack of tandem cells is calculated as 65.4% under 1 Sun and 85% under maximal solar concentration. The concept of maximal solar concentration is discussed in some detail in section 3.1.2.1, ‘Maximal Concentration’. Multi-junction solar cells exploit this phenomenon in the creation of high efficiency conversion devices.

### 5.1.1.2. Multi-junction Solar Cells

MJSCs utilise more of the energy available in the solar spectrum and are capable of surviving much higher concentration conditions than the conventional PV cell, this is in part due to the significant reduction in losses from phononic interactions in each junction as heat. The use of multiple junction band gaps paves the way to a much higher thermodynamic limiting efficiency for MJSCs than for their single junction counterparts.

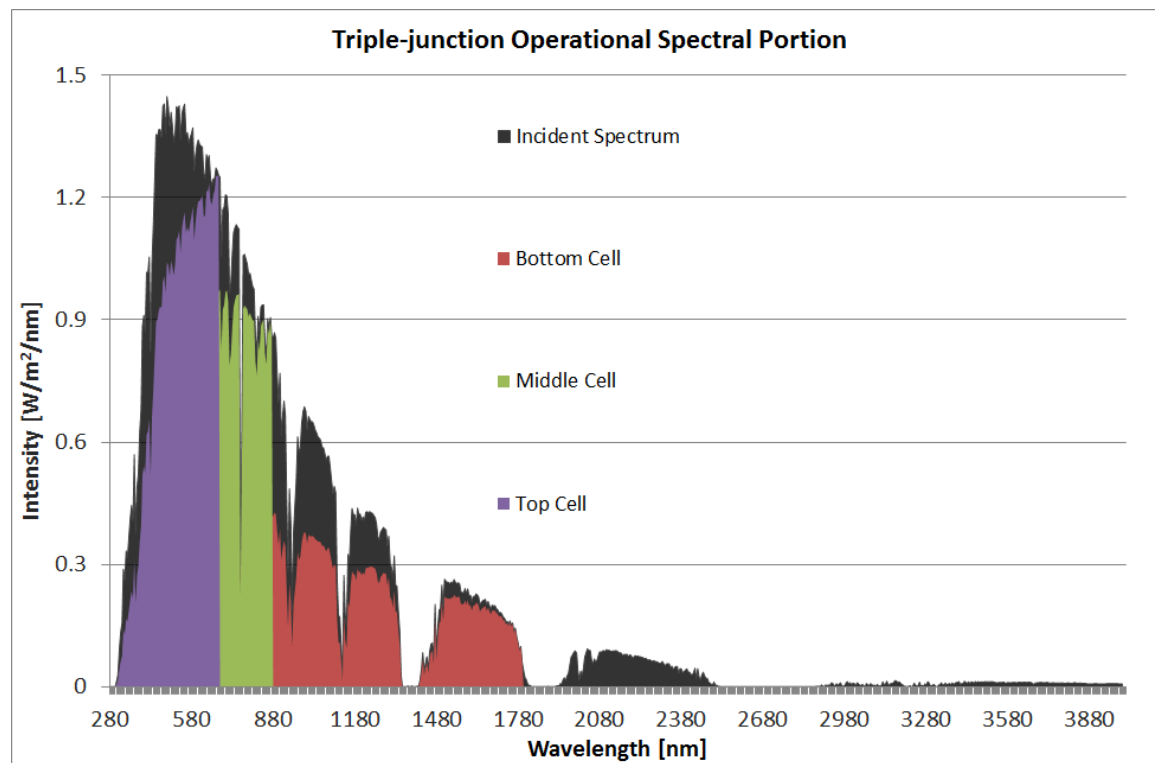


FIGURE 5.5: MAXIMUM OPERATIONAL PORTION OF THE AM1.5G SOLAR SPECTRUM FOR AN EXAMPLE TRIPLE JUNCTION CELL WITH BAND GAPS OF APPROXIMATELY 1.8eV, 1.4eV AND 0.7eV

A multi-junction cell can be considered as a stack of series connected single junction cells. This design serves to effectively partition the solar spectrum, as shown in Figure 5.5 for a triple junction cell design. The high energy photons are first filtered out with a high band gap material. This spectral filtering

occurs progressively with junctions of subsequently lower band gaps. These connected junctions are linked by tunnel junctions that effectively act as diodes, ensuring the forward flow of current and limiting minority carrier recombination losses.

In accordance with Kirchoff's circuit laws, the output power of the multi-junction solar cell is limited by the lowest current generating junction in the device.

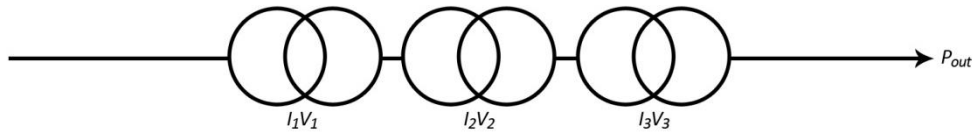


FIGURE 5.6: A STRING OF 3 POWER GENERATORS

The power,  $P_{out}$ , extracted from the triple junction solar cell is limited by the lowest current in the string, such that:

$$P_{out} = (V_1 + V_2 + V_3)I_{min}$$

EQUATION 5.2

Extending the equation to a string of  $i$  power generating devices:

$$P_{out} = \sum_i V_i I_{min}$$

EQUATION 5.3

Currently, it is typical to find triple-junction MJSCs for terrestrial CPV system application[137]. However, it should be noted that there is currently much focus on increasing the efficiency of MJSCs by the addition of further junctions[138]. The current limiting effect adds particular difficulty to the terrestrial optimisation of many-junction solar cells due to the dynamic nature of the terrestrial solar spectrum[139, 140]. The optimisation of many-junction structures is not so problematic for space applications, where the solar spectrum is approximately static, although there are other complications in this field such as the necessary consideration of radiation hardness[141].

Given that the multi-junction cell structure can be further optimised and that the cell efficiency increases under concentration, there is still further room for CPV efficiency improvements[142]. This stands CPV technology in a particularly good setting for future deployment in regions of high irradiance.

Further technological difficulties in CPV solar cells include problems arising from non-uniform illumination – producing significant local heating and ohmic losses[143] – and thermal management issues, especially with very high concentrations. For example, [144] showed that cell band gaps have

a temperature dependency over the CPV cell operational temperature range ( $25^{\circ}\text{C} - 75^{\circ}\text{C}$ ) that significantly affects the spectral response of the multi-junction cell. The results suggest that MJSCs are best optimised to a solar spectrum for an effective air mass greater than 1.5. For the most part, CPV systems are passively cooled, although some forms of CPV have been shown to benefit from active cooling techniques[145].

### 5.1.2. Synopsis

The solar cell is an energy conversion device that performs differently under different illuminations distributions, both in terms of the spectral composition and spatial distribution of power. The multi-junction solar cell can be considered as a series connected stack of single junction solar cells, each with different response parameters.

The purpose of this chapter is to provide an overview of solar cell modelling techniques; identify an appropriate model for the investigation of the varying profiles calculated in chapter 4, ‘Uncertainty’; and to use the model to investigate the differences in solar cell response to the aforementioned illumination profiles.

## 5.2. Solar Cell Modelling

Solar cell device modelling offers a method for predicting the behaviour of solar cells under varying conditions. The extent to which the conditions can be varied is directly related to the complexity of the model. Models of varying complexity are discussed here, initially 1D equivalent circuit models are discussed and their limitations explained. Spatially distributed, 2D, models are then divulged and the spatially resolved model used for this work identified.

### 5.2.1. 1D Solar Cell Modelling

There exist many models for approximating and predicting the behaviour of solar cells. The most commonplace of these models are the diode models. The diode models approximate the behaviour of the solar cell by means of an equivalent electrical circuit analysis. These models are one-dimensional by nature, as they implicitly assume that the operational parameters are distributed uniformly over the device. There are many proven circumstances for which one-dimensional models accurately represent the performance of solar cells. Generally, one-dimensional cell models perform particularly well when the cell is well manufactured, with homogeneous properties, and is operating under homogeneous irradiation.

### 5.2.1.1. One Diode Model

The typical solar cell uses a single p-n junction and is thus referred to as a single junction solar cell. Given that the p-n junction design has a unidirectional electric field, across which energetically promoted electrons are accelerated, the behaviour of a solar cell is similar to that of a diode.

Dark current is the current generated by the potential difference across the terminals caused by the connection of a load. This current acts in the opposite direction to the photocurrent and reduces the net current from its short circuit value. For an ideal diode the current,  $I$ , varies with voltage,  $V$  as:

$$I = I_0 \left( e^{\frac{qV}{k_B T}} - 1 \right)$$

EQUATION 5.4

*Where  $I_0$  is the diode saturation current,  $q$  the elementary charge of an electron,  $k_B$  Boltzmann's constant and  $T$  the temperature of the cell in degrees kelvin*

In reality, dark current shows a voltage dependency. This dark current dependence on voltage is characterised by a diode ideality factor,  $n$ , which is typically between 1 and 2:

$$I_{dark}(V) = I_0 \left( e^{\frac{qV}{nkT}} - 1 \right)$$

EQUATION 5.5

*Where  $n$  is the diode ideality factor*

The effect of a diode ideality factor greater than 1 is to reduce the fill factor of the solar cell. The diode ideality factor may be deduced from[146]:

$$\frac{1}{n} = \frac{kT}{q} \frac{d(\ln I_{dark})}{dV}$$

EQUATION 5.6

The I-V curve of the solar cell is thus similar to that of the conventional diode, with the current shifted in relation to the intensity of incident light. This is shown in Figure 5.7.

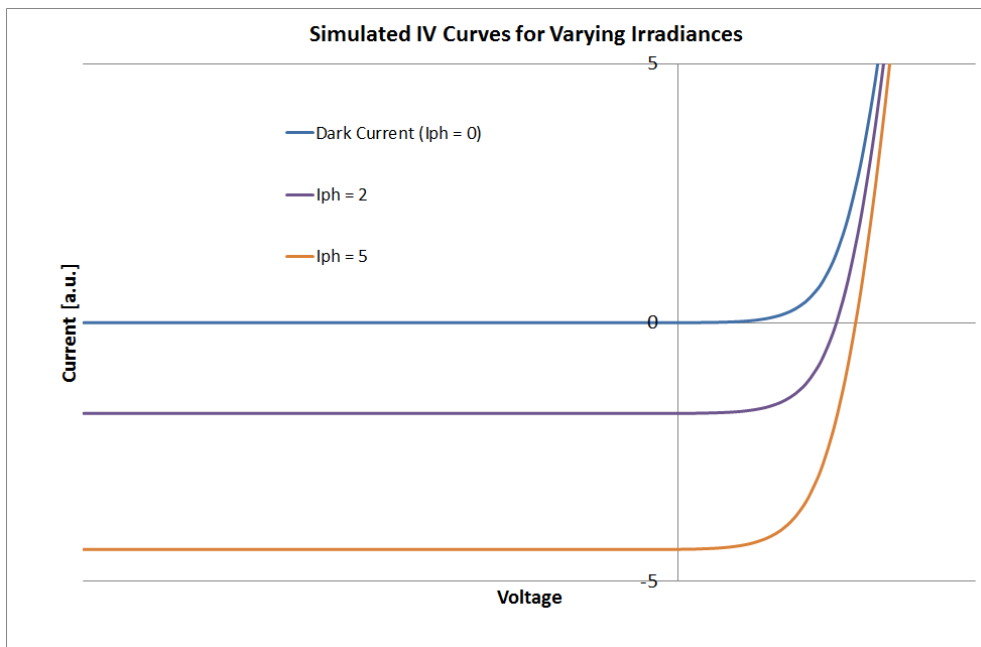


FIGURE 5.7: SOLAR CELL I-V CURVES - DARK I-V AND ILLUMINATED EXAMPLES

It is, however, common practice to consider the I-V curve in the positive quadrant. The electrical behaviour of the solar cell can thus be approximated as:

$$I = I_0 \left( e^{\left( \frac{qV}{nkT} \right)} - 1 \right) + I_{ph}$$

EQUATION 5.7

Where  $I_{ph}$  is the photocurrent – the induced by the incident light

The diode model alone produces representative solar cell I-V curves yet with unrealistically high fill factors and thus efficiencies. In order to better recreate the I-V curve of a solar cell, parasitic resistances are included in the model. The following equivalent circuit diagram shows the single diode solar cell model with parasitic resistances:

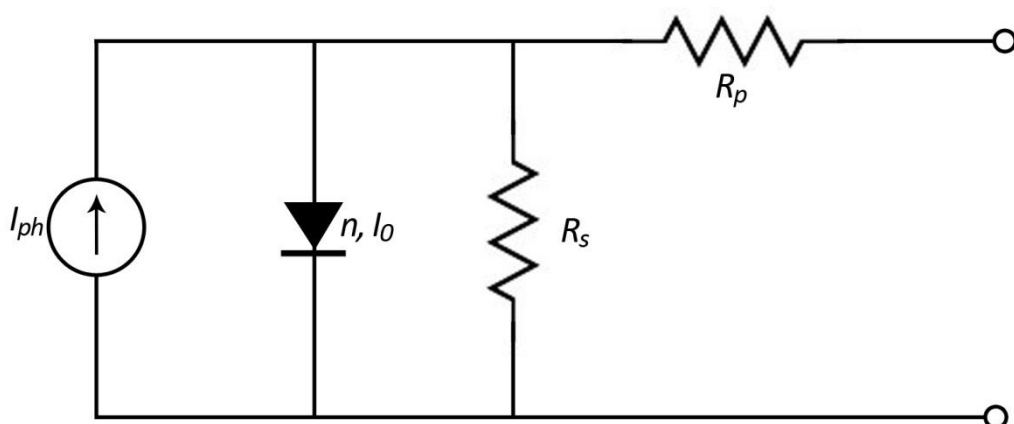


FIGURE 5.8: SCHEMATIC REPRESENTATION OF THE SINGLE DIODE MODEL WITH PARASITIC RESISTANCES

With the inclusion of these parasitic resistances, the single diode model is extended to:

$$I = I_{ph} - I_0 \left( e^{\frac{q(V+IR_s)}{nK_bT}} - 1 \right) - \frac{V + IR_s}{R_p}$$

EQUATION 5.8

Where  $R_s$  is the series resistance, representing the contact resistances and  $R_p$  is the parallel resistance representing the current leakage at the sides of the cell

Generally speaking, the effects of the series and parallel resistances are to alter the gradient of the I-V curve post and pre-knee, respectively.

Although this model is more inclusive than the other, it does not account for the variation of recombination with applied voltage. A solution to this problem is to introduce a second diode.

#### 5.2.1.2. Two Diode Model

The two-diode model better accounts for the recombination of electron-hole pairs in the both in the cell bulk (diffusive) and in the p-n junction (drift). The equivalent circuit diagram is as follows:

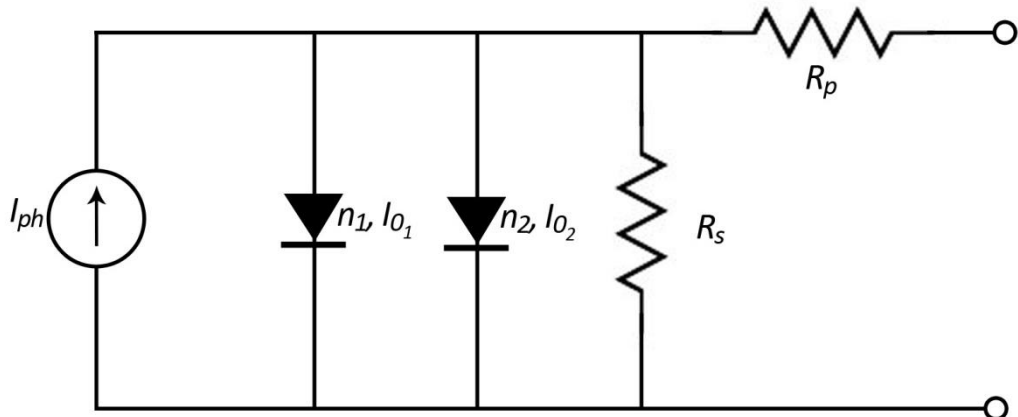


FIGURE 5.9: SCHEMATIC OF THE TWO DIODE MODEL

Resulting in the following equation for current:

$$I = I_{ph} - I_{01} \left( e^{\frac{q(V+IR_s)}{n_1 K_b T}} - 1 \right) - I_{02} \left( e^{\frac{q(V+IR_s)}{n_2 K_b T}} - 1 \right) - \frac{V + IR_s}{R_p}$$

EQUATION 5.9

Where  $I_{01}$  and  $n_1$  are the diode saturation current and ideality factor of diode 1, respectively; and  $I_{02}$  and  $n_2$  the diode saturation current and ideality factor of diode 2, respectively

For a crystalline silicone device, the diffuse and drift currents are normally accounted for by the use of diode ideality factors of approximately 1 and 2.

In both in the single diode with parasitic resistances model and the two diode model, the extraction of I-V curve points is not trivial. The equation cannot be simply rearranged in terms of current or voltage, it can however be rearranged to zero and function minimisation methods applied to extract the I-V curve. Such function minimisation methods as, for example, the simplex method[147], the Newton-Raphson method[148] and quasi-Newton methods[149] can be used to extract the an I-V curve from the above equations.

### 5.2.2. Spatially Resolved Device Modelling

One-dimensional device modelling by its very nature assumes that all areas of the cell are equal both in terms of their electrical, behavioural properties and the illumination that is incident upon them. It is therefore not possible to investigate the effects of inhomogeneities, either in terms of material consistency or illumination, using one-dimensional models.

For the most part, material inhomogeneity is not an issue of concern for performance modelling as material problems tend to be spotted and removed during the production process, thanks largely to fast, investigative imaging techniques such as electroluminescence and photoluminescence. These imaging systems can be used either post-production or in-line in the manufacturing process. They are relatively inexpensive systems and serve well in the effective rejection of faulty solar cells/modules.

In localised flat plate photovoltaic systems where space (or cost of space) is not a concern, homogeneity of illumination is not a modelling concern as the system can be arranged in such a way that there is no self-shading or indeed obstructive object shading. However, due to financial and optimisation concerns this is rarity in practice. Most real life systems exhibit some form of objective and/or self-shading and thus are inhomogeneously illuminated. This can prove detrimental to system performance[150].

Another example of inhomogeneous illumination is CPV systems. Optical concentration systems in CPV cast the approximately homogenously distributed surface light to a focus for conversion. The concentration process creates inhomogeneities and distortions. Often attempts are made to mitigate this by the integration of light diffusers or homogenisers into the concentration system, although inhomogeneities of some degree are inevitable in CPV solar cell illumination. In order to correctly account for the effects of inhomogeneous illumination in solar cell modelling, spatially resolved device models are required.

Spatially distributed solar cell models have been developed in order to analyse the effects of inhomogeneities. In these models, a solar cell is segregated into a number of subsections that are defined by localised properties. There are several validated distributed solar cell models available in

the literature[151-154]. Typically, a subcell is defined as one-dimensional cell model with added lateral connections. The model used herein is that of[155]. Many of the established distributed cell models are extremely computationally expensive and therefore slow in operation. An advantage of the model used herein is that it is relatively fast – due to matrix optimisation, Gaussian elimination and Newton-Raphson minimisation methods.

The distributed model structure is demonstrated schematically in Figure 5.10 and Figure 5.11.

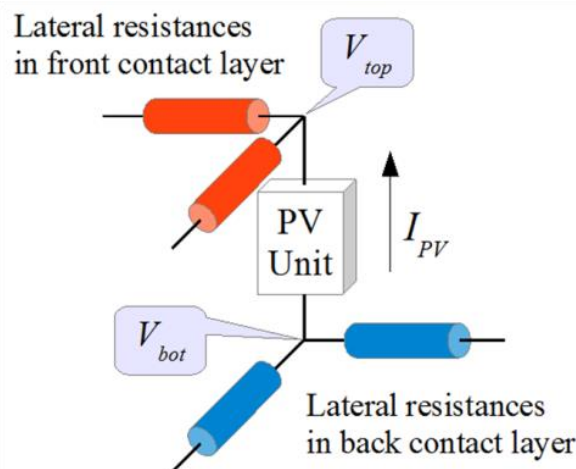


FIGURE 5.10: DISTRIBUTED CELL MODEL SINGLE PV UNIT SCHEMATIC

The PV subcell unit is a 1D cell model. The 1D model used here is the one-diode model (see section 5.2.1.1, ‘One Diode Model’). This is effectively an arbitrary choice, although it is used here for simplicity.

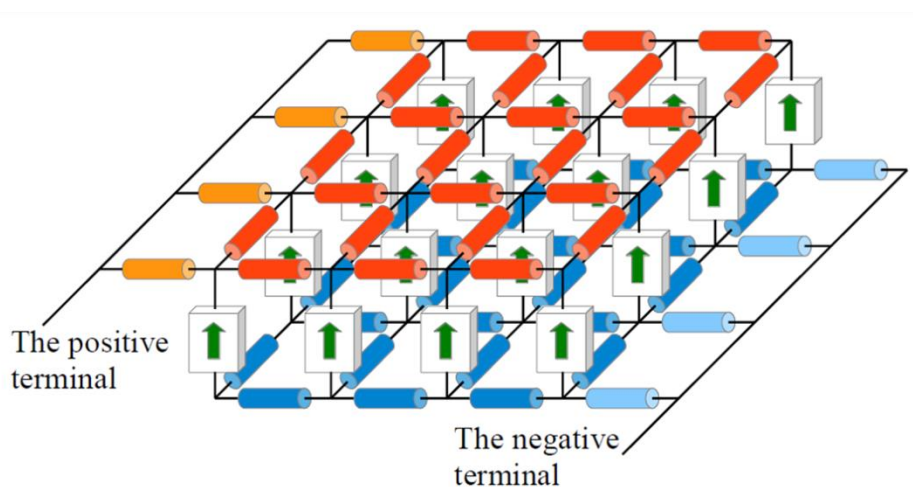


FIGURE 5.11: DISTRIBUTED CELL MODEL INTERCONNECTED SUBCELL MESH SCHEMATIC

In the following section, the profiles generated in chapter 4, ‘Uncertainty’ are here used as inputs to the PVONA spatially distributed simulation tool to analyse the electrical output and the variations in

cell power output that can be attributed to the uncertainties explored therein. The profiles of choice are the ideal and erroneous plano-convex lens and the ideal and erroneous square Fresnel lens.

### 5.3. Illumination – Electrical Modelling

The spatially distributed cell model, PVONA[155], is here used to analyse the differences in solar cell performance for variations in illumination profiles as presented in chapter 4, ‘Uncertainty’.

In order to provide a deeper insight into the electrical behaviour of the device, the I-V curves are plotted alongside spatially distributed operational parameters from the resolved subcells, namely: operational current, junction voltage and terminal voltage.

#### 5.3.1. PVONA Cell Design & Parameter Definition

For simulation purposes, a 99 by 99 subcell grid was chosen with the following design:

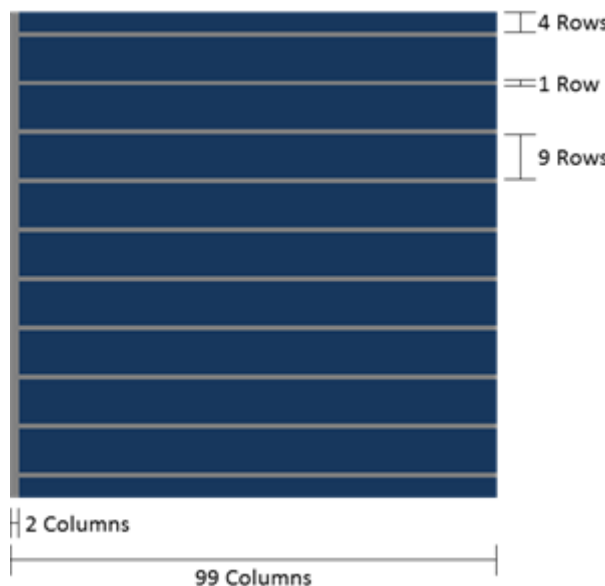


FIGURE 5.12: PVONA CELL DESIGN

The two subcell categories, represented chromatically, are: **active cell material** and **conductive fingers/busbar**. The cell design includes a busbar, 10 fingers and 11 active cell regions. The busbar is 2 by 99 subcells, the 10 fingers 97 by 1 subcells, 8 of the active cell regions 97 by 9 subcells and 2 of the active cell regions 97 by 4 subcells in area. The one diode model PV unit subcell parameters were defined as:

$$I_0 = 5 \times 10^{-7} \text{ A/cm}^2$$

$$R_S = 0.05 \Omega \text{cm}^2$$

$$R_P = 8.35 \times 10^4 \Omega \text{cm}^2$$

$$n = 1.4$$

For reference, the photocurrent density,  $J_{ph}$ , at STC illumination conditions ( $1000\text{W/m}^2$ , AM1.5G) for the active cell material was defined as  $0.035\text{A/cm}^2$ . This was set to zero for the metal contact grid. The interconnecting subcell lateral resistances for the active material were set to  $10\Omega$  and for the metal grid to  $1\text{m}\Omega$ .

### 5.3.2. Plano-convex Lens – Lens Manufacturing Uncertainty

The illumination variations presented in section 4.2, ‘Lens Parameter Variation Effects’, for the plano-convex lens are here analysed. Firstly, the illumination profile is translated into a spatially resolved profile as appropriate for a PVONA input map (see Figure 5.13 and Figure 5.16). The resultant operational parameters of the solar cell are then presented as extracted from the PVONA model.

#### 5.3.2.1. Profile 1

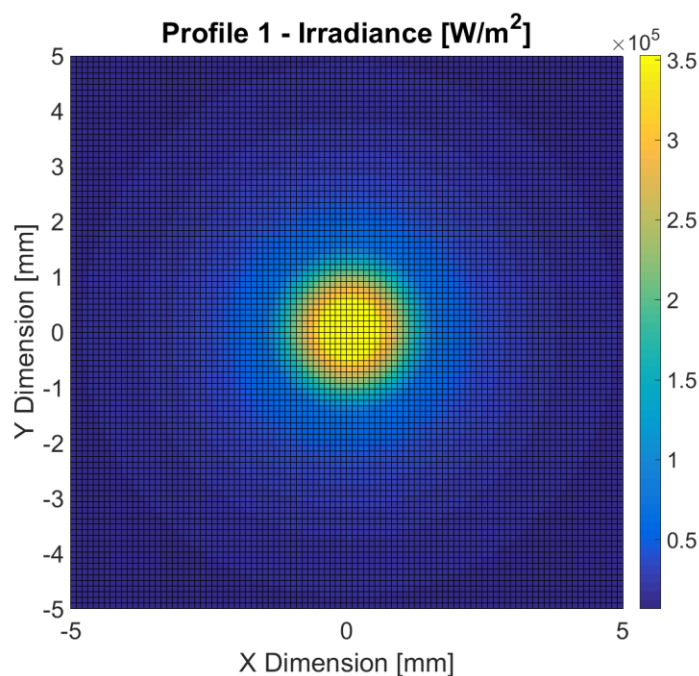


FIGURE 5.13: PLANO-CONVEX LENS RAY TRACED ILLUMINATION PROFILE - EXAMPLE 1

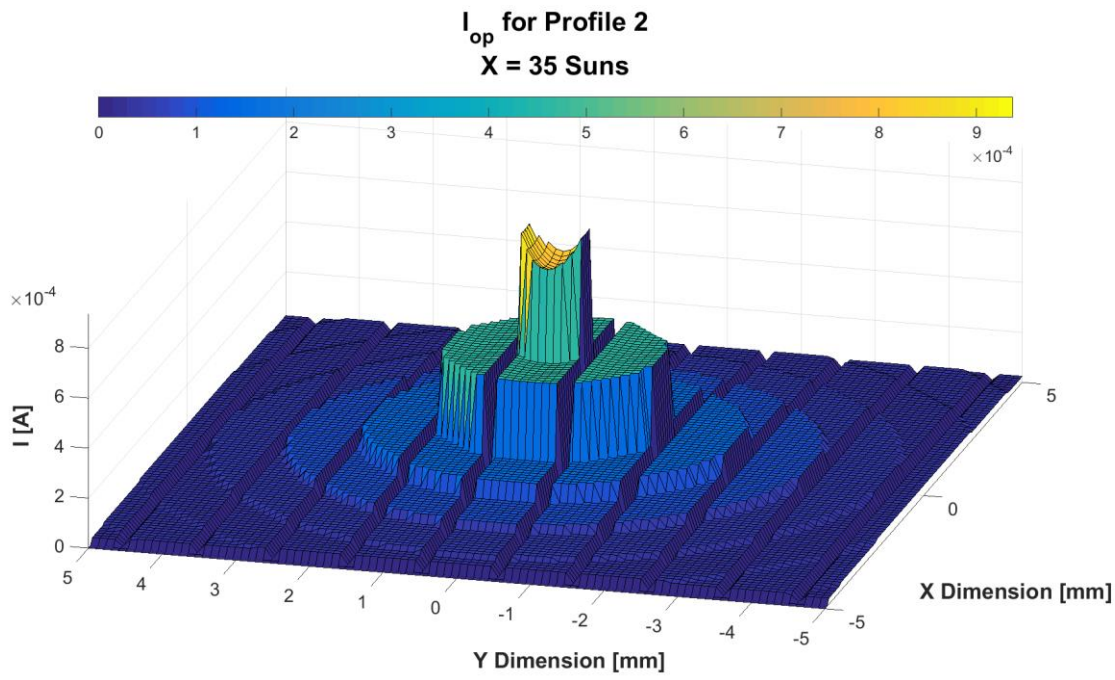


FIGURE 5.14: SPATIALLY RESOLVED SUBCELL OPERATIONAL CURRENT - EXAMPLE 1 (PLANO-CONVEX TRACE)

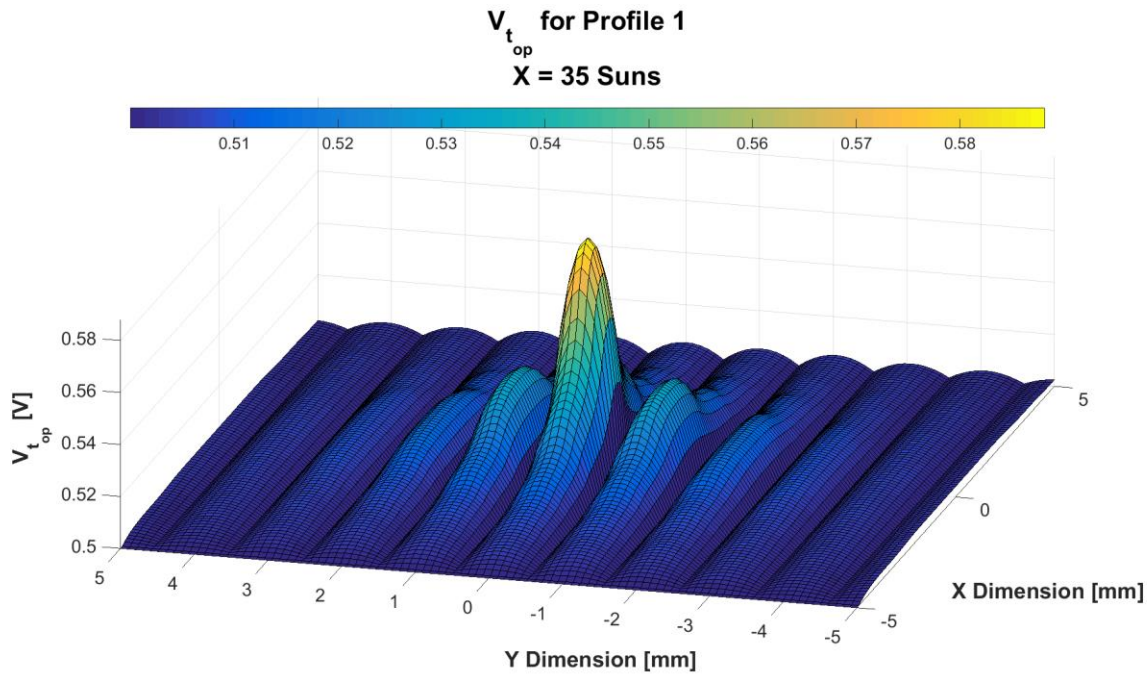


FIGURE 5.15: SPATIALLY RESOLVED OPERATIONAL TERMINAL VOLTAGE - EXAMPLE 1 (PLANO-CONVEX TRACE)

### 5.3.2.2. Profile 2

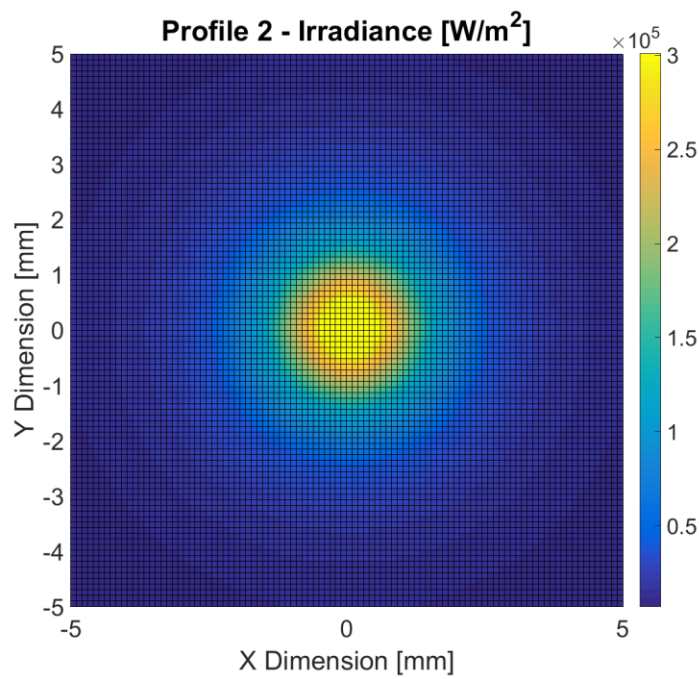


FIGURE 5.16: PLANO-CONVEX LENS RAY TRACED ILLUMINATION PROFILE - EXAMPLE 2

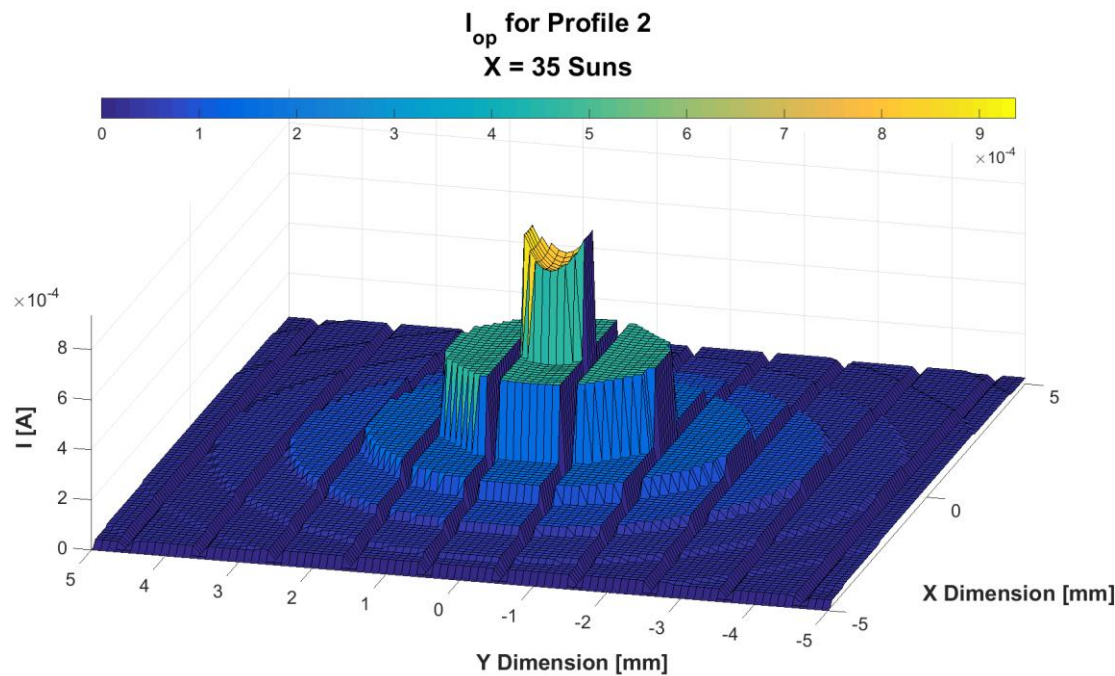


FIGURE 5.17: SPATIALLY RESOLVED SUBCELL OPERATIONAL CURRENT - EXAMPLE 2 (PLANO-CONVEX TRACE)

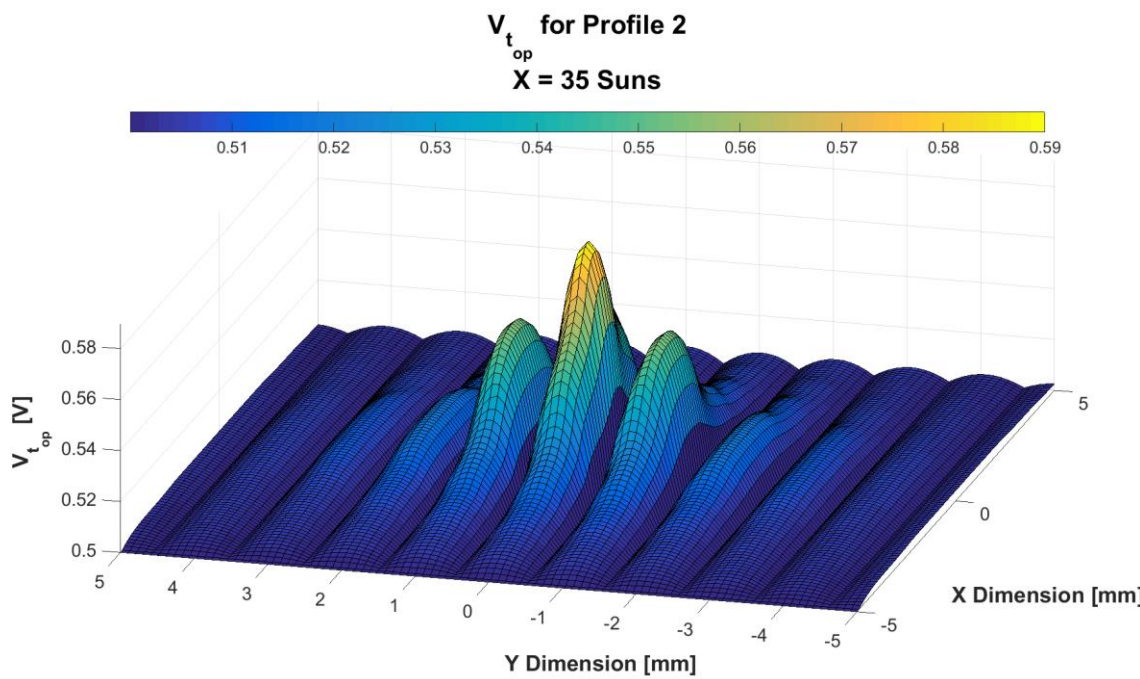


FIGURE 5.18: SPATIALLY RESOLVED OPERATIONAL TERMINAL VOLTAGE - EXAMPLE 2 (PLANO-CONVEX TRACE)

### 5.3.2.3. IV Curve Comparison

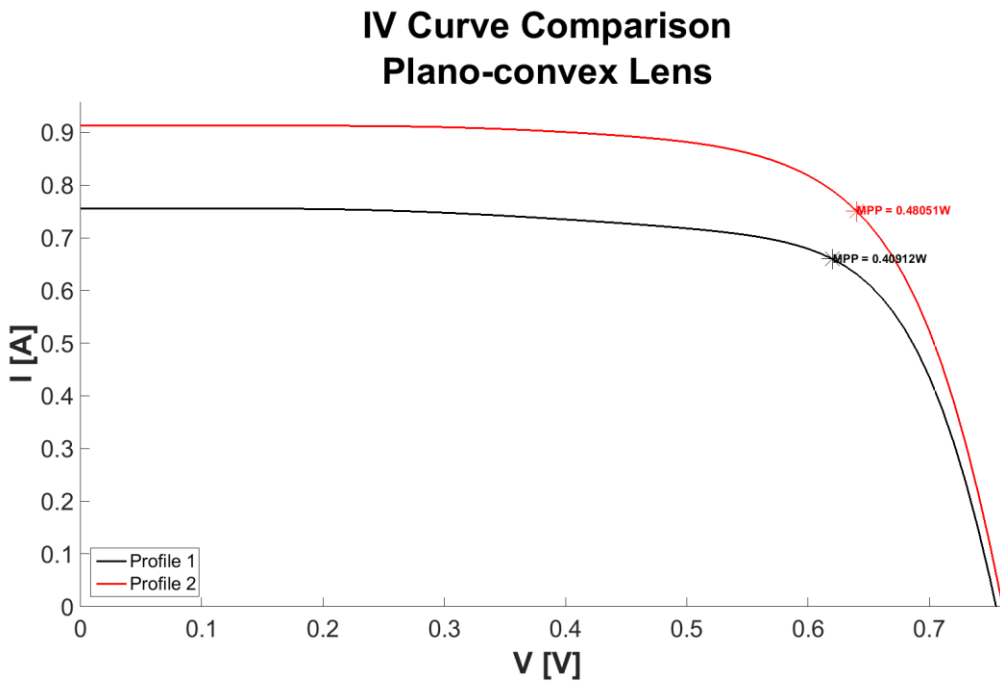


FIGURE 5.19: EXAMPLE I-V CURVES COMPARISON WITH HIGHLIGHTED MAXIMUM POWER POINT (PLANO-CONVEX TRACE)

The resultant I-V curves for the modelled cell behaviour show a substantial difference in the maximum power point of these I-V curves – a variation of approximately 15%. Given that the irradiance distribution over the cell is different in both cases, some of this difference can be apportioned to the difference in net power. The ratio of net powers over both profiles is approximately 0.87. The relative difference in maximum power point is then approximately 4%.

### 5.3.3. Square Fresnel Lens – Module Framing Uncertainty

The illumination variations presented in section 4.3, ‘Framing Variation Effects’, for the plano-convex lens are here analysed. Firstly, the illumination profile is translated into a spatially resolved profile as appropriate for a PVONA input map (see Figure 5.21 and Figure 5.25). The resultant operational parameters of the solar cell are then presented as extracted from the PVONA model.

#### 5.3.3.1. Profile 1

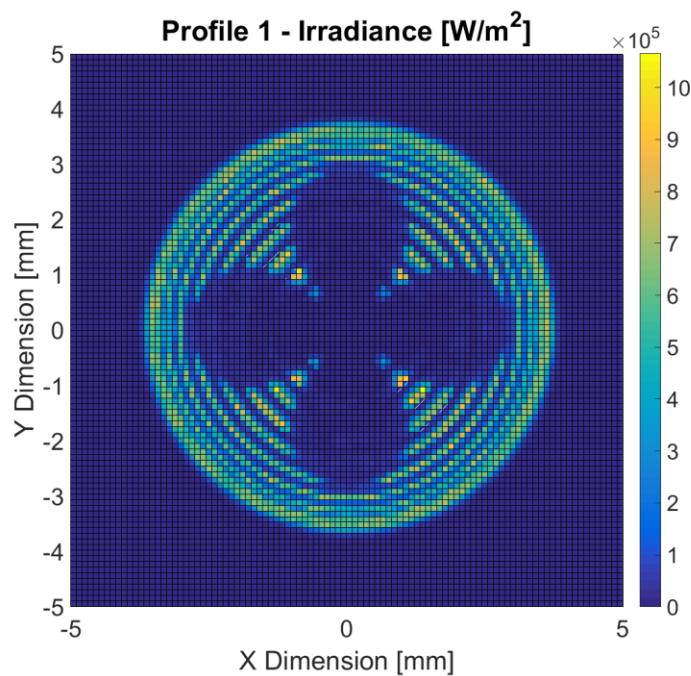


FIGURE 5.20: FRESNEL LENS RAY TRACED ILLUMINATION PROFILE - EXAMPLE 1

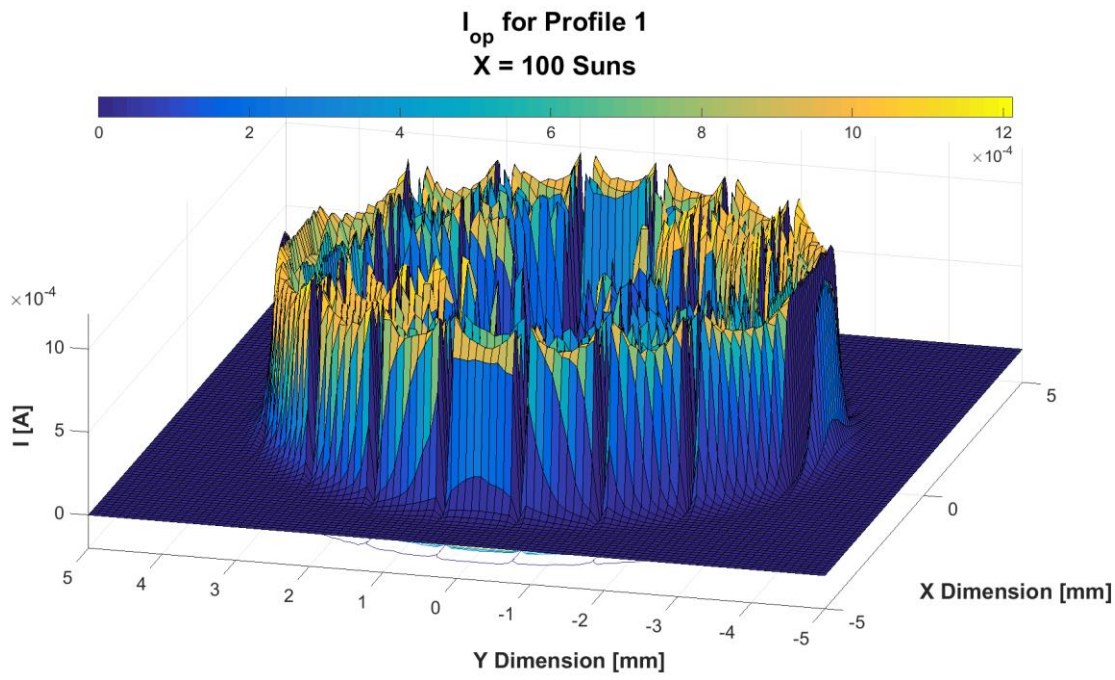


FIGURE 5.21: SPATIALLY RESOLVED SUBCELL OPERATIONAL CURRENT - EXAMPLE 1 (FRESNEL TRACE)

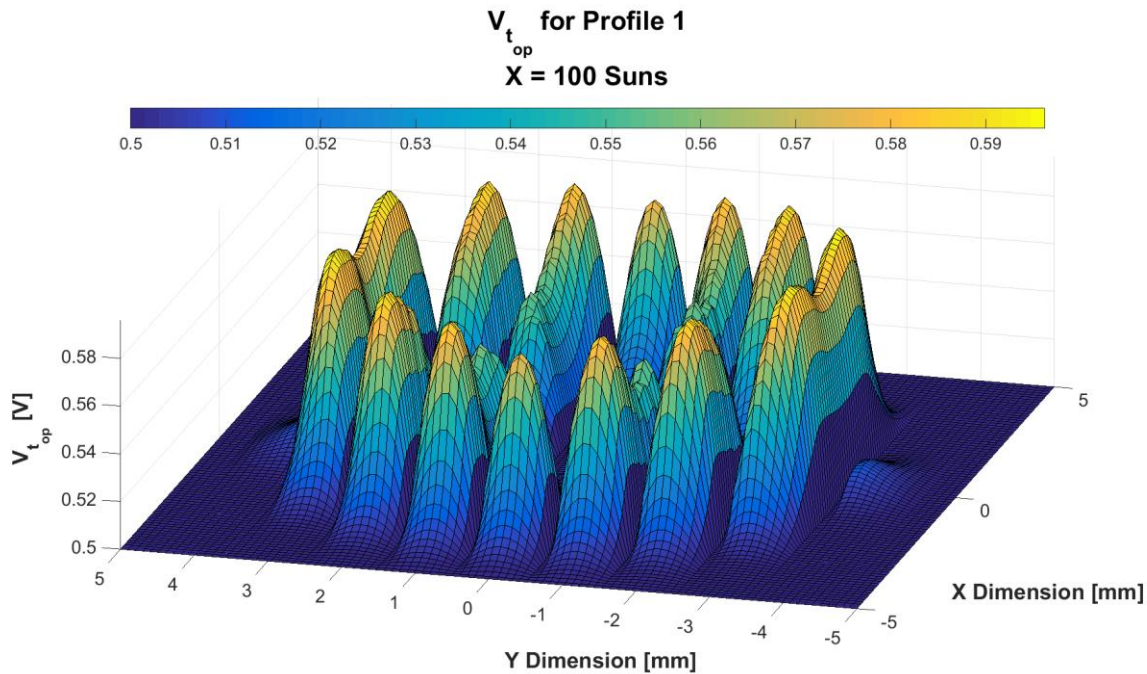


FIGURE 5.22: SPATIALLY RESOLVED OPERATIONAL TERMINAL VOLTAGE - EXAMPLE 1 (FRESNEL TRACE)

### 5.3.3.2. Profile 2

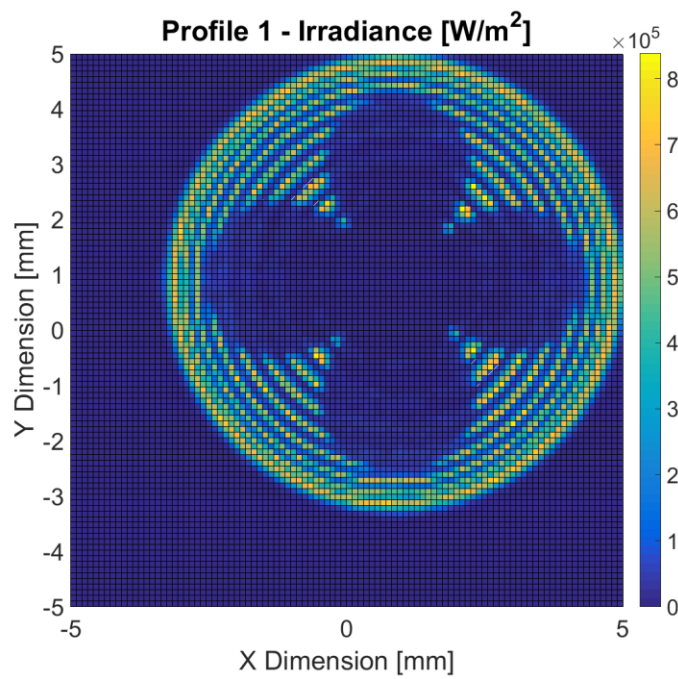


FIGURE 5.23: FRESNEL LENS RAY TRACED ILLUMINATION PROFILE - EXAMPLE 2

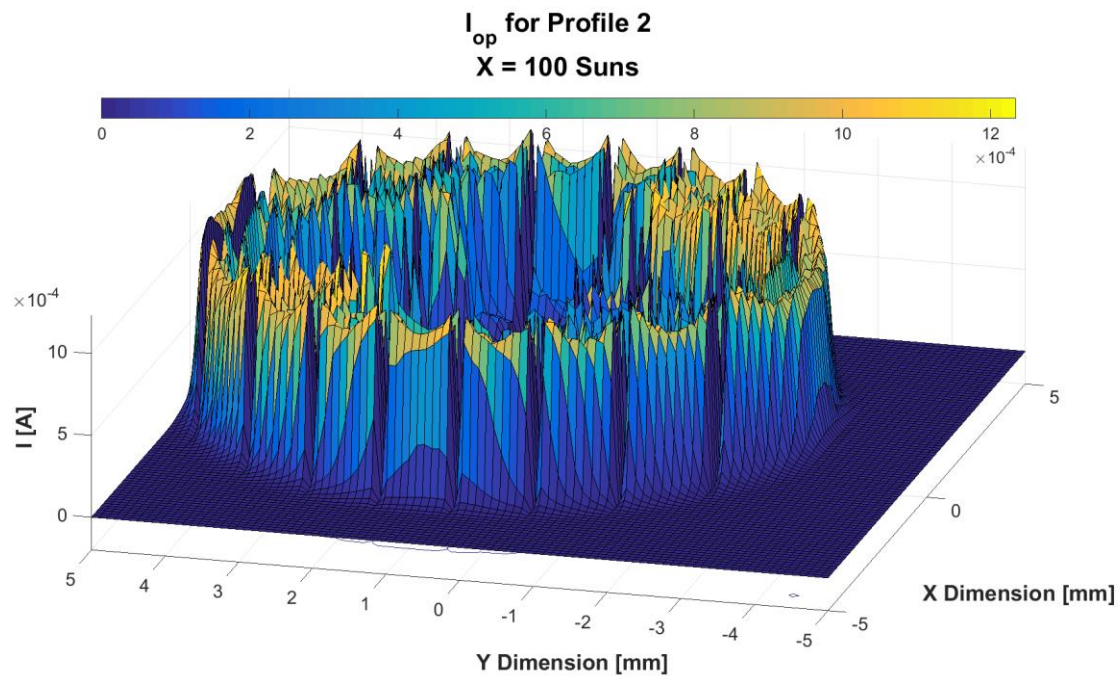


FIGURE 5.24: SPATIALLY RESOLVED SUBCELL OPERATIONAL CURRENT - EXAMPLE 2 (FRESNEL TRACE)

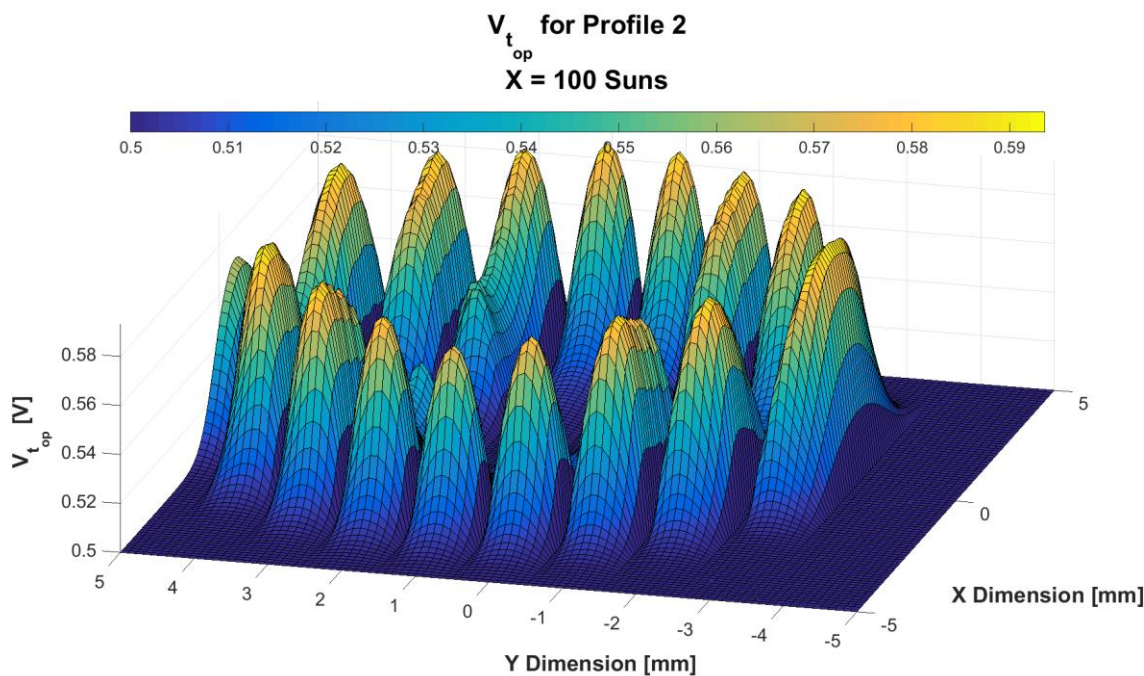


FIGURE 5.25: SPATIALLY RESOLVED OPERATIONAL TERMINAL VOLTAGE - EXAMPLE 2 (FRESNEL TRACE)

### 5.3.3.3. IV Curve Comparison

#### IV Curve Comparison Fresnel Lens

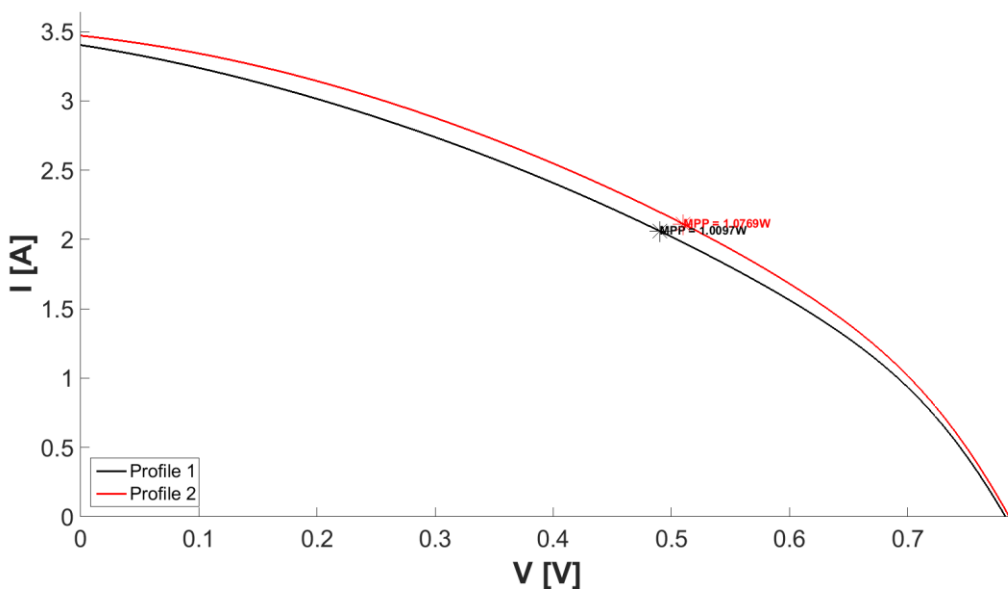


FIGURE 5.26: EXAMPLE I-V CURVES COMPARISON WITH HIGHLIGHTED MAXIMUM POWER POINT (FRESNEL TRACE)

The resultant I-V curves for the modelled cell behaviour show a substantial difference in the maximum power point of these I-V curves – a variation of approximately 6%. In this case the net power over the cell was kept constant at exactly 100 Suns. Thus the full 6% difference can be attributed to the difference in illumination profile.

## 5.4. Conclusions

The spatially resolved modelling approach used here has highlighted differences in solar cell performance under realistic inhomogeneous illumination profiles. It has been shown that the simulated power output variations resulting from the manufacturing production tolerances presented in chapter 4, 'Uncertainty', are significant.

The ideal and erroneous illumination profiles resulting from the example plano-convex lens specification produced a 15% difference in modelled cell IV curve maximum power point, with a 4% relative difference attributed to illumination profile deviations. The ideal and erroneous illumination profiles resulting from the example square Fresnel lens module framing component specifications produced a 6% difference in modelled cell IV curve maximum power point as a result of spatial illumination distribution differences. These substantial differences in power output further highlight the need for the consideration of production and manufacture tolerances in CPV system simulation.

# 6. Conclusions

## 6.1. Thesis Conclusions

The focus of this work was to develop a modelling chain specifically for CPV modules, to identify the constraints of existing modelling methods, and to use the developed chain to highlight CPV design issues that may otherwise not be considered. This has been achieved through the implementation of a CPV model which pays particular attention to the description of incident insolation and the representation of optical components and intricacies of ray tracing methods.

### 6.1.1. Input Modelling

A comparison of existing methods of insolation modelling has been performed and conditions of validity drawn. It has been shown that the use of approximated, static solar distribution models are invalid for CPV modelling where the input aperture half angle of the optical concentration system approaches the angle subtended by the Sun – approximately 0.266°. In particular, the sub-degree range often used by HCPV systems requires the use of spatially resolved insolation models for optical analysis.

An input/output analysis of Buie's model has been performed and inconsistencies identified. A case study of the CSR = 0.3 distribution revealed overestimations of irradiation harvest by the standard model of 0.5 – 1.5% of DNI for a system operation region commonplace in HCPV systems. Such overestimations are significant enough to play a predatory role in CPV energy harvest performance predictions. An extended light source distribution model improvement has been proposed and has been shown to give more consistent CSR output. For an input CSR resolution of 0.01, the mean and standard deviation of the output CSRs are improved from 0.937 and 0.107 to 1.000 and 0.005.

Significant trend differences for spectral variations in the spectral bandwidths corresponding to the multi-junction sub-cell regions have been identified, providing further insight into the variation of MJ cell performance under real insolation conditions.

### 6.1.2. Optical Modelling

A ray tracing program has been developed specifically for the investigation of CPV optical component behaviour under a variety of illumination profiles. Given the computational expense of high resolution spatial and spectral modelling, a spectrally banded ray trace analysis has been performed in the active spectral ranges of a typical triple-junction solar cell. Spectrally banded optical analyses corresponding

to these ranges show significant dependencies on air mass and CSR. The nature of these dependencies changes with each spectral band. Banded beam proportion contributions can change by as much as 10% in absolute terms within the air mass range of 1 to 3.

Spectrally banded illumination profiles for example plano-convex and Fresnel lens designs have been presented. These illumination profiles vary for each insolation model. The extended light source analysis shows significant variation between the power distributions at the receiver plane in each spectral band. These inhomogeneities are mostly unaccounted for when using the alternative, assumptive static insolation models. This further compounds the argument for using extended light source Sun descriptions in CPV modelling, as the spectral variations identified by this model will likely have a negative impact on the performance of MJSCs due to subcell current limiting effects.

### 6.1.3. Uncertainty Modelling

The effects of manufacturing tolerance levels in lens and framing component production have been analysed through the design and specification of ideal components and the comparison of the resultant optical system performance with their possible erroneous counterparts. Notable differences are found in the solar cell illumination profiles in the case of both lens and framing component manufacture errors.

In the case of the lens error investigation, a 15% variation in maximum intensity value was found alongside a linear shift in the focal crossover point of approximately 0.2mm, although the optical efficiency of the lens was found to be the same. For the framing component variation, a linear shift of the focal centre of the cell illumination profile of approximately 0.85mm over a 10mm by 10mm solar cell was identified. These variations are significant. The results here highlight the need for the consideration of production tolerance errors in CPV system simulations. Simply put, when dealing with small components, small errors can make a big difference to performance.

An analysis of wind loading on an example 3m by 3m by 0.1m CPV array, modelled as a solid cuboid, has been performed using real, 2 second resolution wind data. The results highlight the chaotic nature of wind loading force on CPV systems. From the two example days analysed here, a maximum loading force of 1.4kN on the CPV array was calculated, corresponding to a wind speed of approximately 13m/s. This is well within the typical operating range of a CPV tracking array. The load force calculation method presented here could well be used as part of a tracking error analysis or tracking system design process.

### 6.1.4. Electrical Modelling

The electrical modelling of solar cells under realistic illumination profiles as defined in chapter 4, ‘Uncertainty’ has been performed. These profiles were similar in total power as integrated over the full solar cell area, yet were somewhat different in distribution of this power over the surface of the cell although, where appropriate, a separation of the net power and image distortion effects has been given. Given the differences in illumination profiles, a 1D cell model would have been insufficient for assessing the cell behaviour. A spatially resolved cell model was identified and used for the investigation and significant differences were found in the modelled cell output for the example ideal and erroneous component systems

A difference of approximately 15% was found in the maximum power point of the IV curve for the plano-convex lens, of which a 4% relative difference can be attributed to illumination image distortions. A difference of approximately 6% was found for the framing component error system with the Fresnel lens primary. These differences in power production further highlight the need for the inclusion of production and manufacture tolerance uncertainty in the simulation of CPV system performance.

## 6.2. Recommendations for Future Work

A CPV module specific modelling chain has been developed in this work and has proven successful in highlighting the constraints of existing modelling techniques. However, the model could benefit from further adaptations and inclusions. Following the form of the thesis presentation, these recommendations are separated according to the model subsection.

### 6.2.1. Input Modelling

The improved and extended spatially resolved insolation model of chapter 2, ‘Input’, is based on an improvement of a single, empirically derived model. There have been some recent introductions in the field of CSR modelling and it would be prudent to compare the results generated by the use of these models. It is also thought that inclusion of the variation of the apparent size of the Sun could well prove significant for certain scenarios and that the model would benefit from the addition of this feature.

The CSR is an essential parameter for the definition of the solar profiles herein and it is unfortunate that there is little data available as to the variation of CSR and the geographic dependence on this variation. It is recognised that the probabilistic framework for the simulation of location specific CSR variation as employed in 2.4.3.3, ‘Annual Energy Harvests – Example Case’, is not ideal, it is simply the

best option for the determination of CSR variation at the time of publication. It would prove most useful to support existing measurement campaigns and provide extra insight into the variation of CSR as a function of meteorological variables and to redo the analyses performed herein with the consideration of this information.

### 6.2.2. Optical Modelling

It is recognised that the focus on the investigation of the ideally derived Fresnel lens here is somewhat limiting on the useful extent of system evaluation. The Fresnel lens is an ever evolving lens with many different design approaches. This work would benefit from the specific optical analysis of different lens designs and the inclusion of these lens designs as optional in the model. Given that the presented ray trace modelling principle revolves around facet-bound rays with specified surface origins and projected intersections, the model is inherently extensible. Thus, the inclusion of different lens designs is a matter of process switching with appropriate algorithmic differences.

Given the limitations of geometric optics – that it is only a valid investigation tool when the interactive media of concern are of dimensions far greater than the wavelength of light considered – the resolution of these ray trace investigations is somewhat limited. As the useful portion of the solar spectrum extends to a wavelength of 4000nm, the limit of geometric optics as a valid investigative tool is not tested at the 1mm resolution as the ratio of dimensions is 250. However, reducing the dimensions of investigation to, for example, a profile resolution of just 0.1mm is then testing this condition of validity. The condition of validity of geometric optics is effectively reduced from the idea of relative squares – that  $n^2 \gg n$  when  $n$  is large. It is thus challenged in this region. In order to reduce the effective resolution of these investigations light should be considered not as rays governed by the principles of geometric optics but as waves governed by the wave equations.

The methods of 2D and 3D ray tracing presented herein differ in that the 2D method works by aggregated dispersion methods and the 3D trace works by a bucket capture method. Dispersive 3D ray trace methods through plane limited shape determination and resolved area integrations would provide a useful alternative mechanism for the investigation of optical effects.

Furthermore, the ray tracing methods presented herein can be used to investigate optical systems designed specifically to reduce the effects of chromatic aberration, such as Cartesian oval derived systems, and also as a design basis for the specification of new CPV optical system designs.

### 6.2.3. Uncertainty Modelling

The production and manufacture uncertainty modelling performed here was purely demonstrative. Example systems were defined and possible deviations, due to production uncertainties near the

extreme end of the quoted tolerance limits, were investigated. This served well the purpose of highlighting the need for the inclusion of uncertainty modelling in CPV system simulation, yet further insight into the effects of realistic errors can be gained by a more holistic approach to uncertainty modelling.

Uncertainties are typically well described with Gaussian probability distribution functions. This form of uncertainty description lends itself well to Monte Carlo simulation methods in the acquisition of statistical information about the integrated ramifications of individual component uncertainties. Employing such methods in the assessment of CPV performance uncertainty would provide useful information that could be used to form the basis of sensitivity analysis, adding robustness to the system design process.

The wind loading force model presented in section 4.4, ‘Sun Tracking – Wind Loading’, could be extended to an induced tracking error model, given that enough was known about the behaviour of tracking systems under variable load. Furthermore, wind loading force could itself be improved with the acquisition of 3D wind direction data, as all wind directions in the above model were assumed horizontal.

#### 6.2.4. Electrical Modelling

The use of the PVONA spatially resolved solar cell model proved sufficient for analysing differences in cell performance under inhomogeneous illumination. However, in order to fully exploit the capability of the input and optical models presented in chapters 2 and 3, respectively, an extension to a multi-junction cell model is required. This would allow for the individual assessment of the subcell behaviours under illumination profiles inclusive of chromatic aberrations and provide further insight into the output power losses determined by current limiting.

## 7. References

1. NREL. *Research Cell Efficiency Records*. 2015 [cited 2015 26/01/2015]; Available from: [http://www.nrel.gov/ncpv/images/efficiency\\_chart.jpg](http://www.nrel.gov/ncpv/images/efficiency_chart.jpg).
2. Sala, G. and A. Luque, *Past Experiences and New Challenges of PV Concentrators*, in *Concentrator Photovoltaics*, A.L. Luque and A. Viacheslav, Editors. 2007, Springer.
3. Masson, G., et al., *Global Market Outlook for Photovoltaics 2013 - 2017*. 2013, Brussels: European Photovoltaic Industry Association (EPIA).
4. Stolte, W., *Engineering and Economic Evaluation of Central-station Photovoltaic Power Plants*. 1992, Electrical Power Research Institute: California, USA.
5. Symko-Davies, M., R. Noufi, and S. Kurtz. *Identifying Critical Pathways to High-performance*. in *29th IEEE PVSC*. 2002. Louisiana, USA.
6. Whisnant, R., S. Johnston, and J. Hutchby, *Economic Analysis and Environmental Aspects of Photovoltaic Systems*, in *Handbook of Photovoltaic Science and Engineering*, A. Luque, Editor. 2003, John Wiley & Sons Ltd: Chichester, England. p. 971-1003.
7. Kurtz, S., A. Lewandowski, and H. Hayden, *Recent Progress and Future Potential for Concentrating Photovoltaic Power Systems*. 2004, NREL: Colorado, USA.
8. McConnell, R., *Concentrator photovoltaic technologies: Review and market prospects*. Refocus, 2005: p. 35-39.
9. Winston, R., et al., *Nonimaging Optics* 2005, Oxford, England: Elsevier.
10. Leutz, R. and A. Suzuki, *Lenses and Mirrors for Solar Energy*, in *Nonimaging Fresnel Lenses: Design and Performance of Solar Concentrators*. 2001, Springer: Berlin, Germany.
11. Kopp, G. and J. Lean, *Lower Value of Solar Irradiance: Evidence Climate Significance*. Geophysical Research Letters, 2011. **38**.
12. Walraven, R., *Calculating the Position of the Sun*. Solar Energy, 1978: p. 393–397.
13. Walraven, R., *Erratum*. Solar Energy, 1979: p. 195.
14. Pitman, C. and L. Vant-Hull, *Errors in Locating the Sun and Their Effect on Solar Intensity Predictions*. 1978, American Section of the International Solar Energy Society: Denver, USA. p. 701-706.
15. Lamm, L., *A New Analytic Expression for the Equation of Time*. Solar Energy, 1981: p. 465.
16. Michalsky, J., *The Astronomical Almanac's Algorithm for Approximate Solar Position (1950-2050)*. Solar Energy, 1988: p. 227-235.
17. Duffet-Smith, P., *Practical Astronomy with your Calculator*. 1992, Cambridge, England: Cambridge University Press.
18. Reda, I. and A. Andreas, *Solar Position Algorithm for Solar Radiation Applications*. Solar Energy, 2004: p. 577-589.
19. Reda, I. and A. Andreas, *Solar Position Algorithm for Solar Radiation Applications*. 2008, NREL: Colorado, USA.
20. Remund, J. and S. Kunz, *MeteoNorm handbook, Part I, review and software*. 2003, MeteoTest: Switzerland.

21. Wilcox, S., *National Solar Radiation Database 1991–2010 Update: User’s Manual*. 2012, NREL: Colorado, USA.
22. Wong, L. and W. Chow, *Solar Radiation Model*. Applied Energy, 2001: p. 191–224.
23. Grindley, P.C., W.J. Batty, and S.D. Probert, *Mathematical model for predicting the magnitudes of total, diffuse, and direct-beam insolation*. Applied Energy, 1995: p. 89–110.
24. Zakšek, K., T. Podobnikar, and K. Oštir, *Solar radiation modelling*. Computers & Geosciences, 2005. **31**(2): p. 233–240.
25. Gueymard, C., *Parameterized Transmittance Model for Direct Beam and Circumsolar Spectral Irradiance*. Solar Energy, 2001: p. 325-346.
26. Planck, M., *The Theory of Heat Radiation*. 1914, Philadelphia, USA: P. Blakiston's Son & Co.
27. IOCCG, *Minutes of the 7th IOCCG Committee Meeting*. 2002: Villefranche-sur-Mer, France.
28. Thuillier, G., et al., *The Solar Spectral Irradiance from 200 to 2400 nm as Measured by the Solspec Spectrometer from the Atlas and Eureca Missions*. Solar Physics, 2003: p. 1-22.
29. Kutner, M., *Astronomy: A Physical Perspective*. 2003, Cambridge, England: Cambridge University Press.
30. Schoenberg, E., *Theoretische Photometrie*. 1929, Berlin: Springer.
31. Kasten, F. and A. Young, *Revised Optical Air Mass Tables and Approximation Formula*. Applied Optics, 1989: p. 4735-4738.
32. Young, A., *Air Mass and Refraction*. Applied Optics, 1994: p. 1108-1110.
33. Pickering, K., *The Southern Limits of the Ancient Star Catalog and the Commentary of Hipparchos*. The International Journal of Scientific History, 2002. **12**: p. 3-27.
34. Gueymard, C., D. Myers, and K. Emery, *Proposed Reference Irradiance Spectra for Solar Energy Systems Testing*. Solar Energy, 2002: p. 443-467.
35. Myers, D., K. Emery, and C. Gueymard, *Revising and Validating Spectral Irradiance Reference Standards for Photovoltaic Performance*. Journal of Solar Energy Engineering, 2004: p. 645-653.
36. Gueymard, C., *SMARTS, A Simple Model of the Atmospheric Radiative Transfer of Sunshine: Algorithms and Performance Assessment*. 1995, Florida Solar Energy Center: Florida, USA.
37. NREL. *Reference Solar Spectral Irradiance: ASTM G-173*. [cited 2015 26/01/2015]; Available from: <http://rredc.nrel.gov/solar/spectra/am1.5/ASTMG173/ASTMG173.html>.
38. Mermoud, A. and T. Lejeune. *Pefrformance Assessment of a Simulation Model for PV Modules of Any Available Technology*. in *25th European Photovoltaic Solar Energy Conference and Exhibition*. 2010. Valencia, Spain.
39. Friesen, G., et al. *Intercomparison of Different Energy Prediction Methods within the European Project PERFORMANCE - Results on the 2nd Round Robin*. in *24th European Photovoltaic Solar Energy Conference and Exhibition*. 2011. Hamburg, Germany.
40. Friesen, G., et al., *kWh/Wp measurements & predictions of 13 different PV modules*, in *IEEE Photovoltaic Specialists Conference*. 2011: Seattle, USA.
41. Huld, T., et al., *Mapping the performance of PV modules, effects of module type and data averaging*. Solar Energy, 2010: p. 324-338.
42. Blair, N., et al., *System Advisor Model, SAM*. 2014, NREL: Colorado, USA.

43. Yastrebova, N., *High-efficiency Multi-junction Solar Cells: Current Status and Future Potential*. 2007, Centre for Research in Photonics, University of Ottawa: Ontario, Canada.
44. Roccia, J., et al., *SOLFAST, a Ray-Tracing Monte-Carlo Software for Solar Concentrating Facilities*. Journal of Physics: Conference Series, 2012.
45. Shea, S., *Evaluation of Glare Potential for Photovoltaic Installations*. 2012, Suniva, Inc: Norcross, USA.
46. Lovegrove, K. and J. Pye, *Fundamental Principles of Concentrating Solar Power Systems*. Concentrating Solar Power Technology ed. K. Lovegrove and W. Stein. 2012, Philadelphia, USA: Woodhead Publishing Limited.
47. Buie, D., A. Monger, and C. Dey, *Sunshape Distributions for Terrestrial Solar Simulations*. Solar Energy, 2003: p. 113-122.
48. Neumann, A., et al., *Representative Terrestrial Solar Brightness Profiles*. Solar Energy, 2002: p. 325-333.
49. Stafford, B., et al., *Tracker accuracy: field experience, analysis, and correlation with meteorological conditions* in *IEEE Photovoltaic Specialists Conference - PVSC*. 2009: Philadelphia, USA. p. 002256-002259.
50. Puliaev, S., et al., *Solar diameter observations in 1998-1999*. 2000, Observatório Nacional: Rio de Janeiro, Brazil.
51. Noël, F., *On Solar Radius Variations Observed with Astrolabes*. Solar Physics, 2005: p. 127-141.
52. Gueymard, C., *Spectral Circumsolar Radiation Contribution To CPV*, in *CPV 6*. 2010: Freiburg, Germany.
53. Peharz, G., J. Ferrer-Rodriguez, and A. Bett, *Shaping the Angular Divergence at Sun Simulators for Concentrator Modules*, in *24th European Photovoltaic Solar Energy Conference and Exhibition*. 2009: Hamburg, Germany.
54. Noring, J., D. Grether, and A. Hunt, *Circumsolar Radiation Data: The Lawrence Berkeley Laboratory Reduced Data Base*. 1991, NREL: Colorado, USA.
55. NREL. *Circumsolar Radiation Data: The Lawrence Berkeley Laboratory Reduced Data Base*. [cited 2015 26/01/2015]; Available from: <http://rredc.nrel.gov/solar/pubs/circumsolar/>.
56. NREL. *Circumsolar Radiation Data: The Lawrence Berkeley Laboratory Reduced Data Base*. [cited 2015 26/01/2015]; Available from: [http://rredc.nrel.gov/solar/old\\_data/circumsolar/](http://rredc.nrel.gov/solar/old_data/circumsolar/).
57. Wilbert, S., et al. *Measurement of Solar Radiance Profiles with the Sun and Aureole Measurement System (SAM)*. in *SolarPACES*. 2011. Grenada, Spain.
58. Wilbert, S., R. Pitz-Paal, and J. Jaus. *Circumsolar Radiation and Beam Irradiance Measurements for Focusing Collectors*. in *ES1002: Workshop*. 2012.
59. Reis Neto, E., et al., *Observed Variations of the Solar Diameter in 1998/2000*. Solar Physics, 2003: p. 7-21.
60. Buie, D., *Corrigendum to "The effective size of the solar cone for solar concentrating systems"*. Solar Energy, 2005: p. 568-570.
61. Buie, D., C. Dey, and S. Bosi, *The Effective Size of the Solar Cone for Solar Concentrating Systems*. Solar Energy, 2003: p. 417-427.
62. Meteotest. *Meteonorm Software*. [cited 2015 26/01/2015]; Available from: <http://meteonorm.com/en/downloads>.

63. DeVore, J., et al., *Retrieving Properties of Thin Clouds from Solar Aureole Measurements*. Journal of Atmospheric and Oceanic Technology, 2009: p. 2531-2548.
64. Schubnell, M., *Sunshape and Its Influence on the Flux Distribution in Imaging Solar Concentrators*. Journal of Solar Energy Engineering, 1992: p. 260 - 266.
65. Cole, I.R., T.R. Betts, and R. Gottschalg, *Solar Profiles and Spectral Modeling for CPV Simulations*. IEEE Journal of Photovoltaics, 2012: p. 62-67.
66. Winston, R., *Light Collection within the Framework of Geometrical Optics*. Journal of the Optical Society of America, 1970: p. 245-247.
67. Marcuse, D., *Light Transmission Optics*. 1972, New Jersey, USA: Van Nostrand-Reinhold.
68. Welford, W., *Aberrations of the Symmetrical Optical System*. 1974, New York, USA: Academic Press.
69. Born, M. and E. Wolf, *Principles of Optics*. 1975, Oxford, England: Pergamon.
70. Leutz, R. and A. Suzuki, *Classification of Solar Concentrators*, in *Nonimaging Fresnel Lenses*. 2001, Springer: Berlin, Germany. p. 7-14.
71. Vant-Hull, L., *Concentrator Optics*, in *Solar Power Plants*, C. Winter, R. Sizmann, and L. Vant-Hull, Editors. 1991, Springer: Berlin, Germany. p. 84-133.
72. Wollaston, W.H., *A method of examining refractive and dispersive powers, by prismatic reflection*. Philosophical Transactions of the Royal Society, 1802. **92**: p. 365-380.
73. Yang, W., et al., *Omnidirectional light absorption in thin film silicon solar cell with dual anti-reflection coatings*. Solar Energy, 2011. **85**(10): p. 2551-2559.
74. Aiken, D.J., *High performance anti-reflection coatings for broadband multi-junction solar cells*. Solar Energy Materials and Solar Cells, 2000. **64**(4): p. 393–404.
75. Valdivia, C.E., et al. *Optimization of antireflection coating design for multijunction solar cells and concentrator systems*. in *Photonics North 2008, Optoelectronic and Integrated Devices*. 2008. SPIE.
76. Victoria, M., et al., *Antireflective coatings for multijunction solar cells under wide-angle ray bundles*. Optics Express, 2012: p. 8136-8147.
77. Kaminski, P.M., F. Lisco, and J.M. Walls, *Multilayer Broadband Antireflective Coatings for More Efficient Thin Film CdTe Solar Cells*. Journal of Photovoltaics, 2014. **4**(1): p. 452-456.
78. Linn, N.C., et al., *Self-assembled biomimetic antireflection coatings*. Applied Physics Letters, 2007. **91**.
79. Sun, C., et al., *Templated fabrication of large area subwavelength antireflection gratings on silicon*. Applied Physics Letters, 2007. **91**.
80. Reis, F., et al. *Validation of a Model to Study CPV Silicon Solar Cells Behaviour Under Inhomogeneous Irradiation*. in *27th European Photovoltaic Solar Energy Conference*. 2012. Frankfurt, Germany.
81. Vossier, A., et al. *Characterisation of Triple-junction Solar Cells Under High Concentration and Inhomogeneous Illumination*. in *24th European Photovoltaic Solar Energy Conference*. 2009. Hamburg, Germany.
82. Sunex. *Sunex Products*. [cited 2015 26/01/2015]; Available from: <http://www.optics-online.com/>.

83. Thorlabs. *Thorlabs Products.* [cited 2015 26/01/2015]; Available from: <http://www.thorlabs.de/navigation.cfm>.
84. *Optical Components for Fire Control Instruments; General Specification Governing the Manufacture, Specification and Inspection of.* 1963, US Army: Washington D.C., USA.
85. *Optics and Electro-Optical Instruments - Optical Elements and Assemblies.* 2009, Committee for Optics and Electro-Optical Instruments: Washington DC, USA.
86. Hornung, T., M. Steiner, and P. Nitz, *Estimation of the Influence of Fresnel Lens Temperature on Energy Generation of a Concentrator Photovoltaic System*, in *6th International Conference on Concentrating Photovoltaic Systems*. 2011: Las Vegas, USA.
87. Kovacevic, M. and A. Djordjevich. *Temperature Dependence Analysis of Mode Dispersion in Step-Index Polymer Optical Fibers.* in *International School and Conference on Photonics*. 2009. Belgrade, Serbia.
88. Kasarova, S., N. Sultanova, and I. Nikolov, *Temperature Dependence of Refractive Characteristics of Optical Plastics.* Journal of Physics: Conference Series, 2010. **253**.
89. Schult, T., et al. *Temperature Dependence of Fresnel Lenses for Concentrating Photovoltaics.* in *2nd International Workshop on Concentrating Photovoltaic Power Plants: Optical Design and Grid Connection*. 2009. Darmstadt, Germany.
90. Rumyantsev, V., et al. *Thermal Regimes of Fresnel Lenses and Cells in "All-Glass" HCPV Modules.* in *6th International Conference on Concentrating Photovoltaic Systems*. 2010. Valencia, Spain.
91. Hornung, T., et al., *Fresnel Lens Concentrator with Improved Thermal Behavior*, in *6th International Conference on Concentrating Photovoltaic Systems*. 2011: Las Vegas, USA.
92. Van Riesen, S., et al., *Concentrix solar's progress in developing highly efficient modules*, in *7th International Conference on Concentrating Photovoltaic Systems*. 2011: Nevada, USA.
93. Mehta, K. and W. Coulbourne, *Wind Loads: Guide to the Wind Load Provisions of ASCE 7-10.* 2013, American Society of Civil Engineers.
94. Saavedra, A., *Diseño de un Servomecanismo Seguidor Solar para un Instrumento Registrador de la Irradiación Solar directa.* 1963, Universidad Técnica Federico Santa María: Valparaíso, Chile.
95. Gay, C., J. Yerkes, and J. Wilson, *Performance Advantages of Two-axis Tracking for Large Flat-plate Photovoltaic Energy Systems*, in *6th IEEE Photovoltaic Specialists Conference*,. 1982: San Diego, USA. p. 1368-1371.
96. Akhmedyarov, K., et al., *Economic Efficiency of the FV-500 Solar Photoelectric Station with Automatic Tracking of the Sun.* Applied Energy, 1986: p. 44-47.
97. Peippo, K. and P. Lund, *Optimal Sizing of Grid-connected PV-systems for Different Climates and Array Orientations: A Simulation Study.* Solar Energy Materials and Solar Cells, 1994: p. 445-451.
98. Bari, S., *Optimum Slope Angle and Orientation of Solar Collectors for Dfferent Periods of Possible Utilization.* Energy Conversion and Managment, 2000: p. 855-860.
99. Yakup, H. and A. Malik, *Optimum Tilt Angle and Orientation for [a] Solar Collector in Brunei Darussalam.* Renewable Energy, 2001: p. 223-234.
100. Kostić, L., T. Pavlović, and Z. Pavlović, *Optimal Design of Orientation of PV/T Collector with Reflectors.* Applied Energy, 2010: p. 3023-2029.

101. Heslop, S. and I. MacGill, *Comparative Analysis of the Variability of Fixed and Tracking Photovoltaic Systems*. Solar Energy, 2014: p. 351-364.
102. Roth, P., A. Georgieg, and H. Boudinov, *Design and Construction of a System for Sun-tracking*. Renewable Energy, 2004: p. 393-402.
103. Muller, M., *Development of an Outdoor Concentrating Photovoltaic Module Testbed, Module Handling and Testing Procedures, and Initial Energy Production Results*. 2009, NREL: Colorado, USA.
104. Prior, B. and Seshan, C, *Concentrating Photovoltaics 2011: Technology, Costs and Markets*. 2011, GTM Research, Greentech Media: Boston, USA.
105. Stafford, B.D. and D. Sanchez, *Tracker Accuracy; Field Experience, Analysis, and Correlation with Meteorological Conditions*, in *IEEE PVSC-34*. 2008: Philadelphia, USA.
106. Cancro, C., et al. *Field Testing of the PhoCUS Solar Tracker by Means of a novel Optoelectronic Device*. in *4th International Conference on Solar Concentrators for the Generation of Electricity or Hydrogen*. 2007. Lorenzo del Escorial, Spain.
107. Chong, K. and C. Wong, *General Formula for On-axis Sun-tracking System and its Application in Improving Tracking Accuracy of Solar Collector*. Solar Energy, 2009: p. 298-305.
108. Luque-Heredia, I., R. Cervantes, and G. Quemere. *A Sun Tracking Error Monitor for Photovoltaic Concentrators*. in *2006 IEEE 4th World Conference on Photovoltaic Energy Conversion*. 2006. Waikoloa, USA.
109. Rawat, R. and S. Chandel, *Hill Climbing Techniques for Tracking Maximum Power Point in Solar Photovoltaic Systems - A Review*. International Journal of Sustainable Development and Green Economics, 2013: p. 90-95.
110. Koussa, M., et al., *Measured and Modelled Improvement in Solar Energy Yield from Flat Plate Photovoltaic Systems Utilizing Different Tracking Systems and Under a Range of Environmental Conditions*. Applied Energy, 2011: p. 1756-1771.
111. Jantsch, M., et al. *Measurment of PV Maximum Powerpoint Tracking Performance*. in *14th European Photovoltaic Energy Conference and Exhibition*. 1997. Barcelona, Spain.
112. Haeberlin, H., et al. *Measurement of Dynamic MPP-Tracking Efficiency at Grid-Connected PV Inverters*. in *21st European Photovoltaic Solar Energy Conference*. 2006. Dresden, Germany.
113. Haeberlin, H., et al. *Total Efficiency  $\eta_{TOT}$  - A New Quantity for Better Characterization of Grid-connected PV Inverters*. in *20th European Photovoltaic Solar Energy Conference*. 2005. Barcelona, Spain.
114. Stalter, O. and B. Burger, *The Mechanical Maximum Power Point Tracker (MPPTm)*, in *25th European Photovoltaic Solar Energy Conference and Exhibition*. 2010: Valencia, Spain.
115. Mallick, T.K., P.C. Eames, and B. Norton, *Power losses in an asymmetric compound parabolic photovoltaic concentrator*. Solar Energy Materials and Solar Cells, 2007. **91**(12): p. 1137-1146.
116. Vignola, F., F. Mavromatakis, and J. Krumsick, *Performance of PV Inverters*, in *37th American Solar Energy Society Annual Conference*. 2008: San Diego, USA.
117. Menard, E., et al., *Optics Development for Micro-cell Based CPV Modules*, in *High and Low Concentrator Systems for Solar Electric Applications VI*. 2011: San Diego, USA.
118. Fritts, C., *On a New Form of Selenium Photocell*. Proceedings of the American Association for the Advancement of Science, 1883. **33**: p. 97.
119. Bohr, N., *The structure of an atom*. 1922, Nobel Prize.

120. Stem, N. and M. Cid, *Studies of Phosphorus Gaussian Profile Emitter Silicon Solar Cells*. Materials Research, 2001: p. 143-148.
121. Geerligs, L. and D. Macdonald, *Base Doping and Recombination Activity of Impurities in Crystalline Silicon Solar Cells*. Progress in Photovoltaics: Research and Applications, 2004: p. 309-316.
122. Cuevas, A. and D. Russell, *Co-optimisation of the emitter region and the metal grid of silicon solar cells*. Progress in Photovoltaics: Research and Applications, 2000: p. 603-616.
123. Antonini, A., et al., *Contact grid optimization methodology for front contact concentration solar cells*. Solar Energy Materials and Solar Cells, 2003: p. 155-166.
124. Sánchez, M. and N. Stem, *Phosphorus emitter and metal - grid optimization for homogeneous (n+p) and double-diffused (n++n+p) emitter silicon solar cells*. Materials Research, 2009: p. 57-62.
125. Tiedje, T., et al., *Limiting Efficiency of Silicon Solar Cells*. IEEE Transactions on Electron Devices, 1984: p. 711-716.
126. Auger, P., *Sur les rayons  $\beta$  secondaires produits dans un gaz par des rayons X*. Comptes rendus des séances hebdomadaires de l'académique des sciences (C.R.A.S.), 1923: p. 169-171.
127. Shockley, E. and W. Read, *Statistics of the Recombinations of Holes and Electrons*. Physical Review, 1952: p. 835.
128. Hall, R., *Electron-Hole Recombination in Germanium*. Physical Review Letters, 1952: p. 387.
129. Oh, J., H. Yuan, and H. Branz, *An 18.2%-efficient black-silicon solar cell achieved through control of carrier recombination in nanostructures*. Nature Nanotechnology, 2012: p. 743-748.
130. Proctor, C., M. Kuik, and T. Nguyen, *Charge carrier recombination in organic solar cells*. Progress in Polymer Science, 2013: p. 1941-1960.
131. Yamada, Y., et al., *Photocarrier Recombination Dynamics in Perovskite CH<sub>3</sub>NH<sub>3</sub>PbI<sub>3</sub> for Solar Cell Applications*. Journal of the American Chemical Society, 2014: p. 11610-11613.
132. Friesen, G., et al. *Intercomparison of Different Energy Prediction Methods Within the European Project "Performance" - Results of the 1st Round Robin*. in 22nd European Photovoltaic Solar Energy Conference. 2007. Milan, Italy.
133. Meneses-Rodríguez, D., et al., *Photovoltaic solar cells performance at elevated temperatures*. Solar Energy, 2005: p. 243-250.
134. Saga, T., *Advances in crystalline silicon solar cell technology for industrial mass production*. NPG Asia Materials, 2010: p. 96-102.
135. Martí, A. and G. Araujo, *Absolute limiting efficiencies for photovoltaic energy conversion*. Solar Energy Materials and Solar Cells, 1994: p. 213.
136. Martí, A. and G. Araújo, *Limiting efficiencies for photovoltaic energy conversion in multigap systems*. Solar Energy Materials and Solar Cells, 1996: p. 203-222.
137. Swanson, R., *The promise of concentrators*. Progress in Photovoltaics: Research and Applications, 2000: p. 93-111.
138. Dimroth, F., et al. *3-6 junction photovoltaic cells for space and terrestrial concentrator applications*. in 31st IEEE Photovoltaic Specialists Conference. 2005. Freiburg, Germany.
139. Qiu, Y., et al., *The spectral variation effects on energy yield of optimized multi-junction solar cell*, in 34th IEEE Photovoltaic Specialists Conference (PVSC). 2009: Philadelphia, USA. p. 000897 - 000902.

140. Chan, N., et al. *Variation in spectral irradiance and the consequences for multi-junction concentrator photovoltaic systems*. in *35th IEEE Photovoltaic Specialists Conference (PVSC)*. 2010. Honolulu, Hawaii.
141. Strobl, G., et al. *European Roadmap of Multijunction Solar Cells and Qualification Status*. in *IEEE 4th World Conference on Photovoltaic Energy Conversion*. 2006. Waikoloa, USA.
142. Jons, R., et al., *Evolution of Multijunction Solar Cell Technology for Concentrating Photovoltaics*. Japanese Journal of Applied Physics, 2012. **10ND01**.
143. Luque, A., G. Sala, and J. Arboiro, *Electric and thermal model for non-uniformly illuminated concentration cells*. Solar Energy Materials and Solar Cells, 1998: p. 269-290.
144. Kinsey, G. and K. Edmondson, *Spectral response and energy output of concentrator multijunction solar cells*. Progress in Photovoltaics, 2009: p. 279-364.
145. Mallick, T.K., P.C. Eames, and B. Norton, *Using air flow to alleviate temperature elevation in solar cells within asymmetric compound parabolic concentrators*. Solar Energy, 2007: p. 173-184.
146. Nelson, J., *The Physics of Solar Cells*. 2003, London, England: Imperial College Press.
147. Nelder, J. and R. Mead, *A simplex method for function minimization*. Computer Journal, 1965: p. 308-313.
148. Ben-Israel, A., *A Newton-Raphson Method for the Solution of Systems of Equations*. Journal of Atmospheric and Oceanic Technology, 1966: p. 243-252.
149. Broyden, C., *Quasi-Newton Methods and their Application to Function Minimisation*. Mathematics of Computation, 1967: p. 368-381.
150. Goss, B., et al., *Irradiance modelling for individual cells of shaded solar photovoltaic arrays*. Solar Energy, 2014: p. 410-419.
151. Zekry, A. and A. Al-Mazroo, *A distributed SPICE-model of a solar cell*. IEEE Transactions on Electron Devices, 1996: p. 691-700.
152. Galiana, B., C. Algara, and I. Rey-Stolle, *A 3-D model for concentrator solar cells based on distributed circuit units*. IEEE Transactions on Electron Devices, 2005: p. 2552-2558.
153. Voraysyan, P., T.R. Betts, and R. Gottschalg, *Spatially distributed model for the analysis of laser beam induced current (LBIC) measurements of thin film silicon solar modules*. Solar Energy Materials and Solar Cells, 2011: p. 111-114.
154. Pieters, B., *Spatial modeling of thin-film solar modules using the network simulation method and SPICE*. IEEE Journal of Photovoltaics, 2011: p. 93-98.
155. Wu, X., et al., *Distributed electrical network modelling approach for spatially resolved characterisation of photovoltaic modules*. IET Renewable Power Generation, 2014: p. 459-466.

## 8. List of Publications

Goss, B.; Cole, I.R.; Betts, T.R.; Gottschalg, R. *Irradiance modelling for individual cells of shaded solar photovoltaic arrays*. Solar Energy, 2014: p. 410-419.

Cole, I.R.; Gottschalg, R. *Optical Modelling for CPV Systems - Investigating the Fresnel Lens*. Proceedings of the Photovoltaic Science, Applications and Technology Conference (PVSAT 10). Loughborough, UK. 2014.

Cole, I.R.; Betts, T.R.; Gottschalg, R. *Solar profiles and spectral modeling for CPV simulations*. IEEE Journal of Photovoltaics, 2012: p. 62-67.

Cole, I.R.; Gottschalg, R. *RECEIVER PLANE ILLUMINATION PROFILES – RAY TRACING AN EXTENDED LIGHT SOURCE THROUGH OPTICAL SYSTEMS WITH VARIABLE MISALIGNMENT PARAMETERS*. Proceedings of the European PV Solar Energy Conference and Exhibition (EUPVSEC 27). Frankfurt, Germany. 2012.

Cole, I.R.; Gottschalg, R. *Plane restricted illumination profiles – ray tracing an extented light source through optical systems with variable misalignment parameters*. Proceedings of the Photovoltaic Science, Applications and Technology Conference (PVSAT 8). Newcastle-upon-tyne, UK. 2012.

Cole, I.R.; Betts, T.R.; Gottschalg, R. *Solar profiles and spectral modeling for CPV simulations*. Proceedings of IEEE Photovoltaic Specialists Conference (PVSC 37). Seattle, USA. 2011.

Cole, I.R.; Gottschalg, R. *Modelling solar flux distributions for fresnel lens CPV systems*. Proceedings of the Photovoltaic Science, Applications and Technology Conference (PVSAT 7). Edinburgh, UK. 2011.

Cole, I.R.; Gottschalg, R. *Modelling the Efficiency of Terrestrial Photovoltaic Systems*. Proceedings of the Photovoltaic Science, Applications and Technology Conference (PVSAT 6). Southampton, UK. 2010.

Cole, I.R.; Qiu, Y.N.; Gottschalg, R. *EFFICIENCY OF TERRESTRIAL PHOTOVOLTAIC SYSTEMS*. Proceedings of the 19th International Photovoltaic Science and Engineering Conference and Exhibition. (PVSEC-19). Jeju, South Korea. 2009.

# 9. Appendix

## 9.1. Lens Volume Derivations

### 9.1.1. The Plano Convex Lens

First consider the plano-convex lens.

The plano-convex lens essentially a spherical segment confined to the space:

$$c \leq z \leq r$$

EQUATION 9.1

*Where C is the lens depth and R the radius of spherical shell*

The volume of the plano-convex lens is found as a triple integral over x, y and z:

$$V = \iiint dx dy dz$$

EQUATION 9.2

The spherical shell is described by:

$$x^2 + y^2 + z^2 = R^2$$

EQUATION 9.3

Dimensional confinements are then described as:

$$0 \leq x \leq \sqrt{R^2 - y^2 - z^2}$$

EQUATION 9.4

$$0 \leq y \leq \sqrt{R^2 - z^2}$$

EQUATION 9.5

$$C \leq z \leq R$$

EQUATION 9.6

Thus the volume of the plano-convex lens is found as:

$$V = 4 \int_c^R \int_0^{\sqrt{R^2 - z^2}} \int_0^{\sqrt{R^2 - y^2 - z^2}} 1 dx dy dz$$

EQUATION 9.7

Once integrated over x this yields:

$$V = 4 \int_C^R \int_0^{R\sqrt{R^2-z^2}} \sqrt{R^2 - y^2 - z^2} dy dz$$

EQUATION 9.8

A trigonometric substitution can be used here to simplify the calculation:

$$y = \sqrt{R^2 - z^2} \sin \theta$$

EQUATION 9.9

Then the derivative with respect to  $\theta$  is:

$$\frac{dy}{d\theta} = \sqrt{R^2 - z^2} \cos \theta$$

EQUATION 9.10

Limits on the y-dimension integral have the following  $\theta$  equivalents:

$$\begin{cases} y = 0 & \left| \theta = 0 \right. \\ y = \sqrt{R^2 - z^2} & \left| \theta = \frac{\pi}{2} \right. \end{cases}$$

EQUATION 9.11

Thus:

$$\begin{aligned} V &= 4 \int_C^R \int_0^{R\sqrt{R^2-z^2}} \sqrt{R^2 - z^2 - y^2} dy dz \\ &= 4 \int_C^R \int_0^{\frac{\pi}{2}} \sqrt{(R^2 - z^2) - (R^2 - z^2) \sin^2 \theta} \cdot \sqrt{R^2 - z^2} \cos \theta d\theta dz \\ &= 4 \int_C^R \int_0^{\frac{\pi}{2}} \sqrt{R^2 - z^2} (1 - \sin^2 \theta) \cdot \sqrt{R^2 - z^2} \cos \theta d\theta dz \\ &= 4 \int_C^R \int_0^{\frac{\pi}{2}} (R^2 - z^2) \cos^2 \theta d\theta dz = 4 \int_C^R (R^2 - z^2) dz \int_0^{\frac{\pi}{2}} \cos^2 \theta d\theta \end{aligned}$$

EQUATION 9.12

Again, a trigonometric substitution can be used here to simplify the calculation:

$$\cos^2 \theta = \frac{1}{2}(1 + \cos 2\theta)$$

EQUATION 9.13

Therefore the volume of the plano-convex lens is found as:

$$\begin{aligned} 4 \int_C^R (R^2 - z^2) dz \int_0^{\frac{\pi}{2}} \cos^2 \theta d\theta &= 2 \int_C^R (R^2 - z^2) dz \int_0^{\frac{\pi}{2}} (1 + \cos 2\theta) d\theta \\ &= 2 \left[ R^2 z - \frac{1}{3} z^3 \right]_C^R \cdot \left[ \theta + \frac{1}{2} \sin 2\theta \right]_0^{\frac{\pi}{2}} = 2 \left( R^3 - \frac{1}{3} R^3 - R^2 C + \frac{1}{3} C^3 \right) \left( \frac{\pi}{2} \right) \\ &= \frac{2}{3} \pi R^3 - \pi R^2 C + \frac{\pi}{3} C^3 \end{aligned}$$

EQUATION 9.14

Where  $V$  is the volume of a plano-convex lens of radius,  $R$ , and extent of curvature,  $C$

For clarity:

$$V = \frac{2}{3} \pi R^3 - \pi R^2 C + \frac{\pi}{3} C^3$$

EQUATION 9.15

### 9.1.2. The Fresnel Lens

The volume of a Fresnel lens can be computed as an iterative set of volume integrations for each facet.

$$V = \sum_{i=1}^{i=n} 4 \int_C^{R_i} \int_{r_i}^{\sqrt{R_i^2 - z^2}} \int_0^{\sqrt{R_i^2 - y^2 - z^2}} 1 dx dy dz$$

EQUATION 9.16

Where  $V$  is the volume of the Fresnel lens,  $R_i$  the radius of the spherical shell of facet  $i$ ,  $r_i$  the radial extent of the cylindrical wall boundary of facet  $i$ ,  $C$  the extent of curvature of the Fresnel lens and  $n$  the number of facets in the Fresnel lens

However, the computation of this yields an inelegant and unnecessarily complicated solution. A geometric analysis of the problem provides a far more efficient and beautiful solution.

Each facet of the Fresnel lens can be considered as bounded by a plano-convex shell. The volume of each facet is then the volume of the plano-convex shell minus the volume contained within the radial limit of the inner facet wall. This negative volume can be considered as a cylinder and a protruding plano-convex lens atop this cylinder:

$$V_i = V_{i\text{shell}} - V_{i\text{cylinder}} - V_{i\text{protuding}}$$

EQUATION 9.17

The plano-convex shell volume,  $V_{i\text{shell}}$ , for each facet can be calculated from Equation 9.15:

$$V_{i\text{shell}} = \frac{2}{3}\pi R_i^3 - \pi R_i^2 C + \frac{\pi}{3} C^3$$

EQUATION 9.18

The radius of the spherical shell pertaining to a given Fresnel facet is computed as:

$$R_i = \sqrt{\left(\frac{l}{n}i\right)^2 + C^2}$$

EQUATION 9.19

Where  $l$  is the lens front radius:

$$l = \sqrt{R^2 - C^2}$$

EQUATION 9.20

Thus, from Equation 9.18 Equation 9.19:

$$R_i = \sqrt{\left(\frac{\sqrt{R^2 - C^2}}{n}i\right)^2 + C^2}$$

EQUATION 9.21

The cylinder radius is given by:

$$r_i = \frac{l}{n}(i-1)$$

EQUATION 9.22

The cylinder height is given by:

$$h_i = \sqrt{R_i^2 - r_i^2} - C$$

EQUATION 9.23

Thus the, from Equation 9.21 and Equation 9.22, the cylindrical section volume,  $V_{i\text{cylinder}}$ , is given by:

$$V_{i\text{cylinder}} = h_i \pi r_i^2 = \left( \sqrt{R_i^2 - r_i^2} - C \right) \pi \left( \frac{l}{n}(i-1) \right)^2$$

EQUATION 9.24

The protruding plano-convex space,  $V_{i\_protuding}$ , is given by:

$$V_{i\_protuding} = \frac{2}{3}\pi R_i^3 - \pi R_i^2(C + h_i) + \frac{\pi}{3}(C + h_i)^3$$

EQUATION 9.25

Which, from Equation 9.22, is:

$$\frac{2}{3}\pi R_i^3 - \pi R_i^2 \sqrt{R_i^2 - r_i^2} + \frac{\pi}{3}(R_i^2 - r_i^2)^2$$

EQUATION 9.26

Thus the volume of a given Fresnel facet,  $i$ , is found, from Equation 9.17, Equation 9.18, Equation 9.24 and Equation 9.25 as:

$$V_i = \frac{2}{3}\pi R_i^3 - \pi R_i^2 C + \frac{\pi}{3}C^3 - h_i\pi r_i^2 - \frac{2}{3}\pi R_i^3 - \pi R_i^2(C + h_i) + \frac{\pi}{3}(C + h_i)^3$$

EQUATION 9.27

Thus the volume of a Fresnel lens with  $n$  facets is found as:

$$\begin{aligned} V &= \sum_{i=1}^{i=n} -\pi R_i^2 C + \frac{\pi}{3}C^3 - h_i\pi r_i^2 - \pi R_i^2(C + h_i) + \frac{\pi}{3}(C + h_i)^3 \\ &= \pi \sum_{i=1}^{i=n} \frac{1}{3}(C^3 + (C + h_i)^3) - R_i^2(2C + h_i) - h_i r_i^2 \end{aligned}$$

EQUATION 9.28

Explicitly:

$$\begin{aligned} V_i &= \pi \sum_{i=1}^{i=n} \frac{1}{3} \left( C^3 + \left( \left( \frac{\sqrt{R^2 - C^2}}{n} i \right)^2 + C^2 - \left( \frac{\sqrt{R^2 - C^2}}{n} (i-1) \right)^2 \right)^2 \right) \\ &\quad - \left( \left( \frac{\sqrt{R^2 - C^2}}{n} i \right)^2 + C^2 \right) \left( C + \sqrt{\left( \frac{\sqrt{R^2 - C^2}}{n} i \right)^2 + C^2 - \left( \frac{\sqrt{R^2 - C^2}}{n} (i-1) \right)^2} \right) \\ &\quad - \left( \sqrt{\left( \frac{\sqrt{R^2 - C^2}}{n} i \right)^2 + C^2 - \left( \frac{\sqrt{R^2 - C^2}}{n} (i-1) \right)^2} - C \right) \left( \frac{\sqrt{R^2 - C^2}}{n} (i-1) \right)^2 \end{aligned}$$

EQUATION 9.29

## 9.2. Rotation Matrix Derivation

### 9.2.1. Background

Rotation matrices for geometric operations are highly useful multidisciplinary tools. Applications include behavioural operations in the representation of physical systems in Physics & Mathematics; and perspective calculations in computer graphics.

The rotation of a point about an arbitrary axis is often computed as a set of 5 distinct matrix operations. However, it is possible to obtain an elegant matrix that performs the rotation in a single operation. The principle benefit of a single matrix operation here is the significant reduction in the computational time required to perform the rotation. In high resolution computer simulations where these rotations are performed in great numbers on a multitude of variables, computational time is a particular concern.

Although the matrix itself is available in the literature, there is not to the author's knowledge a thorough derivation of the matrix. Seeing as it is generally considered bad practice to employ mathematical operations that one does not understand, the author has taken it upon himself to provide a derivation of the matrix in question (Equation 9.63).

### 9.2.2. Reference Frame

The conventional 3D Cartesian reference frame is depicted geometrically in Figure 9.1.

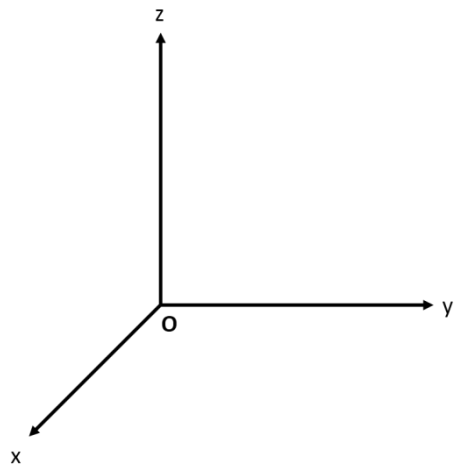


FIGURE 9.1: CONVENTIONAL 3D CARTESIAN REFERENCE FRAME

The origin and unit vectors are defined as:

$$\mathbf{o} = \begin{bmatrix} 0 \\ 0 \\ 0 \end{bmatrix}$$

EQUATION 9.30

$$\hat{i} = \begin{bmatrix} 1 \\ 0 \\ 0 \end{bmatrix}, \quad \hat{j} = \begin{bmatrix} 0 \\ 1 \\ 0 \end{bmatrix}, \quad \hat{k} = \begin{bmatrix} 0 \\ 0 \\ 1 \end{bmatrix}$$

EQUATION 9.31

### 9.2.3. Rotations about Conventional Axes

Rotation matrices about the conventional 3D axes are derived as dimensional extensions from Pythagoras' theorem. Convention dictates that rotation matrices perform rotations in a counter-clockwise direction.

#### 9.2.3.1. Derivation of 2D Rotation Matrix

Consider the counter-clockwise rotation of a 2D vector in the x-y plane about the origin such that vector  $\mathbf{V}$  is rotated to vector  $\mathbf{V}'$ , as depicted in Figure 9.2.

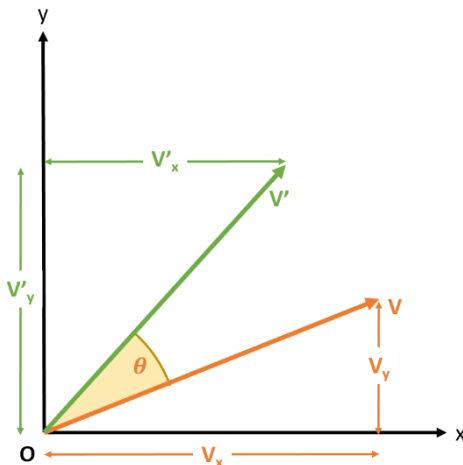


FIGURE 9.2: COUNTER-CLOCKWISE VECTOR ROTATION IN THE X-Y PLANE

The calculation of vector  $\mathbf{V}'$  is identical to the calculation of the components of vector  $\mathbf{V}$  along the axes  $x'$  and  $y'$  where  $x'$  and  $y'$  are equivalent to the  $x$  and  $y$  axes rotated clockwise by the vector rotation angle  $\theta$ . This is shown in Figure 9.3.

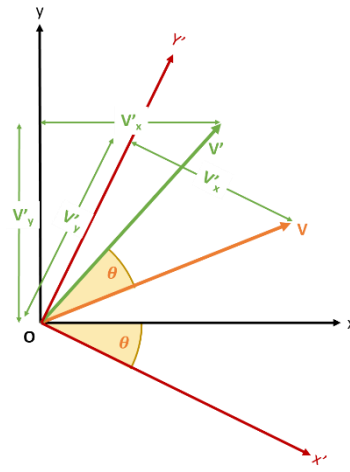
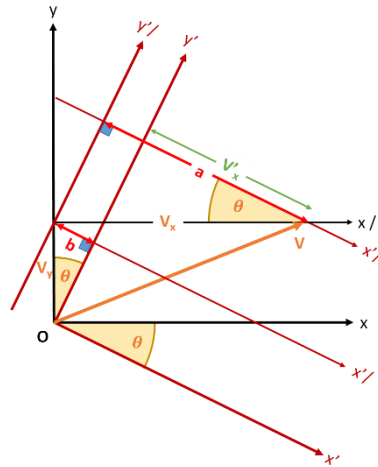


FIGURE 9.3: CLOCKWISE ROTATED REFERENCE FRAME - EQUIVALENT CALCULATION FOR COUNTER-CLOCKWISE VECTOR ROTATION

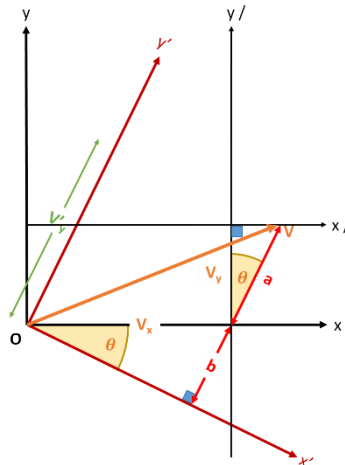
The components of  $V$  along  $x'$  and  $y'$  are obtained by Pythagoras' theorem. Similar triangles are constructed with parallel axes to arrive at the solution. To avoid overly complex diagrams, these calculations are demonstrated separately in Figure 9.4 & Figure 9.5.

FIGURE 9.4: CALCULATION OF ROTATED X-COEFFICIENT  $V'_x$ 

From Figure 9.4:

$$V'_x = a - b = V_x \cos \theta - V_y \sin \theta$$

EQUATION 9.32

FIGURE 9.5: CALCULATION OF ROTATED Y-COEFFICIENT  $V'_y$ 

From Figure 9.5:

$$V'_y = a + b = V_y \cos \theta + V_x \sin \theta$$

EQUATION 9.33

Therefore the rotation matrix,  $\mathbf{R}$ , for counter-clockwise rotation about the origin by an angle  $\theta$ , being that matrix that rotates vector  $\mathbf{V}$  to vector  $\mathbf{V}'$ , must satisfy:

$$\begin{bmatrix} V'_x \\ V'_y \end{bmatrix} = \mathbf{R} \begin{bmatrix} V_x \\ V_y \end{bmatrix} = \begin{bmatrix} V_x \cos \theta - V_y \sin \theta \\ V_x \sin \theta + V_y \cos \theta \end{bmatrix}$$

EQUATION 9.34

Thus

$$\mathbf{R}(\theta) = \begin{bmatrix} \cos \theta & -\sin \theta \\ \sin \theta & \cos \theta \end{bmatrix}$$

EQUATION 9.35

As clockwise rotation is the same a negative counter-clockwise rotation, given that

$$\cos(-\theta) = \cos(\theta) \quad \& \quad \sin(-\theta) = -\sin(\theta)$$

EQUATION 9.36

The matrix for clockwise rotation about the origin can be written as:

$$\mathbf{R}(-\theta) = \begin{bmatrix} \cos \theta & \sin \theta \\ -\sin \theta & \cos \theta \end{bmatrix}$$

EQUATION 9.37

### 9.2.3.2. 3D Rotation Matrices about Conventional Axes

Given the 2D rotation matrix (Equation 9.35) it is possible to calculate the 3D rotation matrices describing rotation about the conventional axes by means of geometric consideration. The rotation of

a vector about an axis by a given angle can be thought of as the action of physically holding the rotation axis and twisting it by the angle. Under this action, the component of a vector along the axis of rotation is invariant.

### Rotation about the x-axis

From Figure 9.1, it can be seen that this is the same case as in the 2D matrix derivation with a switch of axes so that  $x$  goes to  $y$  and  $y$  to  $z$ . For this to co-occur with  $x$  invariance, the matrix,  $R_x$ , describing counter-clockwise rotation about the  $x$ -axis by an angle  $\theta$  is found as:

$$R_x = \begin{bmatrix} 1 & 0 & 0 \\ 0 & \cos \theta & -\sin \theta \\ 0 & \sin \theta & \cos \theta \end{bmatrix}$$

EQUATION 9.38

### Rotation about the y-axis

From Figure 9.1, it can be seen that this is the same case as in the 2D matrix derivation with a switch of axes so that  $x$  goes to  $z$  and  $y$  to  $x$ . For this to co-occur with  $y$  invariance, the matrix,  $R_y$ , describing counter-clockwise rotation about the  $y$ -axis by an angle  $\theta$  is found as:

$$R_y = \begin{bmatrix} \cos \theta & 0 & \sin \theta \\ 0 & 1 & 0 \\ -\sin \theta & 0 & \cos \theta \end{bmatrix}$$

EQUATION 9.39

### Rotation about the z-axis

From Figure 9.1, it can be seen that this is the same case as in the 2D matrix derivation. For this to co-occur with  $z$  invariance, the matrix,  $R_z$ , describing counter-clockwise rotation about the  $z$ -axis by an angle  $\theta$  is found as:

$$R_z = \begin{bmatrix} \cos \theta & -\sin \theta & 0 \\ \sin \theta & \cos \theta & 0 \\ 0 & 0 & 1 \end{bmatrix}$$

EQUATION 9.40

## 9.2.4. Rotations about Arbitrary Axes

Rotation about an arbitrary axis is a somewhat more complex calculation. The complexity can be broken down into smaller, simpler steps.

Consider a point and an axis about which the point is to be rotated. First rotate the point and axis pair so that the axis is equivalent to one of the conventional axes. Next rotate the point by the desired

angle about the conventional axis. Then rotate the pair back to the so that the rotation axis is as it was initially. After this process the point is in a position such that it has rotated about the axis by the desired angle. The rotation matrix about an arbitrary axis can be derived as the matrix products of these steps.

Rotation of an arbitrary axis to a conventional axis can be simplified as two stage process. Rotation of an arbitrary axis to a conventional axis can be achieved by first rotating the axis to a conventional plane and then to a conventional axis.

For ease of visualisation the conventional axis of rotation is here chosen as the z-axis and the conventional plane as the x-z plane.

For clarification, the rotation of a point about an arbitrary axis by a desired angle is equivalent to the following 5-step process:

- Rotate the pair so that the axis is in the x-z plane
- Rotate the pair so that the axis is equivalent to the z axis
- Rotate the point about the z axis by the desired rotation angle
- Reverse rotate the pair from z-axis so that the axis is in the x-y plane as before
- Reverse rotate the pair from the x-z plane so that the axis is as it was initially

#### 9.2.4.1. Rotate to the x-z plane

Rotation of an arbitrary vector to the x-z plane is depicted geometrically in Figure 9.6.

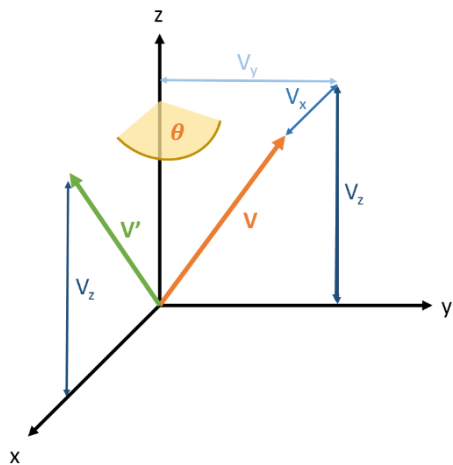


FIGURE 9.6: ROTATION TO A CONVENTIONAL (X-Z) PLANE

This rotation is essentially rotation about the z axis by an angle,  $\theta$ . The angle,  $\theta$ , can be obtained from the dot product:

$$\mathbf{A} \cdot \mathbf{B} = |\mathbf{A}| |\mathbf{B}| \cos \theta$$

EQUATION 9.41

Where vectors  $\mathbf{A}$  and  $\mathbf{B}$  are the vectors from the invariant z point,  $\mathbf{V}_z = \begin{bmatrix} 0 \\ 0 \\ V_z \end{bmatrix}$ , to  $\mathbf{V}'$  and  $\mathbf{V}$ , respectively.

$$\mathbf{A} = \begin{bmatrix} V'_x \\ V'_y \\ V'_z \end{bmatrix} - \begin{bmatrix} 0 \\ 0 \\ V_z \end{bmatrix} = \begin{bmatrix} V'_x \\ 0 \\ 0 \end{bmatrix}$$

EQUATION 9.42

$$\mathbf{B} = \begin{bmatrix} V_x \\ V_y \\ V_z \end{bmatrix} - \begin{bmatrix} 0 \\ 0 \\ V_z \end{bmatrix} = \begin{bmatrix} V_x \\ V_y \\ 0 \end{bmatrix}$$

EQUATION 9.43

Thus

$$\cos \theta = \frac{V'_x V_x}{\sqrt{V'_x^2} \sqrt{V_x^2 + V_y^2}} = \frac{V_x}{\sqrt{V_x^2 + V_y^2}}$$

EQUATION 9.44

From the trigonometric identity

$$\cos^2 \theta + \sin^2 \theta = 1$$

EQUATION 9.45

and Equation 9.44:

$$\sin \theta = \pm \frac{V_y}{\sqrt{V_x^2 + V_y^2}}$$

EQUATION 9.46

To satisfy the condition that the y-value of the rotated vector is 0:

$$\sin \theta = - \frac{V_y}{\sqrt{V_x^2 + V_y^2}}$$

EQUATION 9.47

Thus from Equation 9.40, Equation 9.44 & Equation 9.47; the rotation of an arbitrary vector,  $\mathbf{V}$ , to the x-z plane is described by the matrix:

$$\mathbf{M}_{xz} = \begin{bmatrix} \frac{V_x}{\sqrt{V_x^2 + V_y^2}} & \frac{V_y}{\sqrt{V_x^2 + V_y^2}} & 0 \\ -\frac{V_y}{\sqrt{V_x^2 + V_y^2}} & \frac{V_x}{\sqrt{V_x^2 + V_y^2}} & 0 \\ 0 & 0 & 1 \end{bmatrix}$$

EQUATION 9.48

#### 9.2.4.2. Rotate to the z-axis

The rotation of a vector in the x-z plane to the z-axis is depicted geometrically in Figure 9.7.

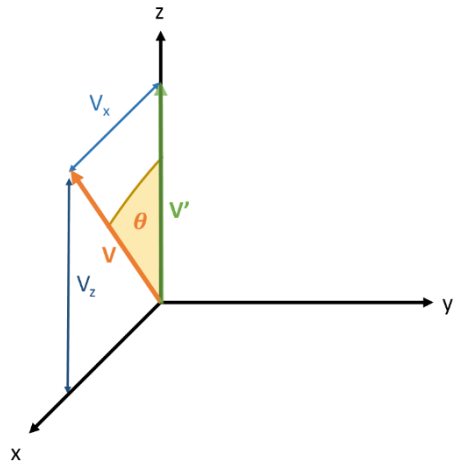


FIGURE 9.7: ROTATION FROM X-Z PLANE TO A CONVENTIONAL (z) AXIS

This rotation is essentially clockwise rotation about the y-axis by an angle,  $\theta$ . The angle,  $\theta$ , can be obtained from the dot product:

$$\mathbf{V}' \cdot \mathbf{V} = |\mathbf{V}'| |\mathbf{V}| \cos \theta$$

EQUATION 9.49

$$\text{Where } \mathbf{V} = \begin{bmatrix} V_x \\ 0 \\ V_z \end{bmatrix} \text{ and } \mathbf{V}' = \begin{bmatrix} 0 \\ 0 \\ V'_z \end{bmatrix}$$

Thus:

$$\cos \theta = \frac{V'_z V_z}{\sqrt{V'^2_z} \sqrt{V_x^2 + V_z^2}} = \frac{V_z}{\sqrt{V_x^2 + V_z^2}}$$

EQUATION 9.50

From Equation 9.45 & Equation 9.50:

$$\sin \theta = \pm \frac{V_x}{\sqrt{V_x^2 + V_z^2}}$$

EQUATION 9.51

To satisfy the condition that the x-value of the rotated vector is 0:

$$\sin \theta = -\frac{V_x}{\sqrt{V_x^2 + V_z^2}}$$

EQUATION 9.52

Equation 9.39, for counter-clockwise rotation then yields:

$$\mathbf{M}_z = \begin{bmatrix} \frac{V_z}{\sqrt{V_x^2 + V_z^2}} & 0 & -\frac{V_x}{\sqrt{V_x^2 + V_z^2}} \\ 0 & 1 & 0 \\ \frac{V_x}{\sqrt{V_x^2 + V_z^2}} & 0 & \frac{V_z}{\sqrt{V_x^2 + V_z^2}} \end{bmatrix}$$

EQUATION 9.53

Contextually, this matrix is operating not on  $\mathbf{V}$  but on  $\mathbf{M}_{xz}(\mathbf{V})$ . Since

$$\mathbf{M}_{xz}(\mathbf{V}) = \begin{bmatrix} \frac{V_x}{\sqrt{V_x^2 + V_y^2}} & \frac{V_y}{\sqrt{V_x^2 + V_y^2}} & 0 \\ -\frac{V_y}{\sqrt{V_x^2 + V_y^2}} & \frac{V_x}{\sqrt{V_x^2 + V_y^2}} & 0 \\ 0 & 0 & 1 \end{bmatrix} \begin{bmatrix} V_x \\ V_y \\ V_z \end{bmatrix} = \begin{bmatrix} \frac{V_x^2}{\sqrt{V_x^2 + V_y^2}} + \frac{V_y^2}{\sqrt{V_x^2 + V_y^2}} \\ 0 \\ V_z \end{bmatrix} = \begin{bmatrix} \sqrt{V_x^2 + V_y^2} \\ 0 \\ V_z \end{bmatrix}$$

EQUATION 9.54

$\mathbf{M}_z$  can be rewritten in terms of  $\mathbf{V}$  as:

$$\mathbf{M}_z = \begin{bmatrix} \frac{V_z}{\sqrt{V_x^2 + V_y^2 + V_z^2}} & 0 & -\frac{\sqrt{V_x^2 + V_y^2}}{\sqrt{V_x^2 + V_y^2 + V_z^2}} \\ 0 & 1 & 0 \\ \frac{\sqrt{V_x^2 + V_y^2}}{\sqrt{V_x^2 + V_y^2 + V_z^2}} & 0 & \frac{V_z}{\sqrt{V_x^2 + V_y^2 + V_z^2}} \end{bmatrix} = \begin{bmatrix} \frac{V_z}{|\mathbf{V}|} & 0 & -\frac{\sqrt{V_x^2 + V_y^2}}{|\mathbf{V}|} \\ 0 & 1 & 0 \\ \frac{\sqrt{V_x^2 + V_y^2}}{|\mathbf{V}|} & 0 & \frac{V_z}{|\mathbf{V}|} \end{bmatrix}$$

EQUATION 9.55

### 9.2.4.3. Rotate About the z-axis

The matrix describing rotation about the z-axis is given in Rotations about Conventional Axes, Equation 9.40:

$$\mathbf{R}_z = \begin{bmatrix} \cos \theta & -\sin \theta & 0 \\ \sin \theta & \cos \theta & 0 \\ 0 & 0 & 1 \end{bmatrix}$$

### 9.2.4.4. Reverse Rotate from z-axis

This is the inverse operation of that described in section 9.2.4.2, 'Rotate to the z-axis'. As per the definition of matrices, this operation is achieved with the inverse of the operation matrix derived there (Equation 9.53):

$$\mathbf{M}_z = \begin{bmatrix} \frac{V_z}{\sqrt{V_x^2 + V_z^2}} & 0 & -\frac{V_x}{\sqrt{V_x^2 + V_z^2}} \\ 0 & 1 & 0 \\ \frac{V_x}{\sqrt{V_x^2 + V_z^2}} & 0 & \frac{V_z}{\sqrt{V_x^2 + V_z^2}} \end{bmatrix}$$

There are various methods one could use to find  $\mathbf{M}_z^{-1}$ . Geometric analysis shall be used here as it yields a simple and elegant solution. The standard computation of  $\mathbf{M}_z^{-1}$  is given afterwards for reference.

Given that  $\mathbf{M}_z$  describes a counter-clockwise rotation about the y-axis by the angle  $\theta = \cos^{-1}\left(\frac{V_z}{\sqrt{V_x^2 + V_z^2}}\right)$ , the inverse of this operation is simply a clockwise rotation about the y-axis by the same angle,  $\theta$ . As described in section 9.2.3.1, 'Derivation of 2D Rotation Matrix', Equation 9.37, this is achieved by switching the signs of the sin terms (or multiplying them by -1). Thus

$$\mathbf{M}_z^{-1} = \begin{bmatrix} \frac{V_z}{\sqrt{V_x^2 + V_z^2}} & 0 & \frac{V_x}{\sqrt{V_x^2 + V_z^2}} \\ 0 & 1 & 0 \\ -\frac{V_x}{\sqrt{V_x^2 + V_z^2}} & 0 & \frac{V_z}{\sqrt{V_x^2 + V_z^2}} \end{bmatrix}$$

EQUATION 9.56

Contextually, this matrix is operating not on  $\mathbf{V}$  but on  $\mathbf{M}_{xz}(\mathbf{V})$ . Thus, from Equation 9.54, this becomes:

$$\mathbf{M}_z^{-1} = \begin{bmatrix} \frac{V_z}{\sqrt{V_x^2 + V_y^2 + V_z^2}} & 0 & \frac{\sqrt{V_x^2 + V_y^2}}{\sqrt{V_x^2 + V_y^2 + V_z^2}} \\ 0 & 1 & 0 \\ -\frac{\sqrt{V_x^2 + V_y^2}}{\sqrt{V_x^2 + V_y^2 + V_z^2}} & 0 & \frac{V_z}{\sqrt{V_x^2 + V_y^2 + V_z^2}} \end{bmatrix}$$

EQUATION 9.57

For reference, the standard calculation of the inverse matrix is presented below. One can see at a glance that this is a comparatively painstaking method in this circumstance.

$$\mathbf{M}_z^{-1} = \frac{\text{Adj}(\mathbf{M}_z)}{\text{Det}(\mathbf{M}_z)}$$

$$\begin{aligned}
&= \left[ \begin{array}{ccc}
\begin{vmatrix} 1 & 0 \\ 0 & \frac{V_z}{\sqrt{V_x^2 + V_z^2}} \end{vmatrix} & - \begin{vmatrix} 0 & -\frac{V_x}{\sqrt{V_x^2 + V_z^2}} \\ 0 & \frac{V_z}{\sqrt{V_x^2 + V_z^2}} \end{vmatrix} & \begin{vmatrix} 0 & -\frac{V_x}{\sqrt{V_x^2 + V_z^2}} \\ 1 & 0 \end{vmatrix} \\
-\begin{vmatrix} 0 & \frac{V_z}{\sqrt{V_x^2 + V_z^2}} \\ \frac{V_x}{\sqrt{V_x^2 + V_z^2}} & \frac{V_z}{\sqrt{V_x^2 + V_z^2}} \end{vmatrix} & \begin{vmatrix} \frac{V_z}{\sqrt{V_x^2 + V_z^2}} & -\frac{V_x}{\sqrt{V_x^2 + V_z^2}} \\ \frac{V_x}{\sqrt{V_x^2 + V_z^2}} & \frac{V_z}{\sqrt{V_x^2 + V_z^2}} \end{vmatrix} & -\begin{vmatrix} \frac{V_z}{\sqrt{V_x^2 + V_z^2}} & -\frac{V_x}{\sqrt{V_x^2 + V_z^2}} \\ 0 & 0 \end{vmatrix} \\
\begin{vmatrix} 0 & 1 \\ \frac{V_x}{\sqrt{V_x^2 + V_z^2}} & 0 \end{vmatrix} & -\begin{vmatrix} \frac{V_z}{\sqrt{V_x^2 + V_z^2}} & 0 \\ \frac{V_x}{\sqrt{V_x^2 + V_z^2}} & 0 \end{vmatrix} & \begin{vmatrix} \frac{V_z}{\sqrt{V_x^2 + V_z^2}} & 0 \\ 0 & 1 \end{vmatrix}
\end{array} \right] \\
&= \frac{1}{\sqrt{V_x^2 + V_z^2}} \left[ \begin{array}{ccc}
1 & 0 & 0 \\
0 & \frac{V_z}{\sqrt{V_x^2 + V_z^2}} & -\frac{V_x}{\sqrt{V_x^2 + V_z^2}} \\
0 & \frac{V_x}{\sqrt{V_x^2 + V_z^2}} & \frac{V_z}{\sqrt{V_x^2 + V_z^2}}
\end{array} \right] - \frac{V_x}{\sqrt{V_x^2 + V_z^2}} \left[ \begin{array}{ccc}
0 & 0 & 0 \\
0 & \frac{V_z}{\sqrt{V_x^2 + V_z^2}} & \frac{V_x}{\sqrt{V_x^2 + V_z^2}} \\
0 & \frac{V_x}{\sqrt{V_x^2 + V_z^2}} & -\frac{V_z}{\sqrt{V_x^2 + V_z^2}}
\end{array} \right] + \frac{V_z}{\sqrt{V_x^2 + V_z^2}} \left[ \begin{array}{ccc}
0 & 0 & 0 \\
0 & 0 & 0 \\
0 & 0 & 1
\end{array} \right] \\
&= \left( \frac{1}{\frac{V_z^2}{V_x^2 + V_z^2} + \frac{V_x^2}{V_x^2 + V_z^2}} \right) \left[ \begin{array}{ccc}
\frac{V_z}{\sqrt{V_x^2 + V_z^2}} & 0 & \frac{V_x}{\sqrt{V_x^2 + V_z^2}} \\
0 & \frac{V_z^2}{V_x^2 + V_z^2} + \frac{V_x^2}{V_x^2 + V_z^2} & 0 \\
-\frac{V_x}{\sqrt{V_x^2 + V_z^2}} & 0 & \frac{V_z}{\sqrt{V_x^2 + V_z^2}}
\end{array} \right] \\
&= \left[ \begin{array}{ccc}
\frac{V_z}{\sqrt{V_x^2 + V_z^2}} & 0 & \frac{V_x}{\sqrt{V_x^2 + V_z^2}} \\
0 & 1 & 0 \\
-\frac{V_x}{\sqrt{V_x^2 + V_z^2}} & 0 & \frac{V_z}{\sqrt{V_x^2 + V_z^2}}
\end{array} \right]
\end{aligned}$$

EQUATION 9.58

#### 9.2.4.5. Reverse Rotate from x-z plane

This is the inverse of the operation described in section 9.2.4.1, ‘Rotate to the x-z plane’. As per the definition of matrices, this operation is achieved with the inverse of the operation matrix derived there (Equation 9.48).

$$\mathbf{M}_{xz} = \begin{bmatrix} \frac{V_x}{\sqrt{V_x^2 + V_y^2}} & \frac{V_y}{\sqrt{V_x^2 + V_y^2}} & 0 \\ -\frac{V_y}{\sqrt{V_x^2 + V_y^2}} & \frac{V_x}{\sqrt{V_x^2 + V_y^2}} & 0 \\ 0 & 0 & 1 \end{bmatrix}$$

Geometric analysis will again be used here as it yields a simple and elegant solution. The standard computation of  $\mathbf{M}_{xz}^{-1}$  is given afterwards for reference.

Given that  $\mathbf{M}_{xz}$  describes a counter-clockwise rotation about the z-axis by the angle  $\theta = \cos^{-1}\left(\frac{V_x}{\sqrt{V_x^2 + V_y^2}}\right)$ , the inverse of this operation is simply a clockwise rotation about the z-axis by the same angle,  $\theta$ . As described in section 9.2.3.1, 'Derivation of 2D Rotation Matrix', Equation 9.37, this is achieved by switching the signs of the sin terms (or multiplying them by -1). Thus

$$\mathbf{M}_{xz}^{-1} = \begin{bmatrix} \frac{V_x}{\sqrt{V_x^2 + V_y^2}} & -\frac{V_y}{\sqrt{V_x^2 + V_y^2}} & 0 \\ \frac{V_y}{\sqrt{V_x^2 + V_y^2}} & \frac{V_x}{\sqrt{V_x^2 + V_y^2}} & 0 \\ 0 & 0 & 1 \end{bmatrix}$$

EQUATION 9.59

For reference, the standard calculation of the inverse matrix is presented below. Again, one can see at a glance that this is a comparatively painstaking method in this circumstance.

$$\begin{aligned}
 \mathbf{M}_{xz}^{-1} &= \frac{\text{Adj}(\mathbf{M}_{xz})}{\text{Det}(\mathbf{M}_{xz})} \\
 &= \frac{1}{\sqrt{V_x^2 + V_y^2}} \begin{vmatrix} \frac{V_x}{\sqrt{V_x^2 + V_y^2}} & 0 \\ -\frac{V_y}{\sqrt{V_x^2 + V_y^2}} & 0 \\ -\frac{V_y}{\sqrt{V_x^2 + V_y^2}} & 0 \\ -\frac{V_x}{\sqrt{V_x^2 + V_y^2}} & \frac{V_x}{\sqrt{V_x^2 + V_y^2}} \end{vmatrix} \\
 &\quad - \frac{1}{\sqrt{V_x^2 + V_y^2}} \begin{vmatrix} \frac{V_y}{\sqrt{V_x^2 + V_y^2}} & 0 \\ 0 & 1 \\ 0 & 1 \\ \frac{V_x}{\sqrt{V_x^2 + V_y^2}} & 0 \end{vmatrix} \\
 &\quad - \frac{1}{\sqrt{V_x^2 + V_y^2}} \begin{vmatrix} \frac{V_x}{\sqrt{V_x^2 + V_y^2}} & 0 \\ 0 & 1 \\ -\frac{V_y}{\sqrt{V_x^2 + V_y^2}} & 0 \\ -\frac{V_y}{\sqrt{V_x^2 + V_y^2}} & 0 \end{vmatrix} \\
 &= \frac{1}{\sqrt{V_x^2 + V_y^2}} \left( \begin{vmatrix} \frac{V_x}{\sqrt{V_x^2 + V_y^2}} & 0 \\ -\frac{V_y}{\sqrt{V_x^2 + V_y^2}} & 0 \\ -\frac{V_y}{\sqrt{V_x^2 + V_y^2}} & 0 \\ -\frac{V_x}{\sqrt{V_x^2 + V_y^2}} & \frac{V_x}{\sqrt{V_x^2 + V_y^2}} \end{vmatrix} - \begin{vmatrix} \frac{V_y}{\sqrt{V_x^2 + V_y^2}} & 0 \\ 0 & 1 \\ 0 & 1 \\ \frac{V_x}{\sqrt{V_x^2 + V_y^2}} & 0 \end{vmatrix} + 0 \begin{vmatrix} -\frac{V_y}{\sqrt{V_x^2 + V_y^2}} & \frac{V_x}{\sqrt{V_x^2 + V_y^2}} \\ 0 & 0 \\ 0 & 0 \end{vmatrix} \right) \\
 &= \left( \begin{array}{c} 1 \\ \frac{V_x^2}{V_x^2 + V_y^2} + \frac{V_y^2}{V_x^2 + V_y^2} \end{array} \right) \begin{bmatrix} \frac{V_x}{\sqrt{V_x^2 + V_y^2}} & -\frac{V_y}{\sqrt{V_x^2 + V_y^2}} & 0 \\ \frac{V_y}{\sqrt{V_x^2 + V_y^2}} & \frac{V_x}{\sqrt{V_x^2 + V_y^2}} & 0 \\ 0 & 0 & \frac{V_x^2}{V_x^2 + V_y^2} + \frac{V_y^2}{V_x^2 + V_y^2} \end{bmatrix} \\
 &= \begin{bmatrix} \frac{V_x}{\sqrt{V_x^2 + V_y^2}} & -\frac{V_y}{\sqrt{V_x^2 + V_y^2}} & 0 \\ \frac{V_y}{\sqrt{V_x^2 + V_y^2}} & \frac{V_x}{\sqrt{V_x^2 + V_y^2}} & 0 \\ 0 & 0 & 1 \end{bmatrix}
 \end{aligned}$$

EQUATION 9.60

#### 9.2.4.6. Rotation About an Arbitrary Axis

Due to the mathematical associativity of matrices, the full transformation of rotation about an arbitrary axis,  $\mathbf{V}$ , by an angle,  $\theta$ , can be described by a single matrix:

$$\mathbf{M}_{V\theta} = \mathbf{M}_{xz}^{-1} \mathbf{M}_z^{-1} \mathbf{R}_z \mathbf{M}_z \mathbf{M}_{xz}$$

EQUATION 9.61

To clarify the correct order of computation this can be written as:

$$\mathbf{M}_{V\theta} = \mathbf{M}_{xz}^{-1} (\mathbf{M}_z^{-1} (\mathbf{R}_z (\mathbf{M}_z (\mathbf{M}_{xz}))))$$

The full calculation simplifies to one elegant matrix:

$$\mathbf{M}_{V\theta} = \begin{bmatrix} \frac{V_x^2 + (V_y^2 + V_z^2) \cos \theta}{|V|^2} & \frac{V_x V_y (1 - \cos \theta)}{|V|^2} - \frac{V_z \sin \theta}{|V|} & \frac{V_x V_z (1 - \cos \theta)}{|V|^2} + \frac{V_y \sin \theta}{|V|} \\ \frac{V_x V_y (1 - \cos \theta)}{|V|^2} + \frac{V_z \sin \theta}{|V|} & \frac{V_y^2 + (V_x^2 + V_z^2) \cos \theta}{|V|^2} & \frac{V_y V_z (1 - \cos \theta)}{|V|^2} - \frac{V_x \sin \theta}{|V|} \\ \frac{V_x V_z (1 - \cos \theta)}{|V|^2} - \frac{V_y \sin \theta}{|V|} & \frac{V_y V_z (1 - \cos \theta)}{|V|^2} + \frac{V_x \sin \theta}{|V|} & \frac{V_z^2 + (V_x^2 + V_y^2) \cos \theta}{|V|^2} \end{bmatrix}$$

For a step by step computation of this see Section 9.2.5.

Under the assertion that  $V$  is a unit vector:

$$|V|^2 = |V| = 1$$

EQUATION 9.62

The matrix is further simplified:

$$\mathbf{M}_{V\theta} = \begin{bmatrix} V_x^2 + (V_y^2 + V_z^2) \cos \theta & V_x V_y (1 - \cos \theta) - V_z \sin \theta & V_x V_z (1 - \cos \theta) + V_y \sin \theta \\ V_x V_y (1 - \cos \theta) + V_z \sin \theta & V_y^2 + (V_x^2 + V_z^2) \cos \theta & V_y V_z (1 - \cos \theta) - V_x \sin \theta \\ V_x V_z (1 - \cos \theta) - V_y \sin \theta & V_y V_z (1 - \cos \theta) + V_x \sin \theta & V_z^2 + (V_x^2 + V_y^2) \cos \theta \end{bmatrix}$$

EQUATION 9.63

### 9.2.5. Reference Calculations

#### 9.2.5.1. To the z-axis

From Equation 9.48 & Equation 9.55:

$$\begin{aligned}
 \mathbf{M}_z \mathbf{M}_{xz} &= \begin{bmatrix} \frac{V_z}{|\mathbf{V}|} & 0 & -\frac{\sqrt{V_x^2 + V_y^2}}{|\mathbf{V}|} \\ 0 & 1 & 0 \\ \frac{\sqrt{V_x^2 + V_y^2}}{|\mathbf{V}|} & 0 & \frac{V_z}{|\mathbf{V}|} \end{bmatrix} \begin{bmatrix} \frac{V_x}{\sqrt{V_x^2 + V_y^2}} & \frac{V_y}{\sqrt{V_x^2 + V_y^2}} & 0 \\ -\frac{V_y}{\sqrt{V_x^2 + V_y^2}} & \frac{V_x}{\sqrt{V_x^2 + V_y^2}} & 0 \\ 0 & 0 & 1 \end{bmatrix} \\
 &= \begin{bmatrix} \frac{V_x V_z}{|\mathbf{V}| \sqrt{V_x^2 + V_y^2}} & \frac{V_y V_z}{|\mathbf{V}| \sqrt{V_x^2 + V_y^2}} & -\frac{\sqrt{V_x^2 + V_y^2}}{|\mathbf{V}|} \\ -\frac{V_y}{\sqrt{V_x^2 + V_y^2}} & \frac{V_x}{\sqrt{V_x^2 + V_y^2}} & 0 \\ \frac{V_x}{|\mathbf{V}|} & \frac{V_y}{|\mathbf{V}|} & \frac{V_z}{|\mathbf{V}|} \end{bmatrix}
 \end{aligned}$$

EQUATION 9.64

Which is the matrix to rotate an arbitrary axis to the z axis.

### 9.2.5.2. To the z-axis and about

From Equation 9.40 and Equation 9.64:

$$\begin{aligned}
 \mathbf{R}_z \mathbf{M}_z \mathbf{M}_{xz} &= \begin{bmatrix} \cos \theta & -\sin \theta & 0 \\ \sin \theta & \cos \theta & 0 \\ 0 & 0 & 1 \end{bmatrix} \begin{bmatrix} \frac{V_z V_x}{|\mathbf{V}| \sqrt{V_x^2 + V_y^2}} & \frac{V_z V_y}{|\mathbf{V}| \sqrt{V_x^2 + V_y^2}} & -\frac{\sqrt{V_x^2 + V_y^2}}{|\mathbf{V}|} \\ -\frac{V_y}{\sqrt{V_x^2 + V_y^2}} & \frac{V_x}{\sqrt{V_x^2 + V_y^2}} & 0 \\ \frac{V_x}{|\mathbf{V}|} & \frac{V_y}{|\mathbf{V}|} & \frac{V_z}{|\mathbf{V}|} \end{bmatrix} \\
 &= \begin{bmatrix} \frac{V_x V_z \cos \theta}{|\mathbf{V}|} + V_y \sin \theta & \frac{V_x \sin \theta - V_y V_z \cos \theta}{|\mathbf{V}|} & -\frac{\cos \theta \sqrt{V_x^2 + V_y^2}}{|\mathbf{V}|} \\ \frac{\sqrt{V_x^2 + V_y^2}}{\sqrt{V_x^2 + V_y^2}} & \frac{\sqrt{V_x^2 + V_y^2}}{\sqrt{V_x^2 + V_y^2}} & \frac{\sqrt{V_x^2 + V_y^2}}{|\mathbf{V}|} \\ \frac{V_x}{\sqrt{V_x^2 + V_y^2}} & \frac{V_y}{\sqrt{V_x^2 + V_y^2}} & \frac{V_z}{|\mathbf{V}|} \end{bmatrix} \\
 &= \begin{bmatrix} \frac{V_x V_z \sin \theta}{|\mathbf{V}|} - V_y \cos \theta & \frac{V_x \cos \theta + V_y V_z \sin \theta}{|\mathbf{V}|} & -\frac{\sin \theta \sqrt{V_x^2 + V_y^2}}{|\mathbf{V}|} \\ \frac{\sqrt{V_x^2 + V_y^2}}{\sqrt{V_x^2 + V_y^2}} & \frac{\sqrt{V_x^2 + V_y^2}}{\sqrt{V_x^2 + V_y^2}} & \frac{\sqrt{V_x^2 + V_y^2}}{|\mathbf{V}|} \\ \frac{V_x}{|\mathbf{V}|} & \frac{V_y}{|\mathbf{V}|} & \frac{V_z}{|\mathbf{V}|} \end{bmatrix}
 \end{aligned}$$

EQUATION 9.65

Which is the matrix to rotate an arbitrary axis to the z-axis and then rotate about that axis by  $\theta$ .

### 9.2.5.3. To the z-axis, about & to x-z plane projection

From Equation 9.57 and Equation 9.65:

$$\mathbf{M}_z^{-1} \mathbf{R}_z \mathbf{M}_z \mathbf{M}_{xz}$$

$$\begin{aligned}
&= \begin{bmatrix} \frac{V_z}{|\mathbf{V}|} & 0 & \frac{\sqrt{V_x^2 + V_y^2}}{|\mathbf{V}|} \\ 0 & 1 & 0 \\ -\frac{\sqrt{V_x^2 + V_y^2}}{|\mathbf{V}|} & 0 & \frac{V_z}{|\mathbf{V}|} \end{bmatrix} \begin{bmatrix} \frac{V_x V_z \cos \theta + V_y \sin \theta}{\sqrt{V_x^2 + V_y^2}} & \frac{V_x \sin \theta - \frac{V_y V_z \cos \theta}{|\mathbf{V}|}}{\sqrt{V_x^2 + V_y^2}} & -\frac{\cos \theta \sqrt{V_x^2 + V_y^2}}{|\mathbf{V}|} \\ \frac{V_x V_z \sin \theta - V_y \cos \theta}{\sqrt{V_x^2 + V_y^2}} & \frac{V_x \cos \theta + \frac{V_y V_z \sin \theta}{|\mathbf{V}|}}{\sqrt{V_x^2 + V_y^2}} & -\frac{\sin \theta \sqrt{V_x^2 + V_y^2}}{|\mathbf{V}|} \\ \frac{V_x}{|\mathbf{V}|} & \frac{V_y}{|\mathbf{V}|} & \frac{V_z}{|\mathbf{V}|} \end{bmatrix} \\
&= \begin{bmatrix} \frac{V_x(V_x^2 + V_y^2) + V_x V_z^2 \cos \theta + V_y V_z \sin \theta |\mathbf{V}|}{|\mathbf{V}|^2 \sqrt{V_x^2 + V_y^2}} & \frac{V_y(V_x^2 + V_y^2) + V_y V_z^2 \cos \theta - V_x V_z \sin \theta |\mathbf{V}|}{|\mathbf{V}|^2 \sqrt{V_x^2 + V_y^2}} & \frac{V_z \sqrt{V_x^2 + V_y^2}}{|\mathbf{V}|^2} (1 - \cos \theta) \\ \frac{V_x V_z \sin \theta}{|\mathbf{V}|^2 \sqrt{V_x^2 + V_y^2}} - \frac{V_y \cos \theta}{\sqrt{V_x^2 + V_y^2}} & \frac{V_x \cos \theta}{\sqrt{V_x^2 + V_y^2}} + \frac{V_y V_z \sin \theta}{|\mathbf{V}| \sqrt{V_x^2 + V_y^2}} & -\frac{\sin \theta \sqrt{V_x^2 + V_y^2}}{|\mathbf{V}|} \\ -\frac{V_x V_z (\cos \theta - 1)}{|\mathbf{V}|^2} - \frac{V_y \sin \theta}{|\mathbf{V}|} & \frac{V_x \sin \theta}{|\mathbf{V}|} - \frac{V_y V_z (\cos \theta - 1)}{|\mathbf{V}|^2} & \frac{\cos \theta (V_x^2 + V_y^2) + V_z^2}{|\mathbf{V}|} \end{bmatrix}
\end{aligned}$$

EQUATION 9.66

Which is the matrix to rotate an arbitrary axis to the z-axis, rotate about that axis by  $\theta$  and then rotate the z-axis back to the projection of the arbitrary axis in the x-z plane.

### 9.2.5.4. To the z-axis, about & back to original axis

$$\mathbf{M}_{xz}^{-1} \mathbf{M}_z^{-1} \mathbf{R}_z \mathbf{M}_z \mathbf{M}_{xz} = \begin{bmatrix} \frac{V_x}{\sqrt{V_x^2 + V_y^2}} & -\frac{V_y}{\sqrt{V_x^2 + V_y^2}} & 0 \\ \frac{V_y}{\sqrt{V_x^2 + V_y^2}} & \frac{V_x}{\sqrt{V_x^2 + V_y^2}} & 0 \\ 0 & 0 & 1 \end{bmatrix}$$

$$\begin{aligned}
& \left[ \begin{array}{ccc}
\frac{V_x(V_x^2 + V_y^2) + V_x V_z^2 \cos \theta + V_y V_z \sin \theta |\mathbf{V}|}{|\mathbf{V}|^2 \sqrt{V_x^2 + V_y^2}} & \frac{V_y(V_x^2 + V_y^2) + V_y V_z^2 \cos \theta - V_x V_z \sin \theta |\mathbf{V}|}{|\mathbf{V}|^2 \sqrt{V_x^2 + V_y^2}} & \frac{V_z \sqrt{V_x^2 + V_y^2}}{|\mathbf{V}|^2} (1 - \cos \theta) \\
\frac{V_x V_z \sin \theta}{|\mathbf{V}|^2 \sqrt{V_x^2 + V_y^2}} - \frac{V_y \cos \theta}{\sqrt{V_x^2 + V_y^2}} & \frac{V_x \cos \theta}{\sqrt{V_x^2 + V_y^2}} + \frac{V_y V_z \sin \theta}{|\mathbf{V}| \sqrt{V_x^2 + V_y^2}} & - \frac{\sin \theta \sqrt{V_x^2 + V_y^2}}{|\mathbf{V}|} \\
-\frac{V_x V_z (\cos \theta - 1)}{|\mathbf{V}|^2} - \frac{V_y \sin \theta}{|\mathbf{V}|} & \frac{V_x \sin \theta}{|\mathbf{V}|} - \frac{V_y V_z (\cos \theta - 1)}{|\mathbf{V}|^2} & \frac{\cos \theta (V_x^2 + V_y^2) + V_z^2}{|\mathbf{V}|}
\end{array} \right] \\
= & \left[ \begin{array}{ccc}
\frac{V_x^2 + (V_y^2 + V_z^2) \cos \theta}{|\mathbf{V}|^2} & \frac{V_x V_y (1 - \cos \theta)}{|\mathbf{V}|^2} - \frac{V_z \sin \theta}{|\mathbf{V}|} & \frac{V_x V_z (1 - \cos \theta)}{|\mathbf{V}|^2} + \frac{V_y \sin \theta}{|\mathbf{V}|} \\
\frac{V_x V_y (1 - \cos \theta)}{|\mathbf{V}|^2} + \frac{V_z \sin \theta}{|\mathbf{V}|} & \frac{V_y^2 + (V_x^2 + V_z^2) \cos \theta}{|\mathbf{V}|^2} & \frac{V_y V_z (1 - \cos \theta)}{|\mathbf{V}|^2} - \frac{V_x \sin \theta}{|\mathbf{V}|} \\
\frac{V_x V_z (1 - \cos \theta)}{|\mathbf{V}|^2} - \frac{V_y \sin \theta}{|\mathbf{V}|} & \frac{V_y V_z (1 - \cos \theta)}{|\mathbf{V}|^2} + \frac{V_x \sin \theta}{|\mathbf{V}|} & \frac{V_z^2 + (V_x^2 + V_y^2) \cos \theta}{|\mathbf{V}|^2}
\end{array} \right]
\end{aligned}$$

EQUATION 9.67